THE UNIVERSITY *of* EDINBURGH

The stellar populations of the first galaxies

Alexander B. Rogers

Doctor of Philosophy
The University of Edinburgh
2014

Abstract

The stellar populations harboured by some of the Universe's earliest galaxies are within observational reach. Determining the details of these stellar populations and their formation histories within the first billion years after the Big Bang is crucial for both understanding the earliest stages of galaxy evolution and for assessing the contribution of early star-forming galaxies to cosmic reionization. This thesis presents observational measurements of the rest-frame UV and optical colours of star-forming Lyman Break galaxies (LBGs) at redshifts $4 < z < 9$, and their inferred stellar population parameters. By combining ground-based ~ 1 deg^2 surveys with deeper, narrower space-based deep-field surveys, we have constrained the rest-frame UV spectral slope of galaxies over a wide-range of cosmic time ($4 < z < 9$) and luminosity ($-23 < M_{\rm UV} < -17$) in a self-consistent way. To do so, we developed simulations to allow the inference of intrinsic colours from noisy, potentially biased observations. With these simulations, a robust UV colour measurement method was devised in preparation for the Hubble Ultra Deep Field 2012 (UDF12) survey. Then, after delivery of the UDF12 data, our technique and simulations were applied to yield the first bias-free measurements of the UV spectral slope of galaxies at $z \approx 7$ and 8. We found no support for the previously claimed dominant sub-population of exotically blue, faint galaxies at $z \approx 7$. In fact with careful consideration of their errors and selection biases, even the most extreme galaxies we observed can have their colours explained by stellar population synthesis models of unremarkable parameters.

Expanding this study to brighter, rarer, galaxies required the inclusion of wide-area ground-based survey data, and consequently a more focused examination of galaxies at $z \approx 5$. We selected high signal-to-noise galaxies from four fields, with absolute magnitudes spanning $M_{\rm UV} = -22.5$ to -17.5, and measured their rest-frame UV spectral slopes. Coupling these measurements with our simulated observations, we were able to determine the width of the *intrinsic* colour distribution of galaxies at $z \approx 5$. We found that brighter galaxies are not only on average redder than their fainter counterparts, but they are also less self-similar in their colours. The redder average UV colours of brighter galaxies can be attributed to those galaxies being either older, or more dust reddened. By pairing these measurements, which are primarily a probe only of the presently forming portion of the stellar population, with those of LBG's Balmer Breaks, which are more sensitive to bygone star formation, we were able to break this age–dust degeneracy and conclude that, at $z \approx 5$, brighter galaxies are more heavily reddened than fainter galaxies even though their stars are no older.

Lay Summary

The earliest galaxies – those which formed a sizeable portion of their stars within the first billion years after the Big Bang – evolved and merged through cosmic time to build the galaxies of the present Universe, like our own Milky Way. Because light travels at finite speed, the images we collect of very distant galaxies are probes of the past: to look back through cosmic time, we need only look at ever greater distances. The present frontier for distant galaxy observations is at a look-back time of approximately 13 billion years; a galaxy observed at such a distance is observed as it was when the Universe was but 5% its current age. These early galaxies, visible thanks to observatories like the *Hubble Space Telescope (HST)*, harbour populations of stars different to those seen in local, present-day galaxies: the stars are still young and form in an environment comparatively free of dust and metals – both of which take time to build up.

While the very first stars remain out of reach (theoretically predicted Population III stars have yet to be observed), representative samples of the first fully fledged *galaxies* exist. These galaxies, whose hot, young stars radiated bright ultra-violet light, are thought to have been a major contributor to ionizing the neutral Hydrogen gas of the inter-galactic medium during the Epoch of Reionization. However, determining their ability to do so alone – and thus the inferred presence of any more exotic parties required to reinforce the effort – requires a detailed measurement of the typical stellar populations of these earliest star-forming galaxies. Just how blue were they, and how quickly did the galaxies evolve?

In this thesis, we present samples of galaxies observed during the first billion or so years of the Universe. These samples were discovered in large survey images captured from ground-based telescopes as well as smaller, higher-resolution images captured from space – including the deepest near-infrared images ever constructed: the Hubble Ultra Deep Field 2012 data. By carefully selecting and analysing these samples, taking particular care to avoid common biases associated with the discovery of such distant galaxies, we have measured the colours of their starlight.

Contrary to earlier claims, we have shown that even the most distant, faint galaxies observable today are not necessarily composed of exotic metal-free stars: that early galaxy population is just dominated by galaxies similar to the youngest seen at later periods of cosmic time. Still, our measurements have been used to determine that those early galaxies are part of a population capable of reionizing the Universe.

We have also concluded that, within those first billion years after the Big Bang, brighter galaxies are on average dustier than their fainter counterparts. Dust is created by stars at the ends of their lives, but can be destroyed or blown out of galaxies. There seems to be more creation, or better retention, of this dust in the brightest and most massive early galaxies.

Together, these observations aid our understanding of how galaxies built their stars and dust during the first epoch of galaxy formation.

Declaration

I declare that this thesis was composed by myself, that the work contained herein is my own except where explicitly stated otherwise in the text, and that this work has not been submitted for any other degree or professional qualification except as specified.

Parts of this work have been published in the Monthly Notices of the Royal Astronomical Society by Rogers et al. (2013; 2014) and Dunlop, Rogers et al. (2013).

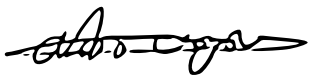

(*Alexander B. Rogers, 2014*)

Acknowledgements

First up I'd like to thank Ross and Jim for excellent supervision and guidance, except for that time Jim led us all down a black ski run instead of a blue. It's been an absolute pleasure.

I'm also hugely grateful to my friends Becca, Emma and Pratika for helping me find all those small contiguous regions of faint red pixels.

To my wonderful office-mates and may-as-well-have-been-office-mates: Chris, Dave, Ferg, JV!, Lars, Lee, Meadie, Nelson, Salome – thank you all! Thanks also to the "cuppa?" and "lunch?" crews: Alice, Ami, Derek, Duncan, Eric, Esther, Fer, Jack, Jesus, Lizzie, Mike, Paula, Sam, Shegy, Tom, Victoria, Vinod, Will and all the other students and postdocs at the ROE for their friendship, support, and for collectively finding small contiguous regions of work-free chat. My thanks go to the ROE staff, particularly Ken Rice, Bob Mann and Phil Best for their roles in quizzing me throughout this PhD programme, and to John Barrow for giving an unreasonably large ammount of his time to help get us all set up.

Back in 2010—11, I was lucky enough to work with Gillian Wright, Adrian Glauser, Alistair Glasse and the rest of the JWST MIRI test team – thank you all for that opportunity. I can't imagine how excited a 10-year-old Sandy would be if you told him he'd one day be staying up all night building a space telescope and eating pot noddles.

I am also most grateful to those in the CANDELS and UDF12 teams, particularly Steve Finkelstein for interesting discussions and for examining my thesis, and Casey Papovich and Brett Salmon for a fascinating (sadly cloudy!) observing run in Chile.

Incredible as it may seem, my Edinburgh friend-group extends outwith the ROE. In particular, Adam, James and JoLo kept me balanced over the last few years with their complaints about accountancy, the NHS, etc., which provided refreshing contrast to complaints about astronomy.

A fair chunk of this thesis was written in the Edinburgh and Cambridge branches of Starbucks, Pret and EAT, so thanks to them for that. On that corporate theme, I'd like to thank the fine folks of Saberr: Ali, Marta, Nik, Sam and Tom, for setting me up with a sweet job post PhD.

Most of all my thanks are to my family: my parents, for buying me a poster of Kitt Peak observatory about 20 years ago and supporting me in this endeavour ever since, my brother Ed, for not taking that poster away even though I'm fairly sure it was actually his, and to Alex, for putting up with me and my presumably quite boring stories about programming.

This research made use of ASTROPY, a community-developed core PYTHON package for Astronomy (Astropy Collaboration et al. 2013), NUMPY and SCIPY (Oliphant 2007), MATPLOTLIB (Hunter 2007), IPYTHON (Pérez & Granger 2007), and NASA's Astrophysics Data System Bibliographic Services. We have also benefitted from the SpeX Prism Spectral Libraries, maintained by Adam Burgasser at `http://pono.ucsd.edu/~adam/browndwarfs/spexprism`. This research made use of TINY TIM/SPITZER, developed by John Krist for the Spitzer Science Center. The Center is managed by the California Institute of Technology under a contract with NASA.

Contents

List of Figures

List of Tables

I think if you do something and it turns out pretty good, then you should go do something else wonderful, not dwell on it for too long. Just figure out what's next.

— Steve Jobs

1 Introduction

Observing the rapid evolution of galaxies and their stellar populations in the first few hundred million years of the Universe represents some of the most promising astrophysical progress of recent years. This thesis is concerned with the robust measurement of the properties of these stellar populations via their rest-frame ultra-violet and optical emission.

In this opening chapter, we introduce the physical processes behind these galaxies' stellar populations, how they relate to the observed colours, and how they are discovered and analysed. We begin by describing the first galaxies in the context of cosmological history (Section 1.2) and their role in the epoch of reionization (Section 1.3). We then discuss the discovery and study of these galaxies in Sections 1.4 – 1.8. In Section 1.9, we review the parameters and processes which give rise to the observed spectral energy distributions of star-forming galaxies. Recent observational advances which have allowed the study of galaxies within the first billion years after the Big Bang are discussed in Section 1.10. Finally, in Section 1.11, we review the most recent literature regarding the stellar populations of these earlier galaxies, as it pertains to this thesis. The layout and publication history of the remainder of the thesis are given in Section 1.12.

1.1 Motivation

The earliest stages of galaxy formation remain the most poorly understood. Galaxy formation models (e.g. Cole et al. 2000) can now, arguably, reproduce the observed global properties of the high-redshift galaxy population over a respectable span of cosmic time. However the details of how galaxies build their initial stellar populations and dust distributions are less well known. These processes are crucial to later galaxy evolution, since the earliest-forming stars rapidly enrich their environment with metals, are presumably responsible for the feedback processes which limit the rate of star formation at early times, and are believed to have initiated and sustained Universal reionization (e.g. Robertson et al. 2010). In order to determine the mechanisms by which these processes progress, the last few decades have seen the observational frontier be steadily pushed further back in cosmic time, such that this century has witnessed the analysis of large samples of galaxies forming within the first billion years after the Big Bang. This thesis therefore focusses on this early epoch of galaxy formation, and in particular on the assembly of the stellar populations harboured by star-forming galaxies. As we shall see, key questions regarding the star-formation, dust build-up, and metallicity histories of these early galaxies have hitherto remained unanswered.

1.2 The Universe before galaxies

For 20 minutes after the Big Bang, the scale and temperature of the Universe were sufficiently small and hot that Universal Nucleosynthesis (e.g. Hinshaw et al. 2013, Olive et al. 2000, Wagoner 1973) created nuclides as heavy as ^{7}Li, before the rapid expansion and cooling brought synthesis to an end. 370 Kyr later, the predominant Hydrogen had cooled sufficiently to recombine, emitting a radiation field now observed as the Cosmic Microwave Background (CMB, Fixsen et al. 1996, Hinshaw et al. 2013, Planck Collaboration et al. 2013). A further 370 Myr separates the CMB emission, now observed at $z \approx 1100$, and the star bursts observed in the earliest galaxies yet (tentatively) detected at $z \approx 12$ (Ellis et al. 2013). During those intervening dark ages, the baryonic matter of the Universe existed largely as neutral atomic Hydrogen (H I). As the first massive stars (which were metal-free, by definition) formed in the deepest dark-matter halos, their intense ultraviolet (UV) emission started to ionize the Hydrogen around them (Heger & Woosley 2002, Schaerer 2002, Tumlinson et al. 2004). Whether these first 'Population-III' stars contributed significantly to the metal enrichment of their environments depends on both their prevalence and the mechanism by which they collapse, neither of which are known.

For instance, Tumlinson et al. (2004) argued that the most effective ionizing sources, stars of mass $50-140\ M_{\odot}$, collapse into black holes and thereby do not release any metals into the inter-stellar medium (ISM). Therefore the ionization and metal enrichment due to the first stars may be decoupled from one another.

1.3 Reionization and the inter-galactic medium

Forming throughout the Universe, those first stars ushered in the epoch of reionization (EOR, e.g. Robertson et al. 2010). Prior to and during the EOR, the Universe was extremely opaque to photons capable of ionizing H I, including Lyman continuum ($\lambda < 912$ Å) and Lyman$-\alpha$ ($\lambda = 1216$ Å) UV light. Even after the end of the EOR, H I clumps remained in the inter-galactic medium (IGM). Because H I is a very efficient absorber of photons at the resonant Lyman$-\alpha$ line, its presence, even at those low densities, effectively extinguishes the flux of a background source at $\lambda_{\rm absorber} = 1216$ Å. Since this attenuation occurs for every absorber along the line of sight to a distant (cosmologically redshifted) source, the rest-frame wavelength of photons resonant with Lyman$-\alpha$ is different for absorbers at different distances (Gunn & Peterson 1965). The UV spectra from high-redshift galaxies and quasars therefore show a 'Lyman$-\alpha$ forest' with many absorption lines, due to many H I clouds not associated with the source, at $\lambda_{\rm rest} < 1216$ Å (e.g. Sargent et al. 1980). For sufficiently high-redshift sources, the sheer number of intervening absorbers causes total absorption of flux at $\lambda_{\rm rest} < 1216$ Å (Guhathakurta et al. 1990, Madau 1995). Such a 'Gunn-Peterson trough' was first observed in the spectrum of a quasar at $z = 6.28$ by Becker et al. (2001), the implication being that the neutral fraction of Hydrogen in the Universe changed significantly at a cosmic time corresponding to $z \approx 6$, marking the end of the EOR.

To create and sustain this ionization, the ~ 500 Myr between the formation of the first stars (thought to have occurred at $z \gtrsim 12$)[1] and the near-complete ionization of the Universe by $z \approx 6$ saw the rapid formation of galaxies throughout the Universe. In order to understand the process of reionization, its energy budget has to be balanced (e.g. Robertson et al. 2013). This requires that both the number density (via the luminosity function, e.g. Section 1.7 and Bouwens et al. 2011, Bowler et al. 2014, McLure et al. 2013, Schechter 1976, Schenker et al. 2013, Steidel et al. 1999) and the ionizing photon output (via the UV spectral slope β, e.g. Section 1.9.2 and Bouwens et al. 2013, Dunlop et al. 2013, Finkelstein et al. 2012b, Meurer et al. 1999, Shapley et al. 2003, Wilkins et al. 2012) of the sources are known. Combining these then allows an ionizing photon production rate to be computed and input into reionization calculations (e.g. Finkelstein et al. 2012a, Robertson et al. 2013). Chapters 3 and 4 of this thesis are concerned with the measurement of β during the EOR.

[1] The CMB temperature was then 35 K - see Section 1.9.2.

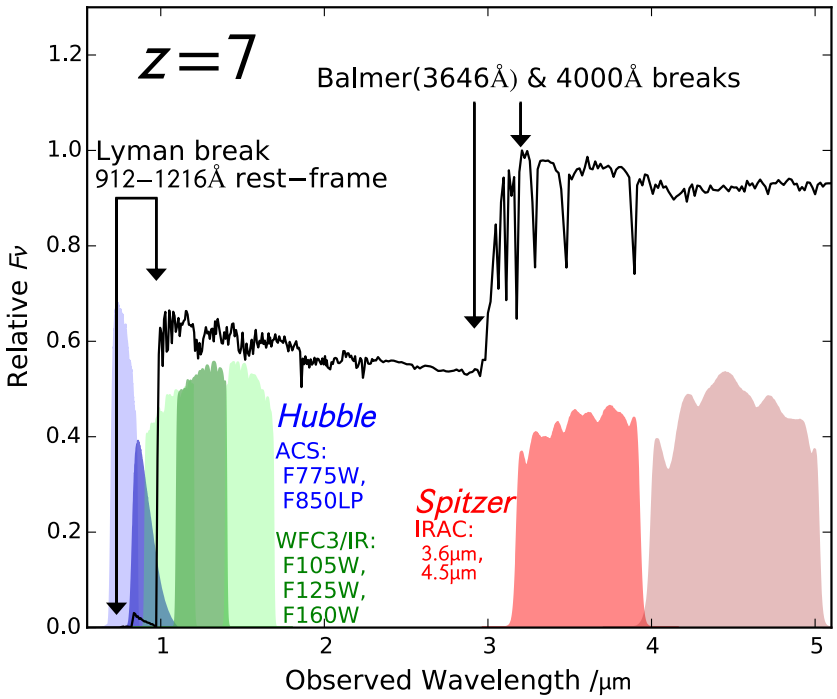

Figure 1.1 An illustration of how the spectral energy distribution of a $z = 7$ Lyman break galaxy (black line) is observed through *HST* and *Spitzer* bands. The primary identifier of these galaxies is the large Lyman break between the *HST* ACS and WFC3/IR bands (blue and green). The rest-frame UV is then probed by colours sampled by the WFC3/IR bands. At these redshifts, *Spitzer* photometry is required to constrain the presence and size of the Balmer and 4000 Å breaks.

1.4 Lyman break galaxies

Because H I is such an effective absorber of $\lambda < 1216$ Å photons, the Lyman–α decrement is a particularly strong spectral feature at high redshift: sufficient to select Lyman break galaxies (LBGs) based on it. However, historically, the 'LBG technique' was used at more moderate redshifts, where the neutral fraction of the IGM is very low. The first LBGs were found instead by a flux decrement at rest-frame 912 Å, caused by neutral Hydrogen *in* galaxies being ionized ($N = 1 \rightarrow \infty$) by Lyman continuum photons (those more energetic than the Lyman limit at $\lambda_{\rm rest} < 912$ Å). In this incarnation of LBG selection, the Hydrogen responsible for the break is that in the photospheres of stars and in the ISM. This selection mechanism proved to be a very reliable method for selecting high-redshift star-forming galaxies. The strength of the break, coupled with an otherwise blue rest-frame UV continuum, made LBG selection possible with efficient, broad-band filters. The suggested existence of a population of star-forming galaxies at $z \gtrsim 3$, by the pioneering

studies of Steidel & Hamilton (1992; 1993), Steidel et al. (1995), and Madau et al. (1996), was soon borne out by spectroscopic confirmation (e.g. Steidel et al. 1996). $z \approx 3$ proved a convenient epoch to study, since it was the lowest redshift at which the Lyman limit fell within optical filters (UGR, Steidel & Hamilton 1993). As observations pushed to higher redshifts, where the increasingly dense Lyman forest created a more complete Gunn-Peterson trough, LBG selection naturally turned to colours straddling the termination of the Lyman series, Lyman$-\alpha$ at 1216 Å, where a large flux step is expected at $z \gtrsim 5$ (Madau 1995). Fig. 1.1 demonstrates the severity of this 1216 Å Lyman break by $z = 7$ and how the break is observed as a 'dropout' in broad-band photometry.

1.5 Lyman$-\alpha$ emitters, and their rise and fall at high redshift

While neutral Hydrogen causes Lyman$-\alpha$ absorption, and eventually the Lyman break, high-redshift quasars have long been known to also be emitters of Lyman$-\alpha$ (e.g. Schmidt 1965). Partridge & Peebles (1967) noted that young star-forming galaxies, should they have observable Lyman$-\alpha$ emission lines like those already observed from high-redshift quasars, should be readily selectable. Despite predicted difficulties due to dust absorption (Charlot & Fall 1993), reports of candidate (and some confirmed) Lyman$-\alpha$ emitters (LAEs) became common through the 1990s, due to their relative ease of selection when the Lyman$-\alpha$ emission is combined with a faint continuum; the ratio of emission-line flux to continuum within a filter increases with redshift as $(1+z)$. The productive technique of looking for the narrow-band excess produced by these Lyman$-\alpha$ lines heralded the discovery of large samples of LAEs at $z \gtrsim 5$ (Hu et al. 1998). The selection of these LAEs is helped to some extent by the seeming lack of decline in the number and luminosity density of LAEs out to $z \approx 5$ (Ouchi et al. 2008); this is in contrast to the LBG density which does decline, at fixed luminosity, from $z = 2$ to $z = 5$ as we shall see.

For some time, LAEs remained the only routinely accessible population of 'normal' (i.e. non-quasar) high-redshift galaxies (Dunlop 2013). Now, high-redshift LAEs are thought to simply be a subset of the star-forming galaxy population at large (all of which could in principle be selected as LBGs, e.g. Dayal & Ferrara 2012). In fact, the first normal galaxy to be spectroscopically confirmed at $z > 5$ was selected serendipitously in a hunt for $z \gtrsim 4$ LBGs, but confirmed by its Lyman$-\alpha$ emission (Dey et al. 1998). Observationally, the presence and strength of Lyman$-\alpha$ emission in LBG-selected galaxies appear to only mildly correlate with other galaxy properties; hence genuine LAE-selected galaxies are only mildly (if at all, e.g. Dayal & Ferrara 2012) different from the average LBG, with some of the apparent differences being attributable to the differing selection functions. However,

notable observations include a lack of massive galaxies with high equivalent width (EW) Lyman−α (Pentericci et al. 2009), and an average lower EW of Lyman−α in the dustiest galaxies (Finkelstein et al. 2008, Pentericci et al. 2009; 2007, Shapley et al. 2003).

In terms of redshift dependence, the aforementioned discrepancy between the decline in the fixed-luminosity density of LBGs compared to LAEs out to $z \approx 5$ (Ouchi et al. 2008) culminates in a high fraction of LBGs being LAEs at $z \approx 6$ (Curtis-Lake et al. 2012, Stark et al. 2010, Stark et al. 2011, Vanzella et al. 2009). Recent evidence has suggested there is then a marked step in the prevalence of LAEs amongst LBGs between $z \approx 6$ and 7 (Hayes et al. 2011, Pentericci et al. 2011, Schenker et al. 2012), such that few $z \approx 7$ LAEs have been confirmed thus far. While both the evolution and mild coupling between LAE properties and their galaxies' stellar population properties are both plausibly explained by a build-up of dust at $z < 7$ (Stark et al. 2010), a different process – a change in IGM transmission – is thought to account for the rapid change at $z \gtrsim 7$. However there is not a complete dearth of LAEs at $z > 7$: spectroscopic follow-up of LBG candidates has successfully, although in some cases tentatively, revealed Lyman−α emission in some of these targets (Finkelstein et al. 2013, Lehnert et al. 2010, Ota et al. 2008, Stark et al. 2007, Vanzella et al. 2011). Overall, it is evident that only a small fraction of the Lyman−α emitted by star-forming regions at $z > 7$ ever escapes those galaxies and traverses the IGM without being absorbed by neutral Hydrogen.

1.6 The global history of star formation

The properties of the first observed LBGs implied that star formation (SF) was already well under way by $z = 3$. In a seminal paper based on Hubble Deep Field (HDF) data, Madau et al. (1996) found that the luminosity density (the integrated light from high-redshift galaxy populations as a whole) increased substantially from $z = 4$ to $z = 2$ (before then decreasing again to $z = 0$, Lilly et al. 1996). However Steidel et al. (1999), based on a larger ground-based survey of typically brighter galaxies, concluded that the luminosity density was essentially constant at $z > 1$. This relied, however, on their inclusion of a correction for interstellar dust extinction which rose with increasing redshift beyond $z = 2$ – 3. As shown in Fig. 1.2, reproduced from Bouwens et al. (2011), later observations out to higher redshifts have shown a marked decline in the luminosity density with increasing redshift. Converting the UV luminosity density to a star-formation rate (SFR) density requires simply making some assumptions about how the UV-emitting stellar population was built up. Typically one assumes that SF has been proceeding at a constant rate for $\gtrsim 100$ Myr up to the time of observation (Madau et al. 1998, but see Verma et al. 2007).

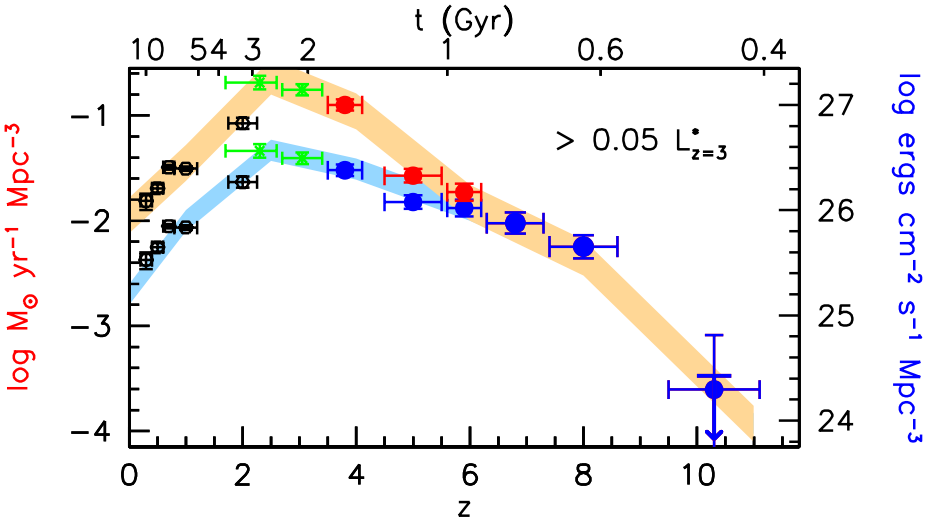

Figure 1.2 The luminosity density and star-formation rate density functions before (blue) and after (red) correcting for interstellar dust. The 'Madau plot' (the luminosity density) was derived by measuring luminosity functions (Section 1.7) at each epoch, and integrating them down to a fixed luminosity – here −17.7 mag (0.05 $L^*_{z=3}$). This was then converted to a SFR density function by assuming that the UV continuum is due to a stellar population built by $\gtrsim$ 100 Myr of constant SF, and according to a Salpeter (1955) initial mass function (Madau et al. 1998). [After Bouwens et al. (2011).]

Doing so results in a SFR density function which increases with cosmic time to $z \approx 2$, and then drops to $z = 0$ (e.g. Sargent et al. 2012).

Although the integrated SFR density drops moving to higher redshifts, the specific star-formation rate

$$\mathrm{sSFR} = \frac{\mathrm{SFR}}{M_*} \tag{1.1}$$

does not. (M_* is the stellar mass of a galaxy.) This proportionality, SFR$\propto M_*$, implies that galaxies follow some form of 'Main Sequence' (e.g Noeske et al. 2007). In this scenario, the buildup of cosmic stellar-mass density (Papovich et al. 2004) then has to approximately trace that of the UV (i.e. star-forming) luminosity density.

However the $z > 2$ evolution of the sSFR has been contentious recently. González et al. (2010) reported that the sSFR remains constant at $z \gtrsim 2$ (replicated in Fig. 1.3). This was immediately controversial because it was hard to reconcile with galaxy-formation models constrained by other observables (Weinmann et al. 2011). Most authors now agree that the sSFR in fact rises at $z > 2$, but more mildly than at $0 < z < 2$ (de Barros et al. 2014, González et al. 2014, Smit et al. 2014, Stark et al. 2013). Part of this revision is due to the realisation that the masses of the highest-redshift galaxies were perhaps being systematically over-estimated due to nebular emission-line contamination (see Section 1.9.5).

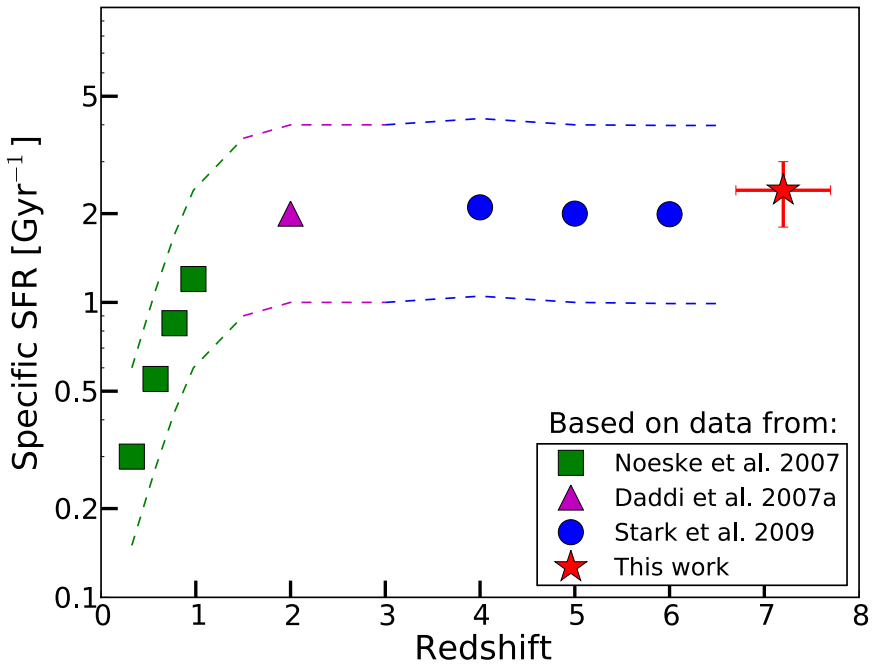

Figure 1.3 The specific star-formation rate (sSFR=SFR/stellar mass) as a function of redshift. While the SFR density decreases with increasing redshift from $z \gtrsim 2$ (Fig. 1.2), the sSFR is here shown to plateau such that SFR $\propto M_*$. This is now disfavoured: the sSFR is observed to rise with increasing redshift at $z > 2$ (see text). [After González et al. (2010).]

1.7 The luminosity function

We have seen that the global UV luminosity density – measured in flux per unit comoving volume – evolves with redshift, tracing the star-formation rate density. However, this integrated property does not specify anything about the properties of those galaxies from which the UV light emanates. Understanding galaxy evolution requires that the total SFR density can be apportioned to galaxies of various properties, and that these can be traced between epochs. This apportioning is provided by the luminosity function (LF), which reports the (co-moving volume) number density of galaxies of a given luminosity at a given redshift or epoch. The shape, luminosity integral, and redshift evolution of the LF are key measurements in galaxy evolution, and primary requirements for galaxy-formation simulations to reproduce (e.g. Cole et al. 2000, Dayal et al. 2013).

Schechter (1976) provided a now widely used parametrization for the LF, which follows a power law in luminosity governed by a slope α with an exponential cut-off at the bright end:

$$\phi(L)\mathrm{d}L = \phi_* \left(\frac{L}{L_*}\right)^{\alpha} \exp\left(-\frac{L}{L_*}\right) \mathrm{d}\frac{L}{L_*}, \tag{1.2}$$

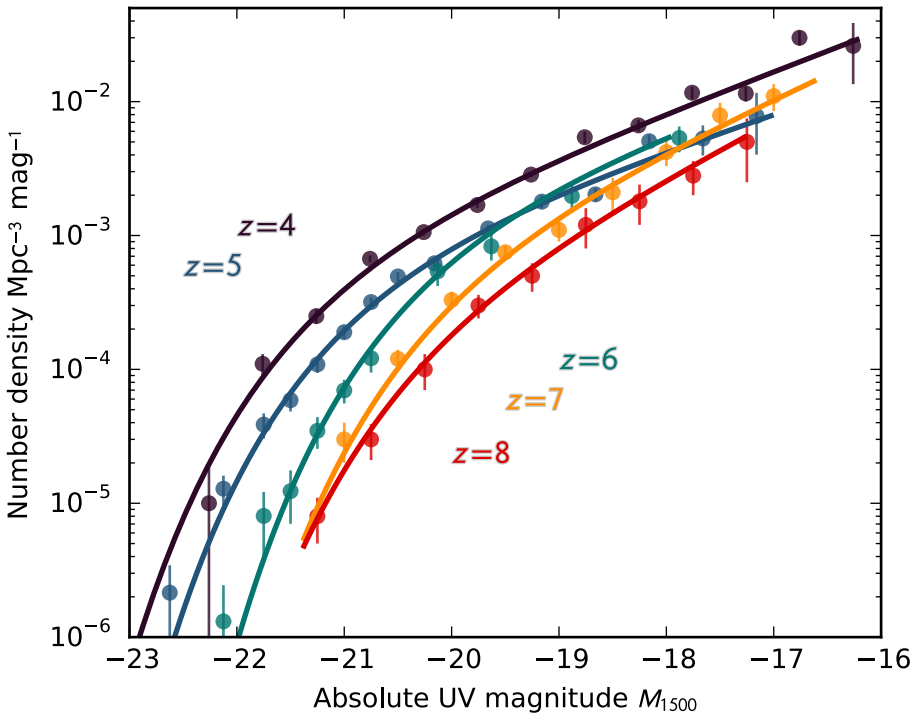

Figure 1.4 The redshift evolution of the LBG rest-frame UV luminosity function, combining data from Bouwens et al. (2007) and McLure et al. (2009) at $z = 4, 5, 6$ and from McLure et al. (2013) at $z = 7$ and 8. With increasing cosmic time at fixed co-moving number density, the luminosity density of galaxies increases as more galaxies form more stars.

where L_* is the characteristic 'knee' value of the luminosity L, and ϕ_* is the normalisation of the number density. Despite being motivated by observations of the local Universe, the Schechter function has outlived this regime, being applied to observations as distant as $z \approx 9$ (McLure et al. 2013) without severely failing to be fit to the available data (but see Bowler et al. 2014). This endurance is particularly remarkable since the mechanisms controlling SF in the early Universe (gas accretion, e.g. Finlator et al. 2011, Papovich et al. 2011) are thought to be different from those at later epochs (feedback from active-galactic nuclei, e.g. Schawinski et al. 2007).

Luminosity functions can be computed at any rest-frame wavelength, thereby targeting different stellar-population properties. For instance the Hα LF, which measures the line-flux distribution of the Hα emission line (the first Balmer transition of Hydrogen, Ba-α), can be used to specifically target the present SFR (Sobral et al. 2013). Similarly, the rest-frame optical LF can be used as a proxy for the galaxy stellar-mass function (e.g. Fontana et al. 2006). At $z \gtrsim 5$, where large galaxy samples have to date only been found through searches for LBGs, only the rest-frame UV LF has been robustly measured. Crucially, it appears that the faint-end slope of the rest-frame UV LF at $z \approx 7$ is sufficiently

steep that extrapolating and integrating the LF to low luminosities (below those actually probed by observations) provides a sufficient supply of ionizing UV photons to maintain reionization during the EOR (Bouwens et al. 2012b, Finkelstein et al. 2012a, McLure et al. 2013, Robertson et al. 2013).

There is also strong evidence for LF evolution over the relatively short span of cosmic time $z = 9 \rightarrow 5$. Fig. 1.4 shows the rest-frame UV LFs of LBGs at $z = 4, 5, 6, 7, 8$. There is general agreement over these LFs of high-redshift galaxies (Bouwens et al. 2012b, Dunlop 2013, McLure et al. 2013), but the physical mechanisms behind the evolution remain unproven: both 'density evolution' – whereby the number of galaxies of a given brightness in a given volume grows with time – and 'luminosity evolution' – where the 'same' population of galaxies is observed to grow brighter with time at constant number density – are plausible explanations. The latest results (McLure et al. 2013) suggest that the $z = 8 \rightarrow 7$ evolution is more akin to density evolution, while the $z = 7 \rightarrow 5$ evolution is more akin to luminosity evolution; however current observational constraints cannot rule conclusively either way.

1.8 Individual star-formation histories

For galaxies to follow the Main Sequence (Section 1.6) on more than merely an average basis, the star formation in individual galaxies has to rise smoothly as their stellar mass is built up. There is evidence that this may be the case at high redshift, with smoothly rising star-formation histories (SFHs) being apparent in both observations (Reddy et al. 2012b, Wuyts et al. 2011) and simulations (Finlator et al. 2006; 2011). Rising SFHs would also account for the observed stellar mass–UV luminosity relation, which implies that galaxies of the same UV luminosity at e.g. $z = 4$ and $z = 6$ are not the same population, but are instead the galaxies which at each epoch have just 'reached' that UV luminosity (Curtis-Lake et al. 2013, Stark et al. 2009). This fact can also, however, be explained by stochastic SFHs, which could still give rise to the average stellar-mass and luminosity density functions.

To derive a consistent understanding of how galaxies are built from $z = 8 \rightarrow 3$, Papovich et al. (2011) selected high-redshift galaxies at constant comoving number density. This approach allowed the study of progenitor and descendant populations of galaxies better than a UV-luminosity limited (≈SFR-limited) sample selection, under the assumption than the constant-density populations are representative evolutions of one another at each epoch. These data were found to be consistent with the average galaxy's SFH increasing

with time as either a power law,

$$\psi(z) = \left(\frac{t}{180 \pm 40\,\mathrm{Myr}} \right)^{1.7\pm0.2} \mathrm{M}_\odot\,\mathrm{yr}^{-1}, \tag{1.3}$$

or perhaps exponentially (see also Maraston et al. 2010, Renzini 2009),

$$\psi(z) \approx 1.4 \exp\left(\frac{t}{420\,\mathrm{Myr}} \right) \mathrm{M}_\odot\,\mathrm{yr}^{-1}. \tag{1.4}$$

One interpretation of this is that the SFR of galaxies at $z \gtrsim 4$ follows directly from the gas accretion rate, but at later epochs the SFR relations diverge from those implied by gas accretion (Papovich et al. 2011). Indeed by $z \sim 2.3$, there exists a population of massive galaxies with apparently heavily suppressed SF (Kriek et al. 2006).

1.9 The spectral energy distributions of star-forming galaxies

We have seen thus far that high-redshift star-forming galaxies, detected as LBGs or LAEs and often confirmed spectroscopically by their Lyman–α emission, evolve such that the global SFR density initially rises from $z \approx 9 \rightarrow 2$, before falling. Fig. 1.5 summarises this picture, and shows that the UV continuum of galaxies gets bluer at higher redshift. In this section, we therefore derive the UV continuum of a star burst based on fundamental properties, and describe the factors which contribute to the rest-frame UV and optical spectral energy distributions (SEDs) of LBGs.

1.9.1 Star-burst galaxies

Local star-burst galaxies, in which a sizeable fraction of the stellar mass has been created in recent, intense periods of SF, are known to differ morphologically from other galaxies (Larson & Tinsley 1978), and of course be bluer (Searle et al. 1973). The recent decline in global SF (Lilly et al. 1996) seems consistent with *most* galaxies experiencing an exponential decline in their SFR over the last ~ 10 Gyr (Searle et al. 1973). However prior to this decline, star-forming galaxies appear more similar to local star-bursts galaxies. This is borne out by both observations (e.g. Lowenthal et al. 1997) and simulations (e.g. Somerville et al. 2001). A physical picture in which high-redshift galaxies evolve quiescently, punctuated by merger-induced star bursts now seems credible at $z \gtrsim 2$ (Gehrz et al. 1983, Kauffmann et al. 2003, Shapley et al. 2005, Somerville et al. 2001).

It remains unclear whether galaxies as early as $z \gtrsim 5$ follow the same SFHs as those at $z \approx 2$. In any case, single, multiple, or integrated star-burst histories are typically assumed when fitting the observed SEDs of these galaxies (Curtis-Lake et al. 2013, McLure et al. 2011, Pacifici et al. 2012).

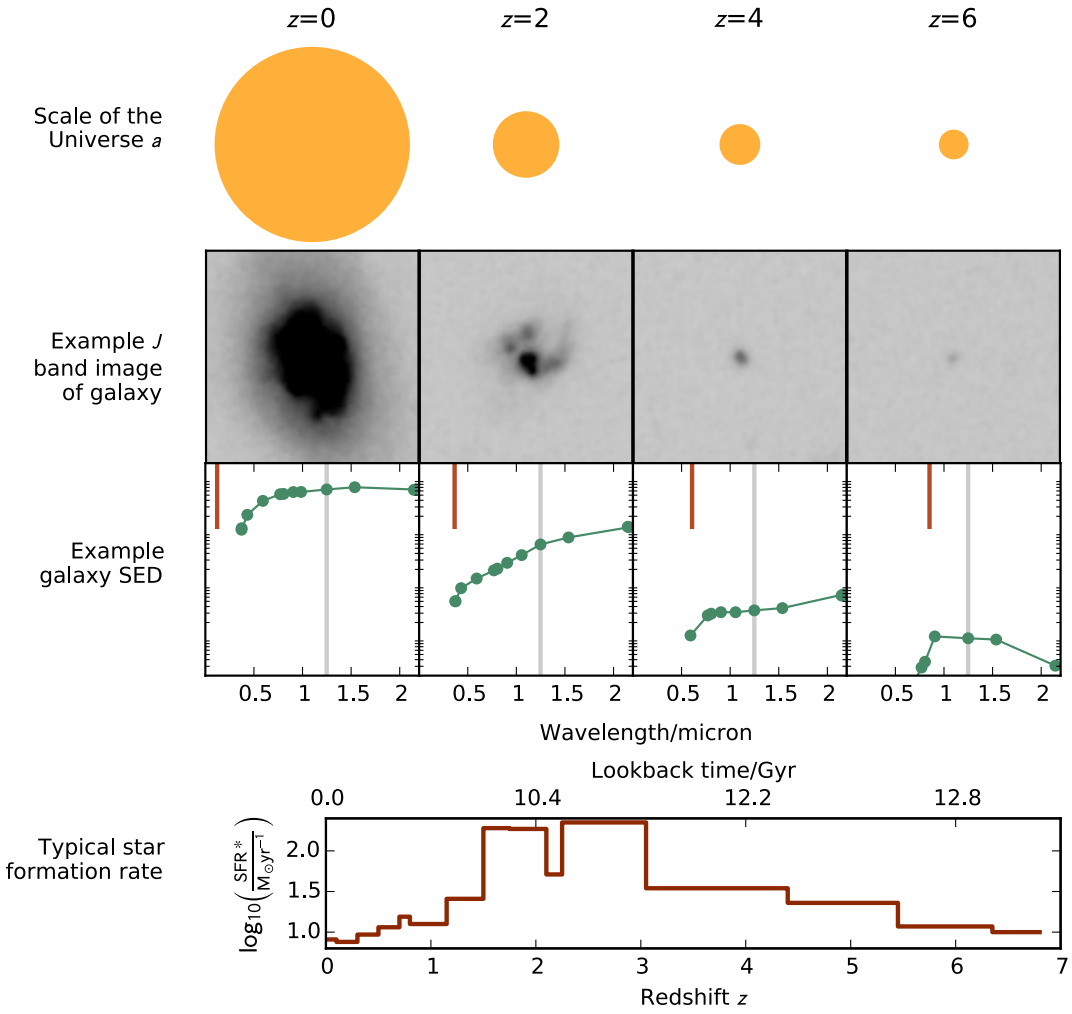

Figure 1.5 The evolution of galaxies throughout cosmic time. The circles in the first (top) row represent the scale of the Universe at redshifts $z = 0, 2, 4, 6$: their radius is $a \propto 1/(1+z)$. The second row shows the J-band (1.25 μm) image of an example galaxy spectroscopically confirmed to lie near each redshift, chosen randomly from the GOODS-S field (images from CANDELS, Grogin et al. 2011, Koekemoer et al. 2011; spectroscopic redshifts from the ESO GOODS/CDF-S Spectroscopy master catalogue). Below each galaxy is its spectral energy distribution, derived from the CANDELS photometric catalogue by Guo et al. (2013). The grey vertical lines mark the J band, while the short red lines mark the redshifted position of the Lyman–α emission line for each galaxy. Higher-redshift galaxies are fainter, smaller, and bluer in the rest-frame UV (near Lyman–α). Finally, the bottom row shows the 'typical' star-formation rate (SFR) of galaxies as a function of redshift, where 'typical' refers to the characteristic parameter SFR* in the measured SFR evolution function of Smit et al. (2012). This steadily increases as time progresses (i.e. lookback time decreases) for the first 3 Gyr, where it peaks at $z \approx 2$ before declining to its present low value.

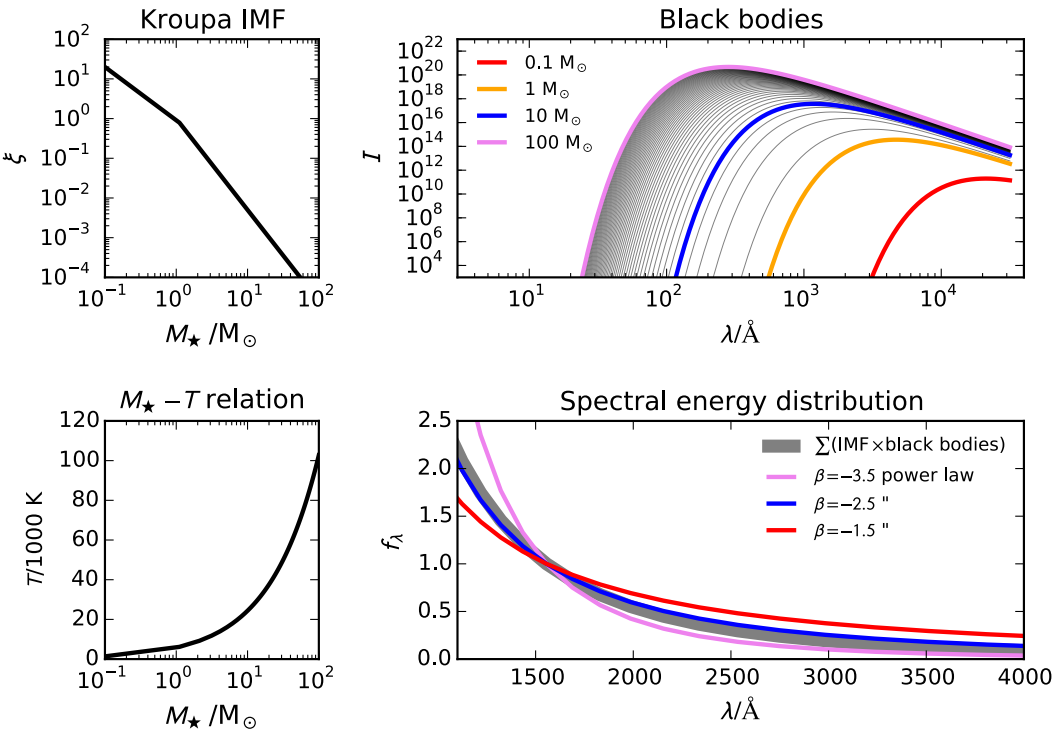

Figure 1.6 An explanation of how the UV continuum of young galaxies arises from the stellar initial mass function and black-body models. The top left panel shows the Kroupa (2001) initial mass function, and the bottom left panel shows the effective (black-body) temperature of stars of given mass (assuming the scaling relation $T \propto M_*^{0.625}$). Black-body spectra for a range of stellar temperatures are shown in the top right panel. By multiplying the IMF by the corresponding black-body curve at a range of masses, and summing together the resultant scaled black-body curves, an overall SED is derived for the stellar population. This is shown in the bottom right panel, alongside pure power-law curves with three spectral indices $\beta \in \{-3.5, -2.5, -1.5\}$.

1.9.2 Deriving the UV continuum of a star-forming galaxy

The UV light of star-forming galaxies is dominated by the most recently formed stellar population. During any star-formation event, the governing relation is the initial mass function (IMF), which quantifies what fraction of the total forming stellar mass is formed in stars of any given mass. All IMFs, which are usually parametrized as $\xi(M_*) \propto M_*^\alpha$ or a piecewise combination thereof (Chabrier 2003, Kroupa 2001, Salpeter 1955), predict massive stars to be much rarer than less massive stars. Still, the strong dependence of luminosity on stellar mass,

$$L_* \propto M_*^{3.5}, \tag{1.5}$$

(e.g. Rolfs & Rodney 1988) allows the rarer massive stars to still dominate the total light for a short period of time.

These rare but briefly dominant massive stars have hot effective temperatures. As shown in Fig. 1.6, where we have assumed a scaling relation between M_* and effective temperature T_* of

$$\left(\frac{T}{\mathrm{T}_\odot}\right)^4 = \left(\frac{M}{\mathrm{M}_\odot}\right)^{2.5}, \tag{1.6}$$

the combined flux of (idealised black-body) stars across the IMF approximates a power-law continuum. This power-law spectral slope is parametrized as β and defined by

$$f_\lambda \propto \lambda^\beta \tag{1.7}$$

(e.g. Calzetti et al. 1994, Meurer et al. 1999). Adopting a Kroupa (2001) IMF,

$$\xi(M_*) \propto \begin{cases} M_*^{-2.3}, & \text{if } M_* \geq 0.5\mathrm{M}_\odot, \\ M_*^{-1.3}, & \text{if } 0.008 \leq M_* < 0.5\mathrm{M}_\odot, \\ M_*^{-0.3}, & \text{if } M_* < 0.008, \end{cases} \tag{1.8}$$

restricted to $M_* \leq 100$ $\mathrm{M}_\odot$, implies that the rest-frame UV continuum of a zero-age star burst should have a spectral index $\beta = -2.4$. This is a slightly bluer than flat spectrum ($\beta = -2$ implies a flat spectrum in f_ν and zero colour in the AB magnitude system of Oke & Gunn 1983).

As we shall see, this derivation is in surprisingly good agreement with the outputs of stellar population synthesis (SPS) models, which model stellar atmospheres in detail, and with observations (e.g. Leitherer et al. 1999).

The IMF

Clearly, based on the preceding argument, the shape of the IMF is of critical importance in relating the stellar mass of a star burst to the light we observe from it. The popular Kroupa (2001), Salpeter (1955) and Chabrier (2003) IMFs predict mass to light ratios discrepant from one another by factors of ~ 2, such that the same observed luminosity is interpreted as different stellar masses in each case:

$$M_*^{\mathrm{Chabrier}} = 0.55 M_*^{\mathrm{Salpeter}}, \tag{1.9}$$

$$M_*^{\mathrm{Kroupa}} = 0.62 M_*^{\mathrm{Salpeter}} \tag{1.10}$$

(Longhetti & Saracco 2009).

The UV colours of star-forming galaxies are, however, slightly less sensitive to *these* differing IMFs than the total stellar mass. For instance based on the simple calculation shown in Fig. 1.6, adopting the single power-law IMF of Salpeter (1955),

$$\xi(M_*) \propto M_*^{-2.35}, \tag{1.11}$$

implies a UV continuum spectral index of $\beta = -2.3$ instead of Kroupa's $\beta = -2.4$.

However, sufficiently modified IMFs can have a bigger effect on β. A 'top-heavy' altered Kroupa IMF,

$$\xi(M_*) \propto \begin{cases} M_*^{-1.8}, & \text{if } M_* \geq 0.5 \\ \dots \end{cases} \tag{1.12}$$

implies $\beta = -2.7$, whereas a 'bottom-heavy' IMF,

$$\xi(M_*) \propto \begin{cases} M_*^{-3}, & \text{if } M_* \geq 0.5 \\ \dots \end{cases} \tag{1.13}$$

implies $\beta = -1.6$.

There is now, arguably, observational evidence to suggest that the IMF is not universal: that it varies with cosmic time, metallicity and (galactic-) stellar mass. There remains debate over whether the IMF should theoretically be universal, what physical mechanisms should underpin any variation, and whether high-redshift galaxies should have a bottom- or top-heavy IMF (Bastian et al. 2010)

If one assumes the once-popular paradigm of bimodal star-formation (e.g. Shu et al. 1987), whereby low- and high-mass stars are formed in cold (∼10 K) and hot (∼20 K) molecular clouds, the presence of a warm IR background would be expected to inhibit low-mass star formation. Since the blackbody temperature of the CMB incident on galaxies observed at high-redshift scales as $T_{\rm CMB} \propto 1 + z_{\rm obs.}$, a galaxy at $z = 6$ has star-forming clouds warmed by a $2.7 \times (1 + 6) = 19$ K radiation field, while the CMB incident upon the Milky Way is cooler than even the coldest molecular clouds. Thus for many years it was thought, and tentatively observed, that high-redshift star-burst galaxies should exhibit a top-heavy (or, bottom-light) IMF (Baugh et al. 2005, Hopkins & Beacom 2006, Larson 1998; 2005, Stanway et al. 2005, Tumlinson 2007, van Dokkum 2008). The observational evidence was however uncertain. The discovery of very blue UV continua in $z \approx 6$ galaxies by Stanway et al. (2005) implied an abundance of high-mass stars, but could equally have been due to a lack of dust. Based on a comparison of the UV—optical colour evolution and luminosity evolution

of massive cluster galaxies, van Dokkum (2008) also found evidence for a top-heavy IMF – but the conclusion hinged on the accuracy of stellar population synthesis models. More recently however, van Dokkum & Conroy (2010; 2011; 2012) and Conroy & van Dokkum (2012) have reported bottom-heavy 'dwarf-enriched' IMFs in massive early galaxies.

Many lines of evidence therefore point to the IMF being non-universal, and this would have a non-negligible effect on the UV continua we observe. But at present, no observation at $z > 5$ – the regime studied in this thesis – has *required* IMF variation to explain it.

Metallicity dependence

Metal-poor stars (those presumably present in the very earliest galaxies) have a decreased internal opacity, since there are fewer metals with high electron counts contributing to bound-free opacity. Since the effective temperature of stars depends on their radius, and therefore opacity, the zero age main sequence of metal-poor stars is shifted blue relative to the solar metallicity main sequence. Hence β is in principle sensitive to metallicity, albeit fairly weakly.

As we shall see throughout this thesis, low metallicities provide one (of several) explanations for the blue colours of high-redshift LBGs.

Dust

So entwined are β and dust reddening that they are often quoted almost interchangeably.

The presence of dust – molecules and grains with a size distribution roughly bracketed by 1 nm to 1 μm (Weingartner & Draine 2001) – has long been known to play an eminent role in high-redshift systems (e.g. Pei et al. 1991). Its presence in galaxies of all types out to the very highest redshifts implies at least some portion of dust is created in rapid processes. However, even on the constricted time-scales available for dust formation at $z \gtrsim 6$, when the Universe was only ≈ 1 Gyr old, the formation mechanism remains illusive. Both massive ($\gtrsim 3\,M_{\odot}$) stars on the asymptotic giant branch and core-collapse supernovae can produce significant quantities of dust on this time-scale (Gall et al. 2011).

Theoretical models of galaxy formation and evolution still typically calculate only the assembly of dark matter, gas, star particles, and metal enrichment – not dust; the assumption is that dust should follow the gas distribution and metal enrichment history (e.g. Dayal et al. 2013), but this is not proven.

Regardless of the unknown formation mechanism, many high-redshift studies require the use of an at least plausible dust reddening curve to convert the observed (i.e. dust obscured) properties into intrinsic (i.e. stellar only) properties (or, alternatively, to dust-redden a stellar population model for comparison to the data). Standard practice is to adopt the empirical star-burst reddening curve by Calzetti et al. (2000). A notable alternative approach is the two-component model of Charlot & Fall (2000), in which young (< 3 Myr) birth clouds are shrouded by a different form of dust attenuation than the older bulk of the stellar population. This model is supported observationally by Kriek & Conroy (2013) and Wild et al. (2011) for some galaxy types at moderate/low redshift; however throughout this thesis, we adopt the Calzetti law except where stated otherwise.

At the typical temperature of the ISM, dust absorbs light in the rest-frame UV, and to a lesser extent optical, and re-radiates in the mid- to far-IR. In the parametrization by Calzetti et al. (2000), the post-dust flux density is reddened from the stellar-only flux density by:

$$F_{\mathrm{dusty}}(\lambda) = \frac{F_{\mathrm{stellar}}(\lambda)}{10^{\,0.4\ E\ (B-V)\ k'(\lambda)}}, \tag{1.14}$$

where λ is wavelength and $E(B-V)$ is the $B-V$ colour excess. As such, the resultant SED depends on the parameters of the reddening curve: the slope k' and colour excess $E(B-V)$. Often, dust reddening is simply reported as the attenuation A_λ, in magnitudes, at some wavelength λ (usually either in the V band, A_V, or in the UV at 1600 Å, A_{1600}). For a fixed k', this attenuation A_λ is then a measurement of the 'amount' of dust through which the star-light passes.

One significant feature not present in the Calzetti law is the 'dust-bump' at 2175 Å, observed in the Milky Way and most sight-lines through the Large Magellanic Cloud (e.g. Fitzpatrick & Massa 1986). This feature, likely due to an abundance of small carbonaceous grains (Weingartner & Draine 2001), obscures additional UV light in a narrow wavelength range. Its presence and strength appear to be linked to the slope of the dust law, and in turn to the sSFR, such that more actively star-forming galaxies have shallower reddening slopes and smaller dust bumps (Kriek & Conroy 2013). There is, as yet, no evidence for a 2175 Å feature in high-redshift LBGs; even at $z \approx 1$ it seems to be very weak (Conroy 2010). We will however see the consequence of its hypothetical presence on β in Chapter 5.

Empirically, from local star-burst galaxies, Meurer et al. (1999) defined a relation such the UV slope β is related to dust reddening by

$$A_{1600} = 4.43 + 1.99 \times \beta. \tag{1.15}$$

While this appeared to remain valid to $z \lesssim 3$, its use at higher redshifts implicitly assumes that the underlying UV continuum (of the stars) is redshift invariant (specifically, $\beta_{\rm stars} = -2.23$). As recently discussed by Wilkins et al. (2013) and Castellano et al. (2014), clearly this assumption must break down at some point: when metal enrichment had not reached the level of local star-burst galaxies. Castellano et al. (2014) have therefore recently proposed a refined "high-redshift" version of Meurer's relation, derived such that it reconciles the dust-corrected UV- and IR-derived SFR indicators for a sample of $z \approx 2.8-3.8$ galaxies with spectroscopically measured metallicities.

In summary, dust formation in high-redshift galaxies remains poorly understood, and determining its abundance requires assumptions or predictions of the underlying stellar population SEDs.

Age

As shown in Fig. 1.7, high-mass stars are short lived. The most massive, hottest, stars have lifetimes of only several Myr, while later stellar types live several Gyr. Therefore the SED of a stellar population formed in a single burst quickly reddens. The UV continuum slope β is thus highly sensitive to the age (i.e. time since formation) of a stellar population.

We have seen that both the combined black-body radiation of the stars and the dust reddening law are well described by power laws. This means there is little to distinguish between the red power-law continuum of an old stellar population and the red power-law continuum of a dusty one. This age–dust degeneracy is problematic, and revisited several times later in this thesis.

1.9.3 The problem with the rest-frame UV

Rest-frame UV light can provide a reliable tracer of current star-formation rates (e.g. Kennicutt 1998). However stellar mass, which is of course the time-integral of the past SFH, is more difficult to measure precisely. The reasons are two-fold: firstly, older components of the stellar population, which may contribute a significant portion of the stellar mass, are now faint in the UV since no massive stars remain on the main sequence from that epoch. This 'outshining' problem, where the UV light is completely dominated by the stars formed in recent epochs, is severe: a 20 Myr stellar population is 20 times more luminous at $\lambda_{\rm rest} = 1500$ Å than its 200 Myr old equivalent (assuming a 0.2 $Z_\odot$ Bruzual & Charlot (2003) model). Secondly, dust attenuates the UV light several times more strongly than

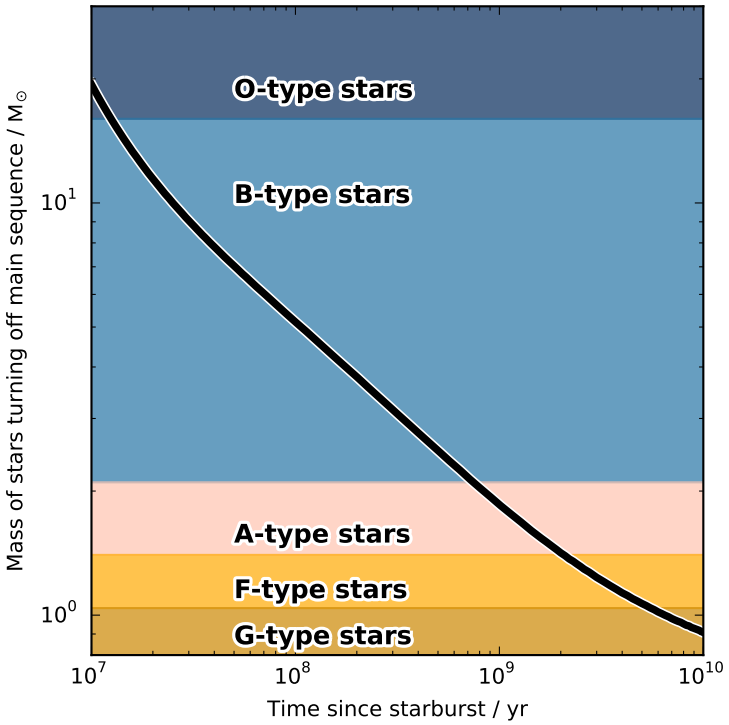

Figure 1.7 The mass of stars turning off the main sequence, which decreases with time since a burst of star formation, as reported by a Bruzual & Charlot (2003) model. The mass ranges of O-, B-, A-, F-, and G-type stars are highlighted by the coloured regions. Low-mass stars outlive high-mass stars, meaning that the SED of a stellar population cools (reddens) with time (Section 1.9.2). After ≈ 1 Gyr, O- and B-type stars have turned off the main sequence, leaving A-type stars, which have the most $n = 2$ excited Hydrogen in their atmospheres, as the dominant stellar type for a short time. During this period, the Balmer break is therefore at its largest (Section 1.9.4).

the optical light. The Calzetti dust extinction curve suggests that a galaxy attenuated by 1 mag in the V-band will be attenuated by 2.6 mag in the UV (1500 Å).

Typically then, stellar masses derived from the UV are uncertain to at least the extent of the dust reddening uncertainty. Furthermore, quoted mass ranges are only meaningful in the context of the assumed star-formation history/ies. Because of outshining, these SFHs are poorly, if at all, constrained. Still, widening the suite of available SFHs in SED fitting has been shown to yield stellar masses differing by only a factor of about 2 (Curtis-Lake et al. 2013, Pacifici et al. 2012).

For these reasons, *Spitzer*'s IRAC instrument (Fazio et al. 2004), with its $3-8\,\mu$m sensitivity probing the rest-frame *optical* at high redshift, is typically employed to derive the masses of high-redshift LBGs (Curtis-Lake et al. 2013, McLure et al. 2011, Yan et al. 2006).

1.9.4 The Balmer break

After the rest-frame UV, with its prominent Lyman break and occasional Lyman−α emission, the Balmer break provides the next most easily accessible probe into high-redshift stellar populations. In this section, its origin and use as both an age indicator and galaxy selector are described.

The origin of the Balmer break

Like the 912 Å Lyman limit, the Balmer break at 3646 Å occurs at the wavelength corresponding to the complete ionization of an electron from a bound state of Hydrogen to freedom. For the Lyman limit, the transition is from $n = 1 \rightarrow \infty$; for the Balmer break, the transition is $n = 2 \rightarrow \infty$. Thus, the Balmer break represents the termination of the Balmer absorption series (which includes the Ba−α and Ba-β lines, more commonly referred to as Hα and Hβ). While photons of only specific energies are absorbed by the bound–bound electron transitions, photons of any energy corresponding to $\lambda < 3646$ Å can be absorbed by the bound–free transition: their excess energy is transferred to the liberated electron. Therefore the prevalence of Hydrogen atoms excited to the $n = 2$ state in the atmospheres of stars can cause a substantial fraction of the stars' UV photons to be absorbed. As an illustration of this, Fig. 1.8 shows the SED of an entire stellar population with a sizable Balmer break (from a Bruzual & Charlot 2003, hereafter BC03, star-burst model), compared to a cartoon of what the SED might have looked like without the Balmer transition absorption.

The Balmer break as an age indicator

Massive O- and B-type stars contain little neutral Hydrogen; it is mostly completely ionized. Late-type stars (F-type and cooler) also contain little neutral Hydrogen; their atmospheres contain H^- hydride atoms. However A-type stars, with masses $1.5 \leq M_\odot \leq 2.1$ and temperatures $7400 \leq T_{\rm eff} \leq 10000$ K (Habets & Heintze 1981), have sufficient neutral, partially excited, Hydrogen in their atmospheres that the Balmer break becomes a dominant spectral feature. Following a burst of star formation, earlier-type stars have a shorter main sequence lifetime than later types. As shown in Fig. 1.7, the mass of stars still on the main sequence falls quickly as time progresses after a star burst; after several hundred Myr, A-type stars are the most massive stars remaining. This age dependency in the main-sequence turnoff mass, combined with neutral Hydrogen being most prevalent

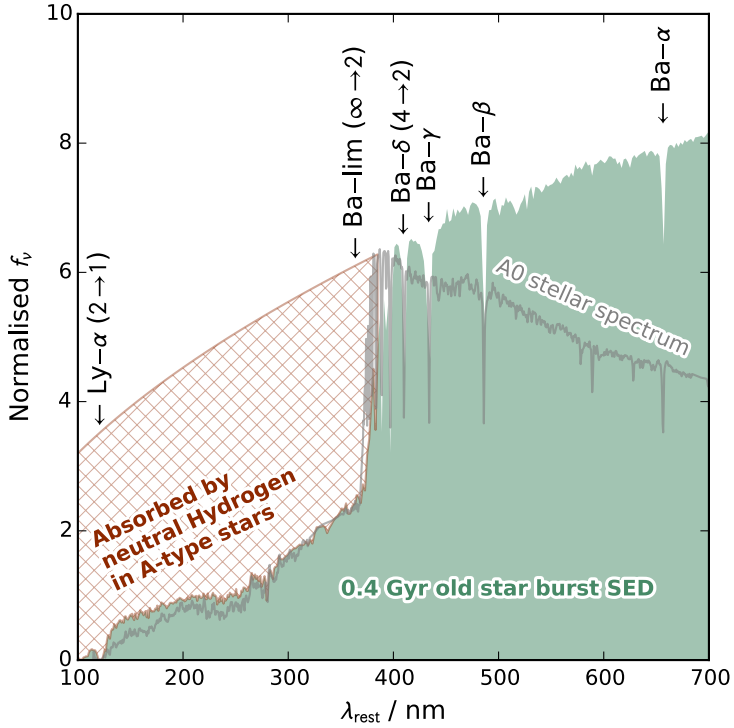

Figure 1.8 A BC03 model SED is shown for a 400 Myr old star-burst galaxy by the green region. Several Balmer- and Lyman-series Hydrogen absorption features are marked. The highest energy Balmer transition, corresponding to the $2 \rightarrow \infty$ electron transition, is the location of the Balmer break. Since all photons more energetic than 3646 Å can ionize Hydrogen from the $n = 2$ state, the presence of neutral Hydrogen in that state attenuates the SED at $\lambda < 3646$ Å. Neutral Hydrogen in the $n = 2$ excited state is most common in the atmospheres of A-type stars, where the Balmer break is then strongest, as shown by the grey line marking an A0 stellar spectrum (from the Pickles (1998) library).

in A-type stars, makes the Balmer break a coarse but effective age indicator for stellar populations formed in a single burst.

The Balmer break as a passive galaxy selector

The rest-frame UV is dominated by the last 100 Myr of SF (Kennicutt 1998). This means that the Lyman break technique, which relies on a reasonably bright, blue UV, is most sensitive to galaxies of these ages. The Balmer break, however, is most prominent for ages of 200 – 1000 Myr, the latter being the age of a galaxy formed at $z = 15$ and observed at $z = 5$. These facts naturally lead one to surmise that there may exist a population of old, $z \gtrsim 5$ galaxies with quenched star formation which, if sufficiently massive, could be detectable via their Balmer breaks. The presence of such galaxies would have astrophysical consequence: an old, massive stellar population at such an early epoch implies an early and *short* formation

duration akin to monolithic collapse (rather than more gradual merging; Mobasher et al. 2005).

Under this premise, Wiklind et al. (2008) searched for Balmer-break galaxies (BBGs) at $z \approx 5$ in an analogous fashion to LBGs: by a large colour spanning the purported break wavelength. In this case, the 3646 Å break lay in the $K-[3.6]$ colour. This is demanding because K-band imaging is not available from *HST* and so must be captured from the ground, and [3.6]-band imaging requires moving to the smaller *Spitzer* telescope's IRAC (Fazio et al. 2004) instrument. At present, there are no *confirmed* BBG-selected $z \gtrsim 5$ galaxies which are so faint and red in the UV that they are not also present in LBG-selected samples (Dunlop 2013). The unequivocal depth advantage of *HST* means that this does not rule out the existence of these massive, passive galaxies; rather, any such population currently inaccessible with *HST* will remain so until the unrivalled NIR sensitivity of the forthcoming *James Webb Space Telescope* reveals it.

1.9.5 Nebular emission

Aside from the stellar light emitted by LBGs, there is continuum and line emission due to the young gaseous nebulae in which the stellar populations form. This nebular emission is predicted to be strong for the young, high-SFR galaxies observed in the early Universe; at some stellar population ages and wavelengths, the contribution of nebular emission can even outweigh that of the stellar population (Anders & Fritze-v. Alvensleben 2003, Raiter et al. 2010, Zackrisson et al. 2008). The nebular continuum emission contributes modestly to the rest-frame UV, but the emission lines (of which Lyman$-\alpha$, Hα, Hβ, [OIII] and [OII] are strongest in the rest-frame UV and optical) can contribute so significantly to even broad-band photometry that they affect fitted galaxy properties. Ages and stellar masses, which are both traced best by the rest-frame optical and IR, are known to be significantly over-estimated in $z \gtrsim 3$ LBGs if nebular emission lines are not considered in the stellar population synthesis (de Barros et al. 2014, Schaerer & de Barros 2009, Smit et al. 2014, Stark et al. 2013). As highlighted earlier, over-estimated stellar masses result in incorrect sSFR measurements – crucial for understanding the build-up of galaxies in the early Universe. The nebular emission contribution is also linked to the Lyman continuum escape fractions discussed earlier, since the energy budget must be balanced within these nebulae.

1.9.6 Stellar population synthesis

Stellar population synthesis models have evolved in complexity significantly over the last 40 years (e.g. Bessell et al. 1998, Bruzual & Charlot 2003, Bruzual A. 1983, Bruzual A. & Charlot 1993, Conroy 2013, Conroy et al. 2009; 2010, Gunn et al. 1981, Jacoby et al. 1984, Leitherer & Heckman 1995, Leitherer et al. 1999, Maraston 2005, Tinsley 1968; 1972; 1973, Tinsley & Gunn 1976). Deriving stellar population properties from galaxy observations requires dissecting the observed aggregate spectral energy distribution into the contributions of many individual stars. This link is provided by stellar population synthesis models, which in their simplest incarnation integrate over the spectra of all the constituent stars formed in a single epoch of star formation – 'single stellar populations' – to provide predicted aggregate spectral energy distributions as a function of time since formation. More realistic scenarios, in which star *formation* is itself a function of time, are modeled as 'composite stellar populations'.

The latter allow the SFH-induced variations in SEDs to be accounted for, and in some cases even constrained. Throughout this thesis we make use of these SPS models to interpret our observations.

1.10 The observational frontier

In the remainder of this introductory chapter, the recent advances in observational capability and scientific results, as they pertain to the work in this thesis, are described.

The 1997 installation of the Near Infrared Camera and Multi-Object Spectrometer (NICMOS) and the 2002 installation of the Advanced Camera for Surveys (ACS) on board *HST* began to allow the first high-resolution, NIR imaging of LBGs out to $z \gtrsim 7$, culminating in the first tentative reionization-era constraints on the LBG LF by, for example, Bouwens et al. (2008). A year later in 2009, *HST* was again upgraded with the Wide Field Camera 3, with an IR channel providing unprecedented Y- to H-band sensitivity and field-of-view. This heralded a period when the first large, statistical samples of $z \gtrsim 7$ LBGs could be assembled. The prompt investment of WFC3/IR time on the Hubble Ultra Deep Field (UDF; Beckwith et al. 2006), and subsequently the Early Release Science field (ERS; Windhorst et al. 2011), resulted in a profusion of papers reporting the discovery of ≈ 100 largely believable $z \gtrsim 7$ galaxy candidates (e.g. Bouwens et al. 2011, Bouwens et al. 2010, Bunker et al. 2010, Finkelstein et al. 2010, Lorenzoni et al. 2011, McLure et al. 2010; 2011, Oesch et al. 2010b, Wilkins et al. 2010; 2011).

These initial targeted and ultra-deep datasets have been complemented by wider, shallower WFC3 imaging programmes. The widest of these are designed to detect rare and bright, or rare and gravitationally-lensed, galaxies: both the Hubble Infrared Pure Parallel Imaging Extragalactic Survey (HIPPIES; Yan et al. 2011) and the Brightest of Reionizing Galaxies survey (BoRG; Trenti et al. 2011; 2012) use *HST* parallel time to survey numerous random pointings of sky at very limited depth. More focussed surveys are also being conducted on blank fields with rich multi-wavelength data, via the Cosmic Assembly Near-infrared Deep Extragalactic Legacy Survey (CANDELS; Grogin et al. 2011, Koekemoer et al. 2011), and on foreground lensing clusters providing access to heavily magnified faint LBGs, via the Cluster Lensing and Supernovae survey with Hubble (CLASH; Postman et al. 2012). These surveys have significantly extended the luminosity baseline over which galaxies at $z \gtrsim 7$ are discovered, thereby allowing the LF measurements discussed in Section 1.7. At the very bright end of the LF, these *HST* data have been combined with square-degree scale ground-based surveys, primarily via the UKIRT Infrared Deep Sky Survey (UKIDSS) Ultra Deep Survey (UDS) and UltraVISTA (McCracken et al. 2012), to improve the constraints on the density of $> L_*$ galaxies (e.g Bowler et al. 2014, McLure et al. 2009).

Finally, the Hubble Ultra Deep Field 2012 (UDF12) programme, which is the subject of much of this thesis, delivered the deepest near-IR (NIR) image ever taken and therefore, for the time being, marks the observational frontier (Ellis et al. 2013, Illingworth et al. 2013, Koekemoer et al. 2013).

1.11 The rest-frame UV continuum of $z > 4$ galaxies

As discussed earlier, the faintest $z \gtrsim 6$ galaxies are expected to be a key source of the ionizing photons required to reionize the universe, yet constraining their contribution relies on measuring their UV colours in order to estimate the galaxies' production rate of Hydrogen ionizing photons and the fraction of such photons which escape their host galaxies to reionize the IGM (e.g. Finkelstein et al. 2012a, Robertson et al. 2010).

As we have seen, the bluest LBG's UV continua are expected to display $\beta \lesssim -2.5$, but to rapidly redden with time after the onset of star formation. Observationally, a UV slope of $\beta \approx -2$ is typical of a young, un-reddened, low-metallicity, star-forming galaxy at $z \approx 2$ (e.g. Erb et al. 2010). The strong relationship between UV slope and reddening (Meurer et al. 1999) appears to be already in place by $z \approx 2$, as shown by Reddy et al. (2012a) using *Herschel* data, even though the youngest galaxies (<100 Myr) may follow a different

extinction curve than their older counterparts (Reddy et al. 2010).

At higher redshifts ($z \geq 3$) the relationship between UV slope, dust attenuation, stellar population age and metallicity is still unclear. However, many previous studies have shown that β reddens with decreasing redshift and increasing UV luminosity (e.g. Bouwens et al. 2013, Dayal & Ferrara 2012, Labbé et al. 2007, Meurer et al. 1999, Overzier et al. 2008, Shapley et al. 2003, Wilkins et al. 2011). This trend is often assumed to reflect increasing dust attenuation at a fixed redshift, and increasing stellar population age at a fixed luminosity (e.g. Labbé et al. 2007) – a hypothesis we asses in Chapter 6.

1.11.1 Recent contention over the average UV continuum slope at $z \approx 7$

The obvious prediction from the apparent trend between UV slope, redshift and luminosity is that the bluest galaxies will naturally be found amongst the faintest detectable galaxies at $z \geq 7$. Particular interest in the UV slopes of $z \approx 7$ galaxies began when the optical ACS data in the UDF (Beckwith et al. 2006) was complemented by the WFC3/IR Y, J, H-band data of the HUDF09 programme (GO11563, PI: Illingworth; Bouwens et al. 2010). The first substantial catalogues of $z \approx 7$ LBGs were available following the first epoch of this programme in 2009. Hereafter, we refer to data taken prior to and during this first HUDF09 epoch as HUDF09E1. Later studies have made use of further data obtained in a second epoch, and we refer to the stack of all the WFC3/IR data from epochs 1 and 2 as HUDF09FULL. Throughout this thesis we also refer to the WFC3 Early Release Science (ERS, Windhorst et al. 2011) programme, which provides shallower imaging over a wider (36.5 sq. arcmin) field than the HUDF (4.5 sq. arcmin).

In an initial foray into the measurement of β at $z \approx 7$, Bouwens et al. (2010) found evidence for a colour–magnitude relation such that the faintest $z \approx 7$ galaxies exhibited sufficiently blue average UV colours ($\langle\beta\rangle = -3.0 \pm 0.2$ at $-19 \leq M_{\rm UV,AB} \leq -18$) that extremely young ages and ultra-low metallicities could be inferred. If confirmed, it would be necessary to not only account for the rapid evolution of stellar populations from $z \approx 7 \rightarrow 6$, but also to conclude that the UV photon escape fraction must be sufficiently high at $z \approx 7$ that nebular continuum emission does not significantly redden the observed SED. With the same dataset – the HUDF09E1 – Finkelstein et al. (2010) found similarly extreme β values, although with a sufficiently large error that it was not necessary to invoke 'exotic' stellar populations. In fact, they suggested that only moderately young, dust-free, stellar populations are required to reproduce the observed colours. With improved data in the final HUDF09FULL, a revised assessment reported by Bouwens et al. (2012a) retained a clear colour–magnitude trend, albeit with the faintest objects averaging only $\langle\beta\rangle = -2.68 \pm$

0.19±0.28 (biweight mean ± random ± systematic uncertainties). Significantly, Finkelstein et al. (2012b) also found that the full HUDF09FULL dataset provides somewhat redder colours for the faintest[2] objects with $\langle\beta\rangle = -3.07 \pm 0.51$ in HUDF09E1 (Finkelstein et al. 2010), and $\langle\beta\rangle = -2.68^{+0.39}_{-0.24}$ (≈ -2.4 after bias correction) in HUDF09FULL (Finkelstein et al. 2012b). Already it should be clear from these revised estimates and their quoted uncertainties that the typical UV spectral slope of the faintest galaxies at $z \approx 7$ is not well constrained.

In response to the initial claims of the discovery of exotic stellar populations at $z \approx 7$, Dunlop et al. (2012) demonstrated that measurement biases can result in a population of normal star-forming galaxies with $\langle\beta\rangle \approx -2$ being observed as a population of extremely blue objects, especially when average properties are calculated for objects close to the detection limit of the imaging. This is because, as the scatter in observed colour inevitably rises when the flux-density limit of the survey is approached, the methods used to select LBGs (either simple colour–colour selection, or multi-band photometric redshift determination) can start to preferentially exclude genuine high-redshift objects whose colours have been scattered to very red values (treating them as likely lower-redshift interlopers). This is not the same as saying that LBG selection is limited to extremely blue objects; in fact the commonly used colour–colour selection criteria, and photometric-redshift selection techniques can admit quite red LBGs, especially if the photometric-redshift technique is not confined to the most secure candidates. Nevertheless, because photometric scatter can result in extreme (indeed often unphysical) values of β for individual objects, the reddest objects can be 'lost' to ostensibly low photometric redshifts, while the extreme blue objects never are (with resulting implications for the calculation of average values of β).

Dunlop et al. (2012) focussed on the inclusion of *all* candidate objects with even a marginally-preferred high-redshift LBG solution, and showed that, with existing data, there still exists a significant blue bias ($\Delta\langle\beta\rangle \approx -0.5$) in the inferred value of $\langle\beta\rangle$ for the faintest LBGs at $z \approx 7$ (the bias is simply more extreme if only the most robust LBG candidates are considered; e.g. McLure et al. 2011). As we show later, in Chapter 3, this level of bias also applies to colour–colour selected samples (e.g. Bouwens et al. 2012a) and is exacerbated by the imposition of a J-band flux threshold in the galaxy sample selection (e.g. Bouwens et al. 2010).

From the above discussion, it is clear that, prior to this thesis, the steepness of the UV slope for sub-L^*, $z \approx 7$ galaxies had remained an open question. Chapters 3 and 4 are therefore devoted to a better measurement of β at $z \approx 7$.

[2] In HUDF09E1, this refers to galaxies in the faintest 1 mag bin; in HUDF09FULL galaxies with $L < 0.25\ L^*$.

1.11.2 The colour–magnitude trend at $z \gtrsim 5$

At more moderate redshifts, where the average $\langle\beta\rangle$ has been better constrained at less controversial values, attention has been focussed on understanding the details of how the relationship between UV slope and luminosity, hereafter the colour–magnitude relation (CMR), evolves at high redshift ($z \geq 4$). In the literature, there has been no consensus on the strength or functional form of the CMR at high redshift, with the two largest studies at $z \geq 4$, those of Finkelstein et al. (2012b) and Bouwens et al. (2013), producing seemingly discrepant results. Although both studies are based on samples with a reasonable dynamic range in UV luminosity, selected from high-quality *HST* imaging, Bouwens et al. (2013) claim the discovery of a significant CMR in redshift bins at $z = 4, 5, 6,$ & 7, whereas Finkelstein et al. (2012a) see no significant correlation between β and $M_{\rm UV}$ in the same redshift range. In contrast, Finkelstein et al. (2012b) find that β is more strongly coupled to stellar mass $M_\star$, with more massive galaxies displaying redder UV slopes.

1.11.3 The intrinsic distribution of colours at fixed luminosity

In addition to fundamental questions related to the existence and form of the CMR at high redshift, constraints on the *intrinsic* (i.e. free of observational effects) colour distribution of $z \geq 4$ galaxies are clearly of interest. For instance, at $z < 3$, Labbé et al. (2007) found evidence for moderate intrinsic colour-variation in the blue sequence, which they attributed to stochastic SFHs. However, previous studies addressing this issue at $z \approx 4-5$ have been hampered by a lack of dynamic range (Bouwens et al. 2012a, Castellano et al. 2012, Wilkins et al. 2011) and no luminosity-dependent trend has been made clear. We therefore undertake a study of the CMR and intrinsic distribution of colours in Chapter 5.

1.12 Layout and publication history of this thesis

The remainder of this thesis is organised as follows. In Chapter 2, technical details of our general analysis methods are described. Prior to the UDF12 programme, we developed simulations to determine and validate a robust method for measuring the rest-frame UV spectral slope of $z \approx 7$ galaxies. Chapter 3 details that study, the majority of which has been published in MNRAS (Rogers et al. 2013). Following the delivery of data from the UDF12 programme, we applied the methods developed in Chapter 3 to the new observations. The results of this are presented in Chapter 4, and were published in MNRAS by Dunlop, Rogers, et al. (2013). Constraining the luminosity dependence of the UV slope at high redshift required a longer luminosity baseline and higher signal-to-noise data, so we then

undertook a study at $z \approx 5$, where we could build a large sample of galaxies by combining ground- and space-based observations. This is described in Chapter 5, the majority of which has been published in MNRAS (Rogers et al. 2014). Understanding the physical origin of the UV spectral slope's luminosity dependence requires breaking the degeneracy between age and dust reddening. In Chapter 6 a method for measuring the ages of our $z \approx 5$ galaxies, free of contamination from nebular emission lines, is presented, as are the results of applying the procedure to the $z \approx 5$ sample from Chapter 5. Chapter 7 presents a summary of our conclusions, and describes future work which would naturally follow that presented here.

2 Observational and computational methods

In this short chapter, methods for analysing high-redshift galaxy data are described. These procedures, devoted to the construction and analysis of spectral energy distributions from broad-band image data, are common to Chapters 3, 5, 4, and 6 of this thesis. Therefore, these procedures are laid out here.

We begin by describing how aperture photometry is performed on multi-wavelength images. This photometry can be used for image depth analysis, and for constructing SEDs, as described thereafter. We conclude by discussing how fitting stellar population synthesis models allows photometric redshifts and stellar population parameters to be inferred.

2.1 Multi-wavelength photometry

Broad-band imaging surveys are an exceptionally efficient method of obtaining crude SEDs for many objects at a time. While targeted spectroscopy, with typical spectral resolution $R \gtrsim 1000$, remains the only definitive way of determining a galaxy's redshift, metallicity, and other line-dependent properties, these time-intensive programmes are only usefully deployed on reasonably plausible candidates found by other means. Recent progress in the NIR has seen deep grism spectroscopy such as the 3D-HST programme (Brammer et al. 2012) provide multi-object spectroscopy at $R \sim 100$ over 0.15 deg^2; medium-band surveys such as the NEWFIRM NMBS (van Dokkum et al. 2009, Whitaker et al. 2011) at $R \sim 10$ over 0.44 deg^2; and narrow-band surveys such as HiZELS (Geach et al. 2008) find high-redshift line emitters over 5 deg^2.

However at $z \approx 7$, where a typical galaxy is $\approx 27^{\text{th}}$ magnitude, only broad-band imaging ($R \sim 4$) can reveal the vast majority of the population (e.g. McLure et al. 2013), save the few sources with detectable Lyman$-\alpha$ emission (e.g. Finkelstein et al. 2013).

2.1.1 Circular aperture photometry

Most of the photometry presented in this thesis has been derived by placing circular apertures in broad-band images. Although not of optimal efficiency in terms of signal-to-noise for extended sources, fixed-diameter circular apertures have the significant convenience of being defined irrespective of a galaxy's size or morphology. This means all sources can be treated equally, as can source-free regions or sky. The same is not true of apertures which purport to be defined by fitting the source's light profile. By their very nature, the early galaxies studied in this thesis are compact and faint, which makes the accurate fitting of those sources' light profiles difficult. The same difficulties are present, to a lesser extent, if one adopts fixed-area elliptical apertures: the orientation of these apertures is essentially unconstrained for faint, compact sources.

However even with simple circular apertures, determining what size of aperture should be used is non-trivial. In order to construct a self-consistent SED from multi-wavelength photometry, the same intrinsic portion of a galaxy must be photometered in each wave-band. Ideal photometry would enclose the galaxy's entirety, but in realistic images this never yields the optimum signal-to-noise. Thus an optimal aperture size must be chosen to enclose a reasonable fraction of the galaxy's light (typically $\sim$80%) while enclosing sufficiently little sky-dominated noise that the source signal-to-noise is maximized. Where

a source is unresolved, circular apertures can be defined based on measurements of the point-spread function (PSF, constructed from a stack of stars). Aperture diameters are typically defined so as to enclose equal fractions of a PSF's flux in each waveband. For marginally resolved sources, typical of faint high-redshift galaxies in spaceborne images, this can sometimes be a poor approximation. For example, consider the $z-J$ (i.e. *HST* ACS F850LP − WFC3/IR F125W) colour of a small but resolved source in *HST* data – a $z=5$ galaxy with $r_{1/2}=1$ kpc. The ACS z−band's PSF is narrower than the WFC3 J−band's, so the 80%-enclosing aperture is smaller for z than J. If the source is the same size in each band (i.e. it has no colour gradient) then the breadth of it is, relative to the PSF size, more dominant in z than J. Convolving the z- and J-band PSFs by model galaxy light profiles of increasing size broadens the PSFs such that, within fixed apertures, flux is lost more quickly in the z band than the J band:

$$\left.\frac{\mathrm{d}f_{\mathrm{enc}}(\mathrm{ACS}\ z)}{\mathrm{d}r_{1/2}}\right|_{\sim 1\,\mathrm{kpc}} > \left.\frac{\mathrm{d}f_{\mathrm{enc}}(\mathrm{WFC3}\ J)}{\mathrm{d}r_{1/2}}\right|_{\sim 1\,\mathrm{kpc.}} \tag{2.1}$$

The result is a red colour-bias for larger sources; however, this can be easily mitigated by adopting sufficiently large apertures, or by targeting sources known to be essentially point-like.

2.1.2 Iso-photal photometry

Another widely used photometric method is to define an object's effective perimeter as the image region, around the source, which is brighter than some threshold value. Traversing this perimeter, the source has the same (threshold) flux at every point: the perimeter is therefore an iso-phot. Treating this iso-phot as the extent of an arbitrarily shaped aperture then allows aperture photometry to be performed. Of course realistic sources with non flat-spectrum SEDs will have a different iso-photal enclosed area in each band, making colours between them meaningless. Thus, iso-phots must be defined in one band (usually the detection band) and honoured in all others. However, bands with narrower PSFs will have more of the source enclosed by a fixed iso-phot than will bands with broader PSFs. Meaningful iso-photal magnitudes are therefore derived from PSF homogenised images, or by dilated iso-photal apertures for bands with broader PSFs.

In the studies reported in this thesis, all photometry we have performed directly used circular apertures. However in Chapters 5 and 6 we make use of external catalogues which were created partially using iso-photal photometry (Galametz et al. 2013a, Guo et al. 2013). In those cases, the H-band was used to define iso-photal apertures and the shorter-wavelength bands were PSF-matched to the H-band to ensure consistency.

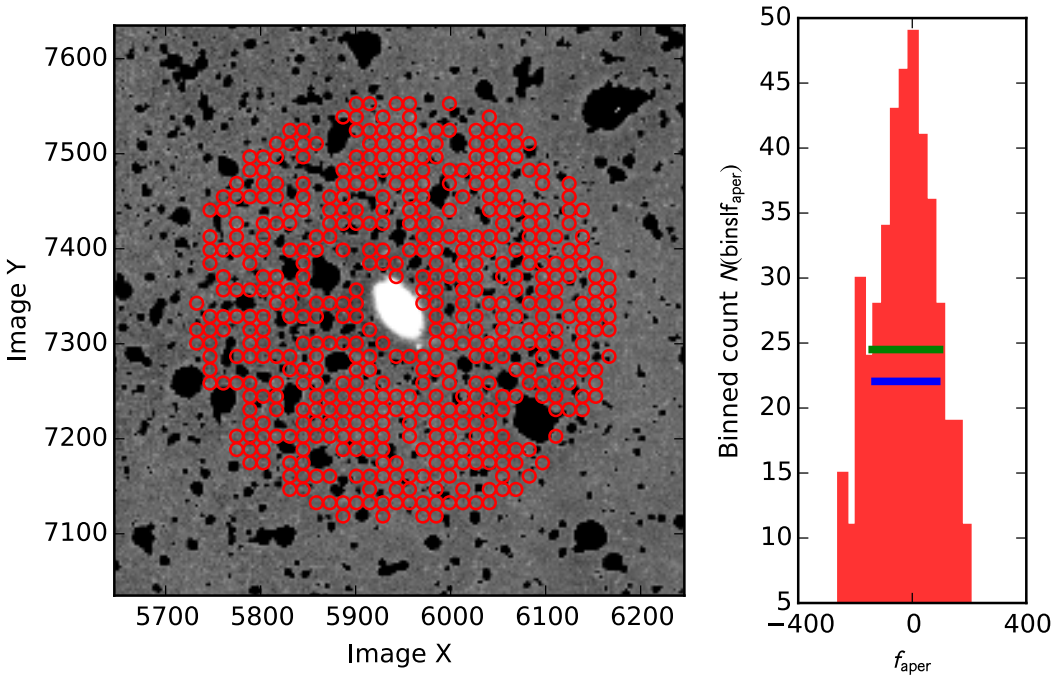

Figure 2.1 An example of how the local depth of an image is found in the vicinity of a source of interest. *Left panel*: a z'-band image of a galaxy in the UDS is shown centred in the field of view. Nearby sources have been masked by a segmentation map produced by SEXTRACTOR (black patches) leaving just the sky background. Red circles mark the nearest 500 apertures which do not overlap sources – the apertures used to measure the local depth. *Right panel*: the approximately Gaussian distribution of aperture summed fluxes of blank sky, clipped at $\pm 2\sigma$. Green and blue bars show the $\pm 1\sigma$ depth of the image as measured by the MAD or standard deviation of the sample, respectively.

2.2 Image depth analysis

The significance of a galaxy's detection is dependent on its photometric signal-to-noise ratio (SNR). In the case of aperture photometry, the SNR is best estimated by considering the probability that the flux in an aperture enclosing a potential source is due to the presence of the source rather than a random fluctuation in the sky noise, $p\left(f_{\text{aperture}} \middle| \text{sky}\right)$. In practice, the significance is measured by the ratio of the aperture-summed flux enclosing the galaxy to the standard deviation of aperture-summed fluxes of source-free patches of sky,

$$\text{SNR} = \frac{f_{\text{aper}}}{\sigma_{\text{depth}}} = \frac{\sum\limits_{\text{aperture}} f_{\text{source}}}{\underset{\text{blank apertures}}{\sigma}\left(\sum\limits_{\text{aperture}} f_{\text{sky}}\right)}. \tag{2.2}$$

The crux of this calculation is the definition of the 'source-free' patches. Typically, these are defined by running source detection (e.g. SEXTRACTOR; Bertin & Arnouts 1996) down

to a very low detection threshold such that small (one or two) pixel contiguous patches brighter than $\approx 2 \times \sigma$(all pixels) are labelled as sources. By creating a binary source-or-not segmentation map of such detections, blank patches are defined. The image depth $\sigma_{\rm depth}$ is then calculated by randomly (or grid-wise) placing many non-overlapping apertures on a background-subtracted version of the image and its segmentation map simultaneously. Only apertures whose enclosed segmentation sum is zero contribute their enclosed image flux to the depth calculation. The left-hand panel of Fig. 2.1 shows an example of an image masked by the segmentation map. For the derived depth to be useful as an indicator of the image-induced noise on a source's flux, the apertures used for both depths and photometry must be identical. This provides a strong incentive to use circular (or more generally, elliptical), rather than iso-photal, apertures, since a single measurement of the image depth then yields a flux uncertainty for the photometry of all sources.

2.2.1 Global depth estimates

An image's global depth is defined as the standard deviation σ of these aperture fluxes. Provided that photometry is performed for objects in identically sized apertures, this σ also provides the significance threshold (magnitude limit) for detecting those objects and an estimate of the image-noise induced uncertainty on the objects' fluxes. The magnitude limit is commonly quoted as the '5σ-depth'= zeropoint $-2.5\log_{10}(5\sigma)$.

2.2.2 Local depth estimates

In cases where the depth varies significantly over an image (e.g. Fig. 2.2), it can be beneficial to compute local depths for each source, where the depth is measured from source-free sky in only the near vicinity of the candidate source. In general, the measurement of σ is sensitive to the shape of the distribution. Usually the distribution of even well-cleaned blank-sky fluxes is non-Gaussian: faint sources, which were not picked up during the source detection run but nonetheless contribute positive flux to their region of sky, can, in some cases, induce a long positive tail to the distribution of purportedly blank aperture fluxes. Moreover, if only a small number of apertures (~ 100) are used to constrain the depth (as is often the case for local depths; right-hand panel of Fig. 2.1) the distribution of aperture fluxes can be sufficiently poorly sampled that automated fitting of a Gaussian distribution fails.

In such cases as it is necessary, σ can be found more robustly via the Median Absolute

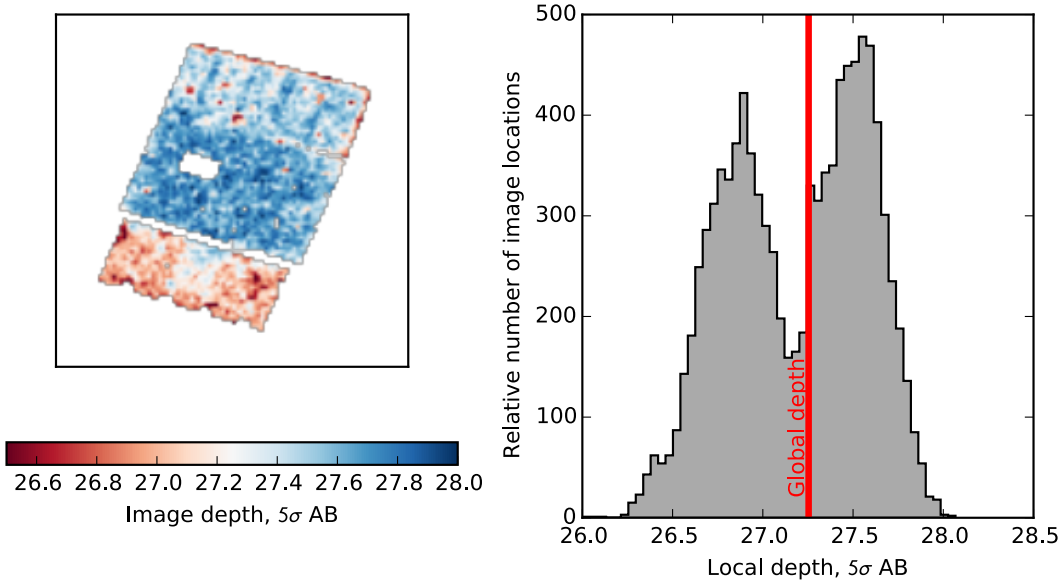

Figure 2.2 An example of how the depth of image can vary across it. The image here (left panel) is the CANDELS GOODS-S region through the *HST* WFC3/IR F125W filter (Grogin et al. 2011, Koekemoer et al. 2011), which we use later in Chapters 5 and 6. Because the image is composed of many *HST* pointings, each with differing exposure times and background levels, the depth is not homogeneous. The southern strip is notably shallower, as per the CANDELS programme's design. This is mirrored in the distribution of depths (right panel), where the shallow and deep regions are clearly differentiated. As a result, the median depth ('global depth', red line) is a poor estimate of the aperture noise for the majority of locations in the image. (In this field, the depths within the three easily distinguishable regions happen to be reasonably homogeneous, so three 'regional' depths could be used as reasonable approximations to the local depths.)

Deviation (MAD), defined as

$$\mathrm{MAD} = \underset{\text{apertures}}{\mathrm{median}}\left[\left|f_{\mathrm{sky}} - \underset{\text{apertures}}{\mathrm{median}}\left(f_{\mathrm{sky}}\right)\right|\right], \tag{2.3}$$

which approximately yields the standard deviation of the distribution by

$$\sigma \approx 1.4826 \times \mathrm{MAD}. \tag{2.4}$$

2.3 Photometric redshift estimation and model fitting

The vast majority of high-redshift galaxy candidates, with putative distances corresponding to $z \geq 4$, are identified photometrically rather than spectroscopically. Like spectroscopic analysis, photometric redshift analysis of course aims to identify a signature within a galaxy's SED and measure the $\lambda_{\mathrm{intrinsic}} \rightarrow \lambda_{\mathrm{observed}}$ shift, yielding the redshift via

$z = \lambda_{\rm observed}/\lambda_{\rm intrinsic} - 1$. While spectroscopy targets the identification of an individual spectral line (emission or absorption), photometric methods typically target spectral breaks, namely the Lyman Limit (912 Å) at $z < 5$ and the Lyman Break (1216 Å) at $z \geq 5$. However the 4000 Å and Balmer (3646 Å) Breaks can, depending on the stellar population properties, be large enough to constrain a photometric redshift solution (e.g. Section 1.9.4).

2.3.1 Colour-colour selection of Lyman break galaxies

As we have seen, LBGs provide the most abundant probe of the high-redshift galaxy population. In principle, LBGs are selected based on a large, red colour spanning the Lyman break in tandem with a reasonably blue colour above the purported Lyman Break; the second colour relies on the star-forming nature of LBGs. For example a $z = 4.5$ galaxy, with its Lyman limit and Lyman break observed at 5016 Å and 6688 Å, should be completely undetected in a B-band image, thus yielding a large $B-R$ colour (V is partially attenuated). $R-I$ should be roughly zero, if it probes a star-forming galaxy's rest-frame UV.

This colour-colour selection principle has now been successfully employed to select (now spectroscopically confirmed) LBGs out to $z \lesssim 8$.

2.3.2 Lower-redshift intelopers

With a contrivance of stellar population parameters (e.g. an old but low-mass stellar population with little ongoing star formation and sufficient dust attenuation to completely obscure the rest-frame UV) the 4000 Å and Balmer breaks of a lower-redshift galaxy can mimic the Lyman break of a higher-redshift LBG. For a galaxy with a LBG solution at $z = z_{\rm LBG}$, a secondary solution is often found at

$$z_{\rm interloper} = (1 + z_{\rm LBG}) \frac{1216\,\text{Å}}{3646\,\text{Å}} - 1, \tag{2.5}$$

e.g. $z_{\rm interloper} \simeq 1$ if $z_{\rm LBG} = 5$.

2.3.3 Model fitting to the full spectral energy distribution

As we have seen in Section 1.9.6, stellar population synthesis models provide calibrated predictions for the UV to IR SEDs of star-forming and post-starburst galaxies. By artificially redshifting these templates, and convolving them with filter transmission profiles, directly

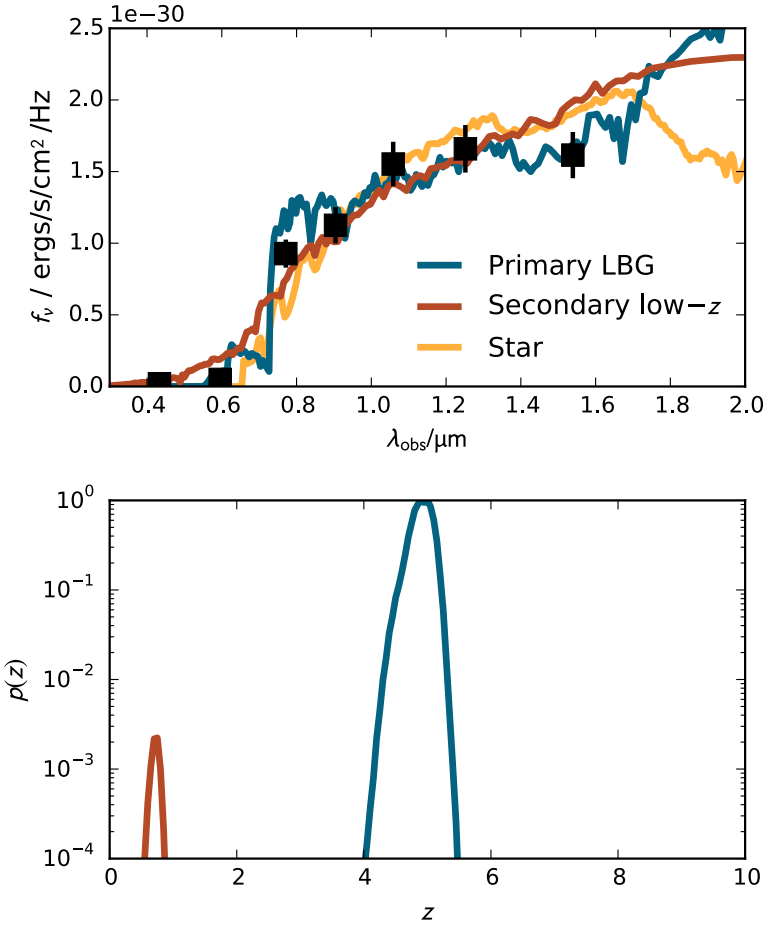

Figure 2.3 An example of full photometric redshift analysis by stellar population synthesis fitting. In the *upper panel*, the black data points with error bars show the SED of a candidate $z \approx 5$ LBG. The best-fitting stellar population synthesis model, redshifted to $z \approx 5$, is shown by the blue line. Two alternative solutions are also shown: a secondary, lower-redshift galaxy is shown in red; the best-fitting Galactic dwarf star SED is shown in yellow. The *lower panel* shows the probability $p(z)$ that the galaxy lies at each redshift z. The $p(z)$ curve has been coloured such that the probability peaks match the template SEDs in the upper panel. In this case, the $z \approx 5$ LBG solution is greatly preferred.

comparable broad-band photometry can be derived. By varying the model redshift and minimizing the χ^2 between that and the data, a best-fitting photometric redshift $z_{\rm phot}$ is found. That $z_{\rm phot}$ is of course dependent on the assumed stellar population ('nuisance') parameters, the effects of which need to be accounted for. Of more interest are the constraints which might be placed on the stellar population parameters themselves, either by obtaining spectroscopic redshifts (e.g Curtis-Lake et al. 2013) for the sample or by studying only galaxies with photometric redshifts which are particularly robust (e.g McLure et al. 2011).

Throughout this thesis, we adopt this model-fitting approach to photometric redshifts. Fig. 2.3 shows an example of the process of fitting high-resolution template SEDs to a low-

resolution observed SED.

2.3.4 Acceptable χ^2 values for galaxy fits

The power of full photometric redshift fitting stems from the statistical robustness with which the models and full SEDs can be compared. Marginalizing, or minimizing, over the plausible ranges of stellar population parameters can yield a simple function of $\chi^2(z)$. The values of this are a measure of how acceptably the observed source can be reproduced by a model at each redshift, and the redshift at which the χ^2 is minimized is the most likely photometric redshift. The lower panel of Fig. 2.3 shows how powerful this process can be at distinguishing between multiple seemingly plausible redshift solutions. (The figure shows $p(z)$ rather than χ^2; $p(z)$ should of course be maximized for the best-fitting template.)

A χ^2 distribution is characterised by a mean (μ) and variance (σ^2), where $\sigma^2 = 2\mu$. For a model with n parameters fit to data with N observations, the number of degrees-of-freedom $\nu = N - n$. The χ^2 distribution for this scenario is then given by $\mu = \nu$, $\sigma = \sqrt{2\nu}$. Therefore, a model which has an acceptable fit at the 2σ confidence level must have a minimum value

$$\chi^2 \leq \mu + 2\sigma, \tag{2.6}$$

$$\Rightarrow \chi^2 \leq \nu + 2\sqrt{2\nu}. \tag{2.7}$$

For example, $N = 9$ band photometry fit by SED models with varying redshift, age, metallicity, dust reddening and a SFR which is constant in time but variable in normalisation ($n = 5$) has $\nu = 4$ and therefore a model with $\chi^2(\text{photometry}|\text{model}) \leq 9.7$ is acceptable at the 2σ level.

2.3.5 Distinguishing stellar contaminants by χ^2 analysis

The SEDs of likely stellar contaminants are described by $n = 2$ parameters: their temperature and distance. However a galaxy candidate with $\chi^2_{\text{galaxy}} \approx \chi^2_{\text{star}}$ is more likely to be a star, since the star model's greater degrees-of-freedom provide a lower reduced χ^2,

$$\chi^2_{\text{red}} = \frac{\chi^2}{\nu}. \tag{2.8}$$

For example a galaxy candidate with $N = 9$, $n_{\text{galaxy}} = 5$, $n_{\text{star}} = 2$ would need $\chi^2_{\text{galaxy}} \leq 9.7$ and $\chi^2_{\text{star}} > 14.5$ to be considered a 2σ galaxy identification with stellar contamination ruled out also at the 2σ level.

Of course, a real catalogue includes a mixture of galaxies, stars and artefacts; these '2σ' χ^2 thresholds effectively also clean the sample and admit many fewer initial candidates than the 95% one might expect.

As we shall see, provided high-resolution (space-based) imagery is available, the light-profile can also be used as an effective stellar determinant.

2.3.6 Star-formation histories

There are many credible ways to parametrize the SFHs of high-redshift LBGs. Of these, authors usually adopt models in which the stars form in a single burst, or at a constant or exponentially declining rate. Recently, as discussed earlier, it has become evident that the average SFH of a high-redshift LBG probably increases with time. At one time, it seemed that the sSFR was constant at $z \gtrsim 2$. This is probably now disfavoured (see Section 1.6); however it provides a convenient physical mechanism to parametrize these increasing SFHs in an alternative way to the so-called 'inverted-τ' models (e.g. Papovich et al. 2011). Since this has been rarely adopted, we discuss the particular parametrization here.

If one assumes individual galaxies maintain constant sSFR, individual galaxies should have SFRs proportional to their stellar mass at all times of their early evolution:

$$\mathrm{sSFR}(t) = \frac{\psi(t)}{M_*(t)} = \text{const.}, \tag{2.9}$$

$$\therefore \psi(t) \propto M_*(t). \tag{2.10}$$

Neglecting mass loss, the SFR is also the rate change of stellar mass:

$$\psi(t) \approx \frac{\mathrm{d}M_*}{\mathrm{d}t}. \tag{2.11}$$

Rearranging and integrating this, we find

$$\frac{\mathrm{d}M_*}{\mathrm{d}t} = \mathrm{sSFR} \times M_*(t) \tag{2.12}$$

$$\therefore \int \frac{1}{M_*(t)} \mathrm{d}M_* = \int \mathrm{sSFR}\, \mathrm{d}t \tag{2.13}$$

$$\log M_*(t) = \mathrm{sSFR}\, t + c \tag{2.14}$$

$$M_*(t) = e^{\mathrm{sSFR}\, t + c} \tag{2.15}$$

$$= C \times e^{\mathrm{sSFR}\, t}. \tag{2.16}$$

Clearly this parametrization requires that $M_*(t=0) \neq 0$, else the SF would never begin. We therefore define a seed mass, $M_0 = M_*(t=0)$, such that $C = M_0$ and

$$M_*(t) = M_0 \times e^{\mathrm{sSFR}\, t}. \tag{2.17}$$

This formalism therefore implies that the SFR also rises exponentially,

$$\psi(t) = \mathrm{sSFR} \times M_*(t) \tag{2.18}$$

$$= \mathrm{sSFR} \times M_0 \times e^{\mathrm{sSFR}\, t}, \tag{2.19}$$

following a timescale determined by the sSFR and a seed mass, which can physically be thought of as the mass of stars formed in an initial burst of SF. Parametrizing the evolution of the sSFR is of course also possible; however this requires at least one further free (and presently unknown) parameter be added. We have therefore maintained the constant sSFR assumption.

Using BC03's GALAXEV CSP utility, we created model SEDs which evolve according to these SFHs, with a grid of seed masses $10^6 \leq M_0 \leq 10^8$ $\mathrm{M}_\odot$ and e-folding times $1 \leq \mathrm{sSFR} \leq 20$ Gyr^{-1}. These models differ from inverted-τ models at early stages of their evolution, where the stars of the seed mass dominate the early light in these models, before any substantial population of stars has been formed by the exponential component. These models were used by Curtis-Lake et al. (2013), and are also used in Chapter 6 of this thesis.

2.4 Absolute magnitudes

It is usually advantageous to compare galaxies in terms of their absolute magnitude, since this is distance (i.e. redshift) independent. (A notable exception is when dealing with observational biases which depend on apparent magnitude, e.g. Chapter 3.) Throughout this thesis, except where otherwise noted, we use a consistent measure of absolute magnitude in the rest-frame UV at 1500 Å: $M_{\mathrm{UV}} \equiv M_{1500}$. To do so, we place a 100 Å-wide top-hat filter, centred at 1500 Å, on the best-fitting stellar population synthesis model to a given SED. This top-filter is similar to windows 4 and 5 defined by Calzetti et al. (1994). Under this method, M_{1500} is not explicitly linked to any observed photometric measurement, but is instead constrained by multiple bands. This reduces the noise-induced error on M_{1500} compared to that on any single band.

Furthermore, M_{1500} is measured consistently across redshifts, regardless of the shape of

the UV continuum. This is important, because over a redshift window of, for example, $4.5 < z < 5.5$, a steep UV continuum of $\beta = -2.5$ would significantly affect the absolute magnitude inferred from a single band. At the two extremes of this example redshift window, the z band is centred at ≈1400 Å and ≈1650 Å. Combined with the non-flat UV spectrum, this implies a difference of 0.1 mag in the z-band *implied* $M_{\rm UV}$ for two galaxies with the same M_{1500}. The importance of consistent measurements of M_{1500} was recently highlighted by Finkelstein et al. (2012b), when considering the colour–magnitude relation of $z \approx 7$ galaxies. As we shall see, these considerations are crucial in deriving accurate and unbiased measurements of the properties of high-redshift galaxies.

3 The unbiased measurement of ultra-violet spectral slopes in low luminosity galaxies at z ≈ 7

The majority of the work presented in this chapter has been previously published (Rogers et al. 2013).

The Ultraviolet (UV) continuum slope β, typically observed at $z \approx 7$ in *HST* WFC3/IR bands via the $J-H$ colour, is a useful indicator of the age, metallicity, and dust content of high-redshift stellar populations. Recent studies have shown that the redward evolution of β with cosmic time from redshift 7 to 4 can be largely explained by a build up of dust. However, initial claims that faint $z \approx 7$ galaxies in the Hubble Ultra Deep Field WFC3/IR imaging (HUDF09) were blue enough to require stellar populations of zero reddening, low metallicity and young ages, hitherto unseen in star-forming galaxies, have since been refuted and revised. In this chapter, we consider the question of how best to measure the UV slope of $z \approx 7$ galaxies through source recovery simulations, in the context of preparing for the ultra-deep UDF12 imaging from *HST*. We consider how source detection, selection and colour measurement have each biased the measurement of β in previous studies. After finding a robust method for measuring β in the simulations (via a power law fit to all the available photometry), we remeasure the UV slopes of a sample of previously published low luminosity $z \approx 7$ galaxy candidates. The mean UV slope of faint galaxies in this sample appears consistent with an intrinsic distribution of normal star-forming galaxies with $\beta \approx -2$, although properly decoding the underlying distribution is found to require further imaging from the UDF12 programme (Chapter 4). We therefore conclude this chapter by considering strategies for obtaining better constraints on the underlying distribution of UV slopes at $z \approx 7$ from these new data, which benefit particularly from the addition of imaging in a second J-band filter: F140W. We find that a precise and unbiased measurement of β is then possible.

3.1 Introduction

In Section 1.11 we argued that measurement biases have plagued the measurement of β at $z \approx 7$ in earlier studies. In particular, we noted that there had been rapid revision in estimates of $\langle\beta\rangle$ for the faintest galaxies and that a lack of consensus was evident in the literature. The situation has been further confused by the fact that different studies have used different datasets, selection methods and techniques for measuring β (e.g. from a single near-IR colour or from SED fitting). The first objective of this chapter is therefore to use simulated data to investigate the impact of image depth, selection biases and measurement techniques on the recovered values of β. Then, based on our findings, we explore possible strategies for the optimum analysis of the new, deeper WFC3/IR imaging of the HUDF which, at the time of writing, was due to be provided by the UDF12 project (including imaging in an additional wave-band (J_{140}); GO12498, PI: Ellis), in order to extract the most robust, least-biased estimate of β for the faintest LBGs at $z \approx 7$.

Throughout this chapter we will consider $z \approx 7$ LBGs to be objects selected with photometric redshift solutions in the range $6.5 \leq z \leq 7.5$. As with previous studies in this area, we do not consider $z \approx 8$ galaxies given the lack of data redward of the Lyman break[1] (which begins to attenuate the J_{125}-band flux at $z \gtrsim 7.9$).

This chapter is laid out as follows. In Section 3.2, we outline three methods of measuring β – from a single colour, a power-law or the best-fitting galaxy-model SED. In Section 3.3, we provide a description of our simulation pipeline. In Section 3.4 we compare with and endorse the conclusions of Dunlop et al. (2012). In Section 3.5, we show the results of simulated HUDF -09E1,-09E2,-12 and ERS datasets, comparing various selection methods and the three β measurement methods. We present a re-analysis of the Dunlop et al. (2012) $z \approx 7$ LBG sample in Section 3.6. Strategies for analysing the UDF12 data are presented in Section 3.7, wherein we briefly discuss the effect of Lyman Alpha Emitters in Section 3.7.3. In Section 3.8, we present the conclusions of this chapter.

Where relevant, we assume a cosmology with $\Omega_0 = 0.3, \Omega_\Lambda = 0.7, H_0 = 70$ km s^{-1} Mpc^{-1} and quote magnitudes in the AB system (Oke & Gunn 1983). For convenience, we use B_{435}, V_{606}, i_{775}, z_{850}, Y_{098}, Y_{105}, J_{125}, J_{140} and H_{160} to refer to the *HST* ACS F435W, F606W, F775W, F850LP and WFC3/IR F098M, F105W, F125W, F140W and F160W filters respectively.

[1] Finkelstein et al. (2012b) do provide estimates of β at $z \approx 8$, but due to the uncertainties do not draw any conclusions.

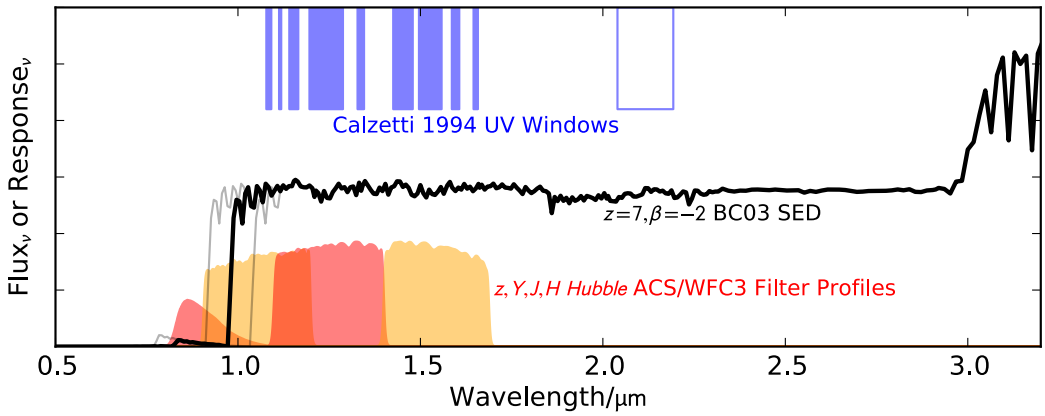

Figure 3.1 The typical spectral energy distribution (SED) of a $z = 7$ Lyman break galaxy, and the filters used to observe it. The SED shown by a thick black line is a $\beta = -2$ Bruzual & Charlot (2003) stellar population model (in this case a 60 Myr old $0.2 Z_\odot$ star-burst), attenuated by Madau (1995) prescribed IGM absorption. The red and orange filter profiles shown are *HST* ACS z_{850}, WFC3/IR Y_{105}, J_{125}, and H_{160} – those filters that probe the rest-frame UV at $z \approx 6$ to 7 in the HUDF09 dataset. Shown in blue above the SED are the locations of the ten Calzetti et al. (1994) UV windows, used in the 'best-fitting model' β measurement method (see Section 3.2.3). The unshaded Calzetti et al. (1994) window is neglected in our fitting (see text). Two grey SED curves show the Lyman break position at $z = 6.5$ and 7.5, illustrating that, within the $z \approx 7$ sample, the Lyman break always attenuates the light within the Y_{105}-band. The Y_{098} (F098M) filter used in the ERS observations approximately spans the shorter two thirds of Y_{105}'s wavelength coverage, without overlapping J_{125}.

3.2 Methods of determining β

In this section, we describe three methods for measuring the UV slope of high-redshift galaxies and show that, for perfect photometry, they yield similar results. Later in Section 3.5, we explore their relative strengths for estimating β in realistic simulated data.

3.2.1 Single colour (β_{J-H})

The UV spectral index β may be approximated from a single colour using no prior assumptions of the underlying spectrum. Where the colour comprises two filters comfortably redward of the Lyman break it is insensitive to small errors in the photometric redshift. Moreover, IGM absorption and any Lyman–α emission present do not contaminate the continuum slope measurement through filters fully redward of 1216 Å in the rest-frame. Given the definition of β,

$$f_\lambda \propto \lambda^\beta \tag{3.1}$$

(e.g. Meurer et al. 1999), the fluxes in two band passes A and B, where the filters' pivot wavelengths (e.g. Tokunaga & Vacca 2005) are $\lambda_B > \lambda_A$, are

$$f_A = c \times \lambda_A^{\beta}, \tag{3.2}$$

and

$$f_B = c \times \lambda_B^{\beta}. \tag{3.3}$$

Therefore the flux ratio is

$$\frac{f_{A,\lambda}}{f_{B,\lambda}} = \left(\frac{\lambda_A}{\lambda_B}\right)^{\beta}, \tag{3.4}$$

or in flux per unit frequency

$$\frac{f_{A,\nu}}{f_{B,\nu}} = \left(\frac{\lambda_A}{\lambda_B}\right)^{\beta+2}. \tag{3.5}$$

To measure β from the colour $A-B$, a relation of the form

$$\beta \equiv C \times (A-B) - 2 \tag{3.6}$$

is sought, where the -2 ensures that an AB colour of $A-B=0$ gives 'flat-spectrum' in f_ν, i.e. $\beta = -2$ in f_λ.

From the colour

$$A-B = -2.5\log\left(\frac{f_{A,\nu}}{f_{B,\nu}}\right) \tag{3.7}$$

$$= -2.5\log\left[\left(\frac{\lambda_A}{\lambda_B}\right)^{\beta+2}\right] \tag{3.8}$$

$$= -2.5(\beta+2)\log\left(\frac{\lambda_A}{\lambda_B}\right), \tag{3.9}$$

the coefficient C is found by substituting in equation 3.6:

$$A-B = -2.5([C \times (A-B) - 2] + 2)\log\left(\frac{\lambda_A}{\lambda_B}\right) \tag{3.10}$$

$$\therefore C = \frac{1}{2.5\log\left(\frac{\lambda_B}{\lambda_A}\right)}. \tag{3.11}$$

With *HST* photometry of objects at $z > 6.5$, the WFC3/IR J and H filters are typically used

for A and B. Then

$$\beta_{\rm colour} = \beta_{J-H} = 4.43(J_{125} - H_{160}) - 2 \tag{3.12}$$

is used to estimate β, since $\lambda_J = 12486$ Å and $\lambda_H = 15369$ Å when the instrument throughput including the detector response function is included (Dressel 2012).

3.2.2 Power-law (β_{YJH})

Objects whose rest-frame UV continuum is present in several filters redward of the Lyman break should in principle have their UV slope better constrained by using all the available information. In the HUDF09 and ERS at $z \approx 6.5$, $Y_{\{098|105\}}$, J_{125}, and H_{160} lie redward of the Lyman break and the additional use of the $Y - J$ colour here should improve the constraint on β over the use of only a single $J - H$ colour. By $z \approx 7.5$, the Lyman break diminishes the Y_{105}-band flux by almost a half, and a power-law fit should begin to approach a single colour. However it is not immediately clear whether employing the Y-band for galaxies in the redshift space ($6.5 \leq z \leq 7.5$) in which the Lyman break is travelling through Y will be beneficial, given the potential for a colour-dependent misplacing of the break within the filter. Moreover, high equivalent-width Lyman–α emission lines could bias β measurements to significantly bluer values than the intrinsic continuum slope, an effect we investigate in Section 3.7.3. In the power-law β measurements presented in the remainder of this chapter, the photometric redshift of an object is used to build a grid of SEDs with varying power-law β values redward of the Lyman break, and zero flux at $\lambda < 1216$ Å. Synthetic photometry of each power-law SED is created, and an object's YJH photometry is used to select the best-fitting β from the grid via a χ^2 fit.

3.2.3 Best-fitting stellar population synthesis model ($\beta_{\rm BC03}$)

To allow a measure of the rest-frame UV continuum slope unaffected by absorption and emission features, Calzetti, Kinney, & Storchi-Bergmann (1994, hereafter C94) defined ten spectral windows in the rest-frame UV avoiding significant spectral features. While defined for use on continuum spectra, Finkelstein et al. (2012b) advocated the use of the windows on photometric data via SED fitting. The use of synthetic population synthesis models allows this 'pseudo-spectroscopic' measurement to make full use of the available photometry. Our implementation of this method uses FAST (Kriek et al. 2009) to perform SED fitting of multi-band photometry, returning both the photometric redshift and the best-fitting Bruzual & Charlot (2003, hereafter BC03) population synthesis model SED. The

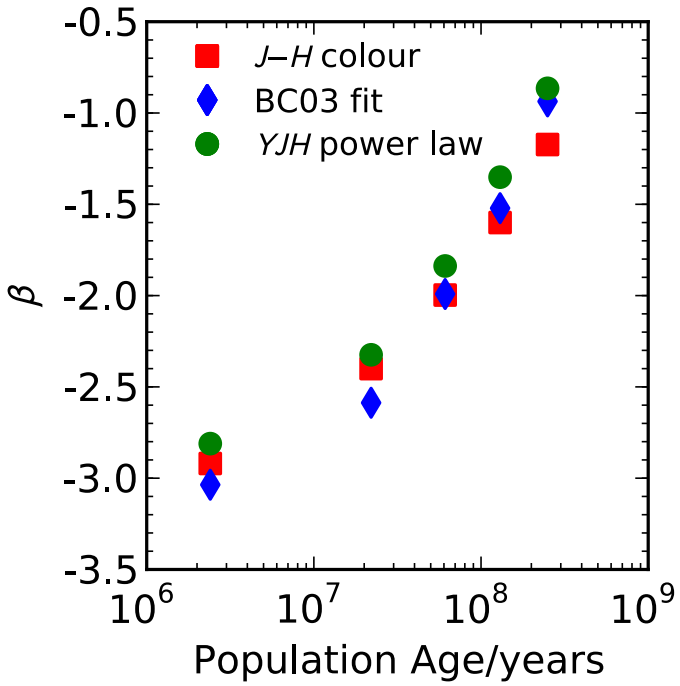

Figure 3.2 The UV slope β, measured using the three methods discussed in Section 3.2, for five input SEDs. The inputs are various ages of a BC03 population synthesis model at $z = 7$ (adopting a Chabrier 2003 IMF, 0.2 $Z_\odot$ metallicity, and a single burst model). Ages of 2.4, 22, 61, 130, 250 Myr give $\beta \approx -3, -2.5, -2, -1.5, -1$. Although all three methods agree perfectly for true power-law SED inputs (not shown), it can be seen that small discrepancies ($\Delta\beta \lesssim 0.2$) exist for more realistic input SEDs.

C94 windows then select the regions of the SED for the power-law fit (a linear fit of $\log f_\lambda$ vs. $\log\lambda$). The blue limit of the resultant β parameter space, $\beta_{\rm min} = -3.2$, is governed by the lowest metallicity (0.05 $Z_\odot$) and youngest (1 Myr) simple stellar population included in the grid. This differs slightly from the approach of Finkelstein et al. (2012b), who used EAZY (Brammer, van Dokkum, & Coppi 2008) to obtain the photometric redshift before further SED fitting with BC03 models (or updated variants). However, locking the redshifts with EAZY prior to fitting the stellar populations with FAST shows no appreciable improvement in the recovery of β or photometric redshift with respect to the input values.

3.2.4 Cross-checking the methods

As shown in Fig. 3.2, the three methods generally agree to within $\Delta\beta \lesssim 0.2$ when provided with perfect photometry of a BC03 SED. With such data, we find that the β_{YJH}, β_{J-H} and $\beta_{\rm BC03}$ methods agree better when the reddest of the ten C94 windows is neglected. As shown in Fig. 3.1, the reddest C94 window is redward of the H_{160}-band at $z \approx 7$ and

therefore purports to probe a region of the intrinsic SED not covered by the photometry. Thus, any spectral features present in the BC03 models in that region (e.g. the slight jump in flux at 1.8 μm observer-frame visible in Fig. 3.1) will cause discrepancies between β as measured from colours alone and from the best-fitting model. We believe this issue may partially explain the offset between β_{J-H} and β_{BC03} seen in fig. 3 of Finkelstein et al. (2012b). For this work, we therefore adopt the nine shortest-wavelength C94 windows.

3.3 Simulation methodology

In this section, we present our method for creating mock catalogues of high-redshift galaxies and producing multi-band images of them with realistic noise properties. The subsequent object recovery, redshift and colour fitting of these simulated galaxies is then described. The resulting simulations are used thereafter to study the measurement of β at $z \approx 7$.

3.3.1 Stellar population choice

For the simulations used for the remainder of this chapter, we adopted two model SEDs for simplicity of comparison. BC03 models of 0.2 $Z_{\odot}$ metallicity with a Chabrier (2003) IMF and ages of 2.4 and 61 Myr were chosen to give SEDs with $\beta_{\mathrm{in}} \approx -3$ and $\beta_{\mathrm{in}} \approx -2$ respectively. The two SEDs are shown in Fig. 3.3, alongside a $\beta = -1$ model for comparison. These models deviate slightly from perfect power law SEDs, allowing the three β measurement methods to yield different results (see Fig. 3.2). In principle, by using BC03 models in preference to pure power-laws we are better able to realistically represent the true SEDs of high-redshift galaxies; in practice the difference is negligible at such high redshift. In these simulations, the input SEDs have not included the reddening due to inter-stellar dust. Whilst not relevant to the β measurement itself – being only an adjustment of the intrinsic β distribution – it is illustrative to see how low the reddening must be to allow galaxies to be observed with $\beta \approx -3$. Fig. 3.4 demonstrates this; for example $\beta = -3$ requires $A_V \leq 0.1$ and an age under 30 Myr with a low metallicity BC03 model. However, dust quantities $A_V < 1$ (perhaps reasonable at high redshift) cannot redden an SED to $\beta = -1$ before the population is tens or hundreds of Myr old. Populations adopting a constant star formation history would additionally require high metallicity to reach $\beta = -1$, as β is almost independent of age. Wilkins et al. (2012) showed simulations detailing how the star formation history and metal enrichment history additionally affect the β distributions.

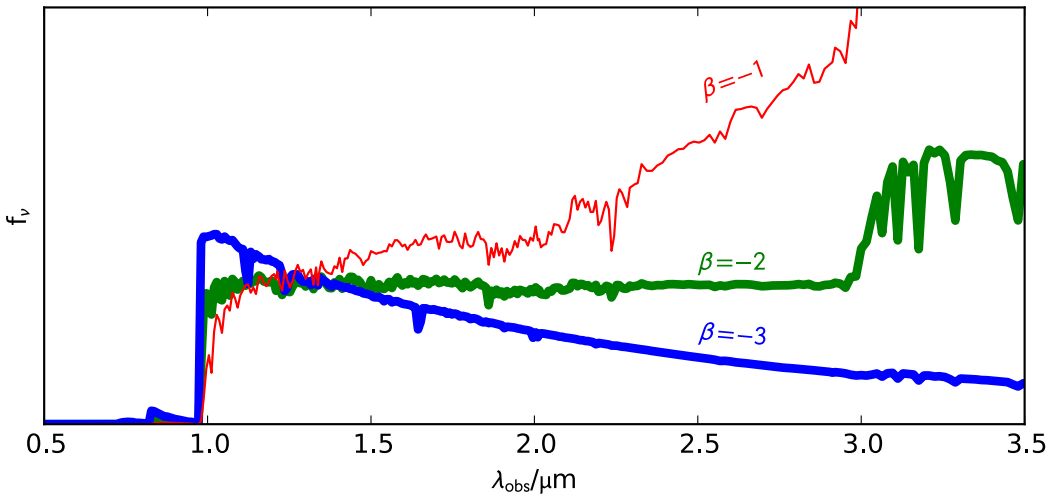

Figure 3.3 BC03 stellar population synthesis model SEDs of age 2.4, 61, 250 Myr (adopting a Chabrier (2003) IMF, 0.2 $Z_{\odot}$ metallicity, and a single burst model) with UV spectral slopes of $\beta = -3, -2, -1$ are shown by the blue, green and red lines respectively. The blue and green SEDs are used as inputs to the simulations described in this chapter.

3.3.2 Simulated image creation

Our simulation design departs somewhat from that used in recent studies. Rather than inserting sources into the real data images, we have performed fully synthetic simulations. This choice allowed predictions for the UDF12 dataset to be made consistently with the treatment of earlier data. In Section 3.3.4 we verify that this choice does not affect the measured scatter in β. Our simulations began by computing theoretical magnitudes for galaxies of both stellar population models, at a range of redshifts and absolute magnitudes, through the observed filters. To create sky images, empirical *HST* Point Spread Functions (PSFs) were initially inserted into blank images. For simplicity, the same (band-dependent) set of PSFs were used in all of the datasets. The inserted PSFs were randomly spatially distributed, but pixel-centred, with the relative number density at each redshift slice given by the evolving luminosity function of McLure et al. (2009, eqn. 3) which reasonably reproduces the observed $z = 7$ (McLure et al. 2010) and $z = 8$ (Bradley et al. 2012) luminosity functions. In the simulations the absolute number density was arbitrarily boosted to allow more robust statistics to be derived. We mitigated source confusion ($n_{\rm sources} \approx 0.1$ per aperture) by an arbitrary choice of image size and by neglecting to insert objects at redshifts significantly distant from those of interest. For instance, the input catalogue did not feature a $z \sim 2$ interloper population (although objects may freely have been designated as such 'low-z escapees' by the photometric redshift code). Redshift $z =$ 5–9 galaxies were included, however, to allow migration of galaxies in-to and out-of the

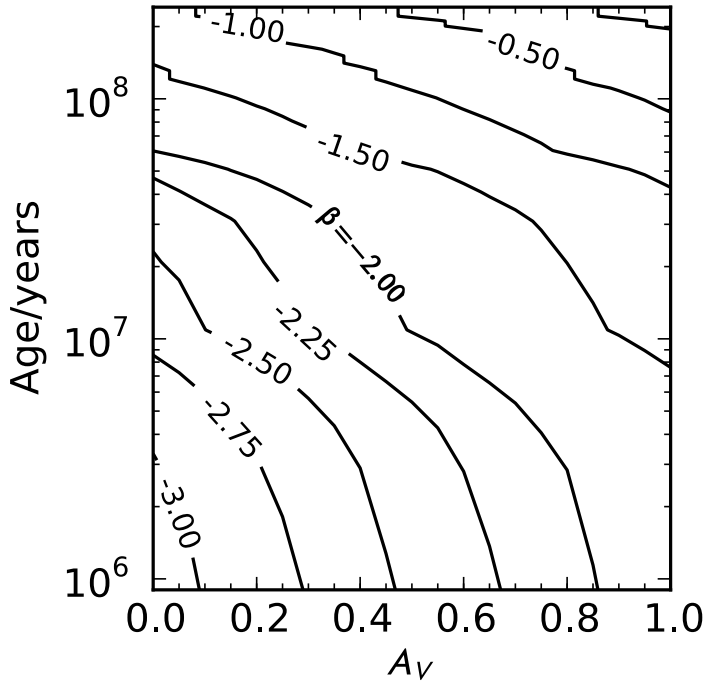

Figure 3.4 Contours showing intrinsic stellar population β values in the Age–A_V parameter space. A_V parametrizes the dust attenuation, calculated according to the Calzetti et al. (2000) prescription. The population model is the same BC03 1/5 $Z_\odot$ burst used throughout our simulations (for solar metallicity, add $\approx +0.25$ to each contour's β value).

redshift bin of interest, an effect which can have a significant impact on the measured UV slopes. The luminosity function was integrated down to $M_{\rm UV}(1500\text{Å}) = -16$, fainter by ≈ 2 mag than the least luminous HUDF objects in the McLure et al. (2011) robust sample of high-redshift galaxies. Those objects below the detection threshold are useful in providing the simulated image background with some of the non-uniformity seen in real data.

Simulated noise properties

We added artificial noise to these 'perfect' images, designed to match the noise properties of a given survey. Table 3.1 lists the measured 5σ limiting detection magnitudes for the ERS, HUDF09E1 and HUDF09FULL surveys and estimated limits for the UDF12. These depths were computed from the standard deviation of 0.6-arcsec diameter aperture fluxes placed on source-free regions of the image, according the procedure detailed earlier in Section 2.2.

The noise images, required for the simulations, consist of pixels with random flux values. For simplicity, we provide the simulations with zero background; in real data, the

background is typically subtracted prior to analysis. Therefore each pixel of the noise image should be assigned a (noise) flux of $n_{\rm px} = \mathrm{rand}(0, \sigma_{\rm px})$. However calculating a realistic value of $\sigma_{\rm px}$ is non-trivial, since in order to obtain a better sampling of the *HST* PSF, WFC3/IR images are obtained in a dither pattern. The multi-band images are then 'drizzled' (Fruchter & Hook 2002, Koekemoer et al. 2002) onto a common pixel grid (typically 0.06 arcsec/px). The drizzle process leads to correlated noise in adjacent pixels, since a single output pixel will in general have multiple input pixels contributing to it (and vice versa). The relevant reduction of HUDF data was drizzled onto a pixel scale $s = 0.5\times$ the native scale, and using the multidrizzle parameter `PIXFRAC`=0.4. A `PIXFRAC`$\neq 0$ value allows the multiple input pixels to all contribute to the final mosaic. Assuming the drizzling is uniform and the image is large, the noise correlation factor (Fruchter, A., Sosey 2009)

$$R = \frac{1}{1-r/3} = 1.36, \qquad r = \frac{\texttt{PIXFRAC}}{s} \tag{3.13}$$

represents the overestimation of the global pixel RMS when calculated relative to the local, correlated RMS noise. Crucially, setting $\sigma_{\rm px} = \mathrm{RMS}_{\rm global}$ would return an unrealistically peaky noise image: the image-wide distribution of pixel values would be comparable to the real data, but adjacent pixels would be excessively uncorrelated.

We simulated the correlation effect by first creating an excessively noisy image, and then smoothing it to partially correlate pixels locally (on the scale of an object). Smoothing the image increases the ratio of pixel noise to global noise, R, as shown in Fig. 3.5. Both the noise image's pixels and the aperture depths represent the uncertainty on the measurement of the background (which is here zero). Since each aperture flux is the sum of its constituent pixels' fluxes, an aperture's variance $\sigma^2_{\rm aper}$ is

$$\sigma^2_{\rm aper} = \sum \sigma^2_{\rm px} \tag{3.14}$$

$$= \pi r^2_{\rm aper} \sigma^2_{\rm px}. \tag{3.15}$$

Each noise image was to be smoothed but also exhibit the correct aperture depth when analysed, so $\sigma_{\rm px}$ was pre-corrected for the smoothing:

$$\sigma_{\rm px} = \sqrt{\frac{(\sigma^{\rm corr}_{\rm aper})^2}{\pi r^2_{\rm aper}}}. \tag{3.16}$$

Neglecting the correlated noise/smoothing, the pixel noise would be given by

$$\sigma^{\rm corr}_{\rm aper} = \frac{-2.5}{5} \log(\mathrm{ZP} - \mathrm{AB}_{5\sigma}), \tag{3.17}$$

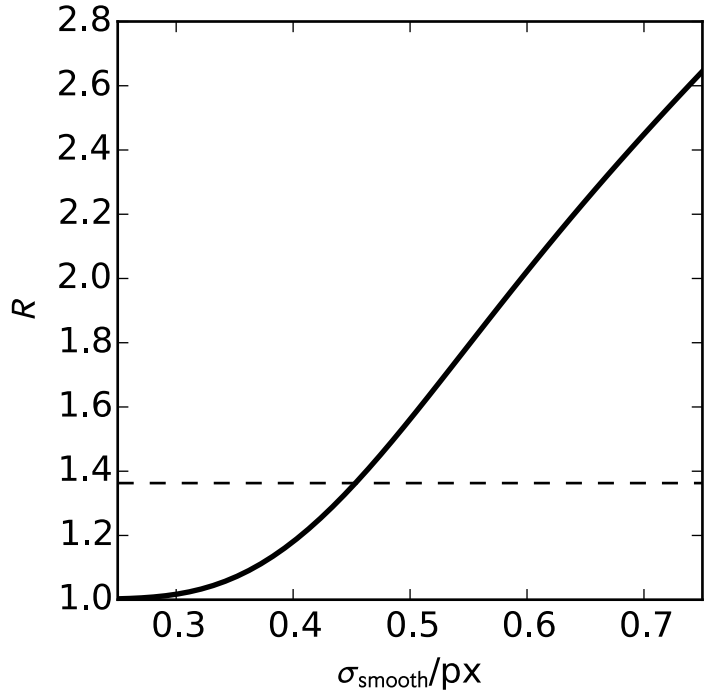

Figure 3.5 An empirical example of how the noise correlation factor R, which relates the global RMS noise to the pixel RMS noise, changes as the noise image is smoothed by a Gaussian of various smoothing lengths $\sigma_{\rm smooth}$. The dashed line is $R = 1.36$, the theoretical value for the relevant HUDF data reductions (WFC3/IR images on a 0.06 arcsec/px grid, with `PIXFRAC`=0.4). To achieve that, the images must be smoothed by $\sigma_{\rm smooth} \approx 0.45$ px.

where $\mathrm{AB}_{5\sigma}$ is the five sigma limiting magnitude in a 2 $r_{\rm aper} = 0.6$-arcsec diameter aperture.

Accounting for smoothing, the pre-correction is defined by the approximation

$$\sigma_{\rm aper}^{\rm corr} = \frac{-2.5}{5} \log\left(\mathrm{ZP} - \left(\mathrm{AB}_{5\sigma} + \frac{\sigma_{\rm smooth}}{5}\right)\right), \tag{3.18}$$

for small $r_{\rm aper} \approx 5$ px apertures. This mechanism yields images for which the standard deviation of aperture fluxes in source-free regions yields the desired limiting magnitude, yet with global RMS noise (as measured by SEXTRACTOR, and thus defining the detection threshold) very comparable to the real HUDF data (see 3.6). For these simulations, the value of $\sigma_{\rm smooth}$ was tuned to best achieve these goals; the depth of a typical noise image matched the real image to around $\Delta\mathrm{AB}_{5\sigma} = 0.05$, and the global pixel RMS (and therefore detection threshold) to around $\Delta\,\mathrm{RMS} = 10\%$.

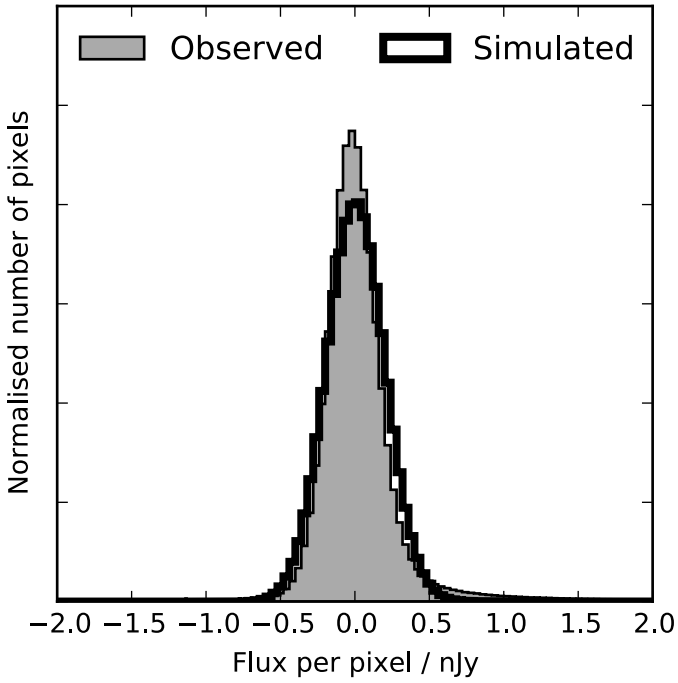

Figure 3.6 A comparison of the pixel-flux distributions of the real HUDF09E1 J_{125} image and our simulated image. The real image has been globally backgrounded subtracted, leaving a distribution well matched by the noise distribution of the simulated image.

3.3.3 Object recovery

For all the simulations, objects were recovered using SEXTRACTOR 2.8.6 (Bertin & Arnouts 1996) in dual-image mode. Objects were selected, unless otherwise noted, from the J_{125} image down to the 1.4σ level (`DETECT_THRESH = 1.4`, `THRESH_TYPE = RELATIVE`) for two adjacent pixels (`DETECT_MINAREA = 2`). This method typically selected $\approx 10-20\times N_{\rm input}$ objects. Photometry was performed in 10-pixel (0.6-arcsec) diameter apertures for all bands. The resulting catalogues were cut such that `MAG_APER` (detection band) was brighter than the 5σ limit, retaining approximately 70 per cent of the input objects that were *intrinsically* brighter than the 5σ limit. The fluxes of objects in these catalogues were corrected to total assuming point source aperture corrections for each band. A $z\approx 7$ sample was then obtained by applying a selection function to the catalogue, either a colour–colour cut or a full photometric redshift selection. In the latter case, we found the redshift and best-fitting stellar population using FAST (Kriek et al. 2009) with a wide library of BC03 models. For clarity, both input and fitted SEDs contained only simple stellar populations. Age and metallicity were fitted, however, and the models available to FAST included those that were used for input. As Finkelstein et al. (2012b) discussed, the actual choice of models should have little influence on the β values, provided a wide range

Table 3.1 *Limiting magnitudes (5σ depths) of the datasets considered in this work are shown for* HST *ACS and WFC3 imaging. The ERS and HUDF09E1 depths are measured following the method of McLure et al. (2011) and using their image reductions; HUDF09FULL depths from a consistent treatment of the data released by Bouwens et al. (2012a); approximate depths for the forthcoming UDF12 WFC3 programme are marked by *. The depths are taken in 0.6-arcsec diameter circular apertures in blank regions of the images as described in McLure et al. (2011). HUDF09E1 and HUDF09FULL refer to the first and both epochs of the HUDF09 programme respectively.* †*While the UDF12 programme features no further observations in F125W, modest depth improvements are expected from improved reductions of existing data.*

Dataset	B_{435}	V_{606}	i_{775}	z_{850}	Y_{098}	Y_{105}	J_{125}	J_{140}	H_{160}
ERS	27.7	27.9	27.3	27.1	27.2	–	27.6	–	27.3
HUDF09E1	29.0	29.5	29.2	28.5	–	28.6	28.7	–	28.7
HUDF09FULL	29.0	29.5	29.2	28.5	–	28.7	28.9	–	28.8
UDF12	29.0	29.5	29.2	28.5	–	29.5*	29.0*†	29.0*	29.0*

of models are available. Thus, fully investigating the degeneracies between population parameters is not necessary in order to measure β (although see Section 3.3.4). Following Dunlop et al. (2012), we split the sample into ROBUST and UNCLEAR categories. The ROBUST sample contained only galaxies whose primary photometric redshift solution at $6.5 \leq z \leq 7.5$ was preferred to any secondary solutions by $\Delta\chi^2 \geq 4$. Galaxies failing to meet this criteria but none the less having a preferred $z \approx 7$ solution were denoted UNCLEAR. Hereafter, we refer to the combination of ROBUST+UNCLEAR as ALL.

Recovered object candidates were paired to input objects based on their recovered positions. Strict position matching (< 2-pixel radial offset) left a sample free of *pure* noise spikes ($\lesssim$ 1 per cent at 5σ), while retaining objects where noise spikes, having randomly boosted the flux in individual bands, significantly altered the colours. Detected objects for which identification of the corresponding input object was ambiguous ware similarly dropped ($\sim$ 1 per cent), although this was minimized by avoiding significant crowding in the simulations. Objects were only deemed 'ambiguous' when two or more input objects lay within 2-pixels of a recovered object's position. With aperture diameters of 10-pixels, there was still ample ability for faint background objects to contribute to the recovered flux of the detected object. In summary, our selection criteria were:

S/N(J) $\geq$ 5.

$6.5 \leq z_{\rm phot}({\rm FAST}) < 7.5$.

Sky position within 2-pixel of a single input object.

ROBUST: χ^2(secondary z) - χ^2 (primary z) $\geq$ 4.

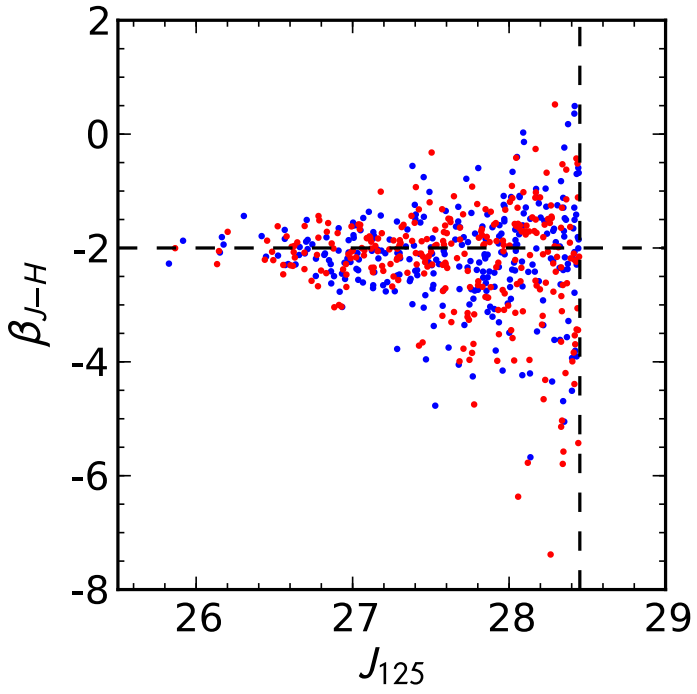

Figure 3.7 Comparison of the colour–magnitude scatter of simulated $z \approx 7$, $\beta_{\rm in} = -2$ galaxies in the HUDF09E1 data using source injection into the real images (blue points) or synthesised noise in blank images (red points). The distribution and scatter of measured UV slopes β_{J-H} is very similar in both cases. One third fewer objects are recovered from a source injection simulation (where some inserted objects fall onto existing sources) than in the simulated noise simulations, but for clarity the number of objects in each data series is identical in this figure. In both cases, ALL (both ROBUST and UNCLEAR) $6.5 \leq z < 7.5$ sources are shown. Dashed lines show the input β and the effective $5\,\sigma$ detection limit of the data.

UNCLEAR: $0 < \chi^2$(secondary z) - χ^2 (primary z) < 4.

Overall these criteria allowed the relevant measurement biases to become manifest while allowing precise tracing of input to recovered parameters. Having created catalogues with both input and output redshift and photometry parameters, the three β measurements for this final sample were made based on the three methods presented above.

3.3.4 Synthesised noise vs. real noise

As discussed above, we opted to simulate the noise properties of deep *HST* images rather than inject sources directly into the real images. This approach was chosen to allow a consistent, predictive, treatment of the UDF12 imaging prior to the observations. We verified that our simulated noise maps yield equivalent results to a source injection

scheme by inserting PSFs both into the real HUDF09E1 imaging and into synthetic images with noise designed to match the measured depths of the real data. Objects were detected and extracted in an identical manner in each case. For the source injection catalogue only, the catalogues were pruned of any objects already present in the unmodified HUDF09E1 images before continuing with the photometric redshift analysis. Fig. 3.7 shows the resulting $\beta - J_{125}$ scatter for each approach. Very similar widths in the scatter of β are seen at each magnitude, with no significant offset in colour or magnitude between the samples: at $J_{125} = 28.0 \pm 0.25$ both $\sigma(\beta)$ and $\langle\beta\rangle$ differ by ≈ 0.1 (simulated noise $\langle\beta\rangle = -2.3, \sigma(\beta) = 1.0$; source injection $\langle\beta\rangle = -2.2, \sigma(\beta) = 1.0$). This confirms that the scatter in β for faint, low SNR objects is well reproduced by the simulated noise scheme used throughout this chapter.

3.3.5 Extended sources vs. point sources

In the simulations presented here, we have simulated faint $z \approx 7$ galaxies with PSFs. While the faint galaxies our simulations were designed to replicate are very nearly unresolved, we have none the less performed a conservative test of this assumption. We drew half-light radii from a gaussian distribution centred on 0.65 kpc with σ=0.15 kpc, consistent with the size-luminosity results of Oesch et al. (2010a) for $L > 0.3L^*$ galaxies at $z \approx 7$, and convolved corresponding GALFIT (Peng et al. 2010) models with the PSF. The measurement of β is unaffected if we use these sources in our simulations rather than PSFs. This is as expected given that our chosen aperture diameter size of 0.6 arcsec corresponds to $\approx 5R_e$ on average.

3.4 Comparison to Dunlop et al. (2012)

In contrast to the main simulation approach adopted in this work, Dunlop et al. (2012) injected PSFs into the real HUDF09E1 and ERS images. Crowding was avoided by inserting sources only within the detection redshift range ($6.5 < z_{\rm in} < 7.5$). Furthermore, only objects with $J_{125}^{\rm input} < 30$ were included – preventing excess noise being supplied by extra ultra-faint sources.

Our present simulations, when limited to the same inputs and selection function, yield results in very good agreement with those of Dunlop et al. (2012). Fig. 3.8 shows the recovered β_{J-H} values for a simulated population of faint $\beta_{\rm in} = -2$ objects in the HUDF09E1 and ERS fields, and is remarkably similar to fig. 7 of Dunlop et al. (2012). There is a clear offset to blue βs, which becomes progressively worse for fainter objects. In the HUDF simulation, objects in the faintest 1 mag bin average $\langle\beta\rangle = -2.4$. This is even more pronounced in

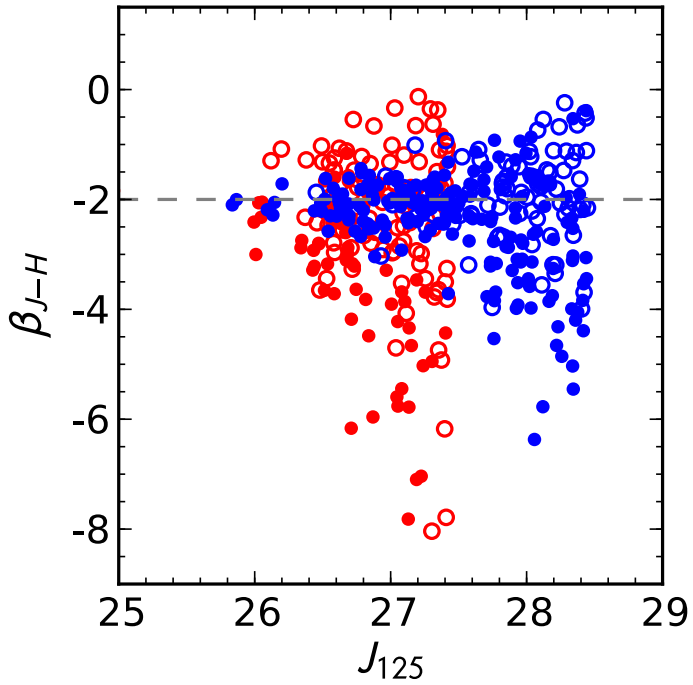

Figure 3.8 Distribution of β vs. apparent magnitude from a simulation in which all objects have an intrinsic UV slope of $\beta = -2$. Similar to fig. 7 of Dunlop et al. (2012), all objects have $6.5 \leq z_{\rm in}, z_{\rm phot} < 7.5$ and $J_{125}^{\rm input} < 30$. Red and blue symbols denote the ERS and HUDF09E1 simulations respectively. Open circles denote objects whose photometric redshift is deemed UNCLEAR, filled circles are objects with ROBUST photometric redshifts. In contrast to Dunlop et al. (2012), this plot includes a colour correction of $\Delta(\beta_{J-H}) \approx +0.2$ to account for the flux of a point source not enclosed by the photometric aperture in each band.

the ERS, where the J-band imaging is deeper than the H-band imaging and where the Y_{098} filter, which cuts off at a shorter wavelength than the HUDF's Y_{105} filter, is used. The bias in the ERS becomes catastrophic for the faintest objects (objects in the faintest 1 mag bin average $\langle\beta\rangle = -2.7$). The photometric redshifts of even relatively high SNR objects are often deemed UNCLEAR when β is red, meaning a ROBUST sample excluding such red objects will show a further blueward bias. Corroborating the work of Dunlop et al. (2012), we find measuring β from a single $J-H$ colour from a sample of $z \approx 7$ galaxies yields a large blue bias for the lowest SNR objects.

3.5 Discussion of simulation results

In this section, we use simulations to investigate how both the $z \approx 7$ LBG selection method and the UV slope measurement method affect the measurement of β. Simulations, as

described above and using $\beta_{\rm intrinsic} = -3$ and -2, were constructed of the HUDF -09E1, -09E2, -12 and the ERS datasets. The depths of these datasets are given in Table 3.1. These eight simulations are used throughout the remainder of this work.

3.5.1 Comparison of $z \approx 7$ selection functions

Many high-redshift galaxy studies have relied on colour–colour criteria for sample selection rather than using a full SED-fitting photometric redshift code. Here we show an illustrative comparison of those colour–colour criteria employed by Bouwens et al. (2012a; 2010) and of our photometric redshift selection using BC03 template SEDs.

The colour–colour selection criteria described by Bouwens et al. (2012a, hereafter B12) differ from those of Bouwens et al. (2010, hereafter B10). In both cases, the main selection criteria was a 'z_{850}-drop': a $z-Y$ colour of > 0.8 (in B10) or > 0.7 (in B12). Both studies also prohibited the selection of red objects, requiring $Y-J < 0.8$. However B12 used an additional $z-Y$ vs. $Y-J$ colour function, excluding low redshift interlopers that would otherwise have been newly selected following the relaxed $z-Y$ criteria. In both studies, various criteria were used to ensure objects with optical detections were excluded. Crucially, B10 report the use of a $J_{125} \geq 5.5\sigma$ cut to their catalogue – a criterion that, as we shall see, is bound produce a bias towards the selection of objects with blue $J-H$ colours. This cut was (apparently) abandoned by B12, the faint limit of the catalogue being determined instead by a probability threshold in the detection image (a χ^2 image which in this case results in a similar selection to a $Y+J+H$ stack; Szalay, Connolly, & Szokoly 1999).

We have approximately replicated the selection methods of B10 and B12, using our HUDF09E1 $\beta_{\rm in} = -2$ simulation. The same simulation was used in both cases to allow a comparison of the selection functions independent of the data variation. In this case a χ^2 detection image, created from the Y, J, H images following the procedure of Szalay et al. (1999), was used for object detection with aperture photometry performed on individual bands as usual. Redshift $z \sim 7$ galaxies were selected according to the criteria of B10 and B12 independently. Two further catalogues were created by selecting ALL sources with photometric redshifts $6.5 \leq z \leq 7.5$, and only ROBUST $6.5 \leq z \leq 7.5$ sources. As colour–colour selections give no precise photometric redshifts, β was measured in all cases from the $J-H$ colours.

In Fig. 3.9, $\langle \beta_{J-H} \rangle$ is shown for each catalogue as a function of J_{125} magnitude. We find that the standard photometric redshift selection and the colour–colour selection of B10 are

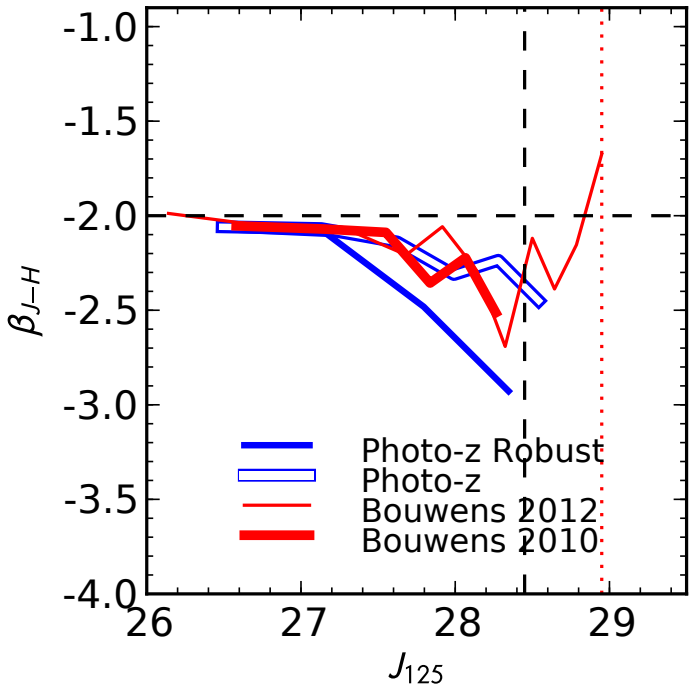

Figure 3.9 Comparison of various selection functions, shown by average UV slopes $\langle\beta_{J-H}\rangle$ from simulated galaxies in the HUDF09E1 in magnitude bins of fixed occupancy. Galaxies have been selected from these images with four selection methods. Thick and thin red lines show objects selected according the the dropout criteria of Bouwens et al. (2010) and Bouwens et al. (2012a) respectively. Hollow and solid blue lines show, respectively, objects selected by a full photometric redshift analysis when ALL $z \approx 7$ candidates are included and when only objects with ROBUST photometric redshifts are included. Comparing the two thick lines, we conclude that an inclusive photometric redshift selection and a traditional colour–colour selection suffer similar bias in β. As expected, a more exclusive photometric redshift selection yields a larger blue bias. The vertical, dashed line shows the effective 5σ flux limit in the J_{125}—band. No J-band SNR cut is used in the B12 selection method, hence the long tail toward faint magnitudes. In that case, the dotted red line is a guide to the J_{125}—band magnitude of a source only just reaching the 5σ limiting magnitude of the χ^2 stack, assuming $z = 7$ and flat-spectrum. These objects, detected from a combined Y, J, H image, only rise above the detection threshold due to noise-spikes boosting the H-band flux – hence their red β_{J-H} colours with respect to the input (horizontal, dashed line).

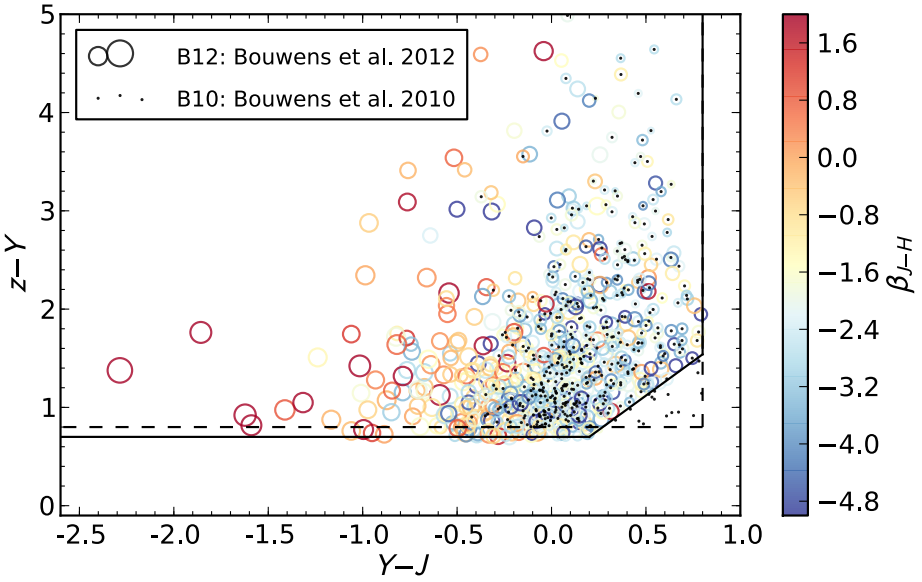

Figure 3.10 Comparison of the colour–colour selection functions, and resulting samples from simulated images, of B10 (Bouwens et al. 2010) and B12 (Bouwens et al. 2012a). Small black dots mark galaxies selected from a HUDF09E1-like simulation, where all galaxies have $\beta_{\rm in} = -2$, using the selection function of B10. The vertical axes shows the Lyman break size ($z \sim 7$, z_{850}-dropouts). The horizontal axes shows the Lyman–α-to-UV colour. Coloured circles show a catalogue, selected from the same images, using the B12 selection criteria. Bluer symbols denote steeper UV slopes β, measured by the $J-H$ colour. Larger symbols denote the galaxies faintest in J_{125} (i.e. largest magnitude). The B12 selection allows galaxies faint in J_{125}, with consequently red $J-H$ colours to be selected – the large, red circles in the lower left of the plot – which were not selected in B10 due to a $J_{125} \geq 5.5\sigma$ cut. Objects selected by B10's criteria in the lower right of the plot are treated as contaminants by B12. As can be seen from the colours of nearby objects, many of these would hold blue $J-H$ colours. This combination of changes will clearly allow B12's selection criteria to yield a redder average β – for the same data – than that of B10.

similarly biased toward blue β values for faint galaxies. A photometric redshift selection is only excessively biased if some additional criteria are used to robustly exclude low redshift interlopers (i.e. $\Delta\chi^2 \geq 4$).

Bouwens et al. (2012a) show, in their fig. 5, that the B12 selection criteria yield an almost negligible bias in the average UV slope $\langle\beta\rangle$ even for very faint simulated galaxies at $z \approx 7$. In contrast, Fig. 3.9 of this work shows substantial bias in the B12 selected catalogue. This discrepancy is due to the choice of which observed data are used as a proxy for UV luminosity. Here we have used J_{125}, as this probes rest-frame M_{1500} most closely throughout the $z \approx 7$ bin. As also noted by Finkelstein et al. (2012b), the clarity of the dependence of β on M_{1500} is reduced if one chooses to use $m_{\rm IR} \approx \langle Y, J, H\rangle$ as a proxy for M_{1500}.

The difference between the faint ends of the B10 and B12 colour–magnitude relations in Fig. 3.9 is striking. The removal of an explicit 5.5σ cut in J_{125} by B12 allows many sources with low J-band SNR to be included, as seen in Fig. 3.10. In order to be detected in an IR stack, these objects must be flux-boosted in the H-band, consequently giving them red $J-H$ colours (the Y-band flux is moderately attenuated at $z = 7$). This is clear from Fig. 3.10, which shows a comparison of the B10 and B12 selection functions based on the same simulation as Fig. 3.9. The addition of faint, red-scattered, sources in the selection function of B12 perhaps accounts for why they report a somewhat redder $\langle\beta\rangle \approx -2.7$ than B10 ($\langle\beta\rangle \approx -3.0$) for the faintest galaxies.

In summary, we find that an inclusive photometric redshift selected sample and a $z \sim 7$ colour–colour selected sample are similarly biased at the faint end by preferential selection of blue-scattered objects.

3.5.2 Comparison of β measurement methods

Fig. 3.11 shows the recovered UV slopes, as a function of brightness, of simulated objects in the HUDF09E1, HUDF09FULL, UDF12 and ERS fields. From each simulation, β has been recovered using the three methods described above. Faint objects show extreme scatter in their UV colours, which is maximized when using only a single colour measurement. The scatter becomes extreme at ~ 0.5 mag brighter than the 5σ limit in each field. In the UDF12, the addition of the J_{140} band primarily benefits the power-law method; although the other methods do benefit indirectly via improved redshift recovery. In Fig. 3.11, the bias toward faint, blue sources appears similar for the two input βs (except for when using $\beta_{\rm BC03}$). If we had considered only ROBUST $z \approx 7$ objects, the bias would be more

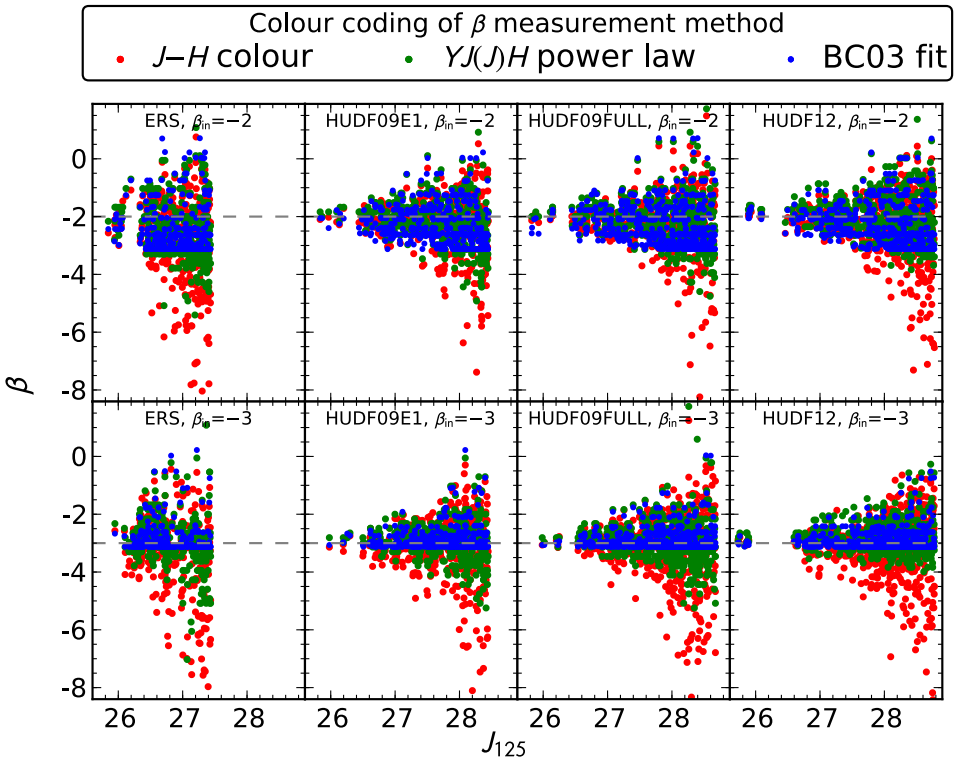

Figure 3.11 Comparison of the three β measurement methods, described in Section 3.2, for simulated objects in the ERS, HUDF09 (epochs 1 and 2) and UDF12 datasets. For each method (differentiated by colour of symbol), objects' UV slopes are plotted as a function of detection-band magnitude (J_{125}, AB mag, corrected to total flux). Within each simulation, all objects have a single $\beta_{\rm intrinsic}$ as shown in the top-right corner of each panel. ALL objects with photometric redshift $6.5 \leq z \leq 7.5$ are included, regardless of the robustness of the redshift fit. The resulting β values as measured from the $J-H$ colour only or a fit to the best-fitting BC03 model's rest-frame UV continuum are shown by red and blue dots respectively. Green dots show β measured using our preferred method: a pure power-law fit to the YJH photometry ($YJ_{125}J_{140}H$ in UDF12), attenuated with a Lyman break cutoff to the power-law at $(1+z_{\rm phot})\times 1216$ Å.

apparent in the $\beta_{\rm in} = -2$ simulation. Although the selection function was identical for both simulations, where $\beta_{\rm in} = -3$ there is a larger colour space available redward of the intrinsic colour. Objects could be scattered into this colour space while still being robustly placed at high redshift. For example, if a galaxy with $\beta_{\rm in} = -2$ is scattered by $\Delta\beta = +2$ it is liable to be considered a potential low-redshift contaminant and therefore deemed UNCLEAR. With the same scatter, a galaxy with $\beta_{\rm in} = -3$ will be left with $\beta_{J-H} = -1$ and will likely be kept as a ROBUST high-redshift candidate.

As can be seen in Fig. 3.1, an SED fit at $z = 7$ is essentially a fit only to $(z)YJH$ photometry, with all bluer bands providing non-detections as they lie blueward of the Lyman break. It is therefore unsurprising that the β distributions as measured from the best-fitting model and from a power-law fit to the YJH photometry are somewhat similar for $\beta_{\rm in} = -2$.

However, objects with *observed* $\beta \lesssim -3$ are unable to have their colours reproduced by the limited parameter space of population synthesis models; this is particularly apparent in the ERS dataset, where the colour-scatter is amplified by the J_{125} imaging being substantially deeper than the H_{160} imaging. Thus an apparent tightening of the recovered β distribution is seen using the best-fitting model method, by virtue only of an *a priori* assumption of how blue the UV slope may be. In fact, were the intrinsic colours of faint $z \approx 7$ galaxies as blue as $\beta = -3$, a population average of $\langle \beta_{\rm BC03} \rangle$ would not yield this result, but rather a red-biased $\langle \beta \rangle \approx -2.8$ (in the faintest 1 mag bin of our $\beta_{\rm in} = -3$ simulation). This creates a complicated bias function, since the method returns a *blue* biased $\langle \beta \rangle \approx -2.4$ when $\beta_{\rm in} = -2$ (in the same bin). The artificial tightening of the scatter is also severe: in the same bin, $\sigma(\beta_{\rm BC03}) = 0.8$ or 0.5 for $\beta_{\rm in} = -2$ and -3 respectively. For comparison, the faintest 1 mag bin of the $\beta_{\rm in} = -2$ and -3 simulations yield $\langle \beta_{YJH} \rangle = 2.3 \pm 0.9$ and -3.0 ± 0.8, respectively. Fundamentally, given that $\langle \beta \rangle$ appears to evolve (albeit mildly) with increasing redshift, the intrinsic β distribution at $z \approx 7$ likely has an average of $\langle \beta \rangle \gtrsim -2.5$. Certainly for the blue extreme of this range, $\langle \beta \rangle \approx -2.5$, truncating one side of the colour scatter will clearly yield unrepresentative measurements of $\langle \beta \rangle$ and $\sigma(\beta)$.

This is not to discount the use of the best-fitting model method outright: Finkelstein et al. (2012b) have shown strong support for the method in similar source recovery simulations. They inserted a population of objects whose distribution of *stellar population parameters* matched those observed in their HUDF sample. For the average galaxy in that population, and particularly at $z < 7$, Finkelstein et al. (2012b) found that β was recovered most successfully from the best-fitting model; a result we reproduce in that the *scatter* is minimal in $\beta_{\rm BC03}$. Finkelstein et al. (2012b) acknowledge that the method would break down were the parameter space edge to be reached, and the crux of our argument against this method is that the faint, blue, $z \approx 7$ galaxies we simulate here exceed that limit (due to the impact of noise). For galaxies detected with high significance, the method performs well and there is no evidence that their colours are not reproducible by the stellar population synthesis models in an SED fit. A power-law fit to YJH photometry, attenuated with a Lyman break as prescribed by the photometric redshift, yields UV slopes closer to their intrinsic values than does the $J-H$ colour, yet without the bias introduced by the assumption that the *observed* colours of low signal-to-noise objects should be reproducible by stellar population models.

The complexity of the bias function for the best-fitting model method (in that it is dependent on the intrinsic β) is compounded by the reliance on accurate photometric redshifts. This reliance is shared by the power-law method. Where the colours of a galaxy are reproducible by models in the photometric redshift model set, redshift recovery is

generally good: $|z_{\rm phot} - z_{\rm in}| \lesssim 0.1$. However, even with perfect HUDF09-like photometry of a galaxy with $\beta_{\rm in} = -4$ (pure power law) at $z_{\rm in} = 7$, a photometric redshift of 6.86 is obtained using BC03 models – the redshift is underestimated in order to account for the galaxy's "excess" flux in the Y-band when compared to a necessarily redder model. Fortunately, the power-law method is reasonably robust to this: adopting $z = 6.86$, a YJH power-law fit for β then yields $\beta \approx -3.8$ – the value of β being tempered slightly toward the colours of the model in the photometric redshift fit. This bias is clearly still smaller than that seen when β is measured directly from the best-fitting model.

3.6 Measurements of β for existing $z \approx 7$ galaxy candidates

Our simulated observations show that, for both the HUDF09 and ERS datasets, a power-law fit to YJH photometry provides a more reliable measurement of the population's UV slopes than a single $J-H$ colour. We have therefore re-analysed the photometry of the $z \approx 7$ sample of HUDF09 and ERS galaxies, provided by Dunlop et al. (2012), using a YJH power-law fit. McLure et al. (2011) provide a detailed description of the photometric redshift selection of a similar sample; the Dunlop et al. (2012) sample we use here is more inclusive in that it includes all high-redshift galaxy candidates with both UNCLEAR and ROBUST photometric redshifts. In line with the rest of this work, these catalogues were pruned of any objects with J_{125}-band photometry fainter than the 5σ limit. In addition, we updated the photometry of the Dunlop et al. (2012) HUDF09E1 sample using the full-depth HUDF09FULL dataset so that we can compare ERS, HUDF09E1 and HUDF09FULL $z \approx 7$ catalogues to our simulations as shown in Fig. 3.12. It is immediately clear that within each dataset there is a trend toward blue βs at faint magnitudes. This is true not only for the ROBUST objects, but for ALL. However, this trend is mirrored by the $\beta = -2$ simulation (green and red dots in the figure). In fact, the faint bin of the HUDF09E1 sample averages $\langle\beta\rangle = -2.6 \pm 0.2$ which is only marginally bluer than $\langle\beta_{\rm sim}\rangle \approx -2.4$, the biased measurement reached by our intrinsically flat-spectrum simulation in the same luminosity bin (see also Fig. 3.9). Moreover, as shown in the right-hand panel of Fig. 3.12, the higher signal-to-noise delivered by the complete HUDF09FULL dataset yields redder values ($\langle\beta\rangle = -2.3$ for the faintest luminosity bin) as expected if $\langle\beta\rangle$ is significantly biased by photometric scatter. Thus, while some of the HUDF's brightest $z \approx 7$ galaxies – which have ROBUST photometric redshifts – appear redder than $\beta = -2$, there is currently no convincing evidence that the faintest objects are significantly bluer than that.

It is of course possible to use a suite of simulations to determine the intrinsic distribution most likely present in the observed galaxy sample. Armed with additional data from the

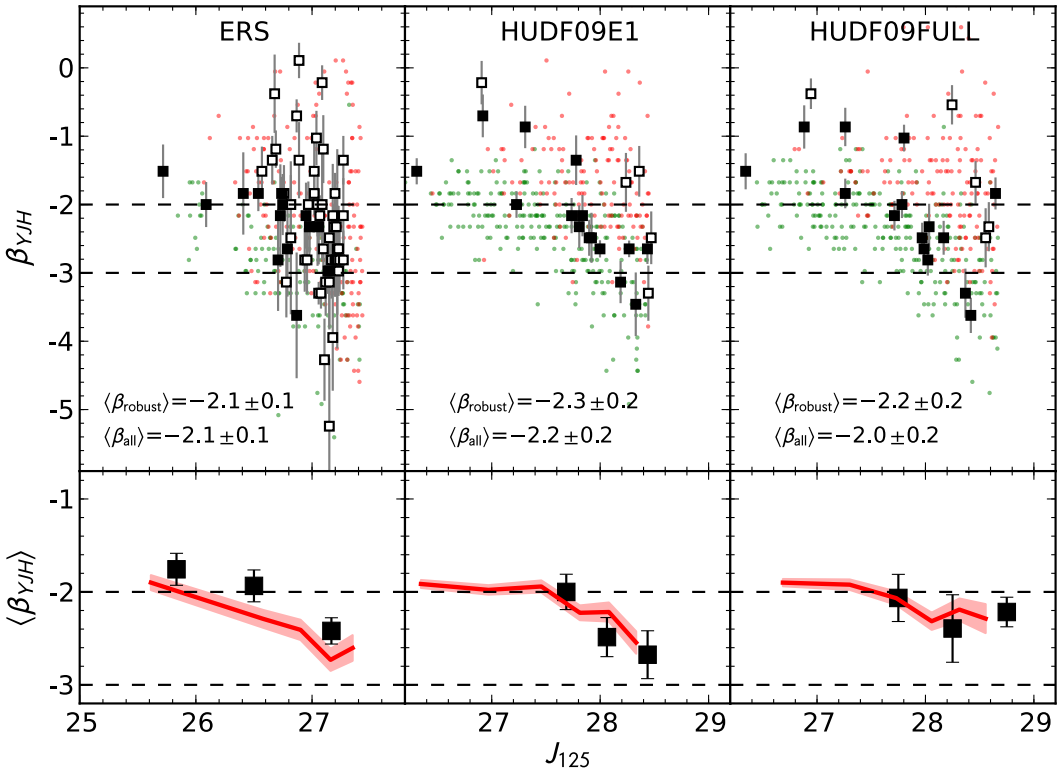

Figure 3.12 HUDF09E1 and ERS $6.5 \leq z < 7.5$ galaxies from the Dunlop et al. (2012) sample and our $\beta_{\rm in} = -2$ simulations. In the upper panels, the data are shown as solid (ROBUST photometric redshift) and open (UNCLEAR photometric redshift) squares. ROBUST and UNCLEAR simulated sources are shown by green and red dots, respectively. The right panel shows the sample selected from the HUDF09E1, but with the objects' photometry updated using the HUDF09FULL dataset. β was measured using a Lyman break truncated power-law fit to the available YJH photometry. The lower panels show running means, $\langle\beta\rangle \pm$ Std. Err., for the simulations (red regions) and the faint (well sampled) end of the data binned by magnitude (black squares). In the lower panels, ALL objects are included. A clear trend is seen for faint, ROBUST objects to have blue UV slopes; all faint, red objects are assigned UNCLEAR photometric redshifts. At the faint end, this trend is reproduced by our $\beta = -2$ simulation, although the scatter is such that the faintest objects are consistent with a $\beta = -3$ simulation (not shown for clarity, but see Fig. 3.11). Galaxies in the ERS are slightly redder than a $\beta = -2$ simulation would predict, as are the brightest galaxies in the HUDF. For each dataset, the inverse-variance weighted mean $\langle\beta\rangle \pm 1$ standard error is given both for ALL sources, and for the ROBUST sub-sample which is consistently slightly bluer. At the faint end ($J_{125} \geq 28$ in the HUDF09, 27 in the ERS), including UNCLEAR sources is more significant. For example their inclusion reddens the faint HUDF09FULL $\langle\beta\rangle$ from −2.7 to −2.3.

UDF12 programme, in Chapter 4 we investigate the constraints which can be placed on the intrinsic β distribution at $z \approx 7$.

3.7 Strategies for the UDF12

Compared to the HUDF09 data (which has been analysed in this chapter and by Rogers et al. 2013), the UDF12 programme (the data from which is analysed in the following chapters) was designed to provide significantly improved photometry of high-redshift galaxies in three complementary ways. First, the depth of the Y_{105} band was to be increased to a detection limit of 30 AB mag (5σ, 0.4-arcsec diameter aperture; 29.6 AB in a 0.6-arsec diameter aperture) providing robust photometric redshifts of 'Y-drop' galaxies at $z \gtrsim 8$. Second, imaging through the additional J_{140} filter was to be added reaching a depth equalling that of the current J_{125}-band data in the HUDF09FULL (see Table 3.1). Finally, the H_{160} imaging was to be increased in depth to match that achieved in J_{140} and J_{125}, allowing more secure colour measurements and minimizing bias in source selection. This was to allow $Y_{105}, J_{125}, J_{140}, H_{160}$ (hereafter $YJJH$) photometry to be used for fitting the UV SED of galaxies at $z \approx 7$, as we have simulated in this chapter. The UDF12 programme's design implies a more selection-independent measurement of β is possible by detecting objects in the J_{140}-band, with $J_{125} - H_{160}$ being used as the colour measurement. Prior to the arrival of the UDF12 data, we investigated strategies for fully exploiting it in the context of β measurements; those strategies are outlined in this section, implemented in Chapter 4 (and also reported by Dunlop et al. (2013)).

3.7.1 $J-H$ colours of J_{140}-selected galaxies

As discussed in Section 3.2, a single colour measurement in $J_{125} - H_{160}$ provides a simple estimate of β at $z \approx 7$. While we have seen that selecting galaxies (via SEXTRACTOR) in the J_{125}-band preferentially selects blue galaxies, yielding biased $\langle\beta\rangle$ values, this can be avoided in the UDF12 by selecting in the J_{140}-band. This method should alleviate some of the 'flux-boosting' induced blue bias that is found when J_{125} is used both to detect and determine the colour of $z \approx 7$ galaxies. To quantify the expected benefit of this approach, galaxies from our UDF12 $\beta_{\rm in} = -2$ simulation were independently selected in both the J_{125}- and J_{140}-bands. Photometric redshift selection of $z \approx 7$ galaxies was performed using all bands for both of these catalogues. In Fig. 3.13, the average UV slope $\langle\beta\rangle$ is shown as a function of selection band magnitude for each catalogue. Measurement of $\langle\beta\rangle$ for bright galaxies is not affected by the choice of selection band, but within 1 mag of the 5σ image depth a J_{140}-selected catalogue clearly provides a less blue-biased measure of $\langle\beta\rangle$ than a J_{125}-selected catalogue. An inclusive J_{140}-selected photometric redshift catalogue allows

an essentially unbiased measurement of $\langle\beta\rangle$, and J_{140}-selection somewhat reduces the bias in a ROBUST photometric redshift catalogue. Reassuringly, an unbiased measurement of $\langle\beta\rangle$ is possible without resorting to the artificial neglect of certain bands from the photometric redshift analysis as was suggested by Bouwens et al. (2012a).

We have argued that detecting objects in a band redward of J_{125} can be advantageous in some circumstances. What would have been the effect of using H_{160} for objects selection in the HUDF09 and ERS datasets? The answer is not a straight-forward reversal of the J_{125} selection's blue bias. Whilst very blue galaxies (either intrinsically or erroneously so) would be less likely to be selected in an H_{160} catalogue, and redder galaxies more likely, the selection function of the photometric redshift (or colour-colour) selection procedure ensures that redder galaxies are *always* biased against later in the selection process. Selecting in H_{160} alone thus retains much of the J_{125} selection's bias against redder galaxies whilst establishing a further bias against blue galaxies. Together, these effectively narrow the selection window for faint objects near the detection limit of the dataset.

3.7.2 Power-law β measurements

We have seen that a J_{140}-selected catalogue, with β measured via the independent $J_{125}-H_{160}$ colour, is less blue biased than a J_{125}-selected catalogue. This is also true when β is measured via a power-law fit to $YJJH$, but for more subtle reasons. The primary cause of bias in β is flux boosting of faint objects to just above the detection threshold. Galaxies boosted in J_{125} are bound to be measured blue: the colour is always blue relative to both J_{140} and H_{160}.[2] However galaxies boosted in J_{140} hold a blue $J_{140}-H_{160}$ colour but a *red* $J_{125}-J_{140}$ colour of similar SNR. Thus, power-law β measurements benefit from a J_{140}-selection to a similar degree as the β measurements obtained via the $J-H$ colour. The addition of J_{140} photometry in the UDF12 also makes possible a multi-band power-law fit to the UV continuum, neglecting the Y_{105}-band in which the Lyman break falls. However with the Y-band offering the greatest depth in the UDF12, it is not immediately obvious whether its exclusion from the β measurement will be beneficial or not. Using the J_{140}-selected catalogues described in 3.7.1, β was measured, separately, using truncated power-law fits to JJH and $YJJH$ photometry. From the results shown in Fig. 3.14, we can see that the inclusion of the Lyman-break affected Y-band photometry does not appreciably reduce the bias in the average UV slope at faint magnitudes. While the inclusion of the Y-band greatly benefited the measurement of β in the HUDF09, it can be excluded in the UDF12 with only the modest cost of an increase in the scatter of β

[2]The Y-band photometry carries lower weight, being partially attenuated by the Lyman break.

for the faintest galaxies (resulting in a β scatter very comparable to the J_{140}-selected β_{J-H} sample shown in Fig. 3.13). This is beneficial as a robust measurement of $\langle\beta\rangle$ can then be obtained, via JJH photometry, without relying on the Lyman break affected Y-band.

3.7.3 Lyman-α emitter contamination

In the UDF12 simulations, we have seen that the inclusion of Y-band photometry only mildly improves the measurement of β in LBGs with no Lyman$-\alpha$ emission. However, the Y-band at $z \approx 7$ probes the Lyman$-\alpha$ line and the comparison of JJH to $YJJH$ fits may be a useful check for the presence of Lyman$-\alpha$ emission. Furthermore, the earlier β_{YJH} measurements for HUDF09 galaxies could potentially be affected by Lyman$-\alpha$ emission; excluding the Y-band photometry for these fits would reduce the measurement to only a single $J-H$ colour.

We have performed simple simulations of the effect of Lyman$-\alpha$ emitters (LAEs) on recovered β values as follows. First, pure power-law spectra were created with $\beta_{\rm in} = \{-3,-2,-1\}$, truncated blue-ward of $(1+z)\times1216$ Å. By integrating under the rest-frame UV continuum in the range 1216 Å – 1216+EW Å, the Lyman$-\alpha$ line flux was calculated and added to the flux at 1216 Å. Fig. 3.15 shows the impact of Lyman$-\alpha$ emission of various equivalent-widths on the power-law derived β value from $Y_{105}, J_{125}, J_{140}, H_{160}$ photometry (as is present for the UDF12 – the effect is marginally stronger in the HUDF09 without J_{140} imaging). Based on observations out to $z \approx 6$, Stark, Ellis, & Ouchi (2011) predict, in their faint luminosity bin ($26.7 < J_{125} < 28.2$), a $z = 7$ Lyman$-\alpha$ EW distribution peaked in the $25 <$ EW < 55 Å bin. Galaxies with EW > 85 Å represent $\sim 5\%$ of the population. Thus we can expect a bias of $\Delta\beta \approx -0.5$, if the LAE fraction does not tail off at $z \approx 7$. (However, Bolton et al. (2012) have shown that only a small ($\approx$10%) neutral fraction in the IGM may be sufficient to significantly reduce the transmission of Lyman$-\alpha$, and therefore the typical EW of Lyman$-\alpha$ at $z \approx 7$.)

This bias was maximized by not floating the redshift here. In practice, the photometric redshift code will select a lower redshift thereby accounting for excess Y-band flux by a lower-wavelength Lyman break. At $z = 7$, 50 Å EW Lyman$-\alpha$ can be countered by misplacing the redshift by $\Delta z \approx -0.3$. Moreover, the inclusion of Lyman$-\alpha$ emission in photometric redshift fits is commonplace. In principle this allows z, β (continuum) and the EW of Lyman$-\alpha$ to be correctly determined.

In fact, for our sample of HUDF09 and ERS objects, including the Y-band in the measurement of β typically returns colours redder than when using only β_{J-H}. Thus any

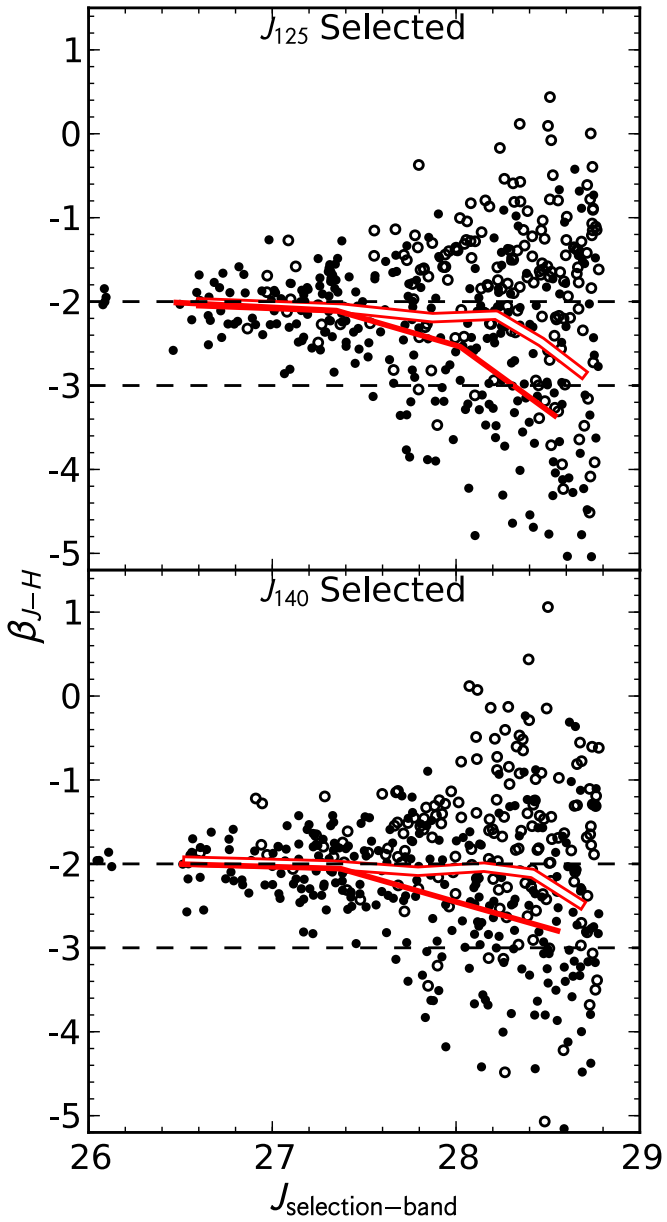

Figure 3.13 Comparison of the β bias in a simulated sample of $z \approx 7$ galaxies in the UDF12, selected in either the J_{125} (upper panel) or J_{140} (lower panel) imaging. UV slopes, measured via $J_{125} - H_{160}$ colours, are shown for galaxies in our UDF12 $\beta_{\text{in}} = -2$ simulation. Filled and hollow circles mark objects with ROBUST photometric redshifts and UNCLEAR objects respectively. Average UV slope values $\langle\beta\rangle$, in bins of selection band magnitude, are likewise shown by solid (ROBUST) and hollow (ALL=ROBUST+UNCLEAR) lines. A catalogue produced by selecting objects in the J_{140}-band (lower panel) shows a less blue-biased $\langle\beta\rangle$ for faint galaxies than does a J_{125}-band selected catalogue (upper panel). This is due to selection band flux boosting in the J_{125}-selected catalogue fostering a sub-sample of sources which is very blue in $J-H$ (see Sections 3.7.1 and 3.7.2 for discussion). The hollow line in the lower panel shows that a J_{140}-selected photometric redshift catalogue including all objects (ROBUST and UNCLEAR) allows an unbiased average UV slope to be measured to low SNR ($< 8\sigma$).

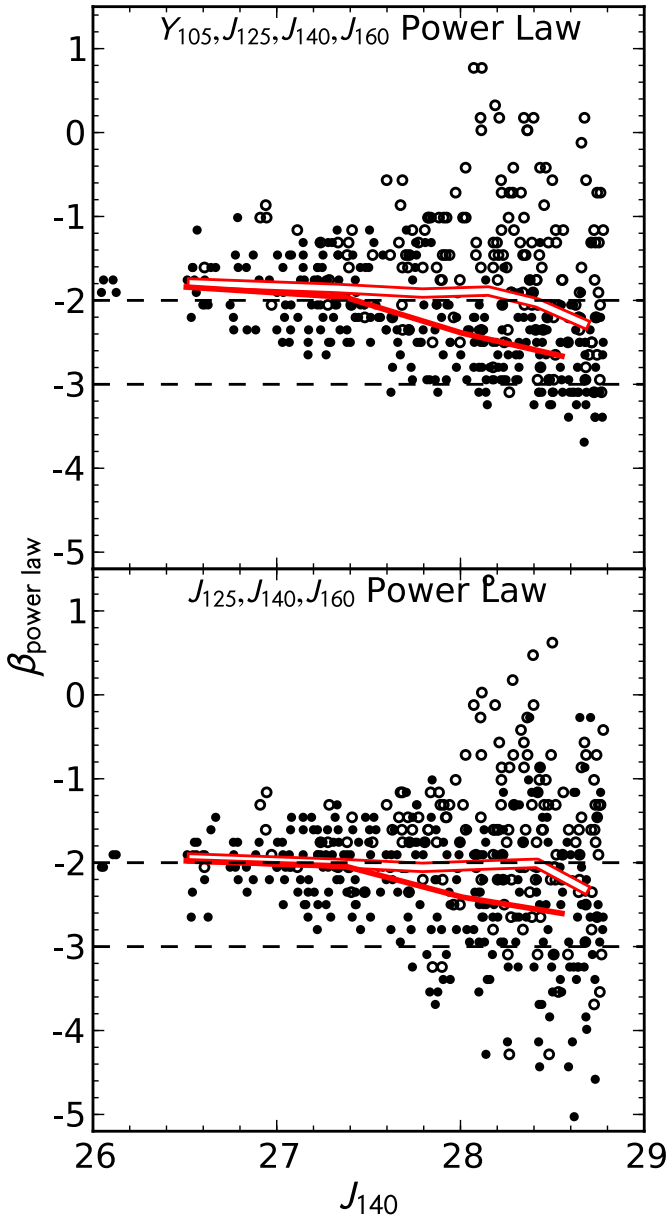

Figure 3.14 Comparison of the β bias in a simulated sample of $z \approx 7$ galaxies in the UDF12, with β measured by a Lyman break truncated power-law fit to $Y_{105}, J_{125}, J_{140}, H_{160}$ (upper panel) or only $J_{125}, J_{140}, H_{160}$ (lower panel). Filled and hollow circles mark objects with ROBUST photometric redshifts and UNCLEAR objects respectively. Average UV slope values $\langle\beta\rangle$, in bins of selection band magnitude, are likewise shown by solid (ROBUST) and hollow (ALL=ROBUST+UNCLEAR) lines. For some objects, the blueward scattering of the $J-H$ colour is tempered by the inclusion of the $Y-J$ colour, although this primarily reduces the width of the scatter and does little to alter $\langle\beta\rangle$. On an average basis, there is therefore little benefit to including the Lyman break affected Y-band photometry in the fit.

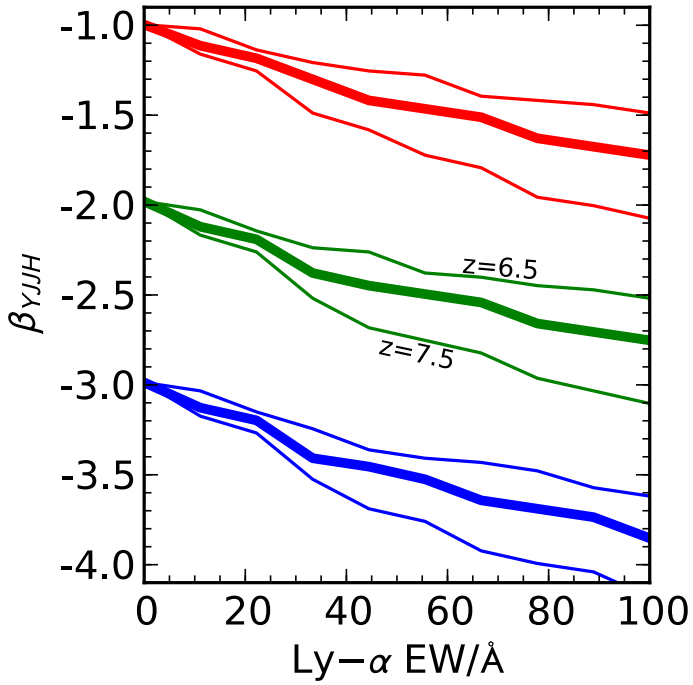

Figure 3.15 The effect of Lyman−α emission of various equivalent-widths on the recovery of the UV slope β. Perfect power-law spectra, with $\beta = \{-1,-2,-3\}$, were created and the flux at 1216 Å boosted to include an emission line of the specified equivalent-width. Thick red, green and blue lines denote the recovered βs at $z = 7$ for each intrinsic β respectively; thin lines (upper/lower) at $z = 6.5/7.5$. Here we assumed perfect redshift and photometric recovery in the UDF12's Y_{105}, J_{125}, J_{140} and H_{160} bands.

Lyman−α present in those galaxies is not boosting the Y-band flux to the extent that β_{YJH} is measured with a blue bias. We can therefore conclude that either no high EW Lyman−α is present, or that the low contribution of Lyman−α is readily countered by an underestimated photometric redshift. Finally, as we have seen, the addition of J_{140} in the UDF12 programme renders the Y-band photometry unnecessary in fitting β at $z \approx 7$, alleviating this problem in the following chapters.

3.8 Conclusions

In this chapter we have described object recovery simulations of $z \approx 7$ objects in the HUDF and ERS fields, and considered how the choice of selection function and β measurement method affect the measured average UV slope $\langle\beta\rangle$.

1. A robust measurement of the UV slope β in the ERS and HUDF09 datasets is obtained when fitting a Lyman break truncated power-law SED to YJH photometry.

In simulations, this method minimizes the scattering of β away from the intrinsic value. The method performs similarly to a method advocated by Finkelstein et al. (2012b), but avoids the parameter space issues associated with that method – whereby the scatter in β is artificially reduced for ultra-faint, blue, $z \approx 7$ objects – and outperforms the use of a single $J-H$ colour.

2. Our now-preferred method for measuring β relies on a precise photometric redshift measurement, thus can only be made using a full photometric redshift analysis. As such, and in contrast to claims in the literature, we have verified that the total bias on the measurement of β is similar for a full photometric redshift selection and for a colour–colour selection.

3. In doing so we have highlighted the sensitivity of recovered UV slope measurements to selection function choices. In particular, a comparison of the colour–colour selection functions of Bouwens et al. (2010) and Bouwens et al. (2012a) goes some way to explaining the difference in the average UV slope for faint $z \approx 7$ galaxies reported in those studies. Furthermore, we have shown that excess bias in a photometric redshift selection function is only seen when optional criteria are added to robustly reject potential low-redshift interlopers.

4. Using our preferred method, new UV slope measurements for a sample of $z \approx 7$ galaxy candidates (Dunlop et al. 2012) have been made. Over this short luminosity baseline, the apparent colour–magnitude relation – whereby the faintest objects appear bluest – is well reproduced by a simulation in which the intrinsic UV colours of objects are flat-spectrum ($\beta = -2$). Thus we find even faint $z \approx 7$ objects are able to have their colours reproduced by stellar population models of normal star-forming galaxies – requiring neither extremely young ages nor exotically low metallicities.

5. We have investigated strategies for minimizing the bias in the measurement of β from the UDF12 dataset, finding that using its new J_{140}-band imaging for detection, in combination with our preferred β measurement method, can yield results with significantly smaller biases than previous estimates.

In Chapter 4 the techniques and strategies developed in this chapter are applied to the UDF12 data at $z \approx 7$. Then, in Chapter 5, these techniques are extended to aid the measurement of the intrinsic colour distribution of galaxies at $z \approx 5$, from a long-luminosity baseline sample sourced from both ground- and space-based datasets. Finally, in Chapter 7, a comparison of the various groups' latest β measurements for high-redshift LBGs is provided.

4 The UV continua and inferred stellar populations of galaxies at $z \approx 7-9$

Some of the work presented in this chapter has been previously published in a paper on which I am second author (Dunlop, Rogers et al. 2013). Work for which I was not responsible, but which is none the less included for completeness, is clearly denoted as such; this is primarily in reference to the sample selection described in Section 4.2. I was directly responsible for the UV continuum slope measurements (Sections 4.3 and 4.4), source-injection simulations and comparisons (Section 4.4.1), redshift and luminosity trends (Section 4.5) and intrinsic scatter constraints (Section 4.6). The model comparisons shown in 4.8 and 4.9 are similar to versions presented by Dunlop et al. (2013), however I have recreated and extended those in this chapter.

In the previous chapter, we concluded that measurements of the UV continuum slope β of low-luminosity $z \approx 7$ galaxies are bound to be biased toward bluer colours unless particularly careful attention is paid to the selection and measurement processes. However, we found that data from the UDF12 programme would ease this bias, particularly by its introduction of imagery in the J_{140} band – a filter not previously deployed on the UDF. In this chapter, we describe work done immediately following the UDF12 programme's delivery; the method optimized in the previous chapter is employed on these new data. In addition, we extend these measurements to $z \approx 8$ – providing the first meaningful constraints on $\langle\beta\rangle$ during that epoch. We find $\langle\beta\rangle \approx -2.1 \pm 0.2$ and $\langle\beta\rangle \approx -1.9 \pm 0.3$ at $z \approx 7$ and $z \approx 8$, respectively, indicating no evolution in the rest-frame UV colours from $z \approx 6$. In addition, we investigate whether the $z \approx 7$ data show any evidence for intrinsic scatter around the average, concluding not. These results, when compared to stellar population synthesis models, are consistent with continuously star-forming galaxies having either zero dust reddening but solar metallicity, or moderately sub-solar metallicity $\approx 1/5$ $Z_{\odot}$) obscured by modest dust reddening $A_v \lesssim 0.2$. We conclude by comparing these measurements to the predictions of galaxy-formation simulations.

4.1 Introduction

The 128-orbit UDF12 programme (Ellis et al. 2013, Koekemoer et al. 2013), completed on 16 September 2012, constitutes a significant advance to the already well-studied Hubble Ultra Deep Field (Beckwith et al. 2006). When combined with the *HST* WFC3/IR data from the HUDF09 programme (Bouwens et al. 2011), the co-added images are the deepest NIR images ever created. The improved Y_{105}-band depth (30 AB, 5σ) was designed to give, and has delivered, more robust photometric redshifts for LBGs at $z > 6.5$ (McLure et al. 2013), while the additional H_{160} depth (now 29.5 AB) provides a more reliable anchor on the rest-frame UV of galaxies up to $z \approx 11$ (Ellis et al. 2013). The addition of J_{140} coverage (equalling H_{160} in depth) was primarily directed at the detection of those highest redshift objects, where the Lyman break enters J_{125} rendering it a drop-out at $z \approx 10$. As detailed in Chapter 3, all three of the UDF12's investments also improve the measurement of β in the crucial $z \gtrsim 6.5$ era.

In Section 1.11, we introduced the importance of the average UV continuum slope $\langle\beta\rangle$, as well as its intrinsic variation $\Delta\beta$, in constraining the build-up of stars, metal, and dust in early star-forming galaxies. In principle, β is a proxy for average stellar age, dust reddening (e.g Meurer et al. 1999), metallicity, and nebular continuum emission (e.g. Schaerer & de Barros 2009). As we shall see in this chapter, degeneracies make the constraints on any of these individual parameters weak. Still, the discovery of sufficiently blue UV continua ($\beta \lesssim -2.5$) would imply some form of 'exotic' stellar population previously unseen in lower-redshift star-forming galaxies. Moreover, the value of β is an indicator of the ionizing photon output of galaxies. At $z \gtrsim 6$, during the EOR, this is a key input into the reionization budget calculation (e.g. Robertson et al. 2013).

For these reasons, the measurement of β at $z \approx 7$ has been of substantial interest in the literature. This debate has been rather extended, as summarised in Section 1.11. However the UDF12 data provide the best opportunity to robustly measure β at $z \gtrsim 6.5$ until the launch of the *James Webb Space Telescope*.

The remainder of this chapter is organised as follows. We begin by detailing the selection of a sample of galaxies at $z > 6.5$ in Section 4.2. In Section 4.3 we compute simple single-colour measurements of β for samples at $z \approx 7$ and $z \approx 8$. Our preferred power-law approach is then put to use in Section 4.4, wherein we also describe new source-injection simulations (Section 4.4.1) used initially to verify that the measurements are unbiased. Trends in β with redshift and luminosity are detailed in Section 4.5. In Section 4.6, we investigate whether there is any evidence for intrinsic scatter in the β

distribution of our $z \approx 7$ galaxy sample. Our results are compared to literature values in Section 4.7. Comparisons first to stellar population synthesis models, and then to galaxy-formation models, are provided in Section 4.8 and Section 4.9, respectively. We present our conclusions in Section 4.11.

4.2 Sample selection

For this work, a new galaxy sample was selected from the full UDF12+HUDF09 dataset by McLure et al. (2013) and Dunlop et al. (2013). The sample selection procedure is detailed fully in those papers, but for completeness it is also described here. In order to maximize the size of the initial sample, galaxy candidates were searched for in a number of NIR datasets. SEXTRACTOR was used to detect objects in one or more of the NIR bands alone or contiguous stacked images. Objects were selected if they were detected at $> 5\sigma$ significance in at least one of these 10 detection images, which were WFC3/IR:

- Y_{105}, J_{125}, J_{140}, H_{160}
- $Y_{105} + J_{125}$, $J_{125} + J_{140}$, $J_{140} + H_{160}$
- $Y_{105} + J_{125} + J_{140}$, $J_{125} + J_{140} + H_{160}$
- $Y_{105} + J_{125} + J_{140} + H_{160}$.

(For images of near-equal depth, these stacks should produce similar results to a 'χ^2 detection image' as advocated by Szalay et al. 1999.) The combined catalogue was then pruned of all sources having any significant ($> 2\sigma$) flux in the B_{435}, V_{606}, or i_{775} band images. This cut serves to keep only sources which show a strong spectral break where the Lyman break of a $z > 6.4$ galaxy should be seen.

As in Chapter 3, SEXTRACTOR was again used to construct multi-wavelength photometry for each candidate. Since many sources were detected in multiple detection images, with slight offsets between the derived source centre in each, the image in which a source held the highest signal-to-noise detection was used to define the source's position for aperture photometry. In contrast to our earlier work, and in pursuit of high signal-to-noise photometry for the expected compact $z > 6$ sources, PSF-'matched' circular apertures were used for photometry. The aperture diameter for each waveband was chosen to enclose 70% of the flux of a point source; the resultant aperture diameters are listed in Table 4.1. As detailed by McLure et al. (2013), *Spitzer* IRAC [3.6] and [4.5] photometry (Labbé et al. 2013) was also obtained via a deconfusion algorithm (McLure et al. 2011), which used the

Table 4.1 *The adopted photometric aperture sizes, and resultant limiting magnitudes, of the datasets used in this chapter. The first and second columns list the* HST *filter names of each image and the adopted aperture diameter, chosen to enclose a similar fraction of a point source's total flux in all bands. The third column lists the typical raw (i.e. aperture-enclosed) noise, quoted as a* 5σ *limiting magnitude. The final column lists 'corrected' magnitudes, after taking into account the flux correction which is applied to correct from aperture-enclosed to 'total' flux assuming a point-source profile.*

Waveband	Aperture diameter /arcsec	Raw 5σ depth /AB	PSF-corrected 5σ depth /AB
B_{435}	0.30	29.9	29.7
V_{606}	0.30	30.4	30.2
i_{775}	0.30	30.1	29.9
z_{850}	0.30	29.5	29.1
Y_{105}	0.40	30.1	29.7
J_{125}	0.44	29.6	29.2
J_{140}	0.47	29.6	29.2
H_{160}	0.50	29.6	29.2

HUDF09+UDF12 H_{160}-band image as a source template. Because of their low luminosities and the shallow IRAC imaging, most of the galaxies in the final sample had, formally, no detection in the [3.6] and [4.5] bands. These IRAC photometric measurements or limits were used in the photometric-redshift fitting, but not in the β determinations since the rest-frame wavelength they probe is beyond the UV.

Following the general principles of photometric-redshift selection (described in Section 2.3), galaxy candidate samples were created for $z \approx 7$ ($6.4 < z_{\rm phot} < 7.5$), $z \approx 8$ ($7.5 < z_{\rm phot} < 8.5$), and $z \approx 9$ ($8.5 < z_{\rm phot} < 9.5$). Because we are unable to employ our robust power-law method for measuring β at $z \approx 9$, that sample is not discussed further here; Dunlop et al. (2013) include a preliminary analysis of it, however. For the $z \approx 7$ and 8 samples studied here, acceptable photometric redshift fits were deemed to be those for which $\chi^2 < 15$. Following Section 2.3.4, this threshold corresponds to the 2σ acceptable fit of a model with seven degrees of freedom and ten data points (including the IRAC [3.6] and [4.5] bands). In addition, the fits were classified as either ROBUST or UNCLEAR depending on how well any secondary, low-redshift solution could be excluded. Specifically, sources with primary $z > 6.4$ solutions separated from secondary solutions by $\Delta\chi^2 < 4$ were denoted UNCLEAR. The fits and imaging were also visually inspected to remove sources with potentially unreliable photometry.

From that sample, a refined cut was then implemented. In Chapter 3, we showed that a J_{140}-selected sample should provide less biased estimates of $\langle\beta\rangle$ than a J_{125}-selected sample. While the sample discussed here was selected from multiple detection bands (to

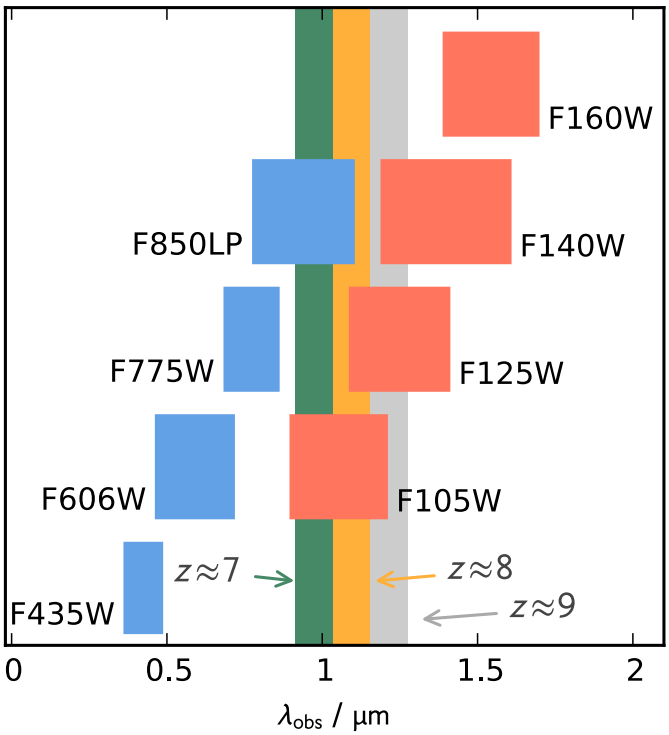

Figure 4.1 The photometric filter bandpasses for the images used in this chapter are shown by the coloured regions. Blue and red regions show the *HST*'s ACS and WFC3/IR filters. The vertical, green, orange, and grey regions denote the wavelength ranges in which the 1216 Å Lyman break is observed at $6.5 < z < 7.5$, $7.5 < z < 8.5$, and $8.5 < z < 9.5$, respectively.

be more complete for the luminosity function analysis of McLure et al. 2013), here the J_{140}-selection can be achieved by simply adopting a signal-to-noise threshold in that band. After applying a $J_{140} \geq 5\sigma$ cut, the sample of 116 $z \approx 7$ and 24 $z \approx 8$ galaxies was decreased to 45 and 12, respectively. Encouragingly, this cut reduced the fraction of the sample which have UNCLEAR photometric redshifts from $\approx 25\%$ to $\approx 10\%$ (see Dunlop et al. (2013) for details). To achieve higher precision measurements of $\langle\beta\rangle$, this new UDF12 sample was combined with a smaller sample of $z > 6.4$ galaxies from the UDF's parallel fields. Because the parallel fields lack the key J_{140}-band coverage of the UDF12, an alternative strategy for bias mitigation was required. (As we have seen in Chapter 3, a $J_{125} > 5\sigma$ cut would inevitably be biased at $z \approx 7$.) Dunlop et al. (2012), in the first critical analysis of β measurements at $z \approx 7$, showed through simulations that raising the signal-to-noise threshold to $J_{125} > 8\sigma$ was sufficient to make the bias on $\langle\beta\rangle$ negligible. Therefore, the parallel-field samples from McLure et al. (2013) were treated with a $J_{125} > 8\sigma$ cut, yielding a further 20 and one galaxies at $z \approx 7$ and $z \approx 8$, respectively.

For the combined samples, absolute magnitudes were calculated using our standard procedure of placing a 100 Å-wide top-hat filter at rest-frame 1500 Å on the best-fitting

Table 4.2 *Properties of the $z \approx 7$ (top) and $z \approx 8$ (bottom) samples studied in this chapter. The first column lists the defined centres of bins of absolute magnitude, while the second column lists the number of galaxies in each bin. Columns 3–5 lists average UV slopes in each bin, obtained respectively via the mean of single colour measurements, the mean of power-law fitting measurements, and by an inverse-variance weighted mean of power-law fitting measurements.*

M_{1500}	Sample size	$\langle\beta\rangle$ $(J-H)$ mean	$\langle\beta\rangle$ (power-law) mean	$\langle\beta\rangle$ (power-law) weighted mean
		$z \approx 7$		
-19.5	17	-1.72 ± 0.12	-1.81 ± 0.12	-1.94 ± 0.12
-18.5	22	-2.23 ± 0.16	-2.08 ± 0.15	-2.08 ± 0.15
-17.5	26	-2.02 ± 0.29	-2.08 ± 0.26	-2.03 ± 0.26
		$z \approx 8$		
-19.5	3	-1.98 ± 0.27	-2.03 ± 0.17	-1.93 ± 0.17
-18.5	10	-1.96 ± 0.27	-1.88 ± 0.25	-1.84 ± 0.25

SED (see Section 2.4). Based on these absolute UV magnitudes, the sample was split into luminosity bins: three at $z \approx 7$ and two at $z \approx 8$. (The bins were chosen to ensure that each bin held more than five galaxies.) The binned sample (including both ROBUST and UNCLEAR sources) is summarised in Table 4.2.

4.3 Simple, single-colour measurements of β

As we have seen, the simplest estimate of β is obtained by relating a single observed colour to one in the rest-frame UV. The $J_{125}-H_{160}$ colour used (via equation 3.6) at $z \approx 7$ in Chapter 3 is also valid for much of the $z \approx 8$ sample; as shown in Fig. 4.1, the 1216 Å Lyman break does not enter J_{125} until $z > 8$ and up to $z = 8.5$ the attenuation is only minor (but may explain why $\langle\beta\rangle$ at $z \approx 8$ is slightly redder than at $z \approx 7$ – see Table 4.2). However, at $z \approx 9$ (also shown in Fig. 4.1), the J_{125}-band photometry becomes increasingly affected by the Lyman break and so the rest-frame UV continuum is probed only by J_{140} and H_{160}. According to equation 3.11, the relation between $J_{140}-H_{160}$ is

$$\beta = 9.32(J_{140}-H_{160})-2, \tag{4.1}$$

with the coefficient 9.32 being a worryingly large multiplier considering the typical photometric uncertainties.

While we have seen that these simple estimates for β are out-performed by more robust power-law measurements, the single-colour estimates are included here for completeness and to aid comparison with earlier literature studies, where this has been the norm. Since

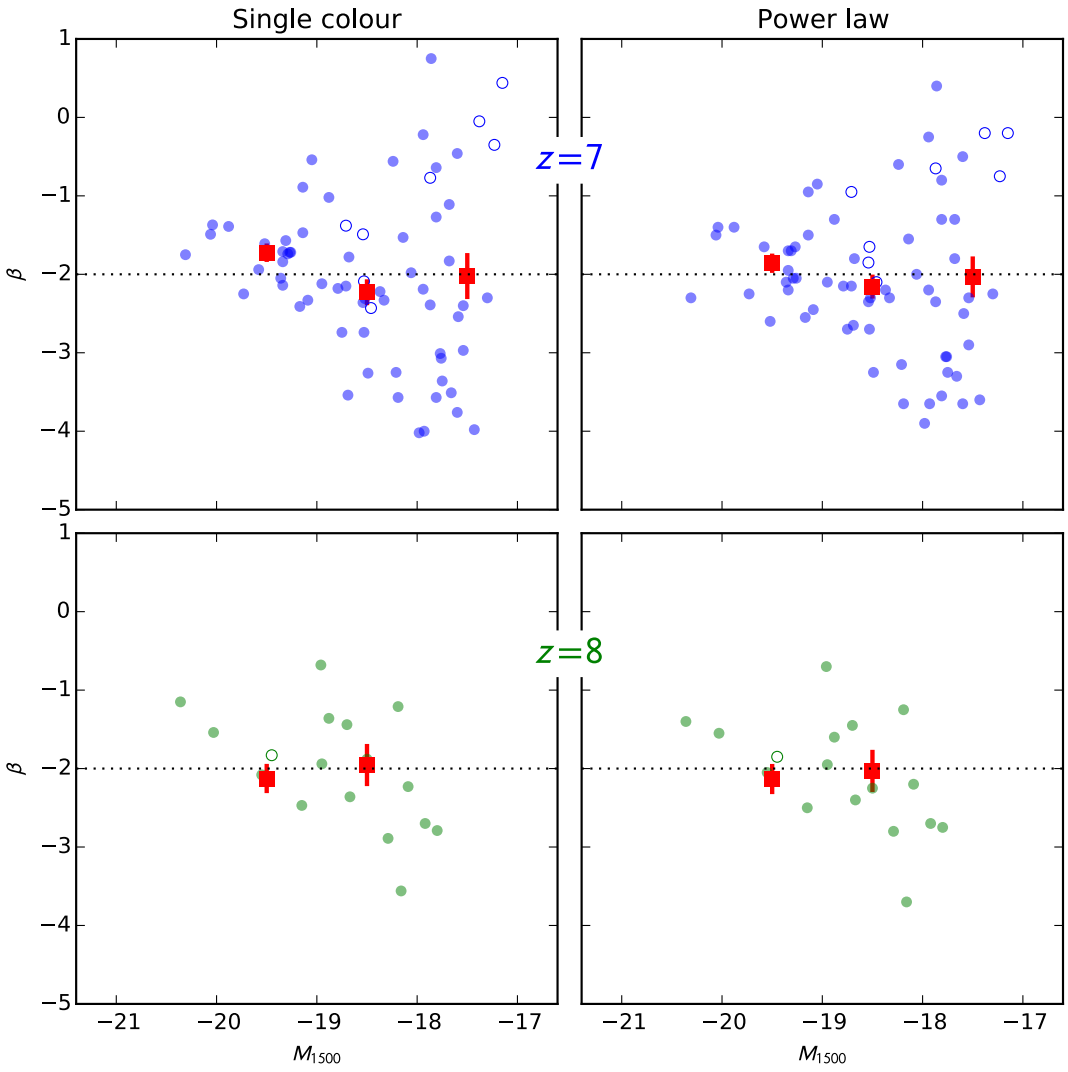

Figure 4.2 Measurements of β for individual UDF12 galaxies at $z \approx 7$ and $z \approx 8$ are shown in upper and lower panels, respectively. The left and right panels show results where β was measured from a single $J_{125}-H_{160}$ colour, and from a power-law fit to $J_{125}, J_{140}, H_{160}$, respectively. Hollow circles denote those candidates for which the photometric redshift was not considered as robust as other galaxies (filled-circle marks). The red squares with error bars denote binned means and standard errors; the bins are $\Delta M = 1$.

the $z \approx 9$ results are markedly less secure than those at $z < 9$, they are treated separately in Section 3.2 of Dunlop et al. (2013). Otherwise, the $(J_{125} - H_{160})$-derived measurements of β are shown in the left-hand panels of Fig. 4.2. The figure also shows luminosity-binned mean colour values $\langle\beta\rangle$, which are tabulated in Table 4.2.

4.4 Power-law measurements of β

We now proceed to determine β using the power-law fitting method as explored and optimized in Chapter 3. Following the method described in Chapter 3, UV continuum slopes were obtained by performing a power-law fit to the $J_{125}, J_{140}, H_{160}$ flux densities (accounting for partial attenuation of the J-band by the Lyman break at $z \gtrsim 8$) or $Y_{105}, J_{125}, H_{160}$ in the parallel fields (there accounting for partial attenuation of the Y-band where appropriate). The grid of power-law models fitted to the WFC3/IR photometry extends over a deliberately very large range, $-8 < \beta < 5$, to ensure that the *observed* β distribution is not artifically truncated. However, in practice (primarily due to the J_{140} significance cut) the sample studied here has photometry of sufficient quality that no object yields a measured $\beta < -4$. This measurement method differs from that of Chapter 3 only in that here, in the interests of speed and simplicity, LEPHARE was used as the SED fitting tool rather than the bespoke software previously used.

The power-law measurements of β, and their luminosity-binned averages, are shown in the right-hand panels of Fig. 4.2. Reassuringly, given the relatively conservative selection of the sample, there is little to distinguish the power-law results from the single-colour results. Fig. 4.3 shows an explicit comparison of the β measurements obtained from each method, with excellent agreement between the two due to the careful selection process.

4.4.1 Source injection, retrieval and measurement simulations

We have also performed a set of end-to-end data-analysis simulations, starting with the injection of sources into the real UDF12 images, in order to quantify any remaining residual bias in our derived average values of $\langle\beta\rangle$. We first describe these simulations, before proceeding to summarise the results.

Our simulations began by defining a distribution of UV slopes. In this chapter we adopt a delta function at $\beta = -2$ as our reference model, but also consider 'top hat' distributions of various widths, as discussed below in Section 4.6.

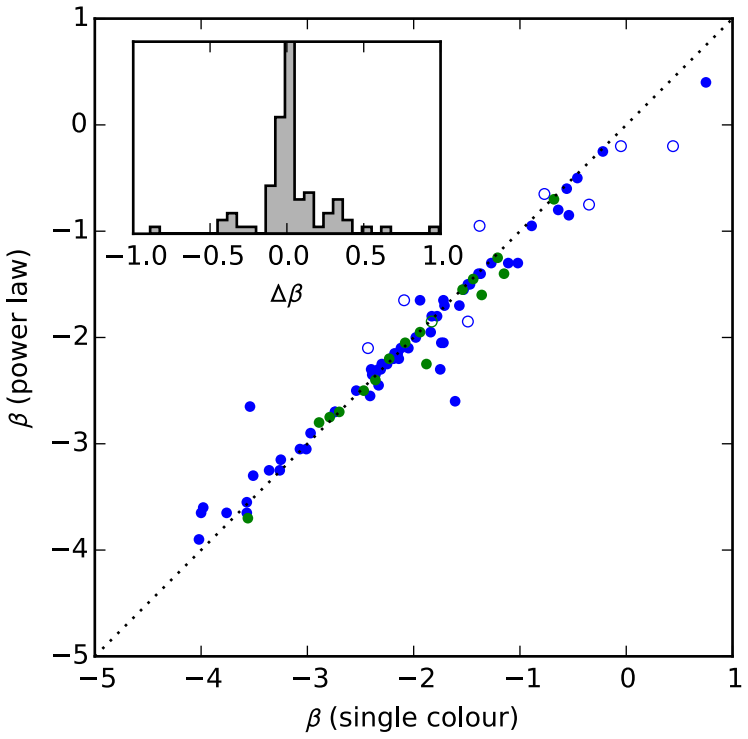

Figure 4.3 Measurements of β for the $z \approx 7$ (blue circles) and $z \approx 8$ (green circles) galaxy samples obtained by two methods: via a single colour or via a power-law fit. Hollow circles denote those candidates for which the photometric redshift was not considered as robust as other galaxies (filled-circle marks). In contrast to the HUDF09 data, there is little difference between a single colour and a power-law fit in these UDF12 samples. The inset shows the distribution of offsets, $\Delta\beta = \beta(\text{single colour}) - \beta(\text{power law})$.

Next, we created an input catalogue of galaxies with β values drawn from the defined distribution, redshifts in the range $6 < z < 9$, and absolute magnitudes spanning $-22 < M_{UV} < -16$ (with the relative number density of objects at different magnitudes governed by the latest $z = 7$ luminosity function of McLure et al. 2013). A model SED was then created for each galaxy, incorporating the intrinsic colour, the IGM attenuation of flux blueward of the Lyman break, the redshifting of the spectrum into the observed frame, and then cosmological dimming. Empirical PSFs were then created with broad-band flux-densities based on the model SEDs (in practice, the PSFs were set to zero in the $B_{435}, V_{606}, i_{775}$ bands where the flux is entirely attenuated). The PSFs were then inserted into the real multi-wavelength UDF12 images, avoiding existing bright sources and regions of high RMS noise where real candidates would have been discarded.

Objects were then reclaimed using SEXTRACTOR; we accepted only objects lying within 2-pixels of an input PSF centre, and then performed aperture photometry on these objects in exactly the same way as for the real galaxies. Photometric redshifts were then obtained using LEPHARE (Arnouts et al. 1999, Ilbert et al. 2006) with the same BC03 models used in

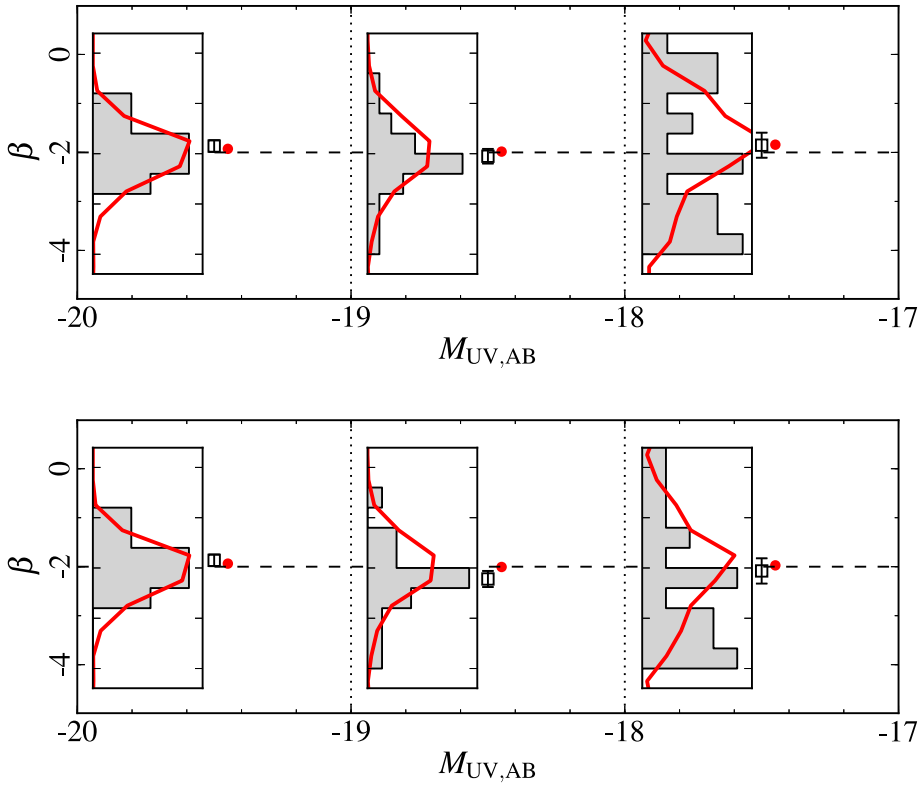

Figure 4.4 The distribution of individual power-law β measurements at $z \approx 7$, along with average values, $\langle\beta\rangle$ (and standard errors), plotted against UV absolute magnitude. Results are shown for all sources (upper row), and for ROBUST sources only (lower row). The simulations shown in red are based on 2000 galaxies inserted with $\beta = -2$. The data from UDF12 are shown in grey/black. The data in the brightest two bins have been supplemented with a few sources from the two HUDF09 parallel fields.

the real data analysis. We adopted an identical selection function to that used for the real data, and measured absolute magnitudes with the same synthetic filter on the best-fitting BC03 model. Again, UV continuum slopes were obtained by performing a power-law fit to the relevant WFC3/IR photometry.

4.4.2 Results at $z \approx 7$

In Fig. 4.4, we show an alternative presentation of the power-law analysis results for the galaxies at $z \approx 7$, split into the same three luminosity bins as in Fig. 4.2, and this time, for completeness, showing results for both the ROBUST+UNCLEAR (upper row) and ROBUST-source only (lower row) samples.

The grey histograms in Fig. 4.4 show the distribution of the power-law derived β values in each bin, and the small squares with error bars indicate the average $\langle\beta\rangle$ values (and

associated standard errors). The results derived from the real data are compared here with the results from our reference simulation in which every fake galaxy is assigned $\beta = -2$ before being inserted into the UDF12 imaging; the red histograms indicate the distribution of power-law β values retrieved from the simulations, with the red points indicating the corresponding average and standard error in each luminosity bin. The red points thus offer a measure of the bias in our measurements of average $\langle\beta\rangle$ which can be seen to be negligible for both the ROBUST+UNCLEAR and ROBUST samples. As expected, it can be seen that confining the sample to ROBUST sources results in the removal of a few of the redder galaxies in the faintest magnitude bin, but because the number of UNCLEAR sources is so small, the results are essentially unchanged (especially when measured relative to simulation expectation, which also moves slightly blueward in the ROBUST-source simulations).

The final values given for the power-law determination of $\langle\beta\rangle$ at $z \approx 7$ in Table 4.2 are taken from the ROBUST+UNCLEAR-sample analysis shown in the upper row of Fig. 4.4, and are calculated relative to the simulated values (to correct for any small residual bias). As long as the appropriate correction is applied, the results are essentially identical if they are derived from the ROBUST-source only analysis presented in the lower row. Within the errors, all three luminosity bins at $z \approx 7$ are clearly consistent with $\beta = -2$, with a best-estimate of $\langle\beta\rangle = -2.1$ in the fainter two bins. Reassuringly, the power-law estimates are fully consistent with the $J_{125} - H_{160}$ colour-based measurements presented in Section 4.3 (see Table 4.2 for details and errors, and Table A1 of Dunlop et al. (2013) for individual object measurements).

4.4.3 Results at $z \approx 8$

In Fig. 4.5 we show our power-law β determinations at $z \approx 8$. The values derived from the real data are again shown by the grey histograms, with the average and standard error indicated by the black squares with error bars. Similarly, the corresponding results for the $\beta = -2$ simulation are indicated in red. At $z \approx 8$, the J_{140} significance threshold leaves only two galaxies fainter than $M_{UV} = -18$ so, as in Fig. 4.2, we limit our analysis to the two brighter bins. The samples are smaller, and so the corresponding random errors are larger; but again it can be seen that the values of $\langle\beta\rangle$ derived from the data are consistent with $\beta = -2$ in both luminosity bins, and the blue bias implied from the simulations is relatively modest (although it is slightly larger if only ROBUST objects are retained, as expected).

As at $z \approx 7$, the final results for the power-law determination of $\langle\beta\rangle$ at $z \approx 8$ given in Table 4.2 are derived from the ROBUST+UNCLEAR-sample analysis shown in the upper row of Fig.

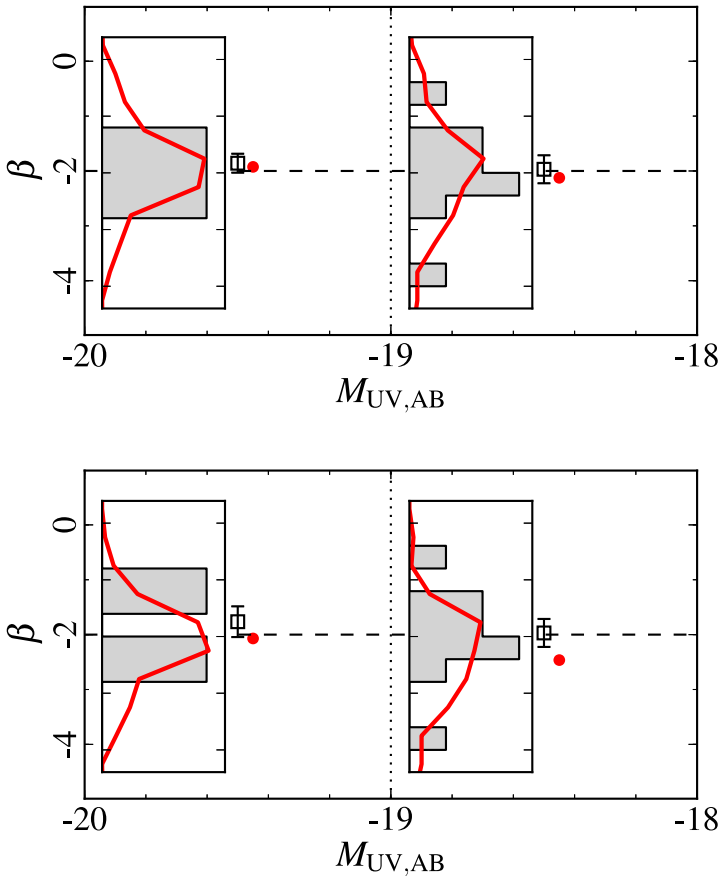

Figure 4.5 The distribution of individual power-law β measurements at $z \approx 8$, along with average values, $\langle\beta\rangle$ (and standard errors), plotted against UV absolute magnitude. Results are shown for all sources (upper row), and for ROBUST sources only (lower row). The faintest bin shown for the $z \approx 7$ sources in Fig. 4.4 only contains two sources in our J_{140} thresholded $z \approx 8$ sample, and so we do not attempt to show results at $M_{UV} \approx -17.5$ here. The simulations shown in red are based on 2000 galaxies inserted with $\beta = -2$. The data from UDF12 are shown in grey/black. The data in the brighter bin have been supplemented with a few sources from the two HUDF09 parallel fields.

4.5, calculated relative to the simulated values. Again, within the errors, both luminosity bins at $z \approx 8$ are clearly consistent with $\beta = -2$, and the power-law estimates are fully consistent with the $J_{125} - H_{160}$ colour-based measurements presented in Section 4.3 (see Table 4.2, and Table A1 of Dunlop et al. (2013) for individual object measurements).

4.5 Trends with redshift and luminosity

In this chapter, we have presented measurements of $\langle\beta\rangle$ at $z \approx 7$ and 8. As this is only a narrow range of redshifts, it is perhaps unsurprising that there is little evidence for any β vs. z relation, particularly given that the conservative approach adopted here does not allow

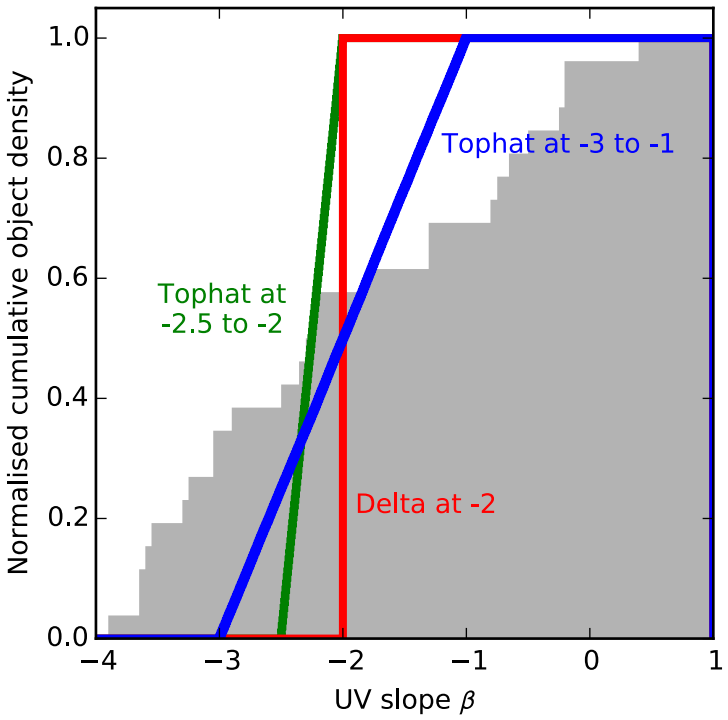

Figure 4.6 A cumulative histogram of galaxy colours in the faint ($-18 < M_{1500} < -17$) bin at $z \approx 7$ is shown by the grey region. The coloured regions denote the three *input* distributions for the comparative simulations studies in this chapter, as indicated by the labels. While all the input distributions are much narrower than the observed distribution, the distributions will be widened by photometric scatter.

the faintest bin used at $z \approx 7$ to be used at $z \approx 8$. However, by comparing to the $z \approx 5$ and 6 data of Dunlop et al. (2012), we can make a stronger statement that there seems to be only mild, if indeed any, evolution of $\langle\beta\rangle$ from $z \approx 8$ to $z \approx 5$: at $M_{1500} = -19.5$, $\langle\beta\rangle = -1.98 \pm 0.27$ at $z \approx 8$ and $\langle\beta\rangle = -1.99 \pm 0.11$ at $z \approx 5$ (Dunlop et al. 2012).

Similarly, these data do not show any evidence for a strong colour–magnitude trend. Again the narrow scope of this study means no strong conclusions can be drawn on the overall trend but, crucially, these measurements do rule out the suggestion that the average $z \approx 7$ colour–magnitude relation reaches as blue as $\langle\beta\rangle < 2.5$ by $M_{1500} = -17$. In Chapter 5, a sample selected over a much wider luminosity baseline (at slightly lower redshift $z \approx 5$) is presented to allow the colour–magnitude relation to be constrained.

4.6 Evidence for intrinsic scatter

In the majority of luminosity bins shown in Figs. 4.4 and 4.5, the data histograms and simulated histograms appear to show similar scatter. Those simulations assume that the

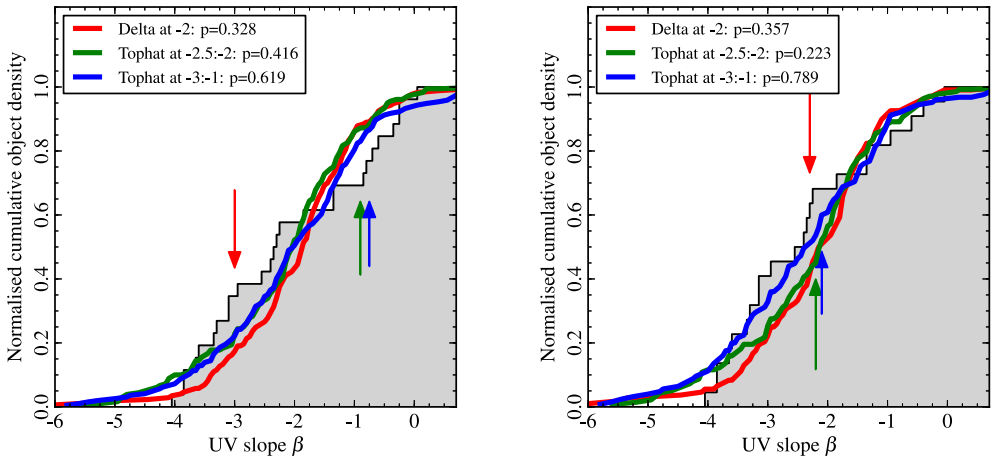

(a) All galaxies.

(b) ROBUST galaxies only.

Figure 4.7 A comparison of the distribution of β values derived for the real galaxies in the faintest luminosity bin probed here at $z \approx 7$ ($-18 < M_{1500} < -17$), with those predicted by alternative models based on different assumed intrinsic distributions of β. The left panel shows all sources, while the right panel contains ROBUST sources only. The grey regions show the cumulative distributions of β as derived from the data, while the coloured lines show the mock cumulative distributions as produced by the output from each alternative simulation. The significance (p) values for each model (under the null hypothesis that the real and simulated distributions are drawn from the same underlying distribution), are given in the top-left corner of each panel. Arrows show where the maximum deviation between the data and each simulation occurs, with the length of the arrow equal to the deviation.

underlying population of galaxies are self-similar, all having a pre-noise colour of $\beta = -2$. Thus, the agreement in scatter implies that the width of the observed colour distribution can be attributed solely to the photometric-noise scatter which equally affects both the data and simulations; no *intrinsic* colour distribution is *required*.

However, the faintest ($M_{1500} = -17.5$) luminosity-bin at $z \approx 7$ (see Fig. 4.4) appears to show excess scatter in the data histogram, as compared to the representative simulation. As this is true whether or not sources with UNCLEAR photometric redshifts are included, this is unlikely to be a contamination effect. This finding warrants further investigation, since it mirrors what would be expected if that bin includes a substantial population of very low metallicity, dust-free galaxies.

To study this we expanded our simulations (beyond a single value of $\beta = -2$) to explore a variety of intrinsic β distributions. In particular, we considered alternative top-hat distributions for the input values of β in order to assess whether a wider intrinsic distribution can provide a significantly improved fit to the data in this faintest bin. To determine the statistical significance of our results, we used a K-S test, which measures the dissimilarity of two samples by the maximum difference between their normalised

cumulative histograms. Of the several alternative input scenarios tested, the three most instructive are shown in Fig. 4.6 as cumulative histograms (for consistency with the definition of the K-S test).

The resultant simulation outputs for these three alternative intrinsic distributions are illustrated in the comparison of the simulated and observed cumulative β distributions presented in Fig. 4.7. For consistency, we again show results for the full sample and for ROBUST sources only. From the K-S test significance values given in Fig. 4.7, it can be seen that the $\beta = -2$ simulation in fact continues to provide a perfectly acceptable description of the data. Unsurprisingly, a wider intrinsic distribution can provide an improved fit, although the highest significance values are achieved if this distribution remains centred on a value close to $\beta = -2$ (consistent with our results for $\langle\beta\rangle$). Thus, while it is clear that we cannot rule out the possibility that our galaxy sample contains some objects with UV slopes as blue as $\beta \approx 3$ (see Table A1 of Dunlop et al. 2013), the current data certainly do not require any significant intrinsic scatter (even in this well-populated luminosity bin). For now, therefore, reliable conclusions can only be drawn on the basis of population-averaged values, $\langle\beta\rangle$.

4.7 Comparison with previous results

As noted earlier, the measurement of β at $z \gtrsim 6$ has been the subject of much debate. However with improvements in data from the UDF12 campaign, and with a more detailed understanding and treatment of measurement biases, there is now apparent consensus amongst most groups that faint ($M_{\rm UV} \gtrsim -18$) $z \approx 7$ galaxies are, on average, no bluer than $\beta = -2.4$, as shown by Fig. 4.8.

4.8 Physical interpretation

As we have seen (e.g. in Fig. 3.4), the various stellar population parameters (age, dust, metallicity, ...) are degenerate to one another when β is the only information available. Still, the new measurements of $\langle\beta\rangle$ presented here are bound by sufficiently small errors that some regions of parameter space are excluded: a very young, dustless and metal-poor stellar population is ruled out by these observations.

To explore this further, we have compared our results to various stellar population synthesis models. In all cases, we have used the BC03 models of Bruzual & Charlot (2003). Fig. 4.9 shows a comparison of our average $z \approx 7$ result (which is also consistent, within

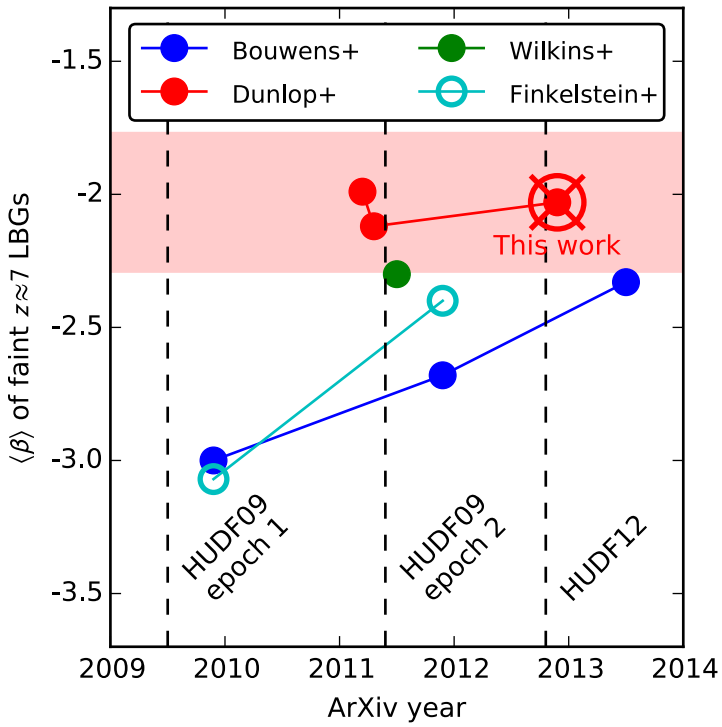

Figure 4.8 A historical comparison of measurements of $\langle\beta\rangle$ for 'faint' $z \approx 7$ LBGs, from results in the literature on the date they were first reported on the pre-print server ArXiv/astro-ph. 'Faint' denotes the result for the faintest galaxies quoted by each study as meaningful, and is variable around $M_{\rm UV} \gtrsim -18$. There appears to be an eventual consensus that these galaxies are, on average, certainly no bluer than $\beta = -2.4$. The result from Finkelstein et al. (2012b) has been corrected for observational bias according to their suggested offset. The red target marks the faintest $z \approx 7$ result presented in this chapter (and by Dunlop et al. 2013), with the red shaded region its standard error on the mean. The date of this work is shown as the ArXiv date for Dunlop et al. (2013).

the errors, with the $z \approx 8$ and 9 results) to the age-dependent colour-tracks of several models, as described by the caption therein. The models include single-burst and constant star-formation histories, pure-stellar and stellar+nebular emission templates, sub-solar and solar metallicities, and a range of dust reddening values. The nebular emission templates are those created and described by Curtis-Lake et al. (2013). All of the models are consistent with the data at some stellar population age within the age of the Universe at $z \approx 7$.

To further investigate the joint-probability distributions which give rise to these poor constraints, we have constructed noise-free photometry for a range of BC03 models at $z = 7$, in the same WFC3/IR filter-set as used for the observations. The models are as before, except here we include several other star-formation history parametrizations between the extremes of a single-burst and a constant star-formation histories: these are

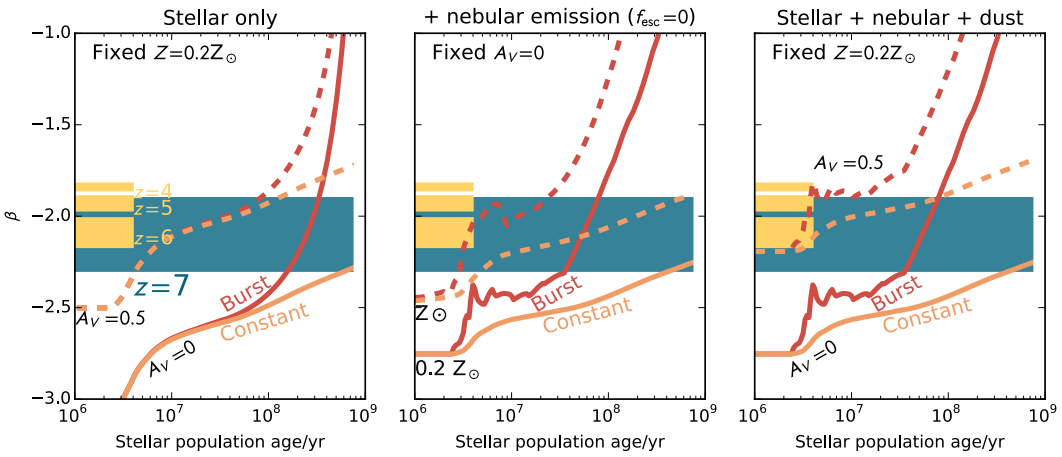

Figure 4.9 The average colour $\langle\beta\rangle$ of the UDF12 $z \approx 7$ galaxy sample is shown by the shaded blue region, superimposed with the age-evolving tracks of various stellar population synthesis models (lines). Also shown are measurements of $\langle\beta\rangle$ at $z = 4$, 5 and 6 by Finkelstein et al. (2012b) (yellow regions). In each panel, red and orange lines show the BC03 model tracks from stellar populations formed either in a single burst, or at a constant rate, respectively. In the *left panel*, solid and dashed lines represent populations with no dust ($A_V = 0$) or some dust ($A_V = 0.5$), respectively. In the *middle panel*, where the colours of galaxies on the tracks also include the effects of extreme ($f_{\rm esc} = 0$) nebular emission, solid and dashed line represents populations with sub-solar metallicity ($Z = 0.2$ Z$_\odot$) or solar metallicity, respectively. In the *right panel*, the effects both of nebular emission and of dust absorption are included simultaneously. In all cases the data are truncated at the age of the Universe at $z = 7$. Since all of the tracks intersect the data region, the data are consistent with the average $z \approx 7$ galaxy harbouring any of these stellar populations.

exponentially declining star-formation histories with a range of e-folding times (τ). For each model, β is measured from the photometry and compared to the average data result, yielding a goodness-of-fit χ^2(model | data). For each pair of parameters, the χ^2 values (minimized over other parameters) are shown in Fig. 4.10. While the grid is in places sparsely populated, the degeneracies are clearly illustrated. The only single-parameter constraint that can be made (within the bounds of this parameter-space) is to rule out dust reddening of $E(B-V) > 0.3$ at $> 2\sigma$. Fixing the metallicity Z and SFH τ obviously allows tighter constraints to be drawn, although neither Z nor τ are well characterized for star-forming galaxies at $z > 3$. Still, an example of these constraints is provided by Fig. 4.11, where solar metallicity is assumed, and again only the single-burst and constant SFHs are (separately) considered.

If the entire stellar population formed with an intense initial burst and with subsequent rapidly declining SF, the typical observed galaxy is moderately young, < 200 Myr. If the SF proceeded more steadily, β is less age dependent and the data are consistent with galaxies which began forming stars as early as the Big Bang. High dust reddening $E(B-V)$ is ruled out in all cases.

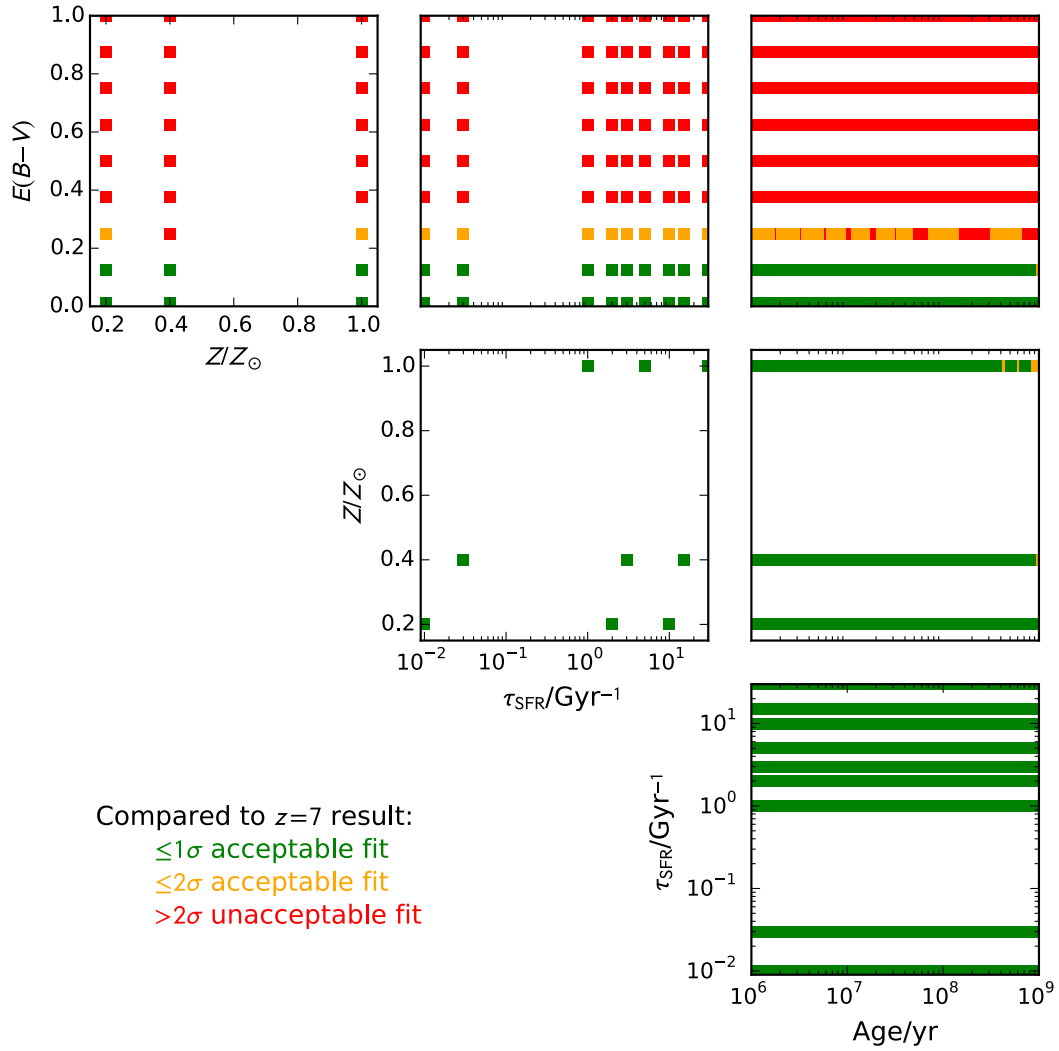

Figure 4.10 The constraints which the $z \approx 7$ measurement of $\langle\beta\rangle$ can place upon typical stellar population parameters, shown by how well combinations of those parameters can reproduce the observed UV colour. Each panel represents the joint parameter space of each pair of population age, SFH timescale $\tau_{\rm SFR}$, metallicity Z and dust reddening $E(B-V)$. Each point corresponds to an SED from a large grid of Bruzual & Charlot (2003) models. The colouring of each point denotes how plausible each model is, given the observed $\langle\beta\rangle$ and minimizing over the other parameters, as described in the legend. The IMF is all cases that of Chabrier (2003), and for simplicity only exponentially declining SFHs are used – the shortest τ is essentially a burst; the longest a constant SFR. Because of degeneracies, almost the entire range of each parameter is acceptable at 1σ; only high dust reddening of $E(B-V) > 0.3$ is completely ruled out.

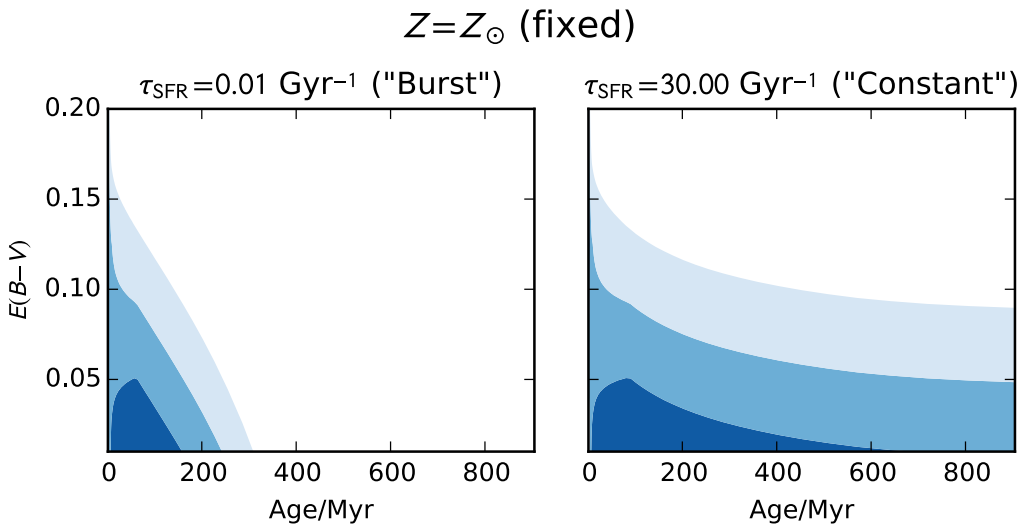

Figure 4.11 By fixing the stellar population metallicity at $Z = Z_{\odot}$, and fixing the SFH timescale to two simple cases (as shown by the the two panels), the $z \approx 7$ measurement of $\langle\beta\rangle$ can place qualified constraints on the typical stellar population age and dust reddening $E(B-V)$ of $z \approx 7$ LBGs. The contours, which from dark to light denote 1, 2 and 3σ acceptable regions of parameter space, were created using the model grid described in Fig. 4.10. Using models of sub-solar metallicity simply expands the height of the contour bands, such that dustier models are more acceptable at fixed age (when compared to the solar metallicity case shown here).

4.9 Comparison to galaxy formation models

In light of the measurements presented in this chapter, Dunlop et al. (2013) compared the results to an illustrative galaxy formation model. The model is described by Dunlop et al. (2013) and its outputs have been compared to observations by Dayal et al. (2013). For completeness, that comparison has been reproduced here, in the left-hand panel of Fig. 4.12.

The figure also includes a new comparison to a CANDELS mock catalogue, based on the semi-analytic models of Somerville et al. (2012; 2008). These 'S12' simulations differ from the 'D13' models presented by Dunlop et al. (2013), in that the S12 models predict markedly bluer colours in the luminosity range which our UDF12 results probe. While our averaged results appear reassuringly typical of galaxies in the D13 simulation, they are atypical for – but not wholly inconsistent with – galaxies in the S12 simulation. Fig. 4.12 also reproduces a luminosity-averaged prediction of the simulations by Finlator et al. (2011), as reported by Finkelstein et al. (2012b). Again these simulations predict colours slightly bluer than our results, similar to the S12 simulation. A full comparison of these simulations is beyond the scope of this work, but it is worth briefly noting one relevant difference between the simulations: their treatment of dust. Reddening in the D13

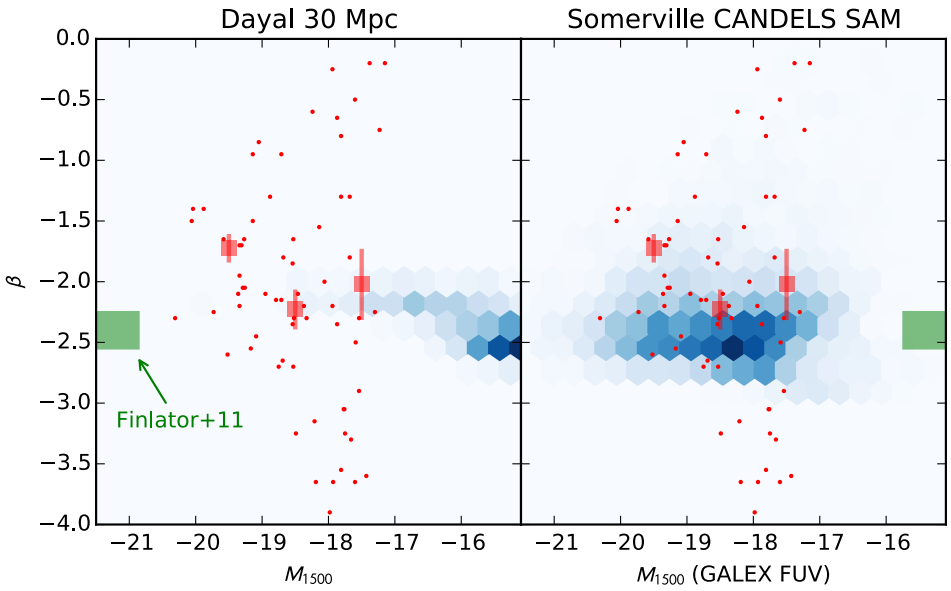

Figure 4.12 The UV colours as a function of absolute magnitude $\beta(M_{1500})$ for the $z \approx 7$ sample are shown in red. The data in the brightest two bins have been supplemented with a few sources from the two UDF09 parallel fields. Superimposed are noise-free predictions from galaxy evolution models: in the *left panel* from a 10 Mpc sided simulation by Dayal et al. (2013), and in the *right panel* a CANDELS mock catalogue, using the semi-analytic models of Somerville et al. (2012; 2008). Additionally, the green regions denote the average range of β predicted for this luminosity range at at $z \approx 7$ by the models of Finlator et al. (2011), as reported by Finkelstein et al. (2012b).

simulations is provided by a supernova dust curve, under the premise that at $z > 6$, since evolved stars have had insufficient time to become substantial dust producers, supernovae must be the dominant dust producer (Todini & Ferrara 2001). The other simulations adopt more traditional dust models, appropriate for lower-redshift starburst galaxies (e.g. the Calzetti dust law).

It is, however, also clear that the *observed* colour scatter is far larger than the simulations' predicted intrinsic colour scatter, a fact which explains the lack of evidence for intrinsic colour scatter found earlier.

4.10 Implications for the reionization budget

Combining $\langle\beta\rangle$ with the luminosity function can provide a prediction for the number of photons contributing to reionization. However, this calculation requires that the escape fraction $f_{\rm esc}$ of the ionizing photons be known. Had we measured $\langle\beta\rangle \approx -3$, we could have placed some constraint on $f_{\rm esc}$. However, since our relatively moderate result of $\langle\beta\rangle \approx -2$ can be reproduced by such a variety of stellar population parameters, $f_{\rm esc}$ remains

essentially unknown. Thankfully progress is being made in this area from other avenues, both from simulations (e.g. Mitra et al. 2013) and observations (Dijkstra et al. 2014, Jones et al. 2013).

In lieu of a precise measurement of $f_{\rm esc}$, Robertson et al. (2013) combined the β measurements presented here, the luminosity density presented by Ellis et al. (2013), McLure et al. (2013), Schenker et al. (2013), and reasonable assumptions on $f_{\rm esc}$ to determine that star-forming galaxies as faint as $M_{1500} \approx -13$ were required to sustain reionization at $z = 7-9$. This regime, some 4 mag beyond the limits of the UDF12 data, is beginning to be accessible by lensing surveys (e.g. CLASH, Bradley et al. 2014).

4.11 Conclusions

In this chapter, we exploited the unparalleled depth of the UDF12 NIR data to select and measure the UV continuum slopes of $z \approx 7$ and $z \approx 8$ galaxies. Motivated by our earlier investigation in Chapter 3, and verified by source-injection simulations, our results represent the first unbiased measurements of β at these redshifts. Our findings can be summarised as follows.

1. Our results, of $\langle\beta\rangle = -2.1\pm0.2$ at $z \approx 7$ and $\langle\beta\rangle = -1.9\pm0.3$ at $z \approx 8$, show no evolution over this relatively short span of cosmic time.
2. Over the luminosity baseline probed, there is no significant evidence for a colour–magnitude trend in either sample.
3. When compared to simulations designed to reproduce the observational scatter on colours, the samples show no evidence of *necessarily* being drawn from a population of galaxies with any intrinsic variation.
4. Even the faintest bins of these data show no significant population of extremely blue galaxies.

In summary, the galaxies sampled here appear to be much the same to one another: steadily star-forming galaxies harbouring moderately young stellar populations, already at least partially metal enriched and perhaps obscured by modest amounts of dust. However working, necessarily, near the noise-limits of these data and at such high redshift, where few wavebands probe the rest-frame UV beyond the Lyman break, means that we cannot rule out a modest variance in the intrinsic β values of high-redshift LBGs. The following chapter seeks to address this issue, using a larger sample of LBGs at $z \approx 5$.

5 The intrinsic rest-frame ultra-violet colour distribution of $z \approx 5$ galaxies

The majority of the work presented in this chapter has been previously published (Rogers et al. 2014).

In this chapter, we present the results of a study investigating the rest-frame ultra-violet (UV) spectral slopes of redshift $z \approx 5$ Lyman-break galaxies (LBGs). By combining deep *Hubble Space Telescope* imaging of the CANDELS and HUDF fields with ground-based imaging from the UKIDSS Ultra Deep Survey (UDS), we have produced a large sample of $z \approx 5$ LBGs spanning an unprecedented factor of > 100 in UV luminosity. Based on this sample we find a clear colour–magnitude relation (CMR) at $z \approx 5$, such that the rest-frame UV slopes (β) of brighter galaxies are notably redder than their fainter counterparts. We determine that the $z \approx 5$ CMR is well described by a linear relationship of the form: $\mathrm{d}\beta = (-0.12 \pm 0.02)\mathrm{d}M_{\mathrm{UV}}$, with no clear evidence for a change in CMR slope at faint magnitudes (i.e. $M_{\mathrm{UV}} \geq -18.9$). Using the results of detailed simulations we are able, for the first time, to infer the intrinsic (i.e. free from noise) variation of galaxy colours around the CMR at $z \approx 5$. We find significant (12σ) evidence for intrinsic colour variation in the sample as a whole. Our results also demonstrate that the width of the intrinsic UV slope distribution of $z \approx 5$ galaxies increases from $\Delta\beta \simeq 0.1$ at $M_{\mathrm{UV}} = -18$ to $\Delta\beta \simeq 0.4$ at $M_{\mathrm{UV}} = -21$. We conclude by suggesting that the increasing width of the intrinsic galaxy colour distribution and the CMR itself are both plausibly explained by a luminosity independent lower limit of $\beta \approx -2.1$, combined with an increase in the fraction of red galaxies in brighter UV-luminosity bins.

5.1 Introduction

In Chapter 4, we concluded that there exists no major population of exotic galaxies, harbouring metal-poor dust-free stellar populations, even amongst the faintest LBGs, at $z \approx 7$. Working, necessarily, at the limits of those data meant we were unable to put any tight constraints on the intrinsic variation in β which may be present. Moreover, focussing on the depth of the UDF12 data meant only a small luminosity baseline was accessible. This in turn meant a mild colour–magnitude trend, if present, would not have been evident in those data.

In this chapter we focus on an epoch just 400 Myr later, and still within the first 1.5 Gyr of cosmic time, at $z = 5$, where we are able to both extend the luminosity baseline with large ground-based datasets and benefit from the more precise measurements of β afforded by brighter, less redshifted sources.

The initial aim of this chapter is to combine the strength of deep, small area, *HST* imaging with shallower, but wide area, ground-based imaging from the UKIDSS Ultra Deep Survey (UDS) to provide a large sample of $z \approx 5$ LBGs spanning an unprecedented dynamic range in UV luminosity (≈ 5 magnitudes). We focus entirely on $z \approx 5$ galaxies because this is the highest redshift for which it is possible to consistently select large samples of galaxies free from Lyman–α contamination using the deep z-band imaging available across our *HST* and ground-based datasets. Based on the techniques developed in Chapter 3, we use bias-free measurements of β to provide the best available constraints on the form of the $z \approx 5$ CMR, before proceeding to exploit the results of detailed simulations to investigate the *intrinsic* galaxy colour distribution as a function of luminosity.

The remainder of this chapter is organised as follows. In Section 5.2 we describe the selection of our $z \approx 5$ galaxy sample from our chosen *HST* and ground-based datasets. In Section 5.3 we briefly recount our method for measuring rest-frame UV colours and present our constraints on the $z \approx 5$ CMR. In Section 5.4 we describe the detailed simulations which were necessary to accurately quantify the contribution of photometric uncertainties to the observed galaxy colour distribution. Based on the results of these simulations, in Section 5.5 we present our measurement of the intrinsic scatter in the galaxy colour distribution as a function of UV luminosity. Our conclusions are summarised in Section 5.6.

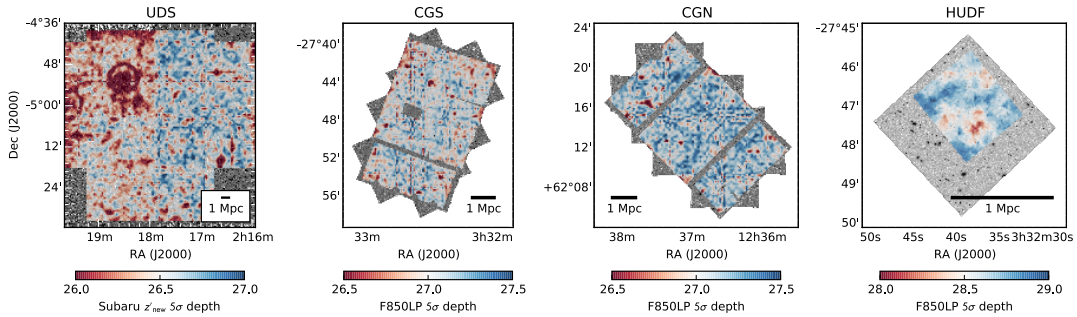

Figure 5.1 The four fields analysed in this chapter. In each, the grayscale image shows the z-band imaging in which the galaxies are detected, while the colour-map shows the local 5σ z-band depth from which SNR cuts are applied. Depths are computed at nodes of a 100×100 grid, based on each node's 200 nearest source-free apertures (see Section 5.2.3 for a discussion). The footprint of each depth-map defines our search area, i.e. the area in which imaging exists in all wavebands. The scalebar denotes a *physical* size of approximately 1 Mpc at $z = 5$.

5.2 Data and sample

In this section we describe the selection of our $z \approx 5$ galaxy sample. The sample is selected from four survey fields: the UKIRT Infrared Deep Sky Survey (UKIDSS) Ultra Deep Survey (UDS), the Cosmic Assembly Near-infrared Deep Extragalactic Legacy Survey (CANDELS) programme's coverage of the Great Observatories Origins Deep Survey (GOODS) North and South fields, and the Hubble Ultra Deep Field (HUDF). Summary details of the four fields and their respective $z \approx 5$ LBG samples are given in Tables 5.1 and 5.2.

5.2.1 Description of imaging

Here, we briefly describe the available imaging in each field. The fields themselves are shown in Fig. 5.1, while the band-passes of the filters are shown in Fig. 5.2.

UKIDSS Ultra Deep Survey (UDS)

The UDS is covered by public Subaru B, V, R, i, z'-band (Furusawa et al. 2008) and UKIRT J, H, K-band imaging[1], with a co-imaged area of 0.6 square degrees. In addition, we have made use of additional z'-band imaging taken after Subaru's SuprimeCam was refurbished with CCDs with improved red sensitivity. For the remainder of this chapter, the public z'-band is referred to as $z_{\rm old}$ and the new, deeper, proprietary z'-band as $z_{\rm new}$.

[1]The images we use are from DR10. See `http://www.ukidss.org`

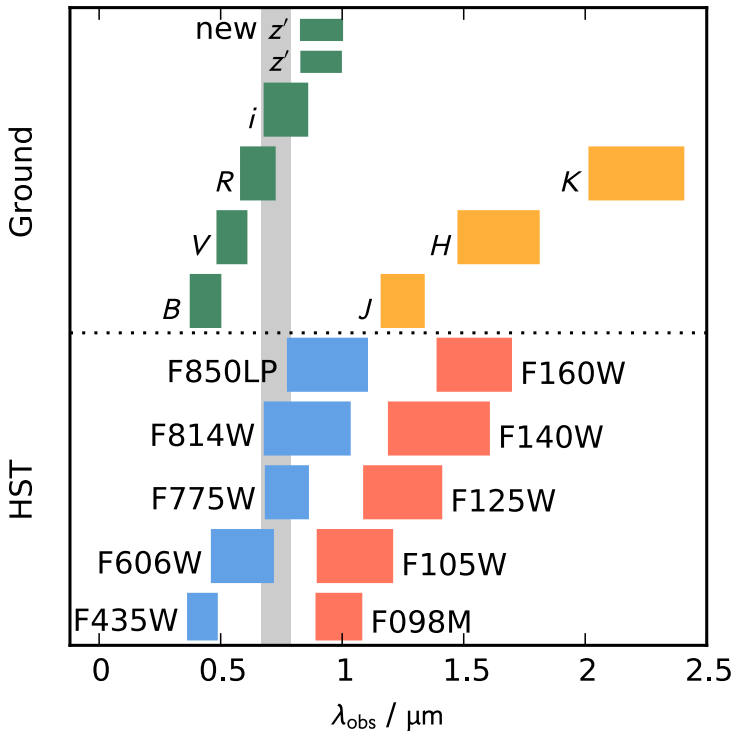

Figure 5.2 The photometric filter bandpasses for the images used in this chapter are shown by the coloured regions. Blue and red regions show the *HST*'s ACS and WFC3/IR filters, while green and yellow regions show the Subaru and UKIRT filters used in the UDS. The vertical, grey region denotes the wavelength range in which the 1216 Å Lyman–α break is observed at $4.5 < z < 5.5$.

CANDELS GOODS-N (CGN) and CANDELS GOODS-S (CGS)

The two CANDELS GOODS fields together provide 283 arcmin^2 of *HST* ACS and WFC3/IR imaging. The survey and data reduction are described by Grogin et al. (2011) and Koekemoer et al. (2011) respectively. In each field the WFC3/IR imaging consists of a deep central region, flanked by two shallower 'wide' strips. In CGS, one of these wide strips is provided by the Early Release Science field (ERS, Windhorst et al. 2011), which features deep Y-band coverage through the Y_{098} filter rather than the Y_{105} filter which is employed over the rest of the CGN and CGS fields (see Table 5.1).

Hubble Ultra Deep Field (HUDF)

The HUDF has been imaged by multiple programmes, most recently in the near-IR by the UDF12 campaign (Ellis et al. 2013, Koekemoer et al. 2013). We have analysed the UDF12 near-IR imaging in tandem with the ACS optical B_{435}, V_{606}, i_{775}, z_{850}-band imaging provided by Beckwith et al. (2006) and the more recently assembled I_{814} imaging provided as part of

the XDF (Illingworth et al. 2013). For this study, we searched only the area covered by the deepest WFC3/IR imaging (≈ 4 arcmin^2).

5.2.2 Photometry

Fixed-diameter circular apertures were used to construct photometric catalogues from each image. In the UDS imaging, 1.8-arcsec diameter apertures were used in all bands, enclosing $\approx$ 80% of a point source's flux. While a point source is a reasonable approximation to a $z \approx 5$ galaxy in the ground-based data, *HST* allows many of the brighter galaxies to be resolved. This is advantageous, as it allows stars to be easily distinguished from galaxies using their measured half-light radii ($r_{1/2}$). However in small PSF-matched apertures, broader sources lose a larger fraction of their light in short wavebands, resulting in a red colour bias for extended objects. There are various options to alleviate this: PSF homogenisation, which relies on a well-constrained transfer function to match the PSF of each image to that of the H_{160} data (which has the poorest spatial resolution); a measured-size dependent correction to the aperture photometry, which relies on well-measured half-light radii; or the adoption of sufficiently large apertures that realistic high-redshift galaxy sizes ($r_{1/2} \lesssim 1.5$ kpc) have a neglible impact, at the expense of image depth. For this work, we assume the third approach and use apertures of diameter 0.6 arcsec for all *HST* photometry. These apertures enclose a sufficient fraction of the total light in all bands that biases in the UV slope are at the level of $\left|\delta\beta\right| \lesssim 0.2$ (see Section 5.4).

In most wavebands these apertures are larger than those used in the previous chapter, where a compromise had to be made between large apertures, which minimize colour bias, and small apertures, which maximize the effective image depth. Here, maximizing image depth is not our goal, since the luminosity baseline will be greatly extended by the addition of multiple fields.

5.2.3 Image depths

Given the variable exposure-time maps of each survey field, and the importance of consistent signal-to-noise cuts across our sample, the SNR of the photometry for each candidate, in each filter, has been computed relative to the local image depths. Following the procedure detailed in Section 2.2, we created an object (segmentation) mask for each mosaic using SEXTRACTOR v2.8.6 (Bertin & Arnouts 1996), set to mask out any area where two or more pixels rise above 1.4σ, and placed non-overlapping apertures across the remaining source-free sky regions. The local depth at a given point on the mosaic was

Field	Area/arcmin^2	SNR cut	5σ depth/AB mag									
			B_{435}	V_{606}	i_{775}	I_{814}	z_{850}	Y_{098} [a]	Y_{105}	J_{125}	J_{140}	H_{160}
HUDF	4	5	29.2	29.6	29.2	28.4	28.6	–	29.5	29.2	29.2	29.3
CGS	143	8	27.6	27.8	27.3	–	27.0	27.1	27.5	27.5	–	27.3
CGN	140	8	27.6	27.8	28.4	–	27.2	–	26.9	27.1	–	27.0
			B	V	R	i	$z_{\rm old}$	$z_{\rm new}$	J	H	K_s	
UDS	2701	12	27.8	27.5	27.2	27.1	26.1	26.5	25.6	25.1	25.3	
TOTAL:	2988											

Table 5.1 *Summary of the fields used in this chapter. Columns 1 and 2 list the field names and the corresponding area of each used to search for $z \approx 5$ galaxies. Column 3 lists the z-band SNR threshold adopted for detecting galaxies in each field. Columns 4–13 list the depth of imaging in each field. Quoted depths are medians across the field, measured in circular apertures of diameter 0.6 arcsec (*HST*) or 1.8 arcsec (UDS); however, for selection, local depth measurements are used (see Section 5.2.3). The CANDELS CGS and CGN have variable depth NIR imaging, typically ranging from 27 – 28 mag, while the UDS imaging varies in the $z_{\rm new}$ selection band as shown in Fig. 5.1.* [a] *– Y_{098} imaging is used in place of Y_{105} for the northern strip (ERS; 44 arcmin^2) of the GOODS-S data.*

then measured by analysing the nearest 200 source-free apertures and computing the 5σ depth using the Median Absolute Deviation (MAD) statistic. The depth maps shown in Fig. 5.1 were created by computing local depths at nodes of a grid across the images, while the values quoted in Table 5.1 are medians over each field.

5.2.4 Selection of $z \approx 5$ galaxies

Similar to the selection procedures used in Chapters 3 and 4, candidates were initially detected within each field using SEXTRACTOR in dual-image mode, detecting in the z-band image and measuring from all others in fixed, circular apertures as discussed above (see Section 2.1). SNR thresholds were then applied in the z-band, to remove sources detected at low significance, and in the B-band, since both the Lyman break ($\lambda_{\rm rest}$ =1216 Å) and limit (912 Å) of a genuine $z \approx 5$ galaxy would lie redward of the B-band. To do so, the catalogues were first reduced in size by keeping only candidates with z-band detections brighter than the $3\sigma_{\rm global}$ depth (in the HUDF) or the $5\sigma_{\rm global}$ depth in CGN, CGS and the UDS, where $\sigma_{\rm global}$ is the median of local depths across a given image. At the same time, the catalogues were pruned of any object with a B-band detection at the $2\sigma_{\rm global}$ level. For the remaining candidates, local depth estimates were computed in each band, using the procedure outlined in Section 5.2.3. A second cull of $B \geq 2\sigma_{\rm local}$ detected sources removed the few contaminants lying in deeper parts of the image. Finally, refined z-band signal-to-noise cuts were imposed at local $5\sigma, 8\sigma, 8\sigma, 12\sigma$ thresholds for candidates in the HUDF, CGN, CGS and UDS (as per Table 5.1). These thresholds were chosen as compromises between sample size and data quality, which is itself dependent on the homogeneity of depths and the number of bands probing the rest-frame UV. The primary driver of these chosen thresholds was to ensure that, regardless of the field, the bands to be used for measuring β would all have high signal-to-noise for sources with a reasonable (i.e. flat) spectral slope. In the UDS for example, the J and H bands, which together with the z band probe the rest-frame UV, have depths 0.9 and 1.4 mag shallower than the $z_{\rm new}$ selection band. A flat-spectrum ($\beta = -2$) source, detected at 5σ in the $z_{\rm new}$ band, would have J- and H-band photometry with SNR of only ≈ 2. Raising the z-band selection threshold counters this problem.

Photometric redshift analysis

Redshift $4.5 \leq z \leq 5.5$ galaxies were selected using the photometric redshift code LEPHARE (Arnouts et al. 1999, Ilbert et al. 2006), adopting the 'COSMOS' galaxy models of Ilbert et al.

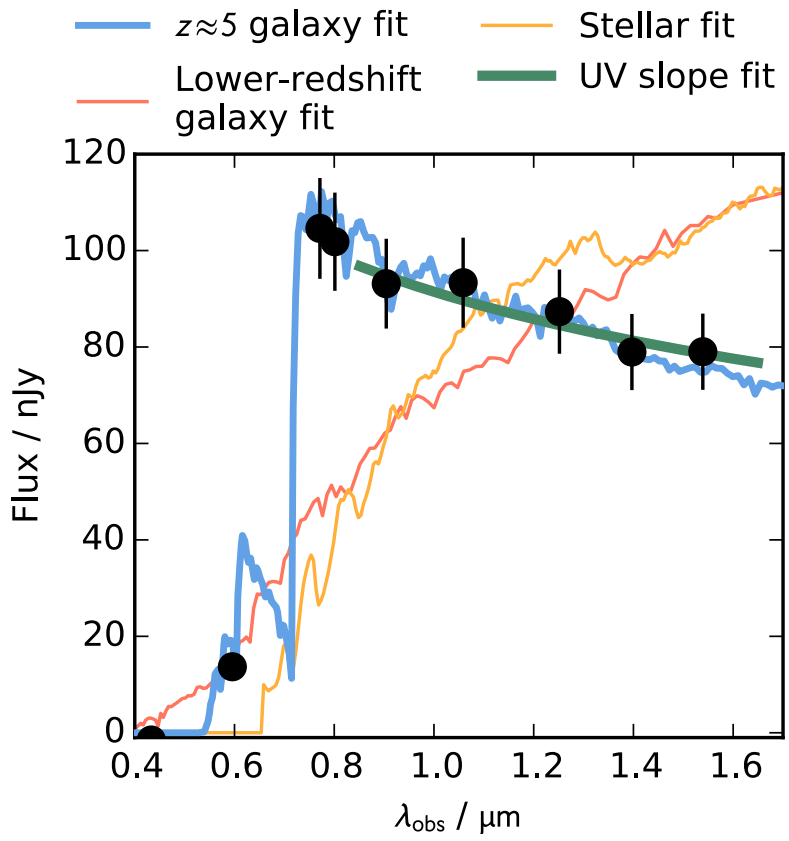

Figure 5.3 The spectral energy distribution of an example $z \approx 5$ galaxy in the HUDF is shown by black points, in the observed frame. The lines show the various fits used to analyse the galaxy. The error bars are inflated to at least 10% of the flux for the fitting (as shown here; and see Section 5.2.4). In blue is the best-fitting primary redshift solution. The possibility of it being a contaminant is ruled out by the poor lower-redshift galaxy and stellar fits (red and yellow). The rest-frame UV spectral index β is deduced by fitting with a power-law model (green) to the observed near-IR data.

(2006) and galactic dwarf star templates from the SpeX library[2]. The 'COSMOS' spectral energy distributions (SEDs) include elliptical, spiral and star-burst templates, which were fit over the redshift range (0, 10) allowing dust reddening of $E(B-V) \leq 1.5$ with a Calzetti et al. (2000) reddening law. While our local depth estimates are robust, we ensure the entire observed SED contributes to the fit by imposing *minimum* flux errors of 10%[3].

Candidate $z \approx 5$ galaxies were thus selected, regardless of how marginally the $z \approx 5$ photometric redshift solution was preferred to any secondary solution. As discussed at length in Chapter 3 (Rogers et al. 2013) and by Dunlop et al. (2013), introducing any form of χ^2(primary) $-$ χ^2(secondary) threshold inevitably biases the selection against faint, intrinsically (or photometrically scattered) red galaxies, although this effect is mostly

[2] `http://pono.ucsd.edu/~adam/browndwarfs/spexprism`.

[3] In practice, these minimum errors were adopted in the NIR bands for around 10% of candidates brighter than $z > 5\sigma$ in the UDS, to 50% of candidates in the HUDF.

alleviated for galaxies detected at SNR $\gtrsim 8\sigma$ (Dunlop et al. 2012). In reality, given our chosen redshift and signal-to-noise windows and large apertures, lower redshift models typically struggle to fit the shape of the observed purported Lyman breaks. Fig. 5.3 shows an example of the model fitting procedure. Genuine high-redshift galaxies were considered to be those for which the primary galaxy model SED (with an assumed four degrees-of-freedom) was acceptable at the 2σ level, i.e. $\chi^2 \leq 11.3, 9.7, 7.9$ in the HUDF, UDS and CGS/N fields respectively. Potential stellar contaminants were rejected if the best stellar fit was acceptable at 2σ and if the source's z-band half-light radius $r_{1/2}$ was consistent with being stellar at that luminosity. The half-light radius threshold was defined by injecting point sources into the z-band image at various luminosities, and measuring the $r_{1/2}$ of re-detected sources using SEXTRACTOR; the edge of an envelope enclosing 95% of recovered point sources in $r_{1/2}$ – luminosity space was then taken as the threshold for being 'consistent with stellar'. In the UDS, where the ground-based imaging makes stellar rejection most critical, the model-fit criteria flagged 22 (of 367 early-stage candidates) as potentially stellar, while the additional $r_{1/2}$ criteria prevented nine of those from being rejected at that stage of the selection process.

Finally, the imaging and SED fits for each candidate were visually inspected. Having survived the selection procedure thus far, objects were only deleted if they were deemed to lie too close to the image edge, or if their SED was acceptably stellar but their proximity to another source led them to be measured with an excessive $r_{1/2}$. Candidate galaxies were also removed from the sample if they were close enough to a large foreground object that the photometry or background subtraction were likely to be insecure, or if they were blended with another smaller object with a significantly different photometric redshift. In deriving those photometric redshifts, SEXTRACTOR was used to determine the photometry for each source with the other(s) masked. Additionally, blending in the low-resolution (ground-based) UDS imaging was checked by cross-matching our catalogue to that of Galametz et al. (2013a;b), which was derived from the HST CANDELS UDS imaging (Grogin et al. 2011, Koekemoer et al. 2011), which covers a small portion of the ground-based UDS (202 arcmin^2 of the total 2701 arcmin^2). Of our 27 UDS candidates also in the CANDELS catalogue, only one is revealed as having two distinct components in the HST imaging. Based on a CANDELS UDS photometric redshift catalogue (Fontana et al. 2006, Galametz et al. 2013a), the two components have $z = 4.61$ and $z = 4.65$, in good agreement with $z = 4.75$ from the ground-based imaging alone, and are visually connected in the *HST* images suggesting the two components are in fact a single source. Assuming that the CANDELS UDS region is representative of the whole UDS field, the fraction of ground-based UDS galaxy candidates which in the other fields would have been treated as multiple individual sources is expected to be $\lesssim 5\%$.

Field	N	$\langle z \rangle$	$\langle M_{\rm UV} \rangle$	$\langle \beta \rangle$	Mean($\delta\beta$)	
					(data)	(sim)
HUDF	33	5.1	−18.5	−2.04±0.05	0.26	0.26
CGS	112	4.9	−20.2	−1.82±0.04	0.27	0.30
CGN	163	5.0	−20.1	−1.90±0.04	0.29	0.29
UDS	276	4.9	−21.2	−1.90±0.03	0.39	0.36

Table 5.2 *Sample properties of galaxies from the four field analysed in this work (column 1). Column 2 lists the number of galaxies selected from each field. Columns 3–5 list the mean redshift, mean absolute magnitude, and the mean UV slope and its standard error. The final two columns list the mean error on the β measurement for an individual galaxy from the data and, for comparison, the simulations described in Section 5.4. Full source lists are given in Appendix B.*

Having applied the above selection procedure, our sample consists of 584 LBG candidates at $z \approx 5$, selected over 2988 arcmin^2. The sample covers a long luminosity baseline of $-22.5 < M_{1500} < -17.5$, large enough to provide strong leverage on the CMR. A summary of the sample's properties, broken down by field, is given in Table 5.2. A complete list of all 584 LBG candidates is given in Appendix B, where M_{1500}, β, $\delta\beta$, $z_{\rm phot}$, position information and literature redshift comparisons are given for each source.

5.2.5 Selection method validation

To check our sample selection method, we have compared our CANDELS GOODS-S (CGS) sample to other catalogues. Comparing to the ESO GOODS/CDF-S Spectroscopy master catalogue[4], we find 23 sources with spectroscopic redshifts from Vanzella et al. (2008), and three with spectroscopic redshifts from Popesso et al. (2009) and Balestra et al. (2010). All 26 spectroscopic redshifts lie in the range $4.4 < z_{\rm spec} < 5.6$, in excellent agreement with our $4.5 < z_{\rm phot} < 5.5$ defined selection window. The results of this comparison are shown in Fig. 5.4, which additionally shows a further 10 galaxies which were matched from our initial catalogue but which failed to survive one of the refined sample selection criteria. For the matched galaxies in our final sample, the photometric redshift accuracy is $\sigma[(z_{\rm spec} - z_{\rm phot})/(1+z_{\rm spec})] = 0.032$. Of our 112 CGS galaxies, 110 have also been studied by Dahlen et al. (2014, in prep.), who compared photometric redshift estimates from 11 different codes (Dahlen et al. 2013). Comparing to their results, we estimate that our lower-redshift interloper contamination fraction is around 5%. This is due to our inclusion of candidates with good high-redshift solutions, but which are only marginally distinguished from lower-redshift solutions. This estimate is also in line with a comparison of the 27 of our UDS galaxies which fall within the CANDELS UDS *HST* coverage: using

[4] `http://www.eso.org/sci/activities/garching/projects/goods/MasterSpectroscopy.html`

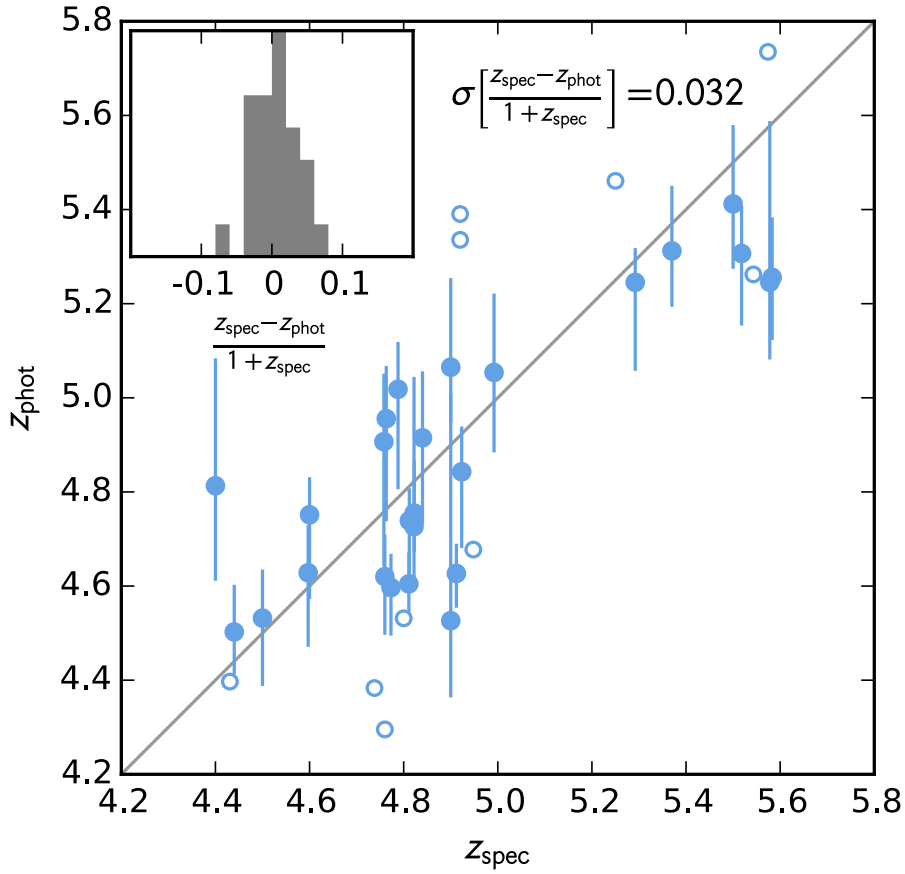

Figure 5.4 Comparison of our photometric redshift selected sample to published spectroscopic redshifts from the ESO GOODS/CDF-S Spectroscopy master catalogue. The filled circles show 26 objects position-matched to galaxies with spectroscopically confirmed redshifts. The open circles denote a further 10 galaxies which were matched from our initial catalogue but which failed to meet one of the final selection criteria. A $z_{phot} = z_{spec}$ line is shown as a guide to the eye. The inset shows the distribution of photometric spectroscopic redshift offsets, from which the photometric redshift accuracy can be derived.

the CANDELS photometry and independent photometric redshifts (Fontana et al. 2006, Galametz et al. 2013a;b) reveals only one of the 27 galaxies to have a preferred lower-redshift fit. The source lists in Appendix B denote these less secure sources, along with the literature spectroscopic and alternative photometric redshifts where available, for all the fields. Fortunately, as we shall see in Section 5.3.1, the exclusion of these potential contaminants, which span a wide range of luminosities, does not affect the results that follow.

5.2.6 Measuring M_{1500}

Absolute UV magnitudes ($M_{\rm UV} = M_{1500}$) were determined using a top-hat filter centred on 1500 Å in the rest-frame of the best-fitting SED template. To make our results comparable to other studies, the absolute magnitudes were boosted by around 0.2 mag, to account for the still incomplete enclosure of a PSF's flux within our already large apertures. In practice, this was achived by correcting the raw photometry of objects in the selection catalogues with a point-source correction: a PSF dependent, and therefore image and wavelength dependent, flux multiplier calculated to correct for the incomplete enclosure of a point source within the apertures. This correction ranged from ≈ 0.12 mag. in the *HST* GOODS fields' B_{435} and V_{606} images, to ≈ 0.28 mag. in H_{160}. In the more seeing-limited UDS data, the corrections were all around $0.23-0.30$ mag. The luminosity distribution of our complete sample is shown in the top panel of Fig. 5.5. By design, this definition of M_{1500} does not include any correction for dust attenuation; it is the 'observed' absolute magnitude. This choice serves to avoid imparting an artificial colour–magnitude relation onto the data. For instance, the simplest correction would be to follow the Meurer et al. (1999) relation, which yields a dust attenuation correction A_{1600} based on the observed colour β: a low β suggests a small A_{1600}, so only a minimal correction is required on M_{1500}. While less direct, the same must be true if the dust attenuation is estimated by SED fitting, since the SED fit has essentially no other information from which to constrain the dust attenuation. Thus, had we adopted such a correction, red galaxies would be luminosity-corrected by a larger degree than blue galaxies at the same *observed* luminosity. Under the null hypothesis that M_{1500} and β are uncorrelated, or are only weakly correlated, the result is to skew the observed β vs. $M_{1500,\rm obs.}$ space, generating a spurious dependency of β on $M_{1500,\rm corrected}$.

5.3 Measurement of UV slopes and the colour–magnitude relation

In this section, we use our sample to constrain the colour–magnitude relation at $z \approx 5$.

5.3.1 Measuring the UV slope

Following the procedure developed in Chapter 3 (Rogers et al. 2013), and as used in Chapter 4 (Dunlop et al. 2013), we fitted for β at fixed redshift using a variety of power-law SED models. Adopting the photometric redshift $z_{\rm phot}$ derived at the selection stage, we re-ran LEPHARE treating $z_{\rm phot}$ as a spectroscopic redshift. The models were pure

power-law models ($f_\lambda \propto \lambda^\beta$), truncated shortward of 912 Å, with no dust attenuation allowed. Attenuation due to the IGM is provided by LEPHARE, following the Madau (1995) prescription. An example of these power-law fits is shown in Fig. 5.3. Minimum photometric errors of 10% are still used; removing these has little effect, with β changing by < 0.1. The fitting procedure yields, for each object, a distribution $\chi^2(\beta_i)$ for a finely gridded set of templates $-8 < \beta_i < +5$. The best-fitting UV slope was taken to be that which minimized χ^2, and the error was obtained by finding the values of β for which $\Delta\chi^2 = 1$ from the χ^2 minimum (where the χ^2 distribution is minimized over the SED normalisation). This procedure excludes the colour uncertainty induced by the photometric redshift uncertainty, but, in our targetted redshift range, this is minimal since the Lyman break falls a good way blueward of the β-measuring wavebands (see Fig. 5.2). In the UDS, we used the two z-bands, J and H to fit β. In the CANDELS fields, we used z_{850}, $Y_{098|105}$, J_{125}, and H_{160}, and in the HUDF, we used z_{850}, Y_{105}, J_{125}, J_{140}, and H_{160}.

A simple linear fit to the entire colour–magnitude distribution of the combined galaxy sample, with each galaxy weighted by its colour error $1/\delta\beta$, yields a slope

$$\frac{\mathrm{d}\beta}{\mathrm{d}M} = -0.12 \pm 0.02,$$

and a zeropoint of

$$\beta(M_{1500} = -19.5) = -1.93 \pm 0.03.$$

Fig. 5.5 shows this relation fitted to the sample. These values are in excellent agreement with the results of B13, who used space-based data alone. This parametrization does differ from the results of F12, who found a much weaker correlation, but our relation is still statistically consistent with their binned data points. As F12 illustrated, restricting their faintest bin to galaxies from the HUDF alone (which moves the bin fainter) also yields a stronger relation, bringing it further in line with this work.

Following the suggested existence of a piecewise-linear relation by B13, whereby $\mathrm{d}\beta/\mathrm{d}M$ is steeper at the bright end (e.g. $M_{1500} < -18.9$) than the faint end, Fig. 5.5 also shows their two-component broken linear fit. Our data show no clear evidence to support the broken power-law CMR (see the binned mean results in Fig. 5.5). Fixing the break at B13's suggestion of $M_{1500} = -18.9$ and fitting the bright- and faint-end slopes of our data does yield values similar to those reported by B13; of -0.16 ± 0.02 and -0.04 ± 0.12 respectively. However, given the uncertainties, there is clearly no significant evidence for the CMR being non-linear. The two-component fit shown in Fig. 5.5 is only very slightly preferred to the linear fit ($\chi^2_{\mathrm{red.}} = 2.18$ vs. $\chi^2_{\mathrm{red.}} = 2.15$ for the two-component and single-component linear

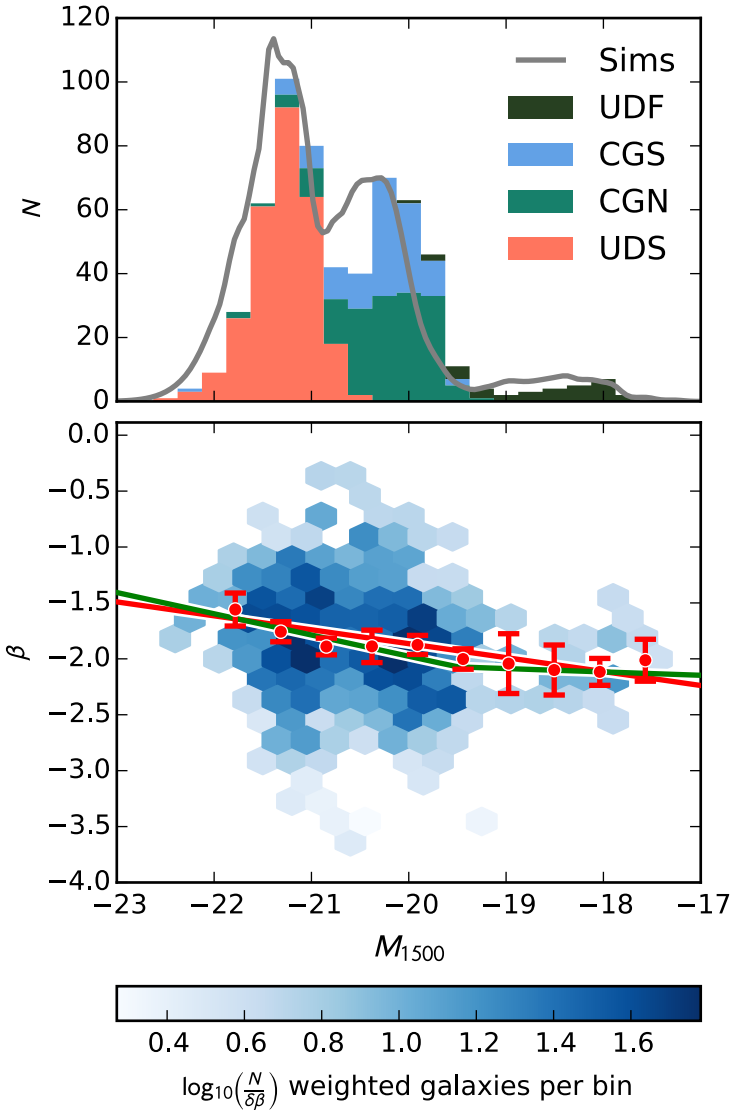

Figure 5.5 *Top:* the luminosity distribution of the sample used to constrain the colour–magnitude relation, shown as a stacked histogram, split by field. The grey line shows the expected distribution based on the $z = 5$ luminosity function and the size and selection function of each field (see later simulations). *Bottom:* the density map shows the combined sample in colour–magnitude space. The red line is a fit to *all the individual galaxies*, with slope −0.12. Both the density map and fit are weighted by the uncertainty, $\delta\beta$, on each galaxy's β colour; this is derived from the $p(\beta)$ distribution obtained by template-fitting the SED of each galaxy. The red circles are binned means, and their error bars are 2× the standard error on the mean in each bin (inflated for visibility). These error bars are driven by photometric scatter, so do not directly constrain any intrinsic variation that may exist in the colours. The green line is the two-component piecewise-linear fit reported by Bouwens et al. (2013). Their single linear relation is in near-perfect agreement with ours, so is not shown.

fits, respectively). Moreover, even the qualitative nature of this result is heavily dependent on the exact choice of the break luminosity. For example, floating the break luminosity fails to yield any meaningful constraint, and fixing the break instead at $M_{1500} = -19.5$ results in a steeper faint- than bright-end CMR gradient. In summary, we confirm the existence of a significant CMR with our sample. However at least in this redshift window (B13 studied a range of redshifts) we lack strong evidence to either confirm or refute the existence of a characteristic luminosity at which the colour–magnitude relation changes gradient.

The impact of potential interlopers

Of the 584 galaxies in the combined sample, 15 have secondary redshift solutions (mostly at $z_{\rm sec} < 1$) which are acceptable at the 2σ level as defined in Section 5.2.4. Removing these 15 galaxies does not alter the measured CMR parameters beyond the stated confidence intervals: $\beta(\text{no interlopers}) = (-0.13 \pm 0.02) M_{1500} - (1.96 \pm 0.03)$.

5.4 Image simulations

In this section we describe the creation and injection of simulated galaxies into the images, and explain how their detection and selection efficiencies compare to the real galaxy sample.

5.4.1 Model galaxies

Simulated galaxies were defined on a grid spanning $\beta, M_{\rm UV}$ and z, in order that the selection probability could be computed for any galaxy with a given intrinsic redshift, luminosity and colour, and so that mappings could be made between intrinsic and observed values of β. The luminosity distribution from which they were drawn conforms to the simple redshift-evolving luminosity function of McLure et al. (2013, section 2.7). This evolving luminosity function was needed since, to simulate some scattering between redshift bins, we input galaxies over the redshift range $4 < z < 6$, through which the luminosity function evolves significantly.

Each model's SED and $M_{\rm UV}$ were derived from a BC03 (Bruzual & Charlot 2003) stellar population synthesis model with metallicity 0.2 $Z_{\odot}$, a declining star formation history with $\tau = 0.03$ Gyr and a Chabrier (2003) IMF. The galaxy population was defined with a uniform distribution of galaxies in the β dimension, achieved by mapping β to pairs of stellar

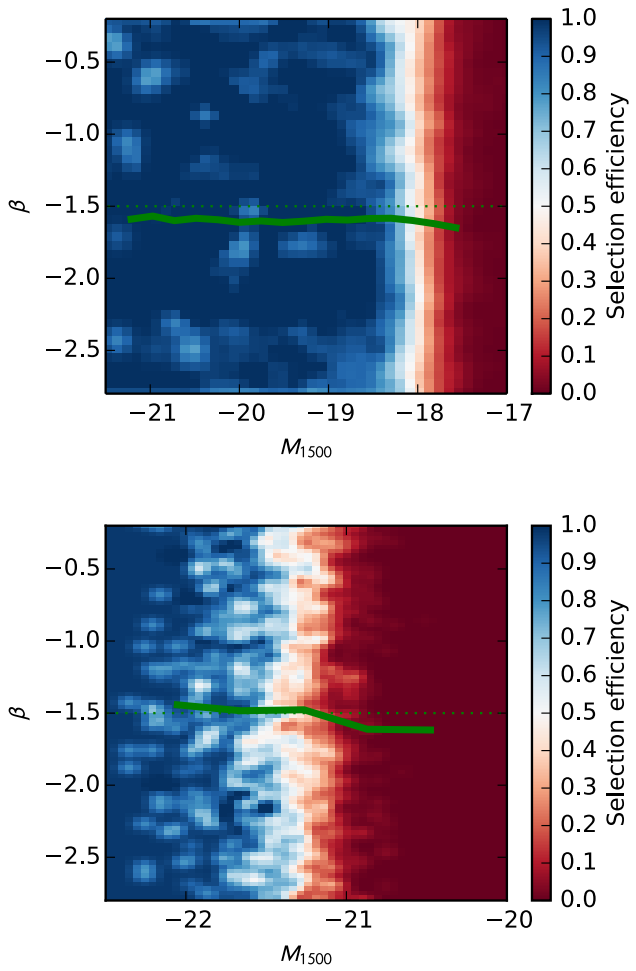

Figure 5.6 The selection efficiency (recovered fraction of total input galaxies) is shown in bins of colour–magnitude space for the HUDF simulation (top panel) and the UDS simulation (bottom panel) In both simulations the completeness limit lies at a fairly uniform magnitude across the range of βs, meaning no large colour bias exists in any luminosity bin. As an example we show the worst-case scenario, picking $\beta = -1.5$ samples from each simulation (dotted green lines) which, after observation, are measured as the biased solid green lines. These lines are typical for colours $\beta > -2$; the bias lines are even flatter for $\beta < -2$. The small offset in the HUDF simulation is (the worst) example of the systematic offsets from the simulations, $\Delta\beta \lesssim 0.1$, due to the way galaxy templates deviate from a perfect power law. The bias lines are truncated at the faint limit of each sample.

population age t and Calzetti et al. (2000) dust reddening $E(B-V)$ (see 3.4). While the entire range of β could have been reproduced by modifying $E(B-V)$ at fixed t, the age evolution was imposed to provide a more physically motivated model at each β. Galaxies were allocated half-light radii $0.2 \leq r_{1/2} \leq 1.6$ kpc, according to the $z = 5$ size–luminosity relationship of Bouwens et al. (2004) with a small scatter ($\sigma = 0.2$ kpc) around the relation. This was implemented in the simulations by broadening the PSF with an appropriate smoothing kernel. As discussed earlier, unknown sizes in this range, when convolved with the PSF and measured in our adopted apertures, imply errors on β of < 0.2. We assume a wavelength-independent morphology over the fairly narrow rest-frame wavelength range of interest ($\lambda \sim$1300-3000 Å).

5.4.2 Simulation pipeline

The model galaxies were inserted into the images, avoiding existing sources by use of the segmentation map. In the HUDF, 50 copies of the field were used to avoid excess crowding. The simulated galaxies were observed in the same way as in the real data. While no 'stars' were injected into the simulations, we performed the same star-rejection routine as for the data such that its effect on the selection efficiency could be determined.

5.4.3 Selection efficiency

Fig. 5.6 shows an example of the selection efficiency of galaxies in colour–magnitude space from our HUDF simulation. Reassuringly, considering our conservative approach, there is little preferential selection of galaxies at any colour: the completeness limits are β independent. Our simulations do however show evidence of some systematic offsets, although even in the worst-case scenario these are at the $\delta\beta \lesssim 0.1$ level (see Fig. 5.6). The remaining bias is due to a combination of aperture/size effects and variations in β which depend on the filter-set or measurement method used (see 3.2).

5.4.4 Comparison to data

To cross-validate the selection efficiency of our simulations with the selection function applied to the real datasets, we compared the predicted and measured luminosity distributions of the combined galaxy sample. However, the simulation inputs only *approximately* followed the high-redshift LBG luminosity function: in order to have a smoothly varying redshift-dependent LF for the simulated galaxies, the input LF was not identical to the 'best-estimate' of the LF at fixed $z = 5$, but rather an approximation to the LFs for redshifts $4-9$. Over the narrow redshift range of our selection window, the fixed-redshift function

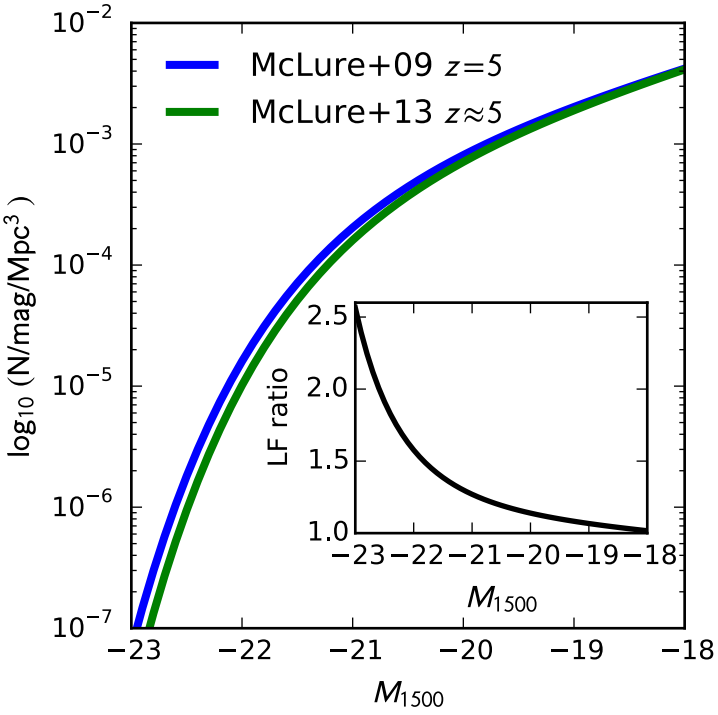

Figure 5.7 A comparison of the redshift-evolving luminosity function used as our simulation input (McLure et al. 2013) with the fixed-redshift measured luminosity function of McLure et al. (2009) used for comparison of our data and simulation outputs. Within the luminosity range of our sample, the deviation between these two functions is up to a factor of 1.5. The rationale behind the adoption of these functions is provided in the text, 5.4.4.

of McLure et al. (2009) provides a better representation of the luminosity distribution of galaxies than does the simple evolving parametrization used for the simulation inputs: as shown in Fig. 5.7, the deviation is up to a factor of 1.5 at the bright end of our sample at $z = 5$.

For the luminosity distribution check, we therefore adopted the $z = 5$ luminosity function determination of McLure et al. (2009). Since the luminosity function used for the simulation inputs is essentially 'divided out' of the selection efficiency calculation, we are free to adopt this alternative luminosity function for this comparison. By multiplying the selection efficiency of the appropriate simulation by the area of each field and integrating down the adopted luminosity function model, a predicted luminosity distribution for our sample was computed. The resultant predicted luminosity distribution is shown as the grey line in Fig. 5.5, and agrees well with the combined luminosity distribution of the actual sample. The simulations also predict uncertainties on individual galaxy β measurements which are very similar to those found for the sample, as shown in Table 5.2.

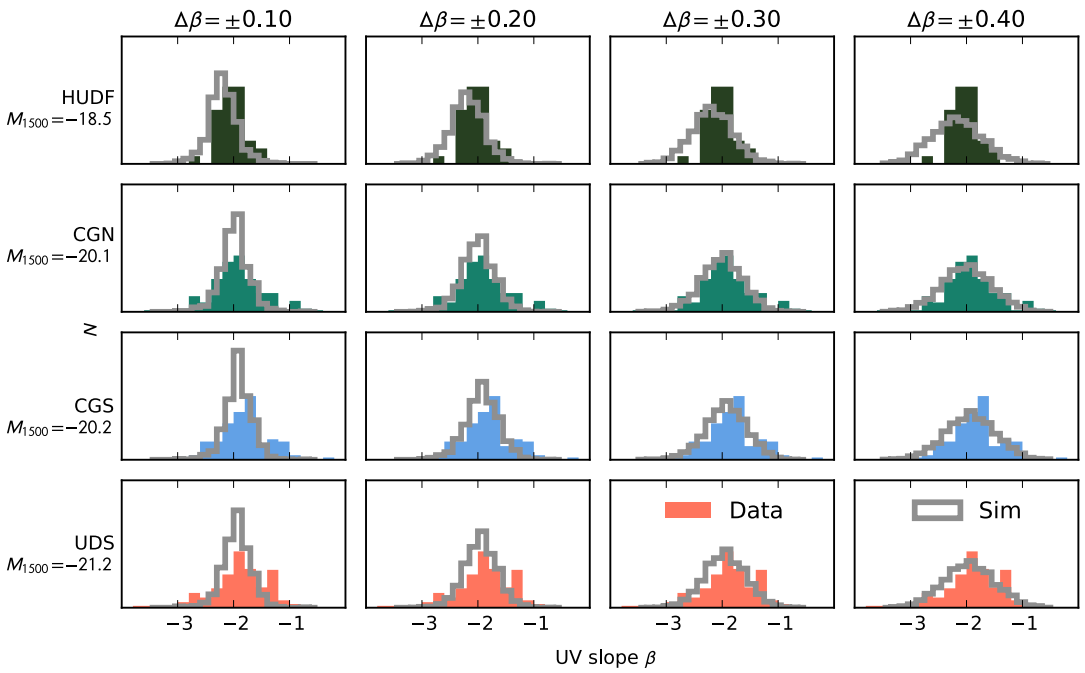

Figure 5.8 A comparison of the intrinsic scatter of faint galaxies (top panels, from the HUDF sample) through to brighter galaxies (lower panels from CGN, CGS, and the UDS). By comparing the distribution of colours in the data (coloured histograms) to those of the simulations (grey lines), which are designed to replicate the combinations of intrinsic and photometric scatter in the data, we can disentangle the intrinsic distribution of colours. Left to right, simulations of increasing intrinsic colour variation are shown superimposed onto the fixed data. For simplicity, we show only four possibilities here: $\Delta\beta \in \{0.1, 0.2, 0.3, 0.4\}$. The fields containing brighter galaxies are better represented by simulations with larger intrinsic colour scatter.

5.5 Intrinsic variation

In this section we derive the *intrinsic* variation in colour across the sample, using the image simulations to decouple the observed β distributions into intrinsic variation and photometric scatter. We have approached this problem from three angles. First and most simply, we assumed that the observed β distribution is a convolution of two Gaussians: one representing the intrinsic colour distribution of the galaxy population, and one due to photometric scatter in some fiducial scenario. Second, by drawing realisations from the simulations according to various intrinsic distributions, we compared the data and simulations using an equal-variance test and maximized the probability that the data and realisation are from the same population. Third, the comparisons of the β distributions of the data and simulations were made by a full maximum-likelihood test. Each method relies on a comparison of the observed distribution to some subset of our simulations. A visual comparison of this is given in Fig. 5.8, where the observed β distribution in each field is shown alongside simulated distributions based on various intrinsic colour scatters.

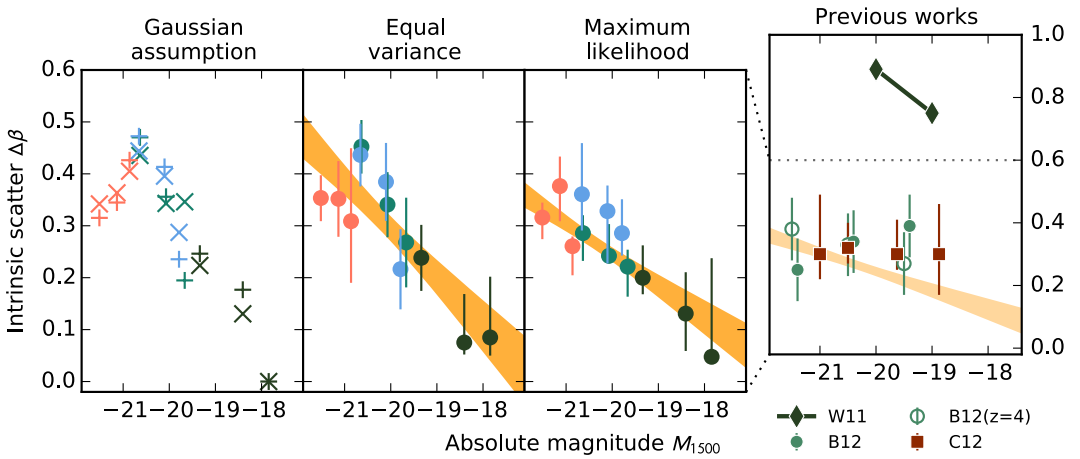

Figure 5.9 The width of the intrinsic colour distribution of galaxies at various luminosities. The first three panels relate to each of our three test methods, as denoted by the panel title and described in Section 5.5. In the first panel, × marks show the results of our Gaussian assumption test, while + marks denote our simulation-free check results. In all cases, each field contributes three bins of equal occupancy. The points are coloured by field, as in Fig. 5.8: salmon=UDS, blue=CGS, green=CGN, dark=HUDF. The error bars each enclose 68% of the total $p(\Delta\beta)$ where applicable. In each case, the yellow regions show the 1σ error limits of a linear fit to the measurements, weighted by the errors on $\Delta\beta$. In all three tests, brighter galaxies are drawn from a more varied intrinsic population than fainter galaxies. The final panel (with an expanded vertical range) shows measurements drawn from the literature over narrower dynamic ranges, from Bouwens et al. (2012a, B12), Wilkins et al. (2011, W11), and Castellano et al. (2012, C12). The maximum likelihood relation is shown in pale yellow in the final panel for comparison.

The intrinsic distribution is in all cases assumed to be Gaussian, and is parametrized by $\Delta\beta$, its standard deviation. We have tested a log-normal distribution and, like Castellano et al. (2012), find no convincing preference for it.

5.5.1 Measuring $\Delta\beta$: Gaussian assumption

The simplest estimate of the intrinsic distribution of colours is to assume that the observed distribution is a combination of two Gaussian distributions: one reflecting intrinsic variation and one due to photometric scatter. Under this assumption, the width[5] of the intrinsic colour distribution is

$$\Delta\beta \approx \sqrt{\sigma_{\rm obs}(\beta)^2 - \sigma_{\rm photo}(\beta)^2}, \tag{5.1}$$

where $\sigma_{\rm photo}(\beta)$ can be measured by looking at the simulated β distribution of a set of galaxies that were input with $\beta_{\rm input} \approx {\rm median}(\beta_{\rm data})$. By relying on the varying average

[5]We use the term 'width' informally; here it denotes the σ of the distribution, rather than the FWHM.

luminosity of galaxies in each field, we can make these comparisons along the luminosity baseline without the difficulties of combining the data and simulations of the different survey fields. To better populate the luminosity space, each field and simulation were split into three luminosity bins of equal occupancy. The results of this measurement are shown as × marks in the first panel of Fig. 5.9. The colours of the brighter galaxies found in the UDS and CANDELS fields populate a much broader distribution than photometric scatter alone would predict: hence, they stem from a more intrinsically varied population.

5.5.2 Measuring $\Delta\beta$: equal-variance test

By testing against only a single simulation, the first test could not measure the uncertainty on $\Delta\beta$. So for the equal-variance test a grid of simulated β distributions, each according to a different $0 < \Delta\beta < 1$, was created for each field. In each case, the simulation was centred on the median β of the data. Centring the distribution in this way, rather than around the linear CMR, avoids making any *a priori* assumption about the shape of the CMR. Following Dunlop et al. (2013), we used a non-parametric test to assess the probability that each bin's simulated distribution and data arose from the same population. Since for this measurement the mean intrinsic value of β is not of interest, the Brown & Forsythe (1974) test for equal variances, rather than a K-S test, was adopted. In this manner, a probability density function $p(\Delta\beta)$ was created for each of the luminosity bins. By finding the maxima of $p(\Delta\beta)$, and the regions of $\Delta\beta$ enclosing 68% of p, robust measurements for $\langle\Delta\beta\rangle$ and its uncertainty were found. Since the actual subset of simulated galaxies returned is random (in order to approximately populate a Gaussian in intrinsic β), we averaged the best value and uncertainties over multiple realisations at each $\Delta\beta$. The variation in $\langle\Delta\beta\rangle$ between realisations was always much smaller the the error derived from $p(\Delta\beta)$. The results are shown in the second panel of Fig. 5.9, and are in excellent agreement with the first test.

5.5.3 Measuring $\Delta\beta$: maximum-likelihood test

For this final test, simulations were created for a grid of $\Delta\beta$ as before. However in this case, each luminosity bin's data and simulation were binned in β to form histograms with N_B bins spanning $-4 < \beta < 0$. We compared the simulated and actual histograms of β and maximized

$$\mathscr{L} = \prod_{i}^{N_B} \frac{s_i(\Delta\beta, \mu_\beta)^{d_i} \exp[-s_i(\Delta\beta, \mu_\beta)]}{d_i!}, \tag{5.2}$$

where s_i and d_i denote the simulated and actual (data) number of galaxies in the ith bin, and s_i depends on $\Delta\beta$ and the centre of the Gaussian distribution from which the simulation is drawn, μ_β. In each case the normalisation of the histograms was fixed to ensure $\sum_i d_i / \sum_i s_i = 1$, and the central colour μ_β of the simulation was allowed to float and was marginalised over. The simulation realisation was also marginalised out. The maximum-likelihood (ML) results are shown in the third panel of Fig. 5.9, and are in good agreement with both of the previous tests.

5.5.4 Measuring $\Delta\beta$: simulation-free check

The three methods above all rely on image simulations. To avoid complete reliance on these simulations, we repeated the Gaussian assumption test in a simulation-free way. For each luminosity bin, we created z- to H-band observer-frame photometry for test galaxies, all with $\beta = -2$ but using the $M_{\rm UV}$ distribution of the data. Using the median image depths given in Table 5.1, we perturbed the photometry with appropriately scaled Gaussian random numbers. The UV slope was then measured using a simple power-law SED fit to the generated photometry, using the same set of filters as for the data. This process yields a measurement of the expected photometric scatter on β which depends only on the image depths (and an assumed fiducial value of $\beta = -2$). Using equation 5.1 again to compare to the observed data gives excellent agreement with our earlier Gaussian assumption test. These simulation-free results are shown as the + marks in the first panel of Fig. 5.9.

5.5.5 Discovery of significant colour scatter

In all but the faintest bins considered, each test shows significant evidence of intrinsic colour scatter, $\Delta\beta > 0$. To quantify the significance of this, we compared a null hypothesis, where all luminosity bins contain intrinsic colour variation in line with the faintest bin ($\Delta\beta = 0.1$), to an alternative hypothesis, where $\Delta\beta$ grows with luminosity ($\Delta\beta = s \times M_{1500} + c$), motivated by the trend of the ML results. Using a maximum-likelihood estimated linear relation, the likelihood ratio test statistic

$$D = -2\ln\left(\frac{\mathscr{L}(\Delta\beta = 0.1)}{\mathscr{L}_{\rm linear}}\right) \approx 150. \tag{5.3}$$

Since the linear fit has two extra degrees of freedom (s, c), this equates to a significance of $\approx 12\sigma$. We have therefore discovered very significant intrinsic colour variation in our sample of $z \approx 5$ galaxies.

5.5.6 A colour-scatter–magnitude relation?

In all of the tests considered, there is clear evidence for the intrinsic variation in colour being not only non-zero, but increasing at brighter luminosities (just as the average $\langle\beta\rangle$ is redder for brighter galaxy populations). To measure the significance of the trend quantitatively, linear fits, weighted by the uncertainties, were made for both the equal-variance test and the ML test results. These resultant 'colour-scatter–magnitude relations' are shown as the yellow regions in Fig. 5.9. Formally, the slopes of the linear fits differ from 0 by $\approx 4.8\sigma$ and 5.1σ for the equal-variance and ML tests respectively. As discussed in Section 5.3.1 regarding the CMR, removing potential lower-redshift interlopers has negligible effect on these results: in doing so the slopes then differ from 0 by 4.8σ is both tests. As a further test of the significance, we computed a likelihood ratio of two hypotheses: that the colour variation is a constant at all luminosities $\Delta\beta(M) = 0 \times M_{1500} + c = c$, or that it grows with increasing luminosity $\Delta\beta(M) = s \times M_{1500} + c$. Taking the maximum likelihood under each hypothesis, the likelihood ratio test statistic

$$D = -2\ln\left(\frac{\mathscr{L}_{\rm flat}}{\mathscr{L}_{\rm relation}}\right) = 6.7, \tag{5.4}$$

which, with the slope s being one degree of freedom, makes the growing relation more likely than the flat relation at the 2.6σ level. This is a more conservative approach and result than the linear-fit derived significance, but the two approaches are in reasonable agreement. In all cases, the existence of a scatter–magnitude relation is confirmed at better than 2.5σ significance.

5.5.7 Effect of varying signal-to-noise thresholds

The four fields from which our sample has been assembled were treated with different SNR thresholds when selecting galaxies. An obvious concern is that this choice may affect our results. However, we can be confident this is not the case for a number of reasons. Firstly the photometric uncertainty on measuring β does not scale directly with the $z-$band detection threshold, since $\delta\beta$ depends on the noise in all the bands from which β is measured. Second, the simulated galaxies inhabit the same noise as the data, since we injected sources into the real images rather than merely perturbing a photometry catalogue according to some noise parametrization. As such they are subject to the same photometric scattering and SNR cuts as the data, so the comparison of data to simulations is 'fair'. Third, the trend for brighter bins to show more intrinsic scatter is visible within each of the fields, as well as between fields. Finally, if the simulations were systematically

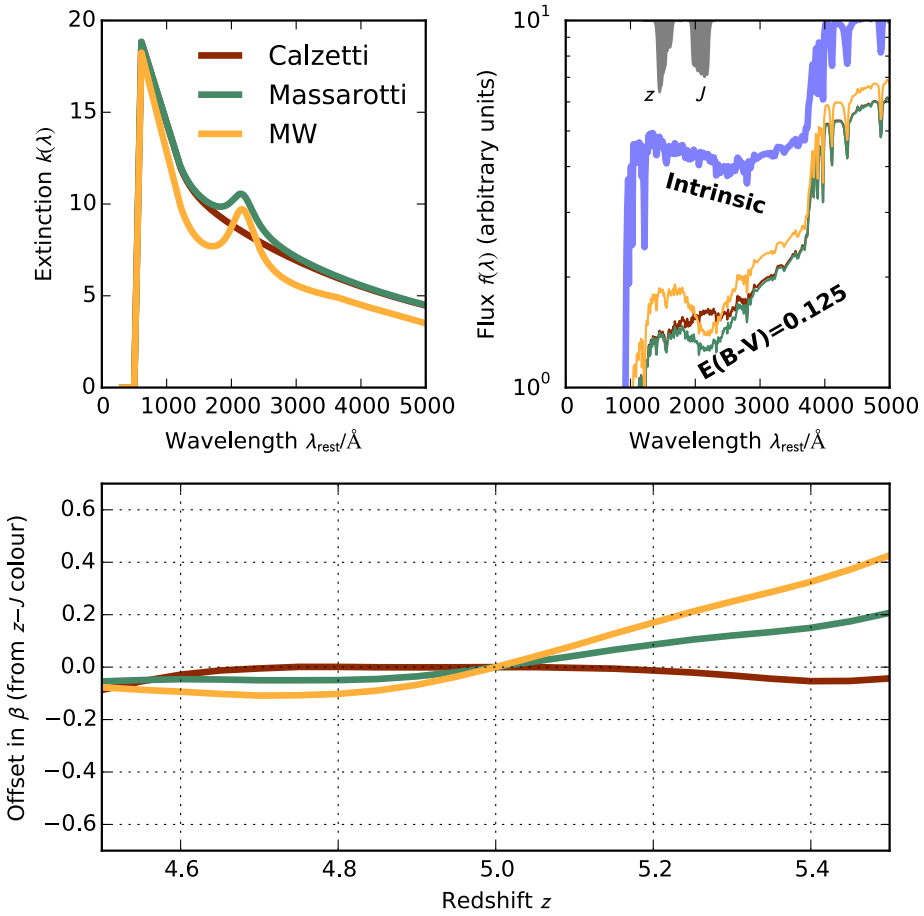

Figure 5.10 The effect of dust-law choice on β. The extinction curves of three dust laws are shown in the top left panel (Calzetti et al. 2000, Massarotti et al. 2001, and a Milky-Way law). Their effect on the UV spectral slope of a young BC03 model is shown in the top-right panel, superposed with the Subaru z and UKIRT J filter profiles. Because the 2175 Å dust bump moves through J in this redshift range, it affects the measurement of β as shown in the lower panel, where the three lines again correspond to the three dust laws.

underestimating $\delta\beta$ then lower-SNR selected fields (i.e. the HUDF) would require more, not less, intrinsic scatter to match the observed distribution than the higher-SNR selected fields.

5.5.8 Simulation stellar population and dust law choices

While other stellar population models could have been chosen for the simulated galaxies, each model having a different mapping between $E(B-V)$, t and β, these would have little effect on the actual photometry for a given β. This is because the rest-frame UV continuum of young star-forming galaxies is in most cases well represented by a power law (Leitherer et al. 1999). The primary exception to this would be the existence of a 2175 Å dust bump in

the UV attenuation curve (e.g. Fitzpatrick & Massa 1986), breaking the otherwise power-law like SED. We have tested the effect such a feature would have on our β measurements by creating photometry for $z \approx 5$ star-burst galaxies using the modified Calzetti dust law of Massarotti et al. (2001), which includes a 2175 Å dust bump of amplitude $\alpha = 0.25$ (calibrated by $z \approx 2$ star-burst galaxies), and for comparison a Milky-Way dust curve which shows a strong bump. At $4.5 < z < 5.5$, the bump (if it exists at these early cosmic times) moves through the J-band. As shown in Fig. 5.10, in the extreme scenario of β being constrained only by a $z-J$ colour (for instance if a galaxy in the UDS sample happened to lie in a particularly shallow region of the H-band image), galaxies having dust attenuation of $A_V = 0.5$ would be measured with a redshift-dependent colour bias of $\delta\beta \leq 0.2$ over the $4.5 < z < 5.5$ interval. Assuming this extreme scenario, the adoption of a Massarotti dust law in place of a Calzetti law in our simulations would have lead to $\Delta\beta \lesssim 0.1$ additional colour-scatter in the simulated galaxies' photometry. In reality, the bias will almost always be less severe: photometry through *HST*'s wider J_{125} filter is less affected by the bump than UKIRT's J band, and the biased $z-J$ colour is always tempered by the use of other bands (Y and H) in the power-law fitting of β. Overall, it is expected that the $\Delta\beta$ results will be affected by dust-law choice by $\lesssim 0.1$.

5.5.9 Comparison to previous works

Estimates of $\Delta\beta$ at $z = 4$ and $z = 5$ have been published by Castellano et al. (2012), Bouwens et al. (2012a) and Wilkins et al. (2011), but each covers only a narrow range of luminosity. The fourth panel of Fig. 5.9 includes these previous estimates alongside our results. Individually the literature results show little evidence of luminosity trends; in particular the trend reverses between the $z = 4$ and $z = 5$ samples of Bouwens et al. (2012a), suggesting that the luminosity dependence of $\Delta\beta$ is poorly constrained in both cases (in line with their suggested uncertainties of ± 0.1). Still, within their errors, the results of Bouwens et al. (2012a) and Castellano et al. (2012) are statistically consistent with our relation.

Unlike the power-law approach of Castellano et al. (2012), Bouwens et al. (2012a) and this work, Wilkins et al. (2011) chose to use a single, short-baseline $z_{850} - Y_{105}$ colour to estimate the UV continuum slope of $z \approx 5$ galaxies. In comparing their results (which were presented in observed colour terms) to ours, a transformation $\beta = 6.21(z_{850} - Y_{105}) - 2$ is required, where the large multiplier on the observed photometry is due to the proximity of the z and Y filters to one another in wavelength. However, doing so assumes, perhaps unreasonably, that the intrinsic variation in the rest-frame [1500 Å]–[1730 Å] colour

traces the variation in the rest-frame [1500 Å]–[2540 Å] colour (approximately the original definition of β by Calzetti et al. (1994) and spanned by $z_{850} - H_{160}$ at $z = 5$). Still, to draw a comparison to the results of Wilkins et al. (2011) we differenced their quoted observed and simulated $z - Y$ colours using equation 5.1 and multiplied the inferred intrinsic colour scatter by 6.21, yielding surprisingly large estimates of $\Delta\beta \approx 0.8$ at $M_{1500} \approx -19.5$. The discrepancy between this result and the other literature values (and ours) can be ascribed to the much larger uncertainty in β provided by the $z-Y$ colour, and the shorter wavelength range it probes. As quantified by Bouwens et al. (2012a) in their appendix B.3, the use of a UV-spanning $z-H$ colour, rather than a z, Y, J, H power-law fit, increases the uncertainty in β by a factor 1.5. The impact is even more dramatic with the narrow $z - Y$ colour: measuring β in this way for our UDF sample yields a standard deviation $\sigma(\beta_{z-Y}) = 1.32$, as opposed to this work's $\sigma(\beta_{\text{power–law}}) = 0.26$. Overall this is unsurprising since, aside from exploiting three additional filters, $\beta_{\text{power–law}}$ is constrained by a wavelength baseline 4.5× longer than that of the $z-Y$ colour. Of course, the simulations of Wilkins et al. (2011) were treated with the same colour measurement as their data, meaning $\Delta\beta$ should still be inferable, albeit with a large uncertainty.

In summary, our relation, which constitutes the first significant measurement of the luminosity dependence of $\Delta\beta$, is not in contention with results from the previous studies which shared our approach to measuring β. Our measured level of colour-scatter (over a wide rest-frame UV baseline) is notably lower than the intrinsic scatter which Wilkins et al. (2011) find using a single $z - Y$ colour, just above the Lyman break. This is due in part to increased uncertainties in their colour, and perhaps also to local variations in the SED at those wavelengths compared to the broader rest-frame UV.

5.5.10 Asymmetric colour scatter

Is the colour–magnitude relation itself merely a product of the scatter–magnitude relation? For this to be true, the scatter must expand in such a way that brighter bins include more red galaxies than fainter bins without many more blue galaxies. Fig. 5.11 offers some evidence that this may be the case. Between the four fields, the 25th percentiles of the observed β distribution grow no bluer ($\beta \approx -2.1$) from the faintest HUDF galaxies to the brightest UDS galaxies. Meanwhile the 75th percentiles redden from $\beta = -1.9 \rightarrow -1.5$. The bluest galaxies are not any bluer in the brightest bins, but the reddest galaxies are much redder. A distribution which grows to the red would be in line with the 'blue-ridge–red-tail' distribution of blue-sequence field galaxies in the $z \lesssim 3$ study of Labbé et al. (2007).

This is perhaps an unsurprising discovery: galaxy formation models predict the dust-free

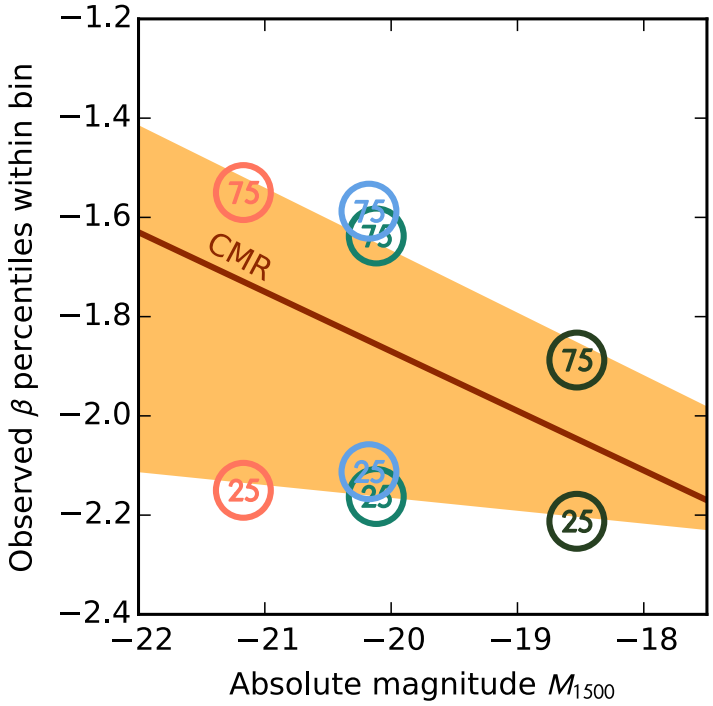

Figure 5.11 The 25th and 75th percentiles of β in each field are shown by coloured circles (marked 25 and 75, respectively). The edges of the shaded region are linear fits to the points, weighted by errors determined via bootstrapping. The region thus denotes a simple measure of how the scatter in β increases to bright luminosities as in Fig. 5.9. Here however, it is clear that while the bluest galaxies are similarly blue at all luminosities, the redder average colours and greater colour scatter at bright M_{1500} are driven by establishing a redder sub-population in the brighter bins. The red line is the average colour-magnitude relation from Fig. 5.5. Otherwise, the field colouring matches that of Fig. 5.8: salmon=UDS, blue=CGS, green=CGN, dark=HUDF.

colours of high-redshift galaxies to follow only a weak luminosity dependence, and be $\beta \gtrsim -2.5$ at $z \approx 5$ (e.g. Wilkins et al. 2013). But with no strict upper limit to their dust reddening, the colour–magnitude relation may simply follow the typical dust reddening at each UV luminosity. In this scenario, the colour–magnitude relation is driven by the increasing fraction, with increasing luminosity, of galaxies which are reddened. Alternatively, the asymmetry may be driven by the ability for more luminous galaxies to harbour somewhat older stellar populations, built up over longer periods of time, than fainter galaxies. In this scenario, UV luminosity traces stellar mass and more massive galaxies are observed at various stages of their star-formation duty cycle: the red wing represents those galaxies with the longest period of quiescence since their last star burst. Less massive galaxies, at the faint end of the CMR, are all currently star forming and do not harbour a significant older stellar population.

5.6 Conclusions

The rest-frame UV colours of high-redshift galaxies provide a probe of the metallicity and dust conditions within which their stellar populations are growing. While recent attention has been focused at $z \geq 7$, moving just 400 Myr later to $z = 5$ has allowed us take a more conservative approach to the detection, selection, and colour analysis of a sample of $z \approx 5$ Lyman-break galaxies. Detected mostly at SNR $> 8\sigma$, and with four or five imaging bands spanning the rest-frame UV, we have been able to robustly determine the UV continuum slope β of each of 584 $z \approx 5$ LBGs (typically to better than $\delta\beta \lesssim 0.4$). Crucially these galaxies span a factor of 100 in luminosity, allowing us to constrain the colour–magnitude relation. Comparing our samples to closely representative image simulations of mock galaxies, we have also disentangled the intrinsic variation in colour at each magnitude from the photometric scatter. Our findings can be summarised as follows.

1. A linear colour–magnitude relation, whereby brighter galaxies are redder than fainter galaxies by $\mathrm{d}\beta/\mathrm{d}M_{\mathrm{UV}} = -0.12 \pm 0.02$ provides a good fit to our data.

2. The data show no convincing evidence either for or against a piecewise-linear relation, whereby galaxies cease to get bluer with decreasing luminosity below some point, as had been suggested elsewhere.

3. For the first time over a wide range of luminosities at high redshift, we have discovered significant (12σ) evidence for *intrinsic colour variation* within the LBG population.

4. This intrinsic colour variation is significantly larger (2.5σ) in high-luminosity bins than low-luminosity bins, after accounting for photometric scatter using our detailed simulations. This result was confirmed by multiple statistical tests, as well as by a final check which was not reliant on our simulations in any way.

5. The luminosity-dependent colour scatter and average colour–magnitude relation appear to be due to the evolution of bright, red galaxies. This appearance of bright, red galaxies coincides with a seemingly luminosity-independent blue floor: in each luminosity bin, the 25th percentiles of colour are always $\beta \approx -2.1$, while the 75th percentiles grow redder from $\beta = -1.9 \rightarrow -1.5$ over $M_{1500} = -18.5 \rightarrow -21.2$.

The rest-frame UV colour β is dependent on all parameters of the stellar population, but is particularly sensitive to light-weighted age and dust attenuation. Our measurements of lower-luminosity galaxies, $\langle\beta(M_{1500} = -18)\rangle \approx -2$, are not so blue as to require dust-free stellar populations. However the lack of intrinsic scatter there ($\Delta\beta < 0.2$) shows

that, if the galaxies are dust reddened, it is by similar amounts for all galaxies in that bin. Similarly the light-weighted ages of galaxies in the faint population must be fairly similar to one another, and < 100 Myr. This can be interpreted as all of those galaxies undergoing intense present or recent star-formation. Comparatively, the average brighter galaxy, with colour $\langle\beta(M_{1500}=-21)\rangle \approx -1.7$, must have built an older stellar population, or have higher metallicity or dust reddening. However at all luminosities a quarter of galaxies have colours bluer than $\beta \lesssim -2.1$, so even at $M_{1500}=-21$ the low reddening, young galaxies remain common.

These observations are consistent with at least two simple scenarios, between which our current observations cannot differentiate: the build up of dust as the galaxy grows and brightens, with some galaxies oriented such that the UV light escapes with less than average reddening; or stochastic star-formation histories, where faint galaxies are always currently star-forming but brighter galaxies are observed during various phases of their star-formation duty cycle. The latter scenario appears less plausible, since stellar and supernova feedback are expected to drive stochasticity in the *least massive*, faintest galaxies (Hopkins et al. 2013), whilst more massive galaxies should form stars more smoothly, following their smooth gas accretion rates (Bouché et al. 2010, Dutton et al. 2010, Papovich et al. 2011).

6 The Balmer-break strengths of $z \approx 5$ galaxies

In this chapter, we investigate whether the colour–magnitude relation which we studied and quantified in Chapter 5 is due primarily to brighter galaxies being older, or dustier, than fainter $z \approx 5$ galaxies. To do so, we use *Spitzer* IRAC [3.6] data to measure the Balmer breaks of a sub-sample of the $z \approx 5$ sample constructed in the previous chapter. This sub-sample was chosen such that the $H-[3.6]$ colours of the galaxies are not contaminated by nebular emission lines, achieved by targeting galaxies in the narrower $5.0 \leq z \leq 5.3$ redshift window. Initially, we find little correlation between the UV slope β and $H-[3.6]$ colours across this sample. We proceed to construct stacked SEDs, based on the average photometry of galaxies in bins of both β and absolute magnitude M_{1500}. From these stacks we fit a suite of stellar population synthesis models to calculate age–magnitude and reddening–magnitude relations. These show that the average reddening increases significantly with increasing UV luminosity (from $E(B-V) = 0$ at $M_{1500} = -17$ to $E(B-V) = 0.2$ at $M_{1500} = -22$), while the average age remains fairly constant at $\lesssim 100$ Myr, tentatively increasing by a factor $\lesssim 2$ over the same luminosity range. Finally, we compare our data in the β–Balmer-break plane to evolutionary tracks of stellar population synthesis models built according to various star-formation histories (SFHs). We find that all smoothly varying SFHs are unable to reproduce galaxies with a combined blue UV slope and red Balmer break. The tentative measurement of some such galaxies in our sample suggests multiple-burst (stochastic) SFHs are required in those cases. The data are consistent with a model whereby $z \approx 5$ galaxies are built by stochastic bursts of star formation, which average out to appear smoothly varying in the most massive, modestly reddened, galaxies.

6.1 Introduction

Over the previous three chapters, we have argued that the rest-frame UV continuum spectral slope β can provide important constraints on the stellar populations of high-redshift galaxies. In particular, a conclusion from Chapter 5 was that there is a mild, but statistically significant, trend for galaxies brighter in the UV to have redder UV continua. With this stand-alone result, we cannot differentiate between the myriad combinations of stellar population parameters which could give rise to the CMR. As we have seen (e.g. Section 1.9.2, Figs. 3.4, 4.9, and 4.11), age, dust, metallicity, and SFH are degenerate as measured by β alone.

Non-degenerate metallicity measurements for typical $z \gtrsim 5$ galaxies may remain out of reach for some time, but both age and SFH can both plausibly be constrained by measurements of the Balmer-break strength. In Section 1.9.4 we detailed how the Balmer break, which is seen as a flux jump at 3646 Å, is strongest for stellar populations formed $10^8 - 10^9$ years prior to observation. It is therefore a reasonable diagnostic of the optical-light-weighted stellar age, and is far less subject to being dominated by newly formed stars than the rest-frame UV.

The situation is slightly confused by the fact that a second spectral feature – the 4000 Å break – is indistinguishable from the Balmer break in broad-band photometry, due to their close wavelength proximty. The 4000 Å break, which is an aggregate effect of many metal absorption lines in stellar atmospheres, increases in size with age steadily, rather than peaking like the Balmer break. Throughout this chapter we refer to the combined, observed spectral feature as the Balmer break, because it is the dominant break for the galaxies of interest here; however its inclusion of the 4000 Å should be remembered.

Prior to *Spitzer*, the technique of measuring the Balmer break to infer the ages of former star bursts had been applied at more moderate redshifts (e.g. Papovich et al. 2001). After *Spitzer*-IRAC (Fazio et al. 2004) photometry became available in 2003, this became feasible for significant samples of $z > 4$ galaxies (Eyles et al. 2005, Yan et al. 2005). Notably, Eyles et al. (2007) found, from a sample of 16 $z \approx 6$ LBGs, that a 'surprisingly large fraction' (40%) of the sample exhibited strong Balmer breaks, indicative of ages in the range 200 – 700 Myr. The inferred ages and formation redshifts of these galaxies is of interest, since they can place constraints on early galaxy formation and on the star-formation rate density in the early Universe – a measurement which is in turn required to understand the drivers of reionization.

6.1.1 Nebular emission line contamination

However, Schaerer & de Barros (2009) argued that many studies have inadequately accounted for the contribution of nebular continuum and line emission to the SEDs. Crucially for high-redshift studies, the impact of emission-line contamination to broad-band photometry becomes stronger by a factor of $1+z$, as measured by the lines' equivalent widths. This, coupled with the high star-formation rates typical of UV-selected high-redshift galaxies, means accounting for flux from emission lines like Hα, Hβ and [OIII] becomes potentially decisive in measuring the ages and masses of these galaxies. For instance, Smit et al. (2014) recently reported the ubiquitous presence of high EW [OIII] and Hβ emission lines amongst bright, gravitationally lensed $6.6 < z < 7.0$ galaxies. They concluded that, if this is not be accounted for, the miscalculation of stellar mass significantly and adversely affects measurements of the sSFR during that epoch. At more moderate redshift, Castellano et al. (2014) recently measured Balmer-break inferred ages of a sample of spectroscopically confirmed $z \approx 3$ LBGs. They accounted for nebular emission contamination by *including* the contribution of nebular emission lines and continuum according to a prescription by Schaerer & de Barros (2009). In this chapter, we take the alternative approach of *avoiding* strong nebular emission lines by targeting a subset of galaxies in our $z \approx 5$ sample (Chapter 5) which fall in a narrow redshift window.

The remainder of this chapter is organised as follows. In Section 6.2 we define a redshift window in which the nebular emission-line free Balmer-break measurements can be made. The details of the sub-sample selection are then given in Section 6.3. In Section 6.4 we investigate the trend between UV slope β and Balmer-break strength. Section 6.5 details the construction of stacked SEDs, which we then fit with stellar population synthesis models in Section 6.6 to derive age–magnitude and reddening–magnitude relations. Finally, we investigate what SFH constraints these data allow in Section 6.8. Our conclusions are summarised in Section 6.9.

6.2 Selecting galaxies free of nebular emission line contamination

Measuring the Balmer-break size requires either a knowledge of the nebular emission line (NEL) strengths, so that their flux contributions can be removed from the observed photometry, or a sample of galaxies from a redshift range where the strong NELs fall outside the relevant filter response windows. The former approach was employed by Eyles et al. (2007), who simply used the Kennicutt (1998) relations to infer an Hα line luminosity from the UV-derived SFR. This approach relies on many assumptions, particularly regarding

how to measure a dust unobscured SFR from the potentially heavily reddened UV.

Fig. 6.1 shows that, for galaxies in a narrow redshift interval $5.0 \leq z \leq 5.3$, the $H-[3.6]$ colour straddles the Balmer break while leaving both anchors of the colour free of line contamination.

In the absence of a large sample of galaxies with spectroscopic redshifts, we have deferred to photometric-redshift estimation to build a sample of galaxies in this window. As a result of the low spectral resolution of broad-band photometry ($R \approx 4$ for the CANDELS GOODS-S catalogue), the probability peaks for photometric-redshift fits derived from the photometry tend to be fairly broad. Consequently, naively selecting galaxies in the narrow contamination-free redshift interval based on their best-fitting photometric redshift is liable to produce an insecure sample. Instead, we have made use of the full $p(z)$ distribution available for each galaxy to calculate the probability that each galaxy lies within the contamination-free window. By integrating the $p(z)$ distribution over the desired redshift interval, we derive a weight for each galaxy,

$$w_{p(z)} = \frac{\int_{5.0}^{5.3} p(z)\mathrm{d}z}{\int_{0}^{7} p(z)\mathrm{d}z}. \tag{6.1}$$

Fig. 6.2 shows an example of this process.

6.3 Sample selection and preparation

We began by revisiting the sample of $4.5 \leq z \leq 5.5$ galaxies from Chapter 5. With a narrower redshift window required for these Balmer-break measurements, we created new $p(z)$ distributions for every galaxy using a more extensive model set: all available ages (up to 1 Gyr) of nine BC03 models with exponentially declining SFHs and sub-solar ($Z = 0.4\ \mathrm{Z}_{\odot}$) metallicity. The SFHs used have e-folding times $0.01 \leq \tau \leq 30$ Gyr, so the quickest and slowest declining are approximately burst and constant SFH models, respectively. The best-fitting redshifts delivered by these models are in good agreement with those used earlier (the 'COSMOS' models of Ilbert et al. 2006), as shown in Fig. 6.3, although in many cases the details of the $p(z)$ distributions differ.

Next, we obtained *Spitzer*-IRAC [3.6]-band photometry for all of the objects where this was readily available.

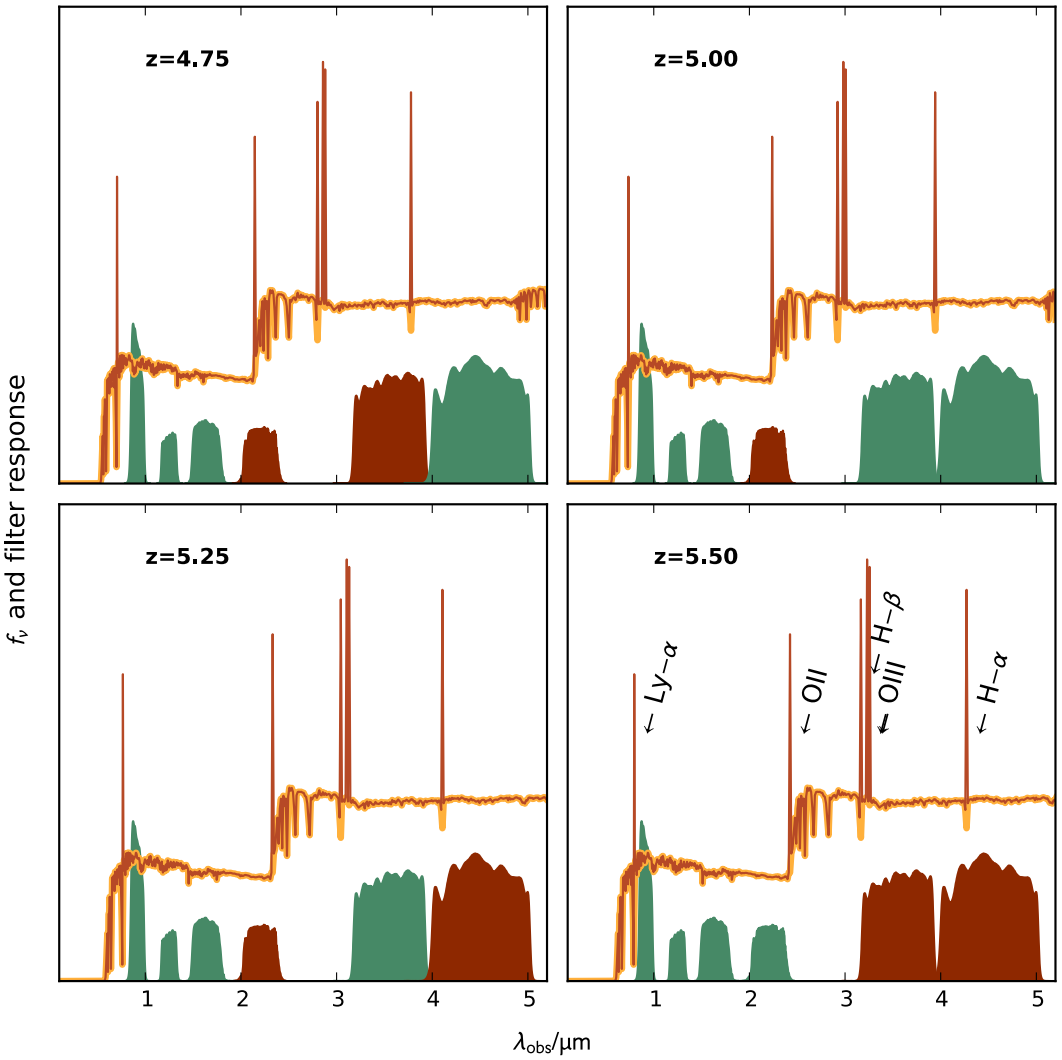

Figure 6.1 The four panels show an SED, with NELs added, at four redshifts $4.75 \leq z \leq 5.50$ as indicated by the labels, in the observer frame. The underlying SED is that of a 50 Myr old BC03 0.2 $Z_{\odot}$ single stellar population, and the NELs considered are those labeled in the lower right panel. The filled regions are the filter response profiles of the Subaru z, UKIRT J, H, K and *Spitzer*-IRAC [3.6] and [4.5] bands, in order of ascending central wavelength. The profiles are coloured red where the region of the SED they probe is contaminated by one of the NELs. In the redshift range $5.0 \leq z \leq 5.3$, both the H and [3.6] bands probe the continuum only, and straddle the Balmer break at $\lambda_{\rm obs} \approx 2.1\,\mu$m.

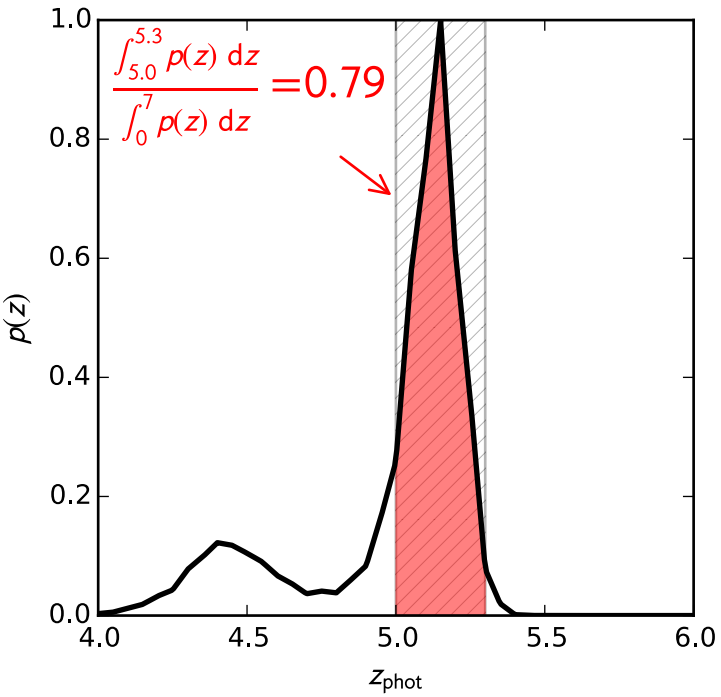

Figure 6.2 An example of how each galaxy's $p(z)$ distribution was used to determine its contribution to the redshift-windowed stacked SED. The black curve is (a portion of) the galaxy's redshift probability distribution $p(z)$. The red region denotes the area under the $p(z)$ curve lying within the redshift window (hatched area) of $4.95 < z < 5.3$: a region where IRAC's [3.6] band is free of NEL contamination. 79% of the overall probability (truncated at $0 < z < 7$) lies within the window, so the galaxy was assigned a weight $w = 0.79$.

CANDELS GOODS-S (CGS)

In CGS, we made use of the CANDELS GOODS-S Multi-Wavelength (CGS-MW) catalogue (Guo et al. 2013), which features template-fitting (TFIT, Laidler et al. 2007, Lee et al. 2012) derived photometry in the U, B, V, i, I, z, Y, J, H, K, [3.6], [4.5], [5.8], [8.0] bands. As discussed in Section 5.2.5, 110 of our 112 CGS galaxies exist in this catalogue (which is H-band selected). To ensure full consistency with the CGS-MW catalogue, the aforementioned $p(z)$ distributions were derived using the photometry from the CGS-MW catalogue in place of our existing photometry. *Spitzer* IRAC photometry was *not* included in the photometric-redshift fits, since we know that these bands will be contaminated by emission lines of unknown strength for many of the objects. As we have seen in Section 5.2.5, photometric redshifts based on this photometry (e.g. Dahlen et al. 2013) are in good agreement with photometric redshifts based on our own aperture photometry.

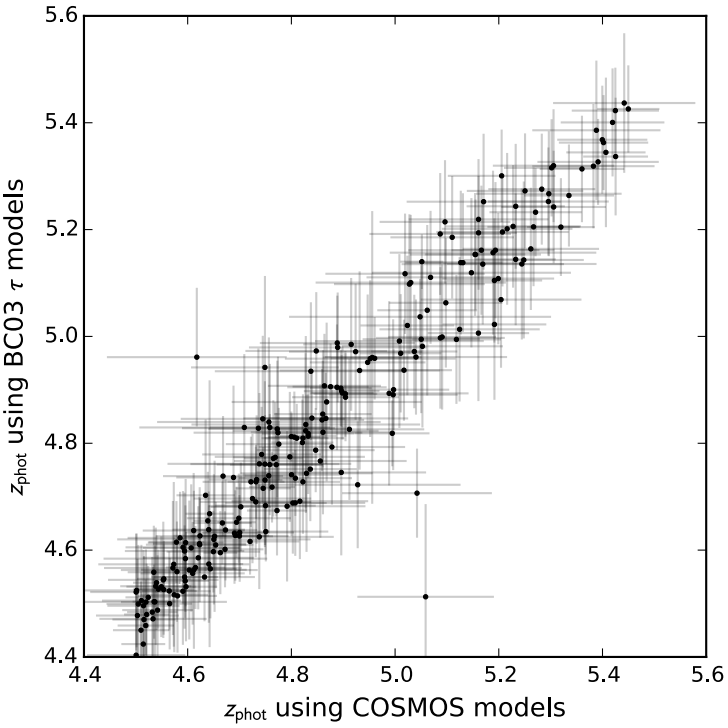

Figure 6.3 A comparison of the photometric redshifts of our 276 purported $z \approx 5$ galaxies in the UDS, as measured using the 'COSMOS' models of Ilbert et al. (2006) (X-axis, see also Section 5.2.4) and a broader suite of BC03 τ models with fixed metallicity $Z = 0.008$ (Y-axis).

Hubble Ultra Deep Field (UDF)

The CGS-MW catalogue (Guo et al. 2013) includes coverage of the UDF, and 29 of our 33 $z \approx 5$ UDF galaxies are present in the catalogue. As with the CGS galaxies, we used the CGS-MW catalogue photometry to re-derive $p(z)$ distributions for each (matched) UDF galaxy as well as to gather consistent IRAC photometry of them.

UKIDSS Ultra Deep Survey (UDS)

For the UDS, we created a new catalogue of *Spitzer*-IRAC photometry using SEXTRACTOR. This was required since the CANDELS UDS Multi-Wavelength catalogue (Galametz et al. 2013a) covers only a small portion of the ground-based UDS from which our sample was initially selected (Section 5.2).

Our UDS IRAC photometry is based on a mosaic with combines data from the *Spitzer* Extended Deep Survey (SEDS; Ashby et al. 2013)[1] and the *Spitzer* UKIDSS Ultra Deep Survey (SpUDS; PI Dunlop)[2]. Identically to the SEXTRACTOR procedure used to derive *B*-

[1] `http://www.cfa.harvard.edu/SEDS/data.html`
[2] `http://irsa.ipac.caltech.edu/data/SPITZER/docs/spitzermission/`

to K-band photometry, the $z'_{\rm new}$ band was again used as the detection image. Circular apertures of diameter 2.8 arcsec were then used on the IRAC image (c.f. 1.8 arcsec for the optical and UKIRT data). These apertures imply that the enclosed flux of a point source needs to be boosted by 0.5 mag to be representative of the point source's total flux. Since this point-source assumption was also made for the ground-based Subaru and UKIRT data, we again apply it here.

Having created our own IRAC photometry, confusion by neighbouring sources also had to be considered separately. We adopted the simple, conservative approach of removing any sources for which aperture photometry would have likely been significantly brightened by the flux contribution of neighbouring sources. To determine this, we assumed that most sources in the field would have flat $H-[3.6]$ colours, and based the confusion calculations on the UKIRT H-band image. (The K-band image, which is closer to [3.6] in wavelength, would have been less reliable for this since it is expected to be contaminated by [OII] emission; if this is bright, neighbouring source confusion would appear less severe in the K band than in the [3.6] band.) The H-band image was convolved, via ASTROPY's CONVOLVE_FFT routine, with a *Spitzer*-IRAC [3.6]-band PSF created by STINYTIM[3]. Circular apertures of diameter 1.8 arcsec and 2.8 arcsec were then placed at the position of each of our 276 $z \approx 5$ galaxies in the H-band image and the convolved H-band image, respectively. After applying enclosed-flux corrections to these photometric measurements, assuming each galaxy is point-like at both UKIRT and IRAC resolution, we computed the flux ratio between the raw and convolved image photometry for each galaxy. Fig. 6.4 shows the distribution of our galaxies in this 'colour': $H_{\rm IRAC-res} - H_{\rm UKIRT-res}$.

Galaxies with nearby, similarly bright neighbours become confused in the IRAC-resolution image and appear brighter as a result. The median offset is -0.18 mag, due both to the average levels of confusion and to the fact that galaxies are more PSF like at IRAC resolution than UKIRT resolution. As shown in Fig. 6.4, the MAD-derived standard deviation is wider on the negative colour side (defined as galaxies which are brighter in the convolved image), due to a long tail of increasingly confused sources. But, as there are no negative-flux sources (other than noise), measuring the breadth of the distribution to the positive side is a good estimate of the noise in this measurement. Based on this σ_+, we calculate that 39 of our galaxies are contaminated by confusion at the 2σ level and remove them from the sample, i.e. we keep sources if

$$H_{\rm IRAC\,resolution} - H_{\rm UKIRT\,resolution} > -2\sigma_+. \tag{6.2}$$

observingprograms/legacy/spuds/

[3]Developed by John Krist, for the Spitzer Science Center.

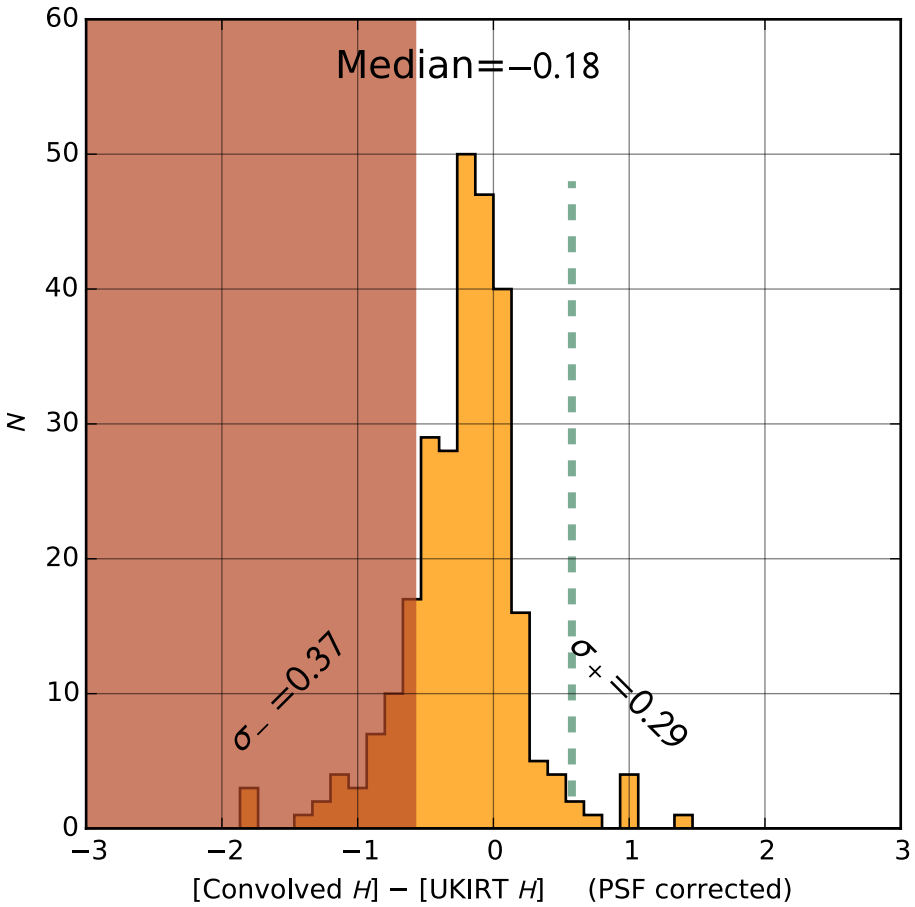

Figure 6.4 The difference in H-band magnitude for aperture photometry of 276 galaxies in the UDS, before and after convolving the UKIRT H-band mosaic with a *Spitzer*-IRAC [3.6]-band PSF. In the pseudo-IRAC mosaic, apertures of diameter 2.8 arcsec were used; in the UKIRT mosaic, 1.8-arcsec diameter apertures were used. In both cases the photometry was corrected from enclosed flux to total, assuming that the galaxies are point sources. There is a systematic offset (as judged by the median colour) toward brighter photometry after convolution, because of the contribution of neighbouring sources. The distribution is also asymmetric: the negative limb is broader than the positive wing ($\sigma_- > \sigma_+$, where the two σs are measured by the Median Absolute Deviation from the median). We consider sources which, after convolution with the IRAC PSF, are brighter by more than $0-2\sigma_+$ to be severely contaminated and remove them from the sample (red region). As a visual aid, the green dashed line marks $0+2\sigma_+$.

The effective level of this cut is probably $< 2\sigma$, since larger galaxies which are marginally resolved in the UKIRT imaging will be offset from zero in this colour. In effect this cut is biased toward deleting more extended galaxies which, combining the colour–magnitude relation and the size–luminosity relation (e.g. Oesch et al. 2010a), might conceivably make it also biased toward deleting redder galaxies. However, both of these relations have such weak dependencies on luminosity that, over the magnitude range populated by our UDS sample, the differential bias is likely to be negligible.

Having removed these confused sources, the median offset between the IRAC-resolution H-band image and the UKIRT-resolution H-band image is reduced to -0.11 mag. We do not correct the IRAC photometry for this apparent remaining offset, since, depending on the wavelength dependence of the morphologies of these galaxies, the real IRAC [3.6]-band image may not be subject to such a large offset.

6.3.1 Weighting by image depth

The optimal measurements of average Balmer-break strengths are obtained by weighting each galaxy's colours according to reliable estimates of their uncertainties. In addition to the uncertainty over whether each source is indeed free of NEL contamination, expressed as $w_{p(z)}$, the signal-to-noise of each flux measurement needs to be incorporated into our calculations. However, weighting by SNR would have an undesirable result: galaxies with [3.6]-band flux contamination from NELs would have a higher than average SNR, and therefore contribute more to the average colours than the uncontaminated measurements. Therefore, we simply weight each galaxy's photometry by its local imaging depth σ, e.g.

$$w_{d(H)} = \frac{1}{\sigma_H^2}, \tag{6.3}$$

where σ is just the flux corresponding to the 1σ limiting magnitude of the image, derived as per Section 5.2.3.

Combining the photometric redshift weight with the image depth weights in the H and [3.6] bands, each galaxy is assigned a combined weight

$$w_{\text{combined}} = w_{p(z)} \times w_{d(H)} \times w_{d([3.6])}, \tag{6.4}$$

which quantifies its contribution to the average results in a robust way.

6.4 Balmer break vs. β trend

Fundamentally, our goal here is to put a constraint on the extent to which the variation in UV colour of $z \approx 5$ galaxies is attributable to dust- and age-related phenomena. To do so, we began by binning our sample by β, and measuring the average Balmer-break strengths via $\langle H-[3.6]\rangle$. To check for dataset-dependent effects, each field was treated separately as in Chapter 5, and not initially combined into a super-sample. For this initial measurement, β was re-calculated for each galaxy from a $z-J$ colour. This simpler measurement of β, which is independent of the H-band flux, was adopted to avoid artificial correlation between β and $H-[3.6]$. The transformation from $z-J$ to β, calculated according to eqn. 3.11, is

$$\beta = 2.91(z_{\rm new} - J) - 2 \tag{6.5}$$

in the UDS, and

$$\beta = 2.83(z_{850} - J_{125}) - 2 \tag{6.6}$$

for *HST* photometry.

In each bin of β, $\langle H-[3.6]\rangle$ was calculated as a weighted average of the constituent galaxy's colours, using $w_{\rm combined}$ for the weights. The error on the $H-[3.6]$ colours was taken to be

$$\delta(H-[3.6]) = 1.09 \times \sqrt{\left(\frac{\delta(f_H)}{f_H}\right)^2 + \left(\frac{\delta(f_{[3.6]})}{f_{[3.6]}}\right)^2}, \tag{6.7}$$

which was used only to calculate weighted error bars for each bin.

Fig. 6.5 shows the resulting $\langle H-[3.6]\rangle - \beta$ distribution. In the figure, bins are only shown if they include a non-negligible fraction of the sample, as determined by the total enclosed weight:

$$\sum_{i,\,\text{in bin}} w_{i,\rm combined} \geq 0.05 \times \sum_{i,\,\text{all}} w_{i,\rm combined}. \tag{6.8}$$

In other words, a single galaxy with a tight $p(z)$ distribution and deep H- and [3.6]-band imaging could populate a bin by itself, as could many less reliable galaxies.

There is no clear trend of $\langle H-[3.6]\rangle$ with β in the range $-3 < \beta < -0.5$. This tentatively suggests that the galaxies with redder UV continuum slopes are not necessarily older than

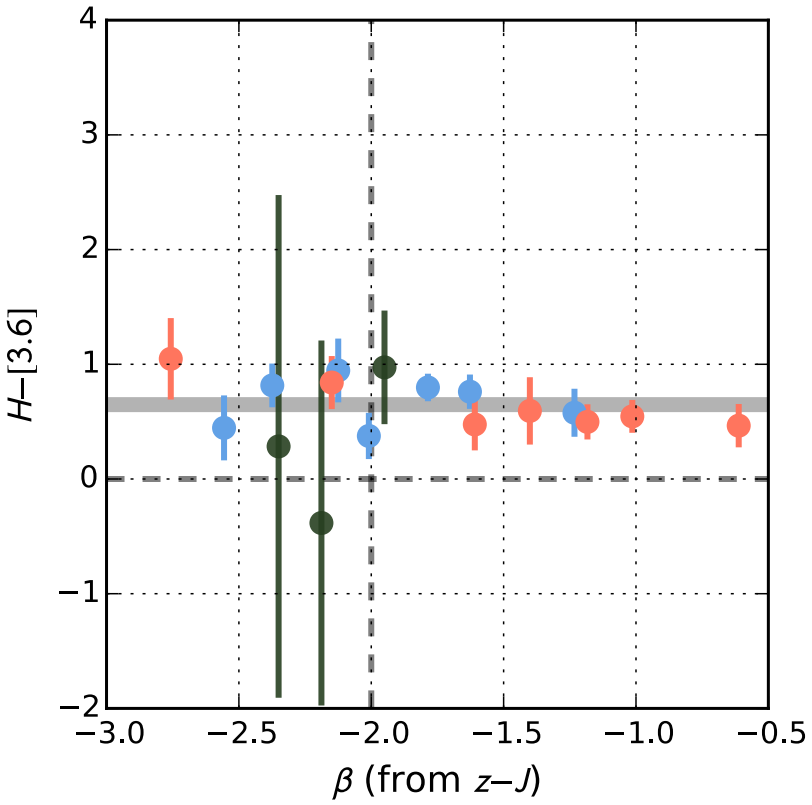

Figure 6.5 The Balmer-break size (here shown by the $H-[3.6]$ colour) of $z \approx 5$ galaxies binned as a function of their rest-frame UV slope β. Here, β is derived from the $z-J$ colour alone, avoiding the use of H-band photometry which would artificially couple the β and $H-[3.6]$ measurements. The dark-green, blue and salmon coloured circles denote samples from the UDF, CANDELS GOODS-S, and the UDS, respectively. In each bin, individual galaxies contribute to the average $\langle H-[3.6]\rangle$ colour according to a weight derived from the probability that they are in a redshift range free of nebular emission line contamination. Bins are only shown if they include more than 5% of the total weight of that sample. Dashed lines mark the colours of a flat-spectrum source, and the thick grey line is the average $\langle H-[3.6]\rangle$ colour across all bins.

the bluer galaxies. However this is not conclusive, since the Balmer break is not a perfect age indicator (especially when the bands used to measure it are so separated in wavelength as H and [3.6]).

To interpret this initial result further, we created synthetic photometry of $z = 5$ galaxies with a variety of stellar populations: two metallicities (solar and one-fifth solar) and three star-formation histories (single burst, exponentially declining, constant) were considered, and LEPHARE was used to generate the photometry through the filter bandpasses of the UDS dataset (the choice of field is arbitrary). For each of those six assumed SFH/metallicity scenarios, BC03 SEDs with various ages and dust-reddening values were included. Fig. 6.6 shows how, under each assumption, the UV slope β and Balmer-break size $H-[3.6]$

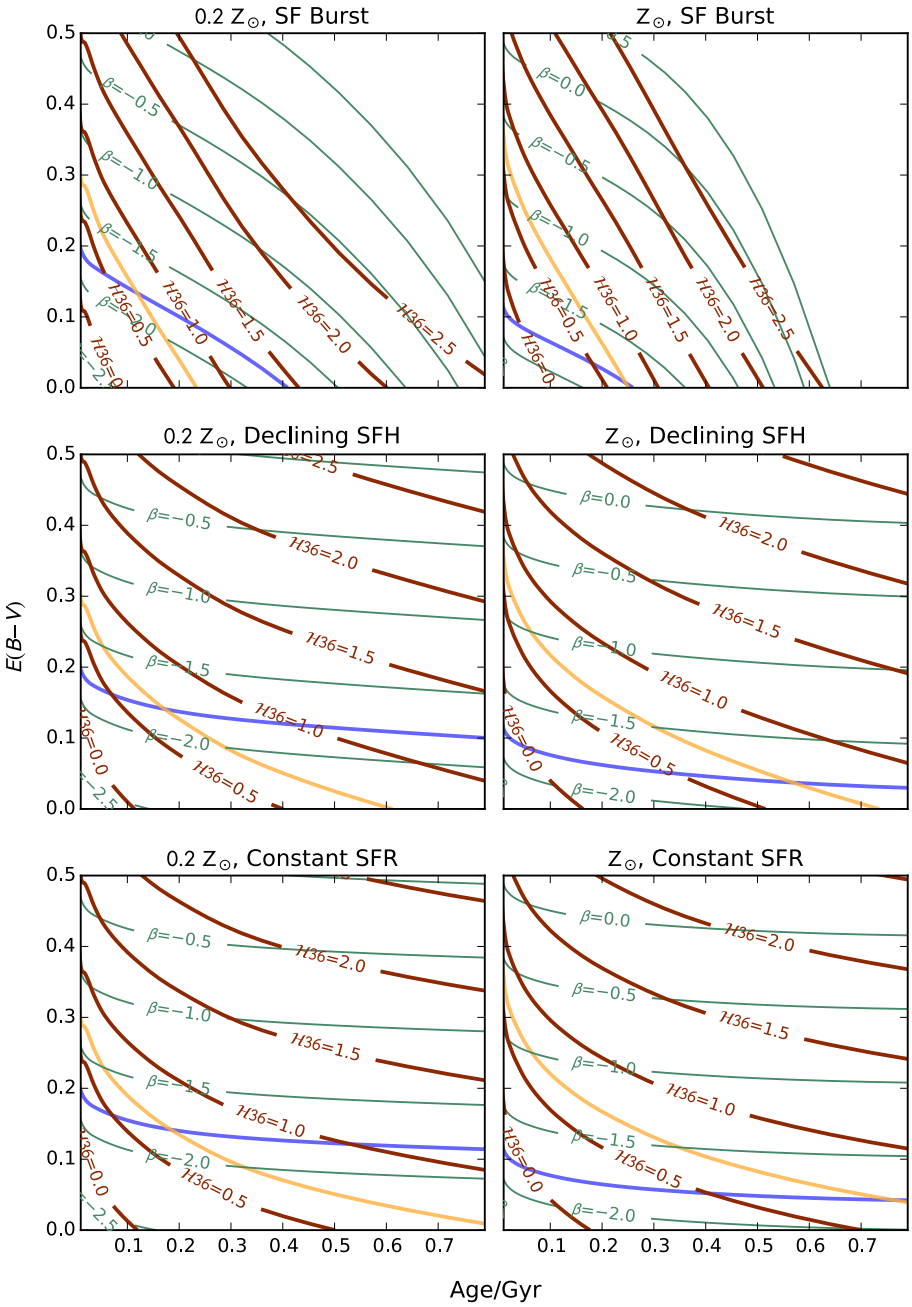

Figure 6.6 How β and the Balmer-break size (here shown as the $\mathscr{H}36 \equiv H - [3.6]$ colour) relate to stellar population age and dust reddening, $E(B-V)$, for two metallicities (columns) and three star-formation histories (SFHs, rows). The three SFHs labeled Burst, Declining and Constant are BC03 'Tau models' with e-folding times $\tau = 0.01$, 1, 30 Gyr respectively. The age axis is truncated at $t = 0.8$ Gyr, the age of a galaxy formed at $z = 12$ and observed at $z = 5$. The labeled green and red contours are iso-lines of β and $H - [3.6]$, respectively. The thicker blue and yellow lines represent the average $\langle\beta\rangle$ and $\langle H - [3.6]\rangle$ colours of our sample of $5.0 \leq z \leq 5.3$ galaxies. The intersection of those two lines represents the best estimate of the age and dust reddening of the galaxy population, under each panel's SFH and metallicity assumptions.

depend on stellar population age and dust reddening. Since, in age–dust parameter space, the contours of β are not parallel to those of $H-[3.6]$, the age–dust degeneracy can in principle be broken – at least within some assumed SFH and metallicity regime. Fig. 6.6 also shows the luminosity-independent *average* $\langle\beta\rangle$ and $\langle H-[3.6]\rangle$ values of our entire sample as additional contours: $\langle\beta\rangle = -1.8$, and $\langle H-[3.6]\rangle = 0.65 \pm 0.07$ (weighted mean and standard error on the mean). Within all of the assumed scenarios, the intersections of those contours agree that the dust reddening $E(B-V) \leq 0.15$ (with a Calzetti dust law). This is a slightly stronger conclusion than the UV slope alone allows ($E(B-V) \leq 0.2$), thanks to the Balmer-break measurement insisting that some of the redness of the UV slope be attributed to non-zero age.

The age itself is still poorly constrained, since each assumed scenario yields very different colours at the same age; however a lower bound of 150 Myr is suggested for the average galaxy in our sample. In no case does the inferred average age of the galaxies exceed that of the Universe – a situation which would have allowed us to attempt to constrain the metallicity or star-formation histories themselves.

There is a notable dust–metallicity degeneracy in these results: assuming solar metallicity models yields lower inferred reddening values for our sample (since the UV is redder, at the same age, in a higher-metallicity stellar population). The inferred ages also tend to be older in the higher-metallicity scenario; but this is complicated by the SFH dependency. If the stellar population forms in a single burst, a higher-metallicity population grows a Balmer break more quickly than a sub-solar metallicity model; however, models with constant or smoothly declining SFHs require a *longer* time to build up the same Balmer-break size in a higher-metallicity environment. This is because the UV light – which is dominated by the presently forming stars – is redder in a higher-metallicity galaxy if star formation continues beyond $t = 0$. With the optical light less affected than the UV, the UV—optical colour is in turn less red.

In summary, combining β measurements with Balmer-break measurements has allowed us to partially break the age–dust degeneracy, although further degeneracies due to metallicities and SFHs remain.

6.5 Stacked SEDs

As a further approach to breaking the age–dust degeneracy, we created stacked SEDs of our galaxies and measured their properties via spectral synthesis model fitting. We again made use of the weights, w_{combined}, to derive stacked SEDs free of NEL contamination. Binned

by similarity of UV continuum slope, four stacked SEDs were made from the galaxies in the UDS, four more from CGS, and three from the UDF. A further four, four and three stacks were made from the UDS, CGS and UDF samples, respectively, binned instead by similarity of absolute UV magnitude M_{1500}. For each stack, the constituent galaxies were normalised to their median z-band magnitude prior to averaging the photometry in each band.

These 22 stacked SEDs are shown in Figs. 6.7, 6.8 and 6.9. Inset in each figure is the $H-[3.6]$ colour of the stacks, and best-fitting BC03 models (at fixed redshift $z = 5.1$) are also shown. These models were fitted only above the Lyman break of the SED, since the galaxies are at slightly different redshifts from one another. In all cases, a BC03 model provides an excellent representation of the data, including the Balmer break, without any NEL contributions being added to the model. The BC03 models were also derived at only a single metallicity, $Z = 0.5\,\mathrm{Z}_{\odot}$, avoiding the age–metallicity degeneracy discussed above.

Only in the UDS stacks is there any obvious trend: there, galaxies which are redder in β are also redder (i.e. have larger) Balmer breaks. This finding is not apparent in either the UDF or CGS data, however. Since the UDS galaxies are the brightest, this may indicate a luminosity-dependent effect.

6.6 Stellar population parameters derived from the stacked SEDs

Based on the model fits to each stacked SED, Fig. 6.10 shows how the stacks' ages and dust reddening measurements depend on absolute UV magnitude. These two trends seek to explain the colour–magnitude relation in terms of physical parameters. The ages of models fitted to the brighter SED stacks are not significantly older than those fitted to the fainter SED stacks. The slope of the 'age–magnitude' relation is $\mathrm{d}t/\mathrm{d}M = (-8 \pm 6)$ Myr (1.4σ). The 'dust–magnitude' relation is more significant: $\mathrm{d}E(B-V)/\mathrm{d}M = (-0.031 \pm 0.007)$ Myr (4.1σ).

Together, these results are evidence that the colour–magnitude relation at $z \approx 5$ is caused by brighter galaxies being more reddened than their fainter counterparts (on average).

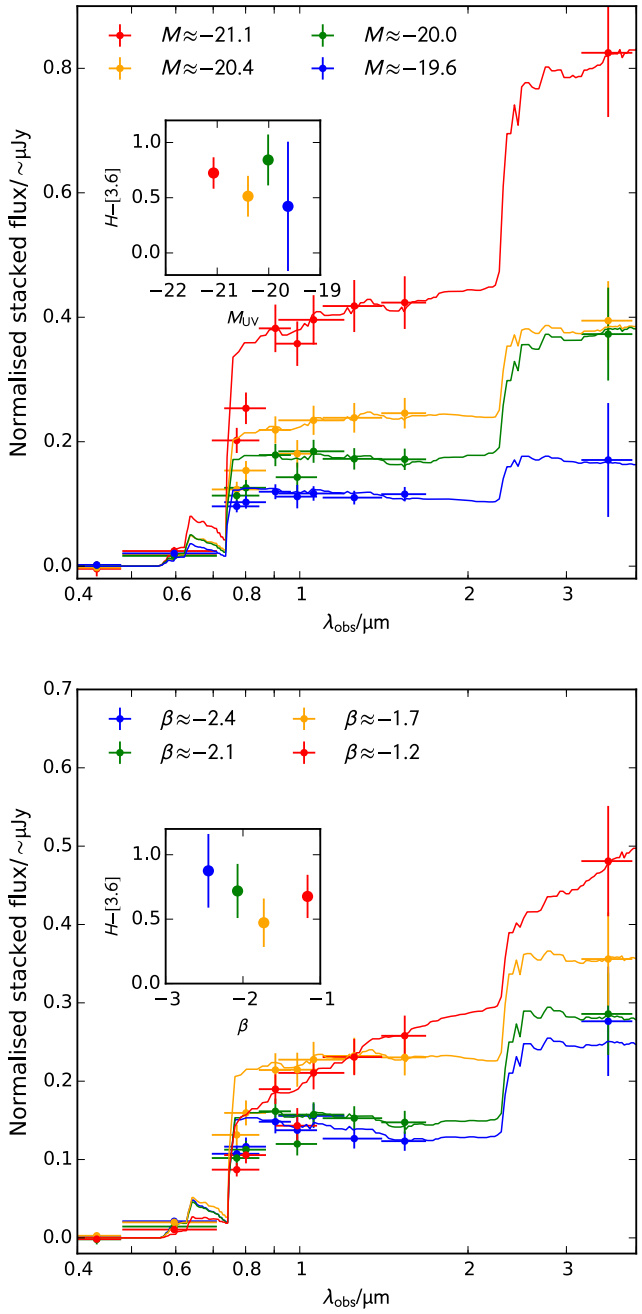

Figure 6.7 In each panel, the four SEDs are weighted stacks of the photometry of galaxies in GOODS-S, while the lines are the best-fitting BC03 model to each. In the *upper* panel, each SED is derived from the photometry of galaxies with similar absolute UV magnitude, as indicated by the legend; in the *lower* panel, the stacks are based on galaxies of similar UV colour β. The stacks are weighted such that they have optimal signal-to-noise, and galaxies contribute according to the probability that they are in a redshift range free of nebular emission line contamination. The insets, which show colours derived from the four stacked SEDs, show that there is no obvious trend of the Balmer-break size ($H-[3.6]$) with absolute magnitude or β.

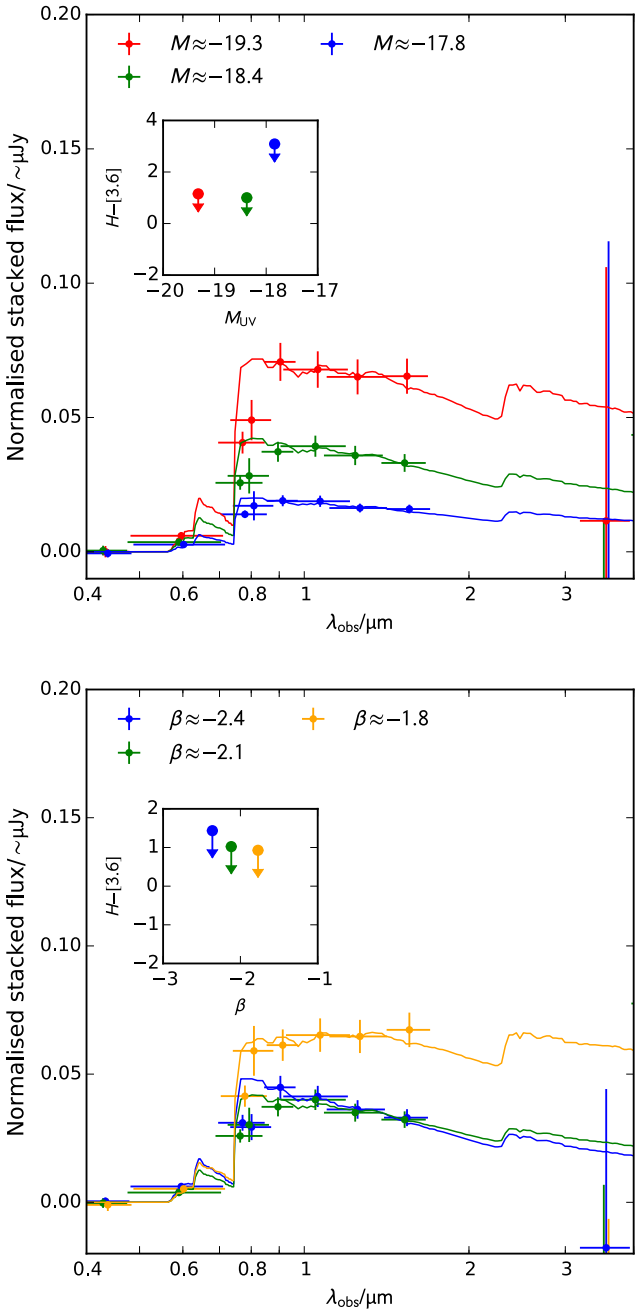

Figure 6.8 In each panel, the three SEDs are weighted stacks of the photometry of galaxies in the UDF, while the lines are the best-fitting BC03 model to each. In the *upper* panel, each SED is derived from the photometry of galaxies with similar absolute UV magnitude, as indicated by the legend; in the *lower* panel, the stacks are based on galaxies of similar UV colour β. The stacks are weighted such that they have optimal signal-to-noise, and galaxies contribute according to the probability that they are in a redshift range free of nebular emission line contamination. The insets, which show colours derived from the three stacked SEDs, show that there is no obvious trend of the Balmer-break size ($H-[3.6]$) with absolute magnitude or β; arrows mark 2σ upper limits where there was a negative, or very low significance, flux in the [3.6] band.

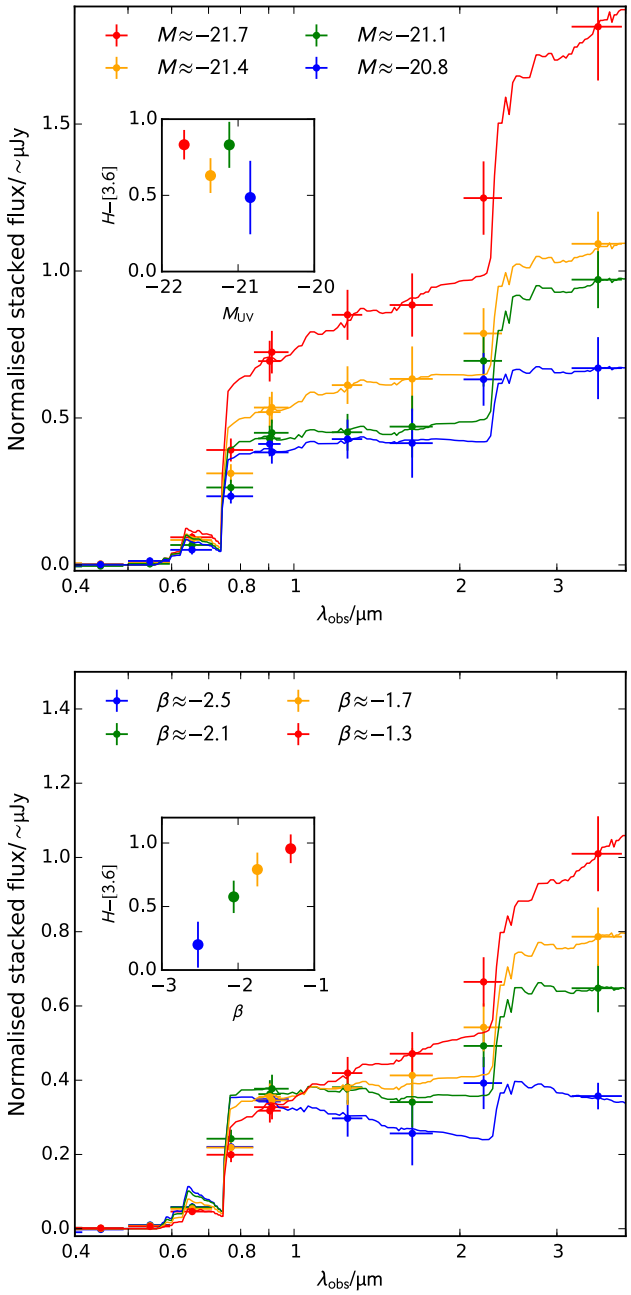

Figure 6.9 In each panel, the four SEDs are weighted stacks of the photometry of galaxies in the UDS, while the lines are the best-fitting BC03 model to each. In the *upper* panel, each SED is derived from the photometry of galaxies with similar absolute UV magnitude, as indicated by the legend; in the *lower* panel, the stacks are based on galaxies of similar UV colour β. The stacks are weighted such that they have optimal signal-to-noise, and galaxies contribute according to the probability that they are in a redshift range free of nebular emission line contamination. The insets, which show colours derived from the four stacked SEDs, show that there is no obvious trend of the Balmer-break size ($H-[3.6]$) with absolute magnitude. Unlike the results from the other fields (Figs. 6.7, 6.8), these data suggest that galaxies which are redder in β are also redder in $H-[3.6]$.

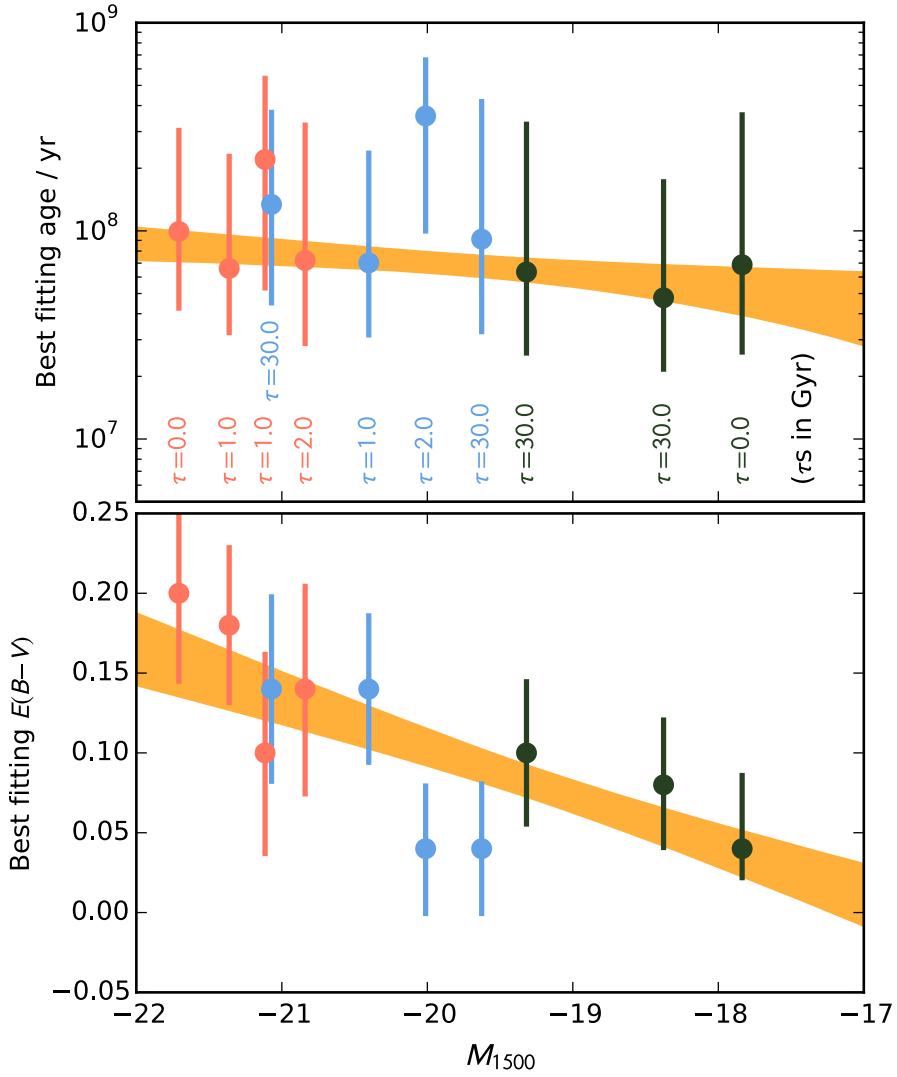

Figure 6.10 The best-fitting stellar population age (*upper* panel) and dust reddening $E(B-V)$ (*lower* panel) of stacked SEDs, each derived from galaxies of similar absolute magnitude. The stacks are those shown in Figs. 6.7, 6.8, 6.9, and the stellar population parameters are found by fitting a suite of BC03 models, with half-solar metallicity and declining star-formation histories 10 Myr$\leq \tau \leq$30 Gyr. There is little correlation between best-fitting age and M_{1500}: brighter galaxies are not found to be significantly older than fainter galaxies. There is however significant correlation between luminosity and dust reddening: the stacked SEDs based on brighter galaxies have stronger dust extinction. The text labels in the upper panel show each best-fitting model's star-formation history, as the e-folding time in Gyr. In all cases, the extinction law is a Calzetti law. The dark-green, blue and salmon colouring denotes stacks of galaxies found in the UDF, GOODS-S (CGS) and the UDS, respectively. The yellow regions show linear fits to each relation and their 1σ confidence intervals.

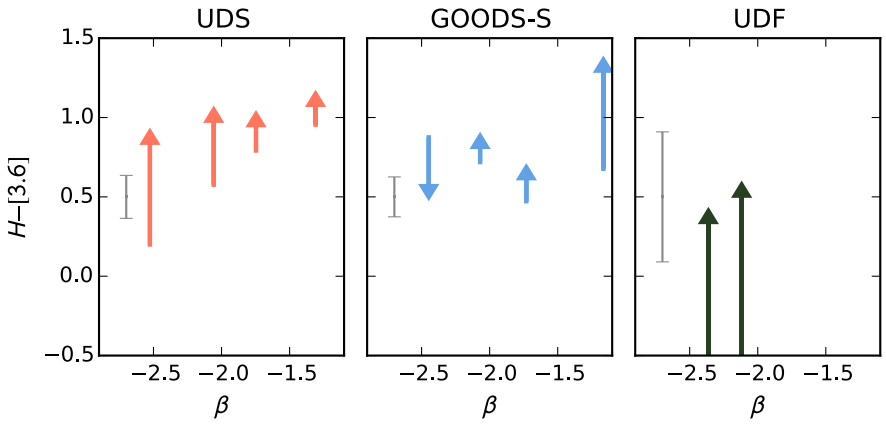

Figure 6.11 A simple check of nebular emission line contamination in the supposedly uncontaminated sample. Stacks, like those described in Section 6.5 but weighed toward galaxies with photometric redshifts $4.5 \leq z_{\rm phot} < 5$, should have contamination from the Hα emission line in the *Spitzer* IRAC [3.6] µm band. In each panel (corresponding to each field as labelled), stacks were created in this manner and their $H-[3.6]$ 'Balmer-break' colours compared to those in the emission-line free redshift range. Here we consider stacks in bins of β only. Arrows then show the change in $H-[3.6]$ moving from emission-line free stacks to Hα-contaminated stacks, i.e. the impact of Hα emission on the colour. In most cases, as expected, Hα reddens the $H-[3.6]$ colour. The grey error bar in each plot is a guide to the uncertainty on the individual colour measurements, derived from the stacks. The GOODS-S points which seem to get bluer with Hα contamination change by only $\approx 1\sigma$. In the UDF, the stacks showed no [3.6] detections until we moved to the lower-redshift, contaminated regime. Hence, the arrows are simply drawn from the bottom of the plot. The reddest (in the UV) UDF stack still shows no detection in [3.6], even with Hα contamination, so is omitted.

6.7 Nebular emission line contamination check

The stacked SEDs discussed above were explicitly designed to avoid the $H-[3.6]$ colour being contaminated by NELs. In particular, the lower-redshift edge of the selection window ($z > 5$) was chosen to avoid Hα contributing to the [3.6]-band flux (see Fig. 6.1). De-tuning this selection window should then yield stacked SEDs *with* contamination. As a simple sanity check, we created stacked SEDs according to such a de-tuned selection. In this case, each galaxy was assigned a weight derived from the integral of $p(z)$ in the redshift range $4.5 \leq z < 5.0$.

Fig. 6.11 shows that these stacks, in which the [3.6] photometry should be contaminated by Hα emission if present, mostly have significantly redder $H-[3.6]$ colours than the emission-line free stacks. This fact serves as evidence that our emission-line free selection procedure has been at least partially successful in producing a sample with continuum-only Balmer-break photometry. In principle, the differences between these two sets of stacked SEDs could be used to constrain the strength of Hα emission in these galaxies, but that is beyond the scope of this work.

6.8 Star-formation history constraints

Stellar population ages derived from broad-band SED fitting are inexorably linked to the star-formation history assumed/fitted. Moreover, the age evolution differs for different rest-frame wavelengths. Here, we explore what constraints can be placed on the SFHs of our galaxy sample by comparing the observed β and Balmer-break colours to evolutionary tracks built according to various SFHs.

As we have seen, some evidence suggests that high-redshift galaxies have SFRs which, on average, do not decline over time (e.g. Papovich et al. 2011). While some galaxy evolution models suggest that SFHs should be smoothly rising (Finlator et al. 2011), there is as yet no observational constraint to the stochasticity of high-redshift LBGs' SFHs.

For convenience and consistency with the literature, in this chapter we have thus far assumed SFHs which decrease, or at most remain constant, with time. In Fig. 6.12 we compare two further suites of SFHs to the β and $H-[3.6]$ measurements from our 11 β-binned SED stacks. The first suite of models are exponentially increasing SFH models, as described in Section 2.3.6, with a seed mass $M_0 = 10^6$ M$_\odot$. The second suite are two-component burst models, where an initial burst of SF is followed $t_{\rm delay}$ Myr later by a secondary burst of the same mass, where $10 \leq t_{\rm delay} \leq 500$ Myr. The latter set of models provide colours in an otherwise inaccessible region of parameter space, where $\beta < -2.3$ and $H-[3.6] > 0$, by allowing an early burst of SF to build a Balmer break but keeping the UV continuum blue with a secondary, more recent epoch of SF.

From each of the three fields shown in Fig. 6.12, we find a subset of galaxies with blue UV colours $\beta < -2.3$ but non-neglible Balmer breaks $H-[3.6] > 0$. The colours of galaxies in those bins cannot be reproduced by any of the smoothly varying SFH models: too fast a rise in SFR and the Balmer break is always outshone by recent SF; too slow a rise (or a decrease) in SFR and the UV is too red by the time a Balmer break forms. The two-component burst models, which represent the simplest form of SFH stochasticity, provide a solution. In this scenario, a galaxy might be observed 500 Myr after an initial epoch of SF, but only 10 Myr after a secondary epoch. The initial stellar population has built a substantial Balmer break, while the second round of SF provides the blue UV.

These (minimally) stochastic SFHs clearly provide a preferable fit for galaxies with blue β but red $H-[3.6]$. However they are not formally *required*: the relevant bin from the UDF data is an upper limit, and the UDS and CGS bins lie only $\approx 2\sigma$ away from the model tracks constructed assuming smoothly varying SFHs. Still, these data and models have provided a plausible suggestion of stochasticity in the build-up of stellar populations at $z \approx 5$.

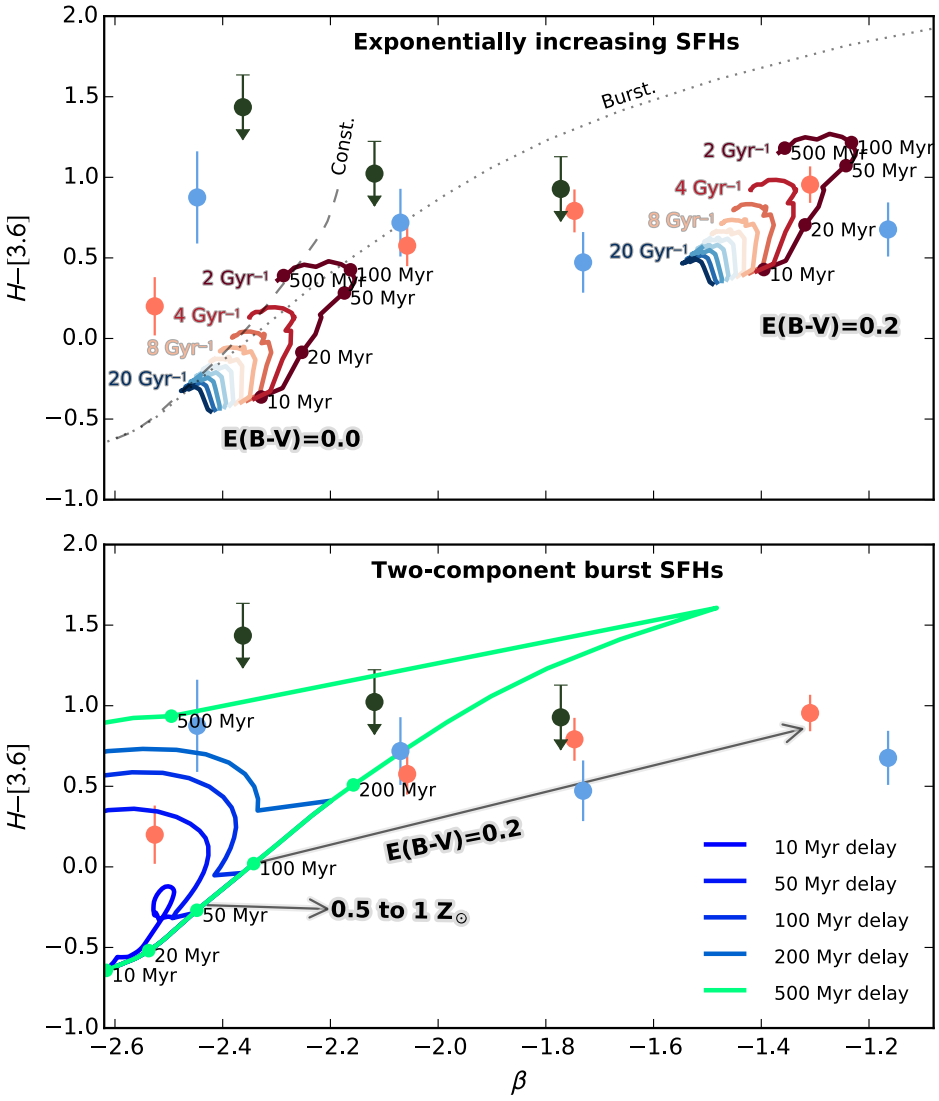

Figure 6.12 A comparison of evolutionary tracks for stellar populations built according to various star-formation histories (SFHs) to the β and $H-[3.6]$ colours of our stacked $z \approx 5$ galaxies. The salmon, green, and blue data points with error bars are the β-binned stacks from the UDS, UDF, and CGS, respectively. In the *upper panel*, the red→blue coloured tracks are exponentially increasing SFH BC03 models, all with half-solar metallicity. The two groups are for $E(B-V) = 0$ and $E(B-V) = 0.2$, as indicated by the labels and assuming a Calzetti dust law. For further comparison, the dashed and dotted lines show the (dustless) tracks of the same stellar population built with a constant SFH or in a single burst, respectively. In the *lower panel*, the blue→green coloured tracks are two-component burst models, again with half-solar metallicity. The two arrows indicate reddening and metallicity vectors as labelled, both of which affect β more than $H-[3.6]$. The data points with blue β but high $H-[3.6]$ are tentatively inconsistent with SFHs which grow monotonically, even with dust or metallicity changes. An older stellar population is required to build the Balmer breaks, combined with a younger component to give a blue rest-frame UV. These colours are plausibly provided by simple two-component, variable-delay, SFHs.

6.9 Conclusions

In this chapter, we have studied the Balmer-break strengths of a sample of $5 \leq z \leq 5.3$ galaxies, which fall in a redshift range such that their $H-[3.6]$ colours measure the Balmer break without contamination by nebular emission lines. Our conclusions can be summarised as follows.

1. We have found no ubiquitous evidence for a trend between galaxy UV continuum colours β and their Balmer-break strengths.

2. By constructing stacked SEDs (including the Balmer break) in bins of absolute UV magnitude, to which stellar population synthesis models were fitted, we derived age–magnitude and reddening–magnitude relations to parallel the β–magnitude relation discovered in Chapter 5.

3. The age–magnitude relation is consistent with being flat; $M_{1500} = -22$ galaxies are at most a factor of two older than $M_{1500} = -17$ galaxies, and consistently ~ 100 Myr.

4. The reddening–magnitude relation has a significant slope; dust reddening increases from $E(B-V) = 0$ to $E(B-V) = 0.2$ over the luminosity range $M_{1500} = -17$ to $M_{1500} = -22$.

5. Most of our stacked SEDs can be explained by this simple, modest, increase in dust reddening. However, the tentative detection of a population of blue β, red Balmer-break galaxies challenges the assumption of smoothly varying star-formation histories. These galaxies are well represented by stellar populations formed in multiple episodes, suggestive of stochastic SFHs.

Overall, the results of this and the previous chapter suggest a physical scenario in which $z \approx 5$ LBGs build their stellar population in an episodic manner. As they do so, they build up greater dust shields, increasing the observed UV reddening. In the faintest (bluest UV) galaxies, the episodes of star formation are apparent: their rest-frame UV colours (sensitive to the prior $\approx$100 Myr of SF) are decoupled from their optical Balmer-break colours (sensitive to $200-1000$ Myr old stars), such that stellar population synthesis models only reproduce these colours if they are formed episodically. In the brightest (reddest UV) galaxies, the episodes are more numerous within each galaxy, and, provided the UV 'reacts' according to some non-zero time-scale, average out to appear consistent with the smoothly varying star-formation histories predicted by galaxy-formation models (e.g. Finlator et al. 2011).

7 Conclusions and future work

In this thesis, we have studied the rest-frame UV and optical colours of galaxies at $4.5 \leq z \leq 8.5$, corresponding to the first ≈ 1.5 Gyr of cosmic history. After developing an unbiased method of measuring the UV continuum spectral slope of these galaxies in Chapter 3, we studied the UV properties of these galaxies in Chapters 4 and 5. These data show that even at $z \approx 8$, the typical star-forming galaxies selected as Lyman break galaxies (LBGs) harbour partially metal-enriched, or modestly reddened, stellar populations. At $z \approx 5$, where we are able to better constrain these UV colours, a mild colour–magnitude relation is evident, whereby galaxies with brighter UV luminosities have mildly, but significantly, redder UV continua. We also discovered a 'scatter–magnitude' relation, whereby brighter luminosity bins hold galaxies with more intrinsically varied colours. In Chapter 6, we combined these results with *Spitzer* IRAC data to measure the Balmer-break strength of these galaxies. This showed that brighter $z \approx 5$ galaxies hold only marginally older stellar populations, but are significantly more dust reddened, than fainter galaxies. In this concluding chapter, we endeavour to form a consistent physical picture for the build up of stars and dust during this early epoch of galaxy evolution.

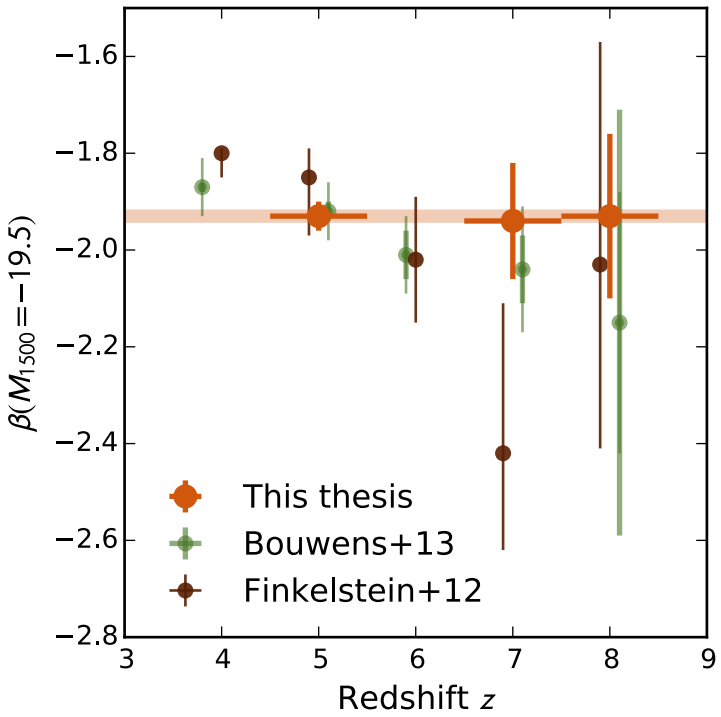

Figure 7.1 Large orange circles denote our measurements of the rest-frame UV spectral slope β at fixed absolute UV luminosity $M_{1500} = -19.5$, at redshifts $z \approx 5$ and $z \approx 7,8$ from Chapters 5 and 4 respectively. The data show no sign of colour evolution at fixed luminosity: $\beta \approx -1.93$ in all cases. This is in contrast to reports by other authors: both Finkelstein et al. (2012b) and Bouwens et al. (2013) report evolution in β with redshift. However, the agreement is reasonable at $z \approx 5$, and, as was discussed in Chapter 4, the tension at $z \approx 7$ has now lessened from the wide disparity of initial studies. It now seems clear that any trend in β with redshift at $z \gtrsim 5$ must be fairly weak.

7.1 The redshift dependence of β

In Chapter 4 we determined the UV continuum slope β at $z \approx 7$ and 8, and in Chapter 5 we did so at $z \approx 5$. Combining these measurements at fixed luminosity $M_{1500} = -19.5$ ($\approx 0.7\,L_*$ at $z = 7$, McLure et al. 2013) reveals no evidence for evolution in β over the 500 Myr separating $z = 8$ and $z = 5$. This is perhaps unsurprising: if the rest-frame UV is always linked to the past 100 Myr of star formation (e.g. Kennicutt 1998), and all UV-selected LBGs have been recently star forming, one would not predict a great deal of change over a relatively short span of cosmic time. However, in Fig. 7.1 we compare this apparent lack of evolution to the results of other recent reports in the literature. Within the associated uncertainties, it remains unclear whether there is strong tension here: both Bouwens et al. (2013) and Finkelstein et al. (2012b) report redder UV colours, at fixed luminosity, for lower-redshift galaxies (still at $z > 4$), a result we do not reproduce. In general, it appears that any evolution in β is fairly weak over this redshift range.

This physical situation may however be clarified by several further studies. The particular fascination with the steep UV continua of low-luminosity $z \approx 7$ LBGs (e.g. Bouwens et al. 2010) arose because $\beta \lesssim -3$ implied the possible presence of metal-free stars. The *James Webb Space Telescope (JWST)* will allow much improved constraints to be placed on the presence of Population-III stars at these redshifts. Evidence for these is likely to be sought from both the He II ($\lambda_{\rm rest} = 1640$ Å) emission line (Schaerer 2003) and other nebular emission-line fluxes (e.g. Hα, Schaerer 2002). The former is thought to be a key indicator of Population-III stars, and may have equivalent width $W_0 \approx 120$ Å, making it potentially observable with future spectroscopy (currently, the Lyman$-\alpha$ emission line is observed at $z \approx 6$ with $W_0 \lesssim 50$ Å, e.g. Stark et al. 2011). Even less extreme colours of $\beta < -2.5$ still suggest very young stellar populations. As we have seen, Balmer-break measurements can help to constrain stellar population ages when combined with β measurements, so extending this combined approach to other redshifts will be beneficial.

7.2 Balmer breaks measurements in additional redshift bins

One conclusion of Chapter 6 was that the $z \approx 5$ colour–magnitude relation is driven by brighter galaxies being more dust reddened. It has been suggested (e.g. Labbé et al. 2007) that this should be the case at fixed redshift, while age evolution should drive the colour–magnitude relation to be offset toward redder colours at lower redshift. We have found that the intercept of the rest-frame UV CMR does not strongly evolve with decreasing redshift $z = 8 \rightarrow 5$; however, depending on the average SFH and therefore the degree to which the rest-frame UV can probe any past star formation, the average galaxy age may still increase in a way measurable via the Balmer break.

Fig. 7.2 gives a speculative outcome of such a study, and illustrates its use in constraining the early evolution of LBGs. The method we implemented at $z \approx 5$ (Chapter 6) could be directly extended to $z \approx 4$, where there is a window at $3.95 < z < 4.40$ in which the $H-K$ colour spans the Balmer break without being contaminated by nebular emission lines. In this case, the ESO GOODS/CDF-S Spectroscopy master catalogue lists 42 spectroscopically confirmed galaxies in the GOODS-S field alone, making the process less reliant on photometric redshift solutions. Matching these 42 galaxies to the CANDELS multi-wavelength catalogue of Guo et al. (2013) yields 29 matches with average $H-K$ colours ≈ 0.4, tentatively suggesting a *decrease* in Balmer-break size from $z \approx 5$. If borne out by a further study, this would, for example, be consistent with galaxies at this later epoch having undergone more sustained recent star formation than our $z \approx 5$ sample. This is, however, potentially complicated since a spectroscopic sample is likely biased toward strong Lyman$-\alpha$ emitters, which are not necessarily representative of the broader LBG population studied here.

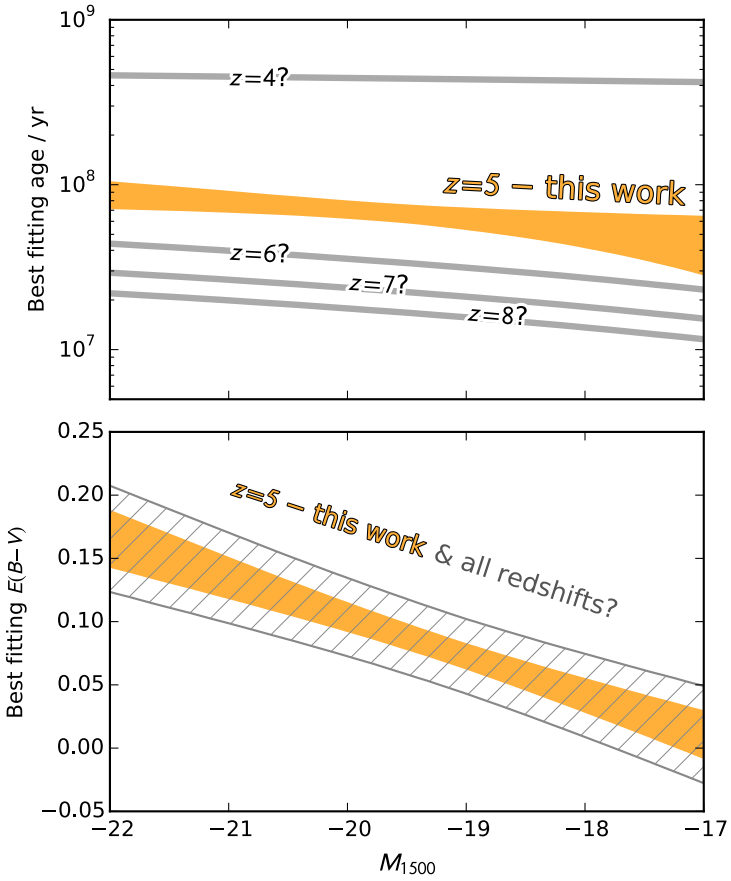

Figure 7.2 A speculative illustration of how the work presented in Chapter 6, concluding in Fig. 6.10, could be extended to other redshifts $4 < z < 8$. Measuring the Balmer breaks of galaxies at these other epochs would help to determine how much of the redshift evolution of the CMR is due to increased dust reddening, or to increased average stellar population age, at later epochs. One possible outcome, illustrated here, is that the dust reddening is a redshift-independent function of magnitude (bottom panel), which follows the relation we have discovered at $z = 5$. The CMR evolution toward redder colours at lower redshifts is then due to stellar populations simply being older at later epochs, without the ages affecting the CMR slope (top panel).

A $z \approx 6$ sample would require a different approach, since no line-free sample can be produced there from standard broad-band photometry. Work has been done here in the past, accounting for nebular emission contamination, and has found similar results to those presented in Section 6.8 (Curtis-Lake et al. 2013). Two further (challenging) windows exist at $6.70 < z < 6.95$ and $7.1 < z < 7.45$, where uncontaminated measurements of the Balmer break are possible from the $K-[4.5]$ and $K-[3.6]$ colours, respectively. Studies in this range may be possible through de-confusion of ultra-deep *Spitzer* IRAC data (e.g. McLure et al. 2011), but the highest redshift range where this is possible ($z > 9.35$, where $K-[4.5]$ is once again contamination free) will almost certainly be out of reach until the *James Webb Space Telescope* era.

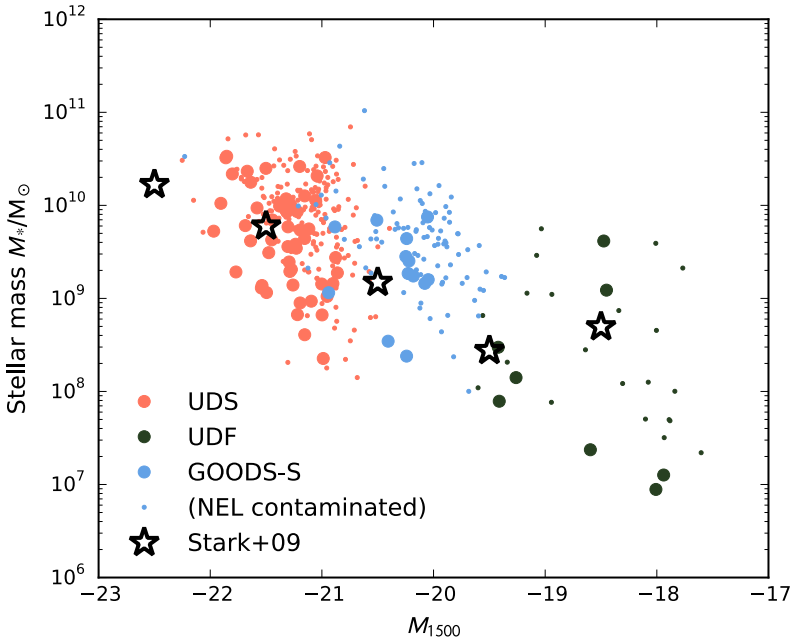

Figure 7.3 The stellar mass of $z \approx 5$ galaxies as a function of absolute UV magnitude. Large and small circles denote galaxies which are probably emission-line free in the *Spitzer* IRAC [3.6] band, and probably contaminated, respectively (see text). The salmon, blue, and dark green colouring denotes galaxies from the UDS, GOODS-S and the UDF, respectively. The black stars show the $z \approx 5$ results of Stark et al. (2009) (which we have made consistent with the Chabrier IMF using equation 1.9); they are in good agreement. The galaxies we expect to be contaminated (small circles) tend to have higher fitted masses, as expected.

7.3 The UV colour – stellar mass relation

Observationally and theoretically, it is known that high-redshift star-forming galaxies have somewhat correlated stellar mass and UV luminosity. UV luminosity traces the SFR (e.g. Kennicutt 1998), so this can be thought of as the sSFR being fairly constant amongst galaxies of very different masses. This is partly because the UV light is dominated by recent and present star-formation, which accounts for a good deal of the mass in necessarily young high-redshift galaxies.

However the mass to light ratio is not one-to-one (González et al. 2011). Finkelstein et al. (2012b) reported a more significant correlation between UV colour β and stellar mass than between β and UV magnitude. The $\beta - M_*$ relation is perhaps a more interesting one to seek, as it lends itself more directly to understanding how galaxies simultaneously build up their stellar and dust masses at early times. However, M_* is less directly observable than M_{1500}, since M_* is, in essence, the integral of past star formation which is no longer

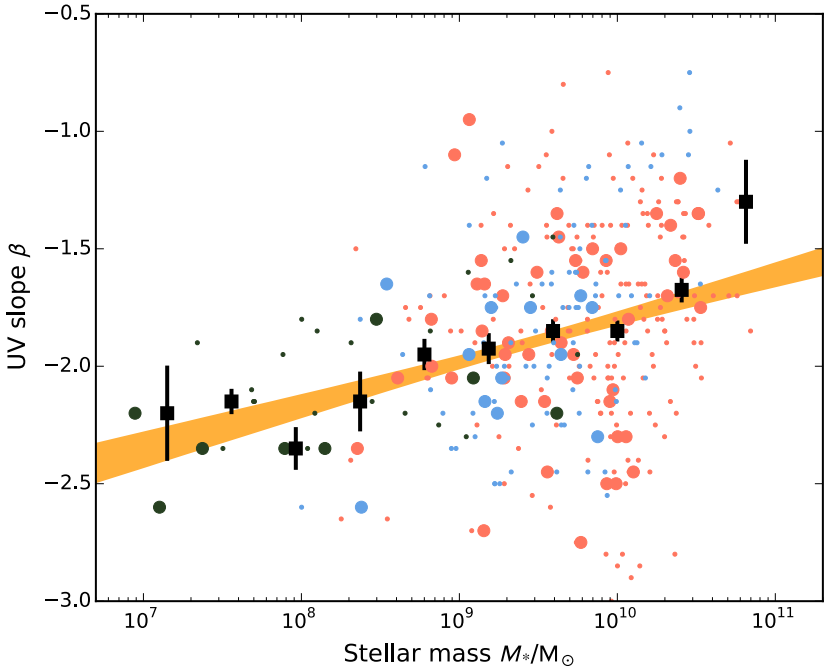

Figure 7.4 The UV continuum slope β as a function of stellar mass. Since the UV luminosity of star-forming galaxies correlates (to an arguable degree) with stellar mass, the colour–magnitude relation is also a colour–mass relation. Large and small circles denote galaxies which are probably emission-line free in the *Spitzer* IRAC [3.6] band, and probably contaminated, respectively (see text). The salmon, blue, and dark green colouring denotes galaxies from the UDS, GOODS-S and the UDF, respectively. The black squares and error bars are binned medians and standard errors on the mean, while the yellow swathe is a linear fit and 1σ error region (weighted by the $p(z)$ enclosed in the contamination-free redshift window for each galaxy).

visible in the rest-frame UV. We have seen in Chapter 6 that the rest-frame optical is better equipped to measure the age of a stellar population than the rest-frame UV; fortunately this is also true of the stellar mass. Using the same nebular-emission-line mitigation technique as in Section 6.2, we have measured the stellar masses of a sub-sample of our $z \approx 5$ LBGs. To briefly recount: we assigned each galaxy a probability that it lay in a redshift window making the [3.6] band free of nebular emission lines, and was therefore a reliable measurement of the rest-frame optical light above the Balmer break. Fitting stellar population synthesis models to all the galaxies, and weighting the best-fitting masses by those probabilities, led to masses shown in the stellar-mass–absolute-magnitude relation presented in Fig. 7.3. Given the correlation of that relation, it is unsurprising that the $\beta - M_*$ trend shown in Fig. 7.4 is also reasonably strong. The slope of the $\beta - M_*$ relation, $\mathrm{d}\beta/\mathrm{dlog}_{10}\, M_* = 0.19 \pm 0.03$, is similar to that reported at $z \approx 4$ by Finkelstein et al. (2012b), but slightly shallower than their $z \approx 5$ result (0.17 ± 0.03 and 0.30 ± 0.06, respectively). Thus it appears that our conclusions regarding the build up of dust with increasing luminosity can be readily translated to a build up of dust as galaxies gain mass.

7.4 A plausible physical picture for early stellar population evolution

By $z \approx 8$, only 640 Myr after the Big Bang, the non-exotic rest-frame UV continua of star-forming galaxies show that the first stage of metal enrichment or dust production must have already occurred (Chapter 4). To $z = 7$ (770 Myr after the Big Bang) and $z = 5$ (1200 Myr), galaxies at fixed absolute luminosity seemingly do not substantially evolve in their UV colours (Fig. 7.1). In agreement with the evolution of the UV luminosity function, this suggests that galaxies selected at fixed luminosity are not simply snapshots of the same, evolving, population, but are galaxies which are, at each point of observation, passing through similar stages of their evolution. The fact that (at least at $z \approx 5$) these galaxies show only a very weak luminosity-dependence in their light-weighted ages suggests that even the brightest galaxies (which are also the most massive) are built in an episodic, stochastic, way (Chapter 6). As galaxies build their stellar mass, they naturally accumulate more dust. This is observed by the increased reddening in brighter galaxies compared to fainter galaxies, which at $M_{1500} \approx -17$ are essentially unreddened (but are otherwise unremarkable in their stellar populations). However, even as the average reddening increases with luminosity, minor factions of the bright galaxies still appear unreddened: there is diversity in the dust properties of the most luminous sources, perhaps indicative of the time-scale over which dust forms following a star-formation episode.

By extending these measurements, particularly of the Balmer-break strengths which allow the separation of age and dust-reddening effects, to other redshifts, the build up of stars and dust with *time*, rather than just mass, should become clear. Finally, the as-yet inaccessible era of Population-III star domination, which is thought to mark the onset of the epoch of reionization and the first stage of metal enrichment, should soon be explored. This will, however, almost certainly be the preserve of the *James Webb Space Telescope*.

A Contributions to publications

In this appendix, my contributions to publications of which I am a co-author are detailed.

Bowler et al. (2012) Measurements of the UV continuum slope β for the sample of $z \approx 7$ galaxies selected from the UltraVISTA survey.

Bowler et al. (2014) Measurements of β for the sample; image simulation input distributions.

Curtis-Lake et al. (2013) Creation of stellar population synthesis models according to exponentially increasing star-formation histories.

Dunlop et al. (2013) Power-law measurements of β for the galaxy sample; and accompanying bias simulations. Chapter 4.

Koekemoer et al. (2013) Image depth tests and comparisons of early data reductions.

McLure et al. (2013) Creation of stellar population synthesis models according to various star-formation histories; independent photometric redshift checks.

Robertson et al. (2013) This paper relied on the β determinations of Dunlop et al. (2013) / Chapter 4.

Ellis et al. (2013), Ono et al. (2013), Schenker et al. (2013) Member of collaboration, and involved in image quality and depth tests which underpinned the scientific analyses.

B | Source lists and UV slope measurements of $z \approx 5$ Lyman-break galaxies

In this appendix, the 584 $z \approx 5$ galaxy candidates studied in Chapter 5 (some of which were also studied in Chapter 6) are listed. Tables B.1, B.2, and B.3 list our sources from CANDELS GOODS-S, the UKIDSS UDS, and the *Hubble* UDF, respectively. Positions, absolute magnitudes, UV continuum slope measurements, and redshifts are given for every candidate galaxy. For those three fields, spectroscopic and independent photometric redshifts are also listed where available. Table B.4 lists the information for sources in CANDELS GOODS-N, but no redshift comparison data are available in that case.

Table B.1 *Complete source list for our* $4.5 \leq z \leq 5.5$ *galaxies selected from the CANDELS GOODS-S field and studied in Chapter 5. Columns 1 and 2 list the Right Ascension and Declination (J2000) of each galaxy candidate. Column 3 lists their measured absolute magnitude at 1500 Å rest-frame. Columns 4 and 5 list measurements and uncertainties of their UV continuum spectral slopes. Column 6, by which the table is sorted, lists our photometric redshifts, while column 7 denotes (with an × mark) those objects which have less robust high-redshift solutions (as determined by* $\Delta\chi^2$ *in the SED fitting). Column 8 lists spectroscopic redshifts, where available, from the ESO GOODS/CDF-S Spectroscopy master catalogue, which is available from* `http://www.eso.org/sci/activities/garching/projects/goods/MasterSpectroscopy.html`. *Column 9 lists photometric redshifts from as determined in an independent study by Dahlen et al. (2013).*

RA	Dec	M_{1500} /AB mag	β	$\delta\beta$	$z_{\rm phot}$	OK low-z?	$z_{\rm spec}$	Alt. $z_{\rm phot}$
03:32:22.88	−27:47:27.57	−21.05	−1.70	0.24	4.50		4.44	4.64
03:32:41.41	−27:48:49.36	−20.04	−1.75	0.24	4.50			4.57
03:32:48.90	−27:52:43.18	−19.39	−2.00	0.41	4.51			4.24
03:32:40.49	−27:48:54.49	−19.96	−1.65	0.25	4.52			4.29
03:32:22.71	−27:51:54.36	−19.75	−1.60	0.25	4.53		4.90	
03:32:21.68	−27:47:50.01	−19.36	−2.50	0.29	4.53			4.54
03:32:09.54	−27:46:23.62	−20.12	−2.20	0.25	4.53			4.47
03:32:22.97	−27:46:29.12	−20.45	−0.90	0.24	4.53	×	4.50	4.66
03:32:15.41	−27:52:26.53	−20.09	−2.00	0.24	4.53			4.55
03:32:16.58	−27:44:45.82	−19.89	−2.10	0.25	4.54			4.69
03:32:15.36	−27:49:36.10	−19.78	−1.60	0.26	4.55			4.48
03:32:04.30	−27:45:36.17	−20.01	−1.60	0.24	4.56			4.72
03:32:32.75	−27:50:08.46	−20.03	−1.90	0.25	4.57			4.79
03:32:41.35	−27:48:43.13	−19.86	−1.55	0.25	4.58			4.51
03:32:59.16	−27:53:32.27	−19.78	−1.75	0.31	4.59			4.58
03:32:16.23	−27:48:44.15	−19.98	−2.45	0.26	4.59			4.55
03:32:42.68	−27:49:39.67	−19.55	−2.20	0.26	4.59			5.16
03:32:40.12	−27:45:35.49	−20.27	−1.75	0.25	4.60		4.77	4.69
03:32:16.58	−27:41:47.49	−20.16	−1.90	0.23	4.60			4.37
03:32:47.54	−27:47:55.38	−19.85	−1.65	0.25	4.60			4.68
03:32:50.05	−27:54:04.03	−19.87	−2.10	0.36	4.60			4.62
03:32:59.01	−27:53:32.21	−20.87	−1.05	0.25	4.60			4.95
03:32:10.03	−27:41:32.66	−21.01	−1.90	0.25	4.60		4.81	4.80
03:32:40.09	−27:50:49.58	−19.70	−2.50	0.28	4.61			4.49

Continued on next page

Table B.1 – continued from previous page

RA	Dec	M_{1500} /AB mag	β	$\delta\beta$	$z_{\rm phot}$	OK low-z?	$z_{\rm spec}$	Alt. $z_{\rm phot}$
03:32:57.17	−27:51:45.03	−21.21	−2.15	0.26	4.62		4.76	4.66
03:32:12.43	−27:47:02.47	−19.58	−2.30	0.29	4.62			4.53
03:32:11.25	−27:50:26.30	−19.86	−1.15	0.26	4.62			4.77
03:32:23.64	−27:43:28.66	−19.60	−1.70	0.28	4.63			4.68
03:32:11.71	−27:41:49.59	−20.66	−2.05	0.24	4.63		4.91	4.87
03:32:32.07	−27:53:50.52	−20.09	−1.75	0.27	4.63			4.57
03:32:28.56	−27:40:55.85	−20.15	−1.75	0.23	4.63		4.60	4.69
03:32:56.50	−27:51:56.50	−20.61	−2.45	0.23	4.63			0.51
03:32:30.88	−27:41:55.78	−19.90	−2.45	0.24	4.64			4.46
03:32:10.31	−27:44:25.30	−19.92	−1.95	0.23	4.64			4.60
03:32:21.62	−27:42:09.65	−20.11	−2.50	0.25	4.66			4.62
03:32:28.71	−27:42:28.95	−19.93	−1.90	0.24	4.67			4.78
03:32:11.45	−27:47:38.63	−20.33	−1.20	0.25	4.67			5.01
03:32:22.45	−27:47:46.17	−19.69	−1.65	0.26	4.70			4.48
03:32:52.69	−27:54:05.09	−20.10	−1.00	0.24	4.72			4.85
03:32:38.34	−27:39:39.43	−20.23	−1.55	0.25	4.72			5.00
03:32:13.94	−27:45:28.19	−19.82	−1.80	0.25	4.73		4.82	4.73
03:32:08.70	−27:47:10.66	−19.90	−1.70	0.26	4.73			4.73
03:32:41.11	−27:45:12.14	−19.74	−1.70	0.26	4.73			4.85
03:32:05.26	−27:43:00.41	−20.80	−1.95	0.23	4.74		4.81	4.78
03:32:16.98	−27:51:23.20	−20.44	−1.70	0.24	4.75		4.60	4.64
03:32:05.08	−27:46:56.52	−22.23	−1.65	0.24	4.76		4.82	4.92
03:32:31.08	−27:51:17.84	−20.10	−1.25	0.24	4.77			4.77
03:32:43.31	−27:43:10.63	−20.04	−1.40	0.24	4.78			4.85
03:32:05.16	−27:47:14.22	−20.30	−1.15	0.26	4.79			5.02
03:32:42.61	−27:54:28.88	−19.95	−1.15	0.26	4.81		4.40	4.97
03:32:33.03	−27:45:18.70	−19.91	−1.60	0.25	4.82			4.72
03:32:18.67	−27:51:00.34	−20.17	−1.10	0.25	4.82			4.74
03:32:56.30	−27:53:31.60	−20.53	−2.30	0.24	4.84			4.66
03:32:59.21	−27:53:32.11	−20.06	−2.25	0.31	4.84			4.54
03:32:24.88	−27:45:47.36	−19.78	−2.00	0.27	4.84			4.89
03:32:44.07	−27:42:27.45	−21.10	−2.05	0.25	4.84		4.92	4.84
03:32:01.29	−27:44:32.20	−20.96	−1.65	0.24	4.84			5.00

Continued on next page

Table B.1 – continued from previous page

RA	Dec	M_{1500} /AB mag	β	$\delta\beta$	$z_{\rm phot}$	OK low-z?	$z_{\rm spec}$	Alt. $z_{\rm phot}$
03:32:42.36	−27:43:00.28	−20.04	−2.00	0.26	4.89			4.85
03:32:37.14	−27:43:38.58	−19.94	−1.40	0.27	4.90			0.71
03:32:25.96	−27:49:30.44	−20.62	−0.25	0.24	4.90	×		4.55
03:32:21.69	−27:45:42.06	−19.53	−2.00	0.33	4.90			4.68
03:32:58.43	−27:52:30.96	−20.05	−2.30	0.32	4.90			4.84
03:32:47.59	−27:52:28.24	−19.88	−2.20	0.34	4.91		4.76	4.82
03:32:30.52	−27:40:25.69	−19.89	−1.90	0.26	4.91			4.92
03:32:42.66	−27:49:38.99	−20.11	−2.35	0.24	4.91		4.84	5.11
03:32:57.69	−27:53:19.68	−20.09	−2.45	0.35	4.92			4.73
03:32:16.17	−27:46:41.57	−20.15	−2.05	0.25	4.93			4.92
03:32:45.31	−27:46:37.57	−19.96	−2.25	0.25	4.94			4.82
03:32:55.37	−27:50:25.34	−19.55	−2.85	0.52	4.95			
03:32:23.32	−27:46:07.26	−19.84	−1.70	0.28	4.95			4.71
03:32:10.33	−27:44:25.39	−20.23	−1.50	0.23	4.96			4.78
03:32:43.53	−27:49:19.23	−20.52	−2.10	0.25	4.96		4.76	4.79
03:32:22.72	−27:51:54.45	−20.12	−1.40	0.24	4.99			4.77
03:32:16.59	−27:46:36.09	−20.46	−1.85	0.25	4.99			4.89
03:32:58.66	−27:52:43.69	−20.31	−2.20	0.28	5.01			4.81
03:32:21.93	−27:45:33.07	−20.36	−1.55	0.24	5.02		4.79	0.83
03:32:16.45	−27:46:39.22	−20.02	−1.75	0.26	5.02			5.04
03:32:31.37	−27:48:13.81	−20.51	−1.75	0.24	5.04			5.14
03:32:37.26	−27:42:02.57	−20.25	−1.75	0.23	5.04			5.14
03:32:32.26	−27:45:23.22	−20.08	−2.15	0.24	5.05			5.08
03:32:25.32	−27:45:30.86	−19.63	−2.35	0.32	5.05		4.99	4.93
03:32:35.46	−27:49:35.22	−19.99	−1.85	0.24	5.06			5.02
03:32:15.97	−27:48:05.60	−20.24	−2.60	0.25	5.06			4.77
03:32:33.47	−27:50:30.00	−20.63	−1.10	0.25	5.07	×	4.90	4.95
03:32:33.27	−27:47:25.02	−19.59	−2.00	0.28	5.09			4.88
03:32:34.28	−27:41:59.69	−19.68	−2.60	0.44	5.14			4.72
03:32:29.80	−27:52:28.04	−20.41	−1.65	0.25	5.14			5.24
03:32:16.98	−27:48:24.85	−19.93	−1.95	0.26	5.15			0.75
03:32:48.14	−27:48:17.71	−20.88	−1.70	0.25	5.17			5.28
03:32:25.44	−27:50:14.13	−20.05	−1.75	0.23	5.24			5.41

Continued on next page

Table B.1 – continued from previous page

RA	Dec	M_{1500} /AB mag	β	$\delta\beta$	$z_{\rm phot}$	OK low-z?	$z_{\rm spec}$	Alt. $z_{\rm phot}$
03:32:21.30	−27:40:51.21	−20.94	−1.95	0.23	5.25		5.29	5.22
03:32:11.93	−27:41:57.10	−19.92	−1.20	0.29	5.25	×	5.58	5.57
03:32:45.23	−27:49:09.95	−20.17	−1.85	0.24	5.26		5.58	5.46
03:32:29.37	−27:55:02.09	−20.56	−1.05	0.23	5.26	×		0.98
03:32:30.38	−27:53:58.44	−20.03	−1.15	0.28	5.27	×		5.56
03:32:16.47	−27:50:05.67	−20.22	−1.45	0.25	5.28			5.46
03:32:21.29	−27:49:59.67	−20.23	−2.05	0.27	5.28			5.25
03:32:25.79	−27:54:12.91	−20.18	−2.20	0.35	5.29			5.29
03:32:37.63	−27:50:22.39	−20.34	−1.60	0.23	5.31		5.52	5.51
03:32:45.42	−27:54:38.50	−21.12	−1.90	0.25	5.31		5.37	5.37
03:32:19.97	−27:54:58.98	−20.56	−1.45	0.28	5.33			5.58
03:32:54.05	−27:51:12.01	−20.15	−2.05	0.33	5.36			5.39
03:32:42.95	−27:43:39.66	−20.24	−1.95	0.26	5.37			5.07
03:32:24.40	−27:50:09.99	−20.93	−0.75	0.24	5.41		5.50	5.67
03:32:33.70	−27:53:21.62	−19.96	−3.10	0.44	5.43			5.19
03:32:13.44	−27:41:35.30	−20.23	−1.70	0.26	5.44			0.81
03:32:11.21	−27:48:21.71	−20.07	−2.55	0.35	5.44			5.35
03:32:40.99	−27:45:44.00	−20.27	−1.40	0.24	5.44			5.42
03:32:50.25	−27:51:27.21	−20.14	−2.25	0.34	5.45			5.37
03:32:25.03	−27:50:24.51	−20.51	−1.25	0.25	5.45			5.66
03:32:39.03	−27:52:23.09	−20.84	−1.25	0.25	5.45			5.55
03:32:13.88	−27:41:48.54	−19.89	−2.15	0.30	5.47			5.39

Table B.2 *Complete source list for our* $4.5 \leq z \leq 5.5$ *galaxies selected from the UDS field and studied in Chapter 5. Columns 1 and 2 list the Right Ascension and Declination (J2000) of each galaxy candidate. Column 3 lists their measured absolute magnitude at 1500 Å rest-frame. Columns 4 and 5 list measurements and uncertainties of their UV continuum spectral slopes. Column 6, by which the table is sorted, lists our photometric redshifts, while column 7 denotes (with an × mark) those objects which have less robust high-redshift solutions (as determined by* $\Delta\chi^2$ *in the SED fitting). Column 8 lists spectroscopic redshifts, where available, from the UDS Spectroscopy by Akiyama et al. (in prep.), which is available from* `http://www.nottingham.ac.uk/astronomy/UDS/data/data.html`. *Column 9 lists photometric redshifts from as determined in an independent study by Dahlen et al. (2013), which covers only the small CANDELS portion of the UDS.*

RA	Dec	M_{1500} /AB mag	β	$\delta\beta$	$z_{\rm phot}$	OK low-z?	$z_{\rm spec}$	Alt. $z_{\rm phot}$
02:17:39.89	−05:32:53.76	−21.39	−2.20	0.43	4.50			
02:16:49.07	−05:19:10.88	−20.57	−2.05	0.59	4.50			
02:16:20.08	−05:14:56.12	−21.03	−2.00	0.34	4.50			
02:17:22.97	−04:57:05.29	−21.21	−2.20	0.33	4.50			
02:18:08.44	−04:53:04.98	−20.71	−2.15	0.40	4.50			
02:17:56.97	−05:25:52.28	−20.85	−1.40	0.30	4.51			
02:17:55.59	−05:15:20.76	−21.50	−1.85	0.24	4.51			4.53
02:17:45.06	−04:47:30.26	−20.39	−3.55	1.16	4.51			
02:16:11.65	−04:43:07.63	−20.79	−1.55	0.37	4.51			
02:19:09.22	−05:17:44.61	−21.37	−2.85	0.38	4.52			
02:17:18.59	−05:15:13.60	−20.52	−2.05	0.56	4.52			4.61
02:18:07.07	−05:09:03.45	−21.01	−1.00	0.26	4.52			4.57
02:19:06.54	−05:06:50.45	−21.07	−2.05	0.32	4.52			
02:17:09.47	−04:50:14.98	−21.38	−1.70	0.29	4.52			
02:16:02.32	−05:15:09.37	−21.04	−2.05	0.38	4.53			
02:16:13.76	−05:09:35.52	−21.28	−2.70	0.42	4.53			
02:17:30.14	−05:01:22.31	−21.18	−2.35	0.36	4.53			
02:17:20.59	−04:51:34.13	−21.18	−1.40	0.32	4.53			
02:16:30.06	−04:51:09.29	−20.71	−2.30	0.59	4.53			
02:16:35.90	−04:47:31.65	−21.34	−1.60	0.24	4.53			
02:17:59.69	−05:28:12.58	−20.82	−1.75	0.42	4.54			
02:17:29.61	−05:16:17.17	−20.50	−1.45	0.47	4.54			4.50
02:17:16.58	−05:14:27.24	−20.86	−1.85	0.37	4.54			4.58
02:18:58.43	−04:58:31.58	−20.98	−2.25	0.32	4.54			

Continued on next page

Table B.2 – continued from previous page

RA	Dec	M_{1500} /AB mag	β	$\delta\beta$	$z_{\rm phot}$	OK low-z?	$z_{\rm spec}$	Alt. $z_{\rm phot}$
02:16:14.05	−04:43:57.55	−21.21	−1.30	0.26	4.54			
02:16:25.08	−04:46:25.70	−20.99	−2.40	0.39	4.54			
02:17:15.45	−05:26:26.50	−20.69	−1.20	0.35	4.55			
02:17:36.32	−04:57:40.18	−20.72	−2.30	0.53	4.55			
02:17:14.39	−04:55:58.17	−21.09	−2.85	0.41	4.55			
02:16:36.25	−04:47:30.74	−21.06	−1.85	0.31	4.55			
02:18:57.37	−04:42:18.88	−21.05	−1.10	0.25	4.56			
02:17:16.02	−05:23:03.82	−20.72	−2.20	0.52	4.57			
02:16:08.08	−05:16:35.19	−20.76	−1.40	0.32	4.57			
02:19:27.29	−05:13:34.72	−21.42	−1.70	0.27	4.57			
02:17:42.01	−05:11:55.51	−21.04	−2.10	0.34	4.57			4.59
02:17:02.11	−04:57:10.57	−20.80	−3.50	0.70	4.57			
02:17:03.81	−04:39:08.55	−20.71	−2.15	0.97	4.57			
02:17:56.98	−05:25:44.49	−21.58	−1.40	0.20	4.58			
02:19:11.68	−05:16:23.72	−21.08	−1.95	0.38	4.58			
02:16:09.86	−05:15:22.92	−21.00	−1.45	0.28	4.58	×		
02:18:46.44	−05:25:50.35	−21.29	−2.05	0.27	4.59			
02:19:29.84	−05:12:45.08	−21.15	−1.90	0.35	4.59			
02:17:34.77	−05:08:36.55	−20.96	−1.05	0.29	4.59			4.65
02:17:46.29	−04:39:09.26	−21.26	−2.90	0.86	4.59			
02:17:49.13	−04:44:16.42	−20.85	−1.80	0.44	4.59			
02:19:05.70	−05:31:44.75	−20.99	−2.00	0.42	4.60			
02:18:21.50	−05:31:24.00	−20.74	−1.85	0.48	4.60			
02:18:23.01	−05:27:53.44	−21.44	−1.80	0.26	4.60			
02:18:25.04	−05:27:02.64	−21.40	−1.65	0.28	4.60			
02:16:31.52	−05:11:32.58	−21.84	−1.05	0.21	4.60			
02:17:35.58	−05:11:27.51	−20.93	−1.60	0.33	4.60			4.58
02:17:24.15	−05:08:59.56	−20.90	−1.80	0.39	4.61			4.54
02:16:10.83	−05:05:48.47	−21.03	−2.25	0.38	4.61			
02:17:07.59	−04:55:50.50	−20.89	−2.05	0.46	4.61			
02:16:59.59	−04:40:28.74	−20.96	−1.40	0.31	4.61			
02:18:55.92	−05:31:18.48	−20.96	−2.65	0.45	4.62			
02:16:19.83	−05:08:50.38	−20.72	−1.80	0.40	4.62			

Continued on next page

Table B.2 – continued from previous page

RA	Dec	M_{1500} /AB mag	β	$\delta\beta$	$z_{\rm phot}$	OK low-z?	$z_{\rm spec}$	Alt. $z_{\rm phot}$
02:17:22.60	−04:56:51.05	−21.25	−2.80	0.37	4.62			
02:17:15.91	−04:55:48.08	−20.93	−1.50	0.38	4.62			
02:19:33.62	−04:54:35.11	−21.24	−1.40	0.27	4.62			
02:18:55.36	−04:51:14.88	−21.04	−1.35	0.24	4.62			
02:18:10.37	−04:48:40.87	−20.95	−1.95	0.40	4.62			
02:17:47.60	−05:31:05.99	−21.28	−2.50	0.35	4.63			
02:16:52.38	−05:12:55.71	−20.95	−1.85	0.36	4.63			
02:18:21.41	−04:47:03.60	−20.97	−1.85	0.33	4.63			
02:18:19.50	−05:29:05.53	−20.71	−1.75	0.46	4.64			
02:17:06.94	−05:21:49.50	−21.10	−1.10	0.22	4.64			
02:17:43.71	−05:12:16.01	−20.91	−2.85	0.49	4.64			4.88
02:16:10.41	−05:05:45.87	−21.08	−2.20	0.35	4.64			
02:17:47.39	−05:05:36.04	−21.76	−1.70	0.20	4.64			
02:17:00.42	−05:02:39.56	−20.70	−3.65	1.08	4.64			
02:16:53.19	−04:51:10.80	−20.98	−0.80	0.30	4.64	×		
02:18:51.69	−05:17:14.41	−21.07	−1.80	0.46	4.65			
02:16:11.78	−05:11:20.21	−20.96	−1.25	0.31	4.65			
02:16:44.33	−04:59:33.63	−21.05	−2.15	0.38	4.65			
02:16:43.39	−04:53:34.88	−21.04	−1.80	0.35	4.65			
02:16:09.02	−04:50:12.21	−21.05	−1.40	0.35	4.65			
02:18:42.06	−05:23:40.15	−22.15	−1.65	0.20	4.66			
02:18:19.11	−05:24:13.59	−20.89	−3.00	0.63	4.67			
02:16:39.65	−05:07:02.58	−21.12	−1.50	0.32	4.67			
02:17:59.50	−04:58:33.05	−21.38	−1.95	0.26	4.67			
02:18:08.13	−04:48:45.63	−20.87	−2.25	0.47	4.67			
02:17:56.60	−04:59:19.41	−21.13	−1.85	0.28	4.68			
02:17:04.61	−05:23:07.85	−21.39	−2.25	0.28	4.69			
02:17:27.78	−04:59:55.42	−20.90	−1.50	0.31	4.69			
02:17:52.59	−04:57:58.49	−21.11	−1.30	0.27	4.69			
02:17:04.17	−04:52:15.70	−21.05	−1.60	0.43	4.69			
02:18:18.19	−05:29:48.41	−21.53	−1.20	0.24	4.70			
02:18:43.18	−05:24:09.96	−21.04	−1.30	0.29	4.70			
02:18:49.85	−05:19:20.32	−21.52	−2.20	0.27	4.70			

Continued on next page

Table B.2 – continued from previous page

RA	Dec	M_{1500} /AB mag	β	$\delta\beta$	$z_{\rm phot}$	OK low-z?	$z_{\rm spec}$	Alt. $z_{\rm phot}$
02:17:15.09	−05:09:10.64	−20.75	−2.65	0.56	4.70			4.62
02:17:49.23	−05:00:40.02	−21.54	−2.30	0.30	4.70			
02:19:17.80	−04:59:32.71	−21.25	−1.35	0.24	4.70			
02:19:21.20	−04:57:12.50	−21.23	−1.90	0.29	4.71			
02:17:36.18	−05:20:59.31	−20.58	−3.70	1.00	4.72			
02:18:09.59	−05:03:38.05	−21.47	−1.40	0.21	4.72			
02:17:58.09	−04:57:15.06	−20.87	−1.75	0.34	4.72			
02:17:14.46	−04:55:56.11	−21.07	−3.30	0.51	4.72			
02:17:47.36	−04:49:40.61	−21.07	−2.05	0.38	4.72			
02:19:23.62	−05:04:51.78	−21.26	−2.50	0.47	4.73			
02:19:33.66	−04:54:37.03	−21.57	−1.70	0.26	4.73			
02:17:25.49	−04:44:31.86	−20.85	−1.20	0.33	4.73			
02:16:51.93	−05:28:36.15	−21.35	−1.90	0.26	4.74			
02:18:13.73	−05:27:52.93	−20.87	−0.80	0.35	4.74			
02:18:04.15	−05:12:52.41	−21.05	−1.85	0.35	4.74			4.86
02:17:27.56	−04:52:16.52	−20.68	−1.95	0.62	4.74			
02:17:33.39	−04:49:12.92	−20.87	−1.40	0.40	4.74			
02:18:54.46	−05:32:42.02	−21.30	−1.40	0.39	4.75			
02:19:33.12	−05:15:45.04	−21.13	−1.70	0.38	4.75			
02:17:52.07	−05:13:21.38	−21.78	−1.70	0.21	4.75			4.81
02:16:40.12	−05:06:57.26	−20.99	−1.45	0.35	4.75			
02:19:25.73	−05:02:31.04	−21.47	−1.65	0.22	4.75			
02:18:20.46	−05:01:47.60	−21.15	−2.40	0.33	4.75			
02:17:37.67	−05:14:46.34	−20.76	−2.55	0.61	4.76			4.68
02:17:46.54	−05:03:32.12	−21.00	−2.30	0.42	4.76			
02:16:53.19	−05:02:35.42	−20.57	−2.00	0.54	4.76			
02:17:20.47	−04:58:27.24	−21.66	−1.75	0.23	4.76			
02:17:00.35	−04:58:17.53	−21.39	−1.65	0.30	4.76			
02:17:35.13	−04:42:27.84	−20.87	−1.70	0.40	4.76			
02:18:41.37	−05:28:31.53	−20.90	−1.35	0.33	4.77			
02:16:56.11	−05:23:48.84	−21.16	−1.90	0.31	4.77			
02:17:56.34	−05:10:32.24	−20.97	−1.70	0.34	4.77			4.83
02:18:52.15	−05:05:50.60	−21.02	−1.30	0.24	4.77			

Continued on next page

Table B.2 – continued from previous page

RA	Dec	M_{1500} /AB mag	β	$\delta\beta$	$z_{\rm phot}$	OK low-z?	$z_{\rm spec}$	Alt. $z_{\rm phot}$
02:17:57.97	−04:53:20.30	−21.45	−1.80	0.24	4.77			
02:18:28.15	−04:41:58.49	−21.41	−1.40	0.23	4.77			
02:19:31.61	−05:14:33.84	−21.07	−1.75	0.38	4.78			
02:16:12.33	−05:11:10.94	−20.97	−1.40	0.36	4.79			
02:16:44.40	−05:13:30.53	−21.15	−1.15	0.27	4.80			
02:17:11.60	−05:01:39.47	−20.86	−2.60	0.65	4.80			
02:16:02.04	−04:59:10.00	−20.96	−1.35	0.55	4.80			
02:17:39.11	−04:46:59.34	−22.25	−1.80	0.20	4.80			
02:17:59.48	−04:47:41.67	−21.44	−2.10	0.30	4.80			
02:19:07.18	−05:22:45.46	−21.10	−1.75	0.32	4.81			
02:18:49.95	−05:04:16.50	−21.35	−2.40	0.27	4.81			
02:16:59.42	−04:49:17.43	−21.68	−1.30	0.25	4.81		4.82	
02:19:30.61	−04:44:08.84	−21.03	−2.80	0.44	4.81			
02:17:14.39	−05:10:19.42	−20.90	−1.65	0.43	4.82			4.69
02:17:27.50	−05:06:02.52	−21.14	−1.10	0.30	4.82			
02:17:17.29	−04:57:06.21	−21.09	−2.45	0.48	4.82			
02:16:59.78	−04:44:19.79	−20.87	−2.15	0.51	4.82			
02:17:34.79	−05:20:35.17	−20.97	−2.75	0.59	4.83			
02:16:16.19	−05:11:23.89	−20.68	−2.35	0.63	4.83			
02:16:46.10	−05:03:03.08	−21.07	−1.30	0.37	4.83			
02:17:34.53	−04:56:26.85	−21.13	−1.30	0.31	4.83			
02:16:38.29	−04:49:20.96	−21.03	−1.65	0.44	4.83			
02:16:59.82	−04:46:54.63	−21.40	−2.45	0.38	4.83			
02:18:09.09	−05:13:02.00	−21.05	−1.45	0.27	4.84			5.14
02:17:25.49	−05:08:28.96	−20.88	−2.30	0.54	4.84			4.69
02:17:20.91	−04:51:46.78	−20.84	−1.95	0.45	4.84			
02:17:31.66	−04:47:30.15	−20.79	−1.50	0.42	4.84			
02:17:38.52	−04:46:24.45	−21.00	−1.85	0.40	4.84			
02:18:32.14	−05:30:12.07	−21.56	−2.00	0.29	4.85			
02:18:08.34	−04:44:43.09	−21.32	−2.15	0.33	4.85			
02:18:23.87	−05:28:32.38	−21.09	−1.70	0.37	4.86			
02:17:42.38	−05:26:48.72	−20.97	−2.70	0.49	4.86			
02:17:42.74	−05:25:36.36	−21.02	−1.90	0.39	4.86			

Continued on next page

Table B.2 – continued from previous page

RA	Dec	M_{1500} /AB mag	β	$\delta\beta$	$z_{\rm phot}$	OK low-z?	$z_{\rm spec}$	Alt. $z_{\rm phot}$
02:18:44.57	−05:19:56.15	−21.25	−1.45	0.27	4.86			
02:18:49.05	−04:49:03.47	−20.82	−2.75	0.62	4.86			
02:17:07.19	−05:03:31.41	−21.31	−2.20	0.49	4.87			
02:17:48.72	−04:59:28.74	−21.18	−1.75	0.32	4.87			
02:18:13.77	−05:18:41.00	−21.54	−1.70	0.25	4.88			
02:16:08.24	−05:16:01.36	−21.24	−2.00	0.32	4.88			
02:17:34.11	−05:10:11.05	−21.02	−2.30	0.46	4.88			4.74
02:19:00.31	−05:09:48.14	−20.89	−1.80	0.39	4.89			
02:17:03.01	−04:54:49.79	−21.64	−1.75	0.24	4.89			
02:17:25.62	−04:44:01.14	−21.43	−1.55	0.24	4.89			
02:18:31.83	−05:14:20.32	−20.99	−1.85	0.39	4.90			
02:19:18.71	−05:07:20.69	−21.11	−3.05	0.56	4.90			
02:17:36.54	−04:57:13.39	−21.03	−1.30	0.38	4.90			
02:17:24.10	−04:54:55.44	−21.31	−2.00	0.36	4.90			
02:16:57.20	−04:52:56.86	−21.30	−2.00	0.34	4.90			
02:19:13.55	−04:45:09.14	−21.56	−2.00	0.25	4.90			
02:19:34.72	−05:01:49.84	−21.45	−1.95	0.40	4.91			
02:17:03.71	−04:44:37.04	−21.06	−1.65	0.42	4.91			
02:17:04.96	−05:23:39.25	−21.05	−1.45	0.30	4.92			
02:17:46.43	−04:49:34.34	−21.22	−1.85	0.33	4.92			
02:17:39.38	−05:24:59.53	−21.37	−1.40	0.29	4.93			
02:17:47.28	−05:14:42.01	−21.19	−1.35	0.32	4.93			4.95
02:17:51.44	−04:42:44.92	−20.88	−1.70	0.38	4.95			
02:17:04.89	−04:43:01.04	−21.28	−1.15	0.30	4.95			
02:17:43.00	−05:12:29.99	−20.93	−1.90	0.44	4.96			0.60
02:19:01.60	−04:58:19.42	−21.31	−2.30	0.28	4.96			
02:16:20.86	−05:16:57.62	−20.80	−1.25	0.37	4.99			
02:19:02.96	−04:46:16.93	−22.06	−1.50	0.20	4.99			
02:19:25.03	−05:17:03.48	−21.47	−2.15	0.31	5.00			
02:17:49.49	−04:49:43.47	−21.02	−1.95	0.45	5.00			
02:17:45.78	−04:49:39.73	−21.02	−2.05	0.45	5.00			
02:16:06.09	−05:12:15.96	−20.61	−2.45	0.71	5.01			
02:17:11.18	−04:46:44.03	−21.30	−2.80	0.51	5.01			

Continued on next page

Table B.2 – continued from previous page

RA	Dec	M_{1500} /AB mag	β	$\delta\beta$	$z_{\rm phot}$	OK low-z?	$z_{\rm spec}$	Alt. $z_{\rm phot}$
02:17:57.57	−05:26:09.88	−21.29	−2.15	0.33	5.02			
02:17:18.39	−05:18:34.24	−20.89	−2.75	0.65	5.02			
02:19:14.53	−04:58:05.96	−21.21	−2.15	0.34	5.02			
02:17:39.12	−04:55:59.19	−21.44	−1.50	0.24	5.02			
02:17:56.25	−04:58:40.48	−21.48	−1.60	0.26	5.03			
02:18:45.47	−04:45:20.32	−21.20	−1.60	0.30	5.03			
02:18:45.26	−05:13:50.65	−21.21	−1.65	0.31	5.04			
02:17:55.97	−05:10:25.47	−21.22	−2.05	0.34	5.04			5.00
02:19:11.81	−04:46:02.83	−21.70	−1.70	0.24	5.04			
02:18:58.54	−05:26:05.50	−21.72	−1.85	0.26	5.05			
02:18:52.44	−05:22:39.83	−21.64	−1.35	0.27	5.05			
02:16:38.32	−04:50:41.15	−21.45	−2.05	0.45	5.05			
02:16:52.55	−04:47:19.31	−21.32	−1.80	0.36	5.05			
02:17:38.69	−05:24:37.75	−21.34	−1.35	0.31	5.06			
02:17:53.07	−04:49:08.81	−21.15	−1.20	0.27	5.06	×		
02:17:32.45	−05:05:29.35	−21.20	−2.05	0.41	5.07			
02:18:19.58	−05:17:53.79	−21.32	−2.15	0.39	5.09			
02:16:18.60	−04:56:33.49	−21.05	−2.30	0.59	5.09			
02:16:52.59	−04:45:10.76	−21.22	−2.00	0.39	5.09			
02:17:16.92	−05:06:18.31	−20.86	−1.70	0.38	5.10			
02:19:20.78	−04:53:27.28	−21.15	−2.45	0.41	5.10			
02:19:21.91	−04:46:52.01	−21.30	−2.60	0.38	5.10			
02:16:49.59	−05:09:04.28	−20.95	−3.25	0.72	5.11			
02:19:09.54	−05:18:17.17	−21.67	−1.55	0.31	5.12			
02:18:40.91	−05:11:16.24	−21.80	−1.40	0.23	5.12			
02:17:36.42	−04:44:25.98	−21.39	−2.00	0.31	5.12			
02:17:11.01	−05:05:23.82	−21.24	−1.85	0.39	5.13			
02:17:46.59	−04:57:11.92	−21.90	−1.50	0.21	5.13			
02:17:18.35	−04:47:57.85	−20.88	−1.95	0.48	5.15			
02:18:41.42	−04:42:37.44	−21.30	−2.45	0.38	5.15			
02:16:40.93	−05:12:26.65	−21.54	−1.65	0.26	5.16			
02:17:18.37	−05:08:13.85	−21.85	−1.75	0.25	5.16			5.25
02:17:10.93	−05:00:21.72	−21.19	−1.55	0.34	5.16			

Continued on next page

Table B.2 – continued from previous page

RA	Dec	M_{1500} /AB mag	β	$\delta\beta$	$z_{\rm phot}$	OK low-z?	$z_{\rm spec}$	Alt. $z_{\rm phot}$
02:16:47.46	−04:45:04.25	−21.97	−1.95	0.24	5.16			
02:17:06.20	−05:02:20.20	−21.50	−1.20	0.27	5.17			
02:17:45.62	−04:59:00.56	−21.54	−1.55	0.27	5.17			
02:19:06.16	−04:46:19.24	−21.15	−1.90	0.36	5.17			
02:16:50.94	−05:06:32.45	−21.13	−2.70	0.48	5.18			
02:18:08.51	−04:56:54.53	−21.06	−2.30	0.50	5.19			
02:16:10.75	−04:54:06.59	−21.26	−1.85	0.37	5.19			
02:18:49.58	−04:48:05.15	−21.86	−1.35	0.19	5.19			
02:16:36.06	−04:42:19.55	−20.99	−2.35	0.47	5.19			
02:18:02.27	−05:05:28.56	−21.12	−2.05	0.32	5.20			
02:16:29.11	−05:00:34.95	−21.27	−1.90	0.39	5.20			
02:17:13.50	−05:11:00.29	−21.28	−2.30	0.38	5.21			5.22
02:17:04.17	−05:02:57.62	−21.02	−1.90	0.57	5.21			
02:19:23.35	−04:46:45.36	−21.30	−2.75	0.46	5.21			
02:18:21.08	−05:14:14.48	−21.04	−1.70	0.43	5.22			5.43
02:17:16.80	−05:12:14.90	−22.04	−1.55	0.23	5.22			5.34
02:18:21.83	−05:05:04.60	−21.45	−1.45	0.27	5.23			
02:16:22.75	−04:55:08.75	−21.29	−1.95	0.44	5.23			
02:18:44.65	−04:47:56.85	−21.31	−1.55	0.29	5.23			
02:17:15.20	−04:47:29.92	−20.97	−1.35	0.42	5.24			
02:18:27.26	−05:10:16.26	−21.00	−1.80	0.46	5.25			
02:17:16.91	−04:47:43.50	−21.10	−1.10	0.36	5.25			
02:17:49.96	−05:20:41.08	−21.64	−1.35	0.26	5.26			
02:17:23.31	−04:59:47.05	−21.15	−2.05	0.47	5.27			
02:16:27.41	−04:57:41.67	−21.22	−2.50	0.49	5.27			
02:19:22.22	−04:45:43.68	−21.58	−2.10	0.27	5.28			
02:17:33.73	−04:42:24.82	−21.14	−1.90	0.44	5.29			
02:16:45.51	−05:07:34.95	−20.90	−1.65	0.45	5.30			
02:16:46.69	−05:06:34.10	−21.43	−1.50	0.29	5.30			
02:16:01.68	−05:00:45.99	−21.50	−0.95	0.37	5.30			
02:17:20.50	−05:28:14.13	−21.38	−2.50	0.46	5.31			
02:17:32.49	−04:48:14.48	−20.97	−2.80	0.81	5.31			
02:19:36.62	−04:48:42.32	−21.77	−2.05	0.39	5.32			

Continued on next page

Table B.2 – continued from previous page

RA	Dec	M_{1500} /AB mag	β	$\delta\beta$	$z_{\rm phot}$	OK low-z?	$z_{\rm spec}$	Alt. $z_{\rm phot}$
02:17:06.30	−05:01:31.38	−21.09	−2.20	0.52	5.33			
02:17:26.36	−05:25:15.86	−21.69	−1.60	0.27	5.34			
02:17:26.59	−05:03:41.33	−20.96	−2.10	0.70	5.35			
02:16:20.24	−05:10:19.84	−21.65	−1.90	0.27	5.36			
02:16:18.29	−05:01:16.50	−21.72	−1.80	0.34	5.38			
02:16:03.10	−05:05:05.76	−21.47	−0.75	0.34	5.39	×		
02:18:36.28	−04:45:15.35	−21.52	−1.40	0.28	5.39			
02:18:35.14	−05:28:40.80	−21.30	−2.40	0.47	5.40			
02:16:39.82	−05:05:49.24	−21.12	−2.50	0.68	5.40			
02:17:38.19	−04:42:13.19	−20.97	−1.60	0.36	5.40			
02:16:44.38	−05:14:31.13	−21.00	−2.70	0.66	5.41			
02:18:33.13	−05:06:35.51	−21.09	−1.80	0.42	5.42			
02:19:16.15	−05:01:53.40	−21.24	−1.60	0.35	5.42			
02:17:47.83	−05:20:01.71	−21.23	−2.15	0.41	5.43			
02:16:56.43	−04:49:51.25	−20.87	−1.90	0.64	5.44			
02:16:34.76	−04:57:42.17	−21.28	−2.00	0.46	5.45			
02:17:38.88	−04:40:37.28	−21.50	−1.75	0.32	5.45			
02:16:15.93	−04:43:08.49	−21.26	−1.90	0.40	5.45			
02:18:56.55	−05:22:15.34	−21.25	−1.35	0.27	5.46			
02:18:56.29	−05:26:24.70	−21.52	−2.15	0.36	5.48			
02:16:03.11	−04:56:35.95	−21.07	−2.95	0.92	5.49			

Table B.3 *Complete source list for our* $4.5 \leq z \leq 5.5$ *galaxies selected from the UDF field and studied in Chapter 5. Columns 1 and 2 list the Right Ascension and Declination (J2000) of each galaxy candidate. Column 3 lists their measured absolute magnitude at 1500 Å rest-frame. Columns 4 and 5 list measurements and uncertainties of their UV continuum spectral slopes. Column 6, by which the table is sorted, lists our photometric redshifts, while column 7 denotes (with an × mark) those objects which have less robust high-redshift solutions (as determined by* $\Delta\chi^2$ *in the SED fitting). Column 8 lists spectroscopic redshifts, where available, from the ESO GOODS/CDF-S Spectroscopy master catalogue, which is available from* `http://www.eso.org/sci/activities/garching/projects/goods/MasterSpectroscopy.html`. *Column 9 lists photometric redshifts from as determined in an independent study by Dahlen et al. (2013).*

RA	Dec	M_{1500} /AB mag	β	$\delta\beta$	$z_{\rm phot}$	OK low-z?	$z_{\rm spec}$	Alt. $z_{\rm phot}$
03:32:41.66	−27:47:32.87	−17.77	−1.55	0.31	4.50			4.37
03:32:37.94	−27:47:10.80	−19.03	−1.95	0.23	4.54		4.78	4.53
03:32:37.96	−27:47:11.05	−19.91	−2.10	0.23	4.54			
03:32:39.04	−27:48:08.28	−18.94	−2.30	0.23	4.64		4.88	4.62
03:32:39.48	−27:46:25.97	−18.34	−2.25	0.23	4.79			4.60
03:32:35.06	−27:47:07.51	−18.31	−2.20	0.23	4.82			4.80
03:32:41.31	−27:47:42.33	−19.08	−1.70	0.23	4.83		5.00	4.80
03:32:41.08	−27:46:42.44	−19.60	−2.35	0.23	4.89		4.55	4.79
03:32:41.22	−27:46:36.91	−17.60	−1.90	0.28	4.91			4.87
03:32:33.77	−27:47:12.05	−17.88	−2.10	0.27	5.01			4.93
03:32:44.44	−27:46:49.31	−18.45	−2.05	0.23	5.03			5.01
03:32:43.95	−27:46:44.04	−18.10	−2.15	0.23	5.05			4.70
03:32:33.84	−27:47:30.11	−17.84	−1.80	0.29	5.06			5.03
03:32:39.52	−27:46:10.47	−18.54	−1.75	0.24	5.07			
03:32:40.15	−27:46:18.28	−17.93	−2.35	0.29	5.10			4.84
03:32:42.86	−27:46:52.74	−18.94	−1.95	0.23	5.10			4.99
03:32:40.12	−27:46:28.30	−19.34	−1.90	0.23	5.11		4.90	4.93
03:32:39.86	−27:47:08.41	−19.16	−1.60	0.24	5.13			0.51
03:32:39.41	−27:46:24.27	−18.01	−1.45	0.29	5.14	×		0.71
03:32:40.77	−27:46:36.74	−18.60	−2.35	0.22	5.14			4.92
03:32:41.07	−27:47:04.51	−17.94	−2.60	0.30	5.15			4.49
03:32:34.94	−27:47:17.96	−17.57	−1.95	0.35	5.16			
03:32:37.89	−27:46:47.99	−18.01	−2.20	0.26	5.16			4.94
03:32:43.98	−27:46:43.87	−17.86	−1.90	0.28	5.18			

Continued on next page

Table B.3 – continued from previous page

RA	Dec	M_{1500} /AB mag	β	$\delta\beta$	$z_{\rm phot}$	OK low-z?	$z_{\rm spec}$	Alt. $z_{\rm phot}$
03:32:40.21	−27:45:55.51	−18.08	−1.85	0.28	5.18			5.08
03:32:39.78	−27:47:05.47	−18.48	−2.20	0.25	5.20			5.19
03:32:38.80	−27:45:47.19	−18.64	−2.15	0.23	5.23			4.98
03:32:36.25	−27:46:58.30	−19.41	−2.35	0.23	5.23		5.40	5.14
03:32:34.96	−27:47:17.53	−19.26	−2.35	0.24	5.26		5.10	5.12
03:32:42.83	−27:47:17.59	−19.42	−1.80	0.23	5.34			5.27
03:32:35.32	−27:47:35.08	−18.00	−2.20	0.29	5.38			5.35
03:32:40.10	−27:47:38.99	−17.89	−2.15	0.33	5.40			5.39
03:32:35.20	−27:47:10.08	−19.56	−1.85	0.23	5.47		5.50	5.55

Table B.4 *Complete source list for our* $4.5 \leq z \leq 5.5$ *galaxies selected from the CANDELS GOODS-N field and studied in Chapter 5. Columns 1 and 2 list the Right Ascension and Declination (J2000) of each galaxy candidate. Column 3 lists their measured absolute magnitude at 1500 Å rest-frame. Columns 4 and 5 list measurements and uncertainties of their UV continuum spectral slopes. Column 6, by which the table is sorted, lists our photometric redshifts, while column 7 denotes those objects which have less robust high-redshift solutions (as determined by* $\Delta\chi^2$ *in the SED fitting). There are no uniquely identifiable spectroscopic redshifts available for these candidates in the CANDELS team* $z_{\rm spec}$ *compilation (Hathi et al., private communication), nor is there a complete independent photometric redshift catalogue for comparison with.*

RA	Dec	M_{1500}/AB mag	β	$\delta\beta$	$z_{\rm phot}$	OK low-z?
12:36:54.58	+62:15:05.21	−20.20	−1.80	0.25	4.50	
12:36:57.78	+62:15:02.59	−19.67	−2.65	0.25	4.51	
12:36:46.17	+62:07:01.53	−20.73	−2.30	0.27	4.52	
12:37:37.47	+62:19:37.19	−20.33	−1.65	0.26	4.52	
12:37:05.55	+62:19:30.97	−19.85	−1.80	0.27	4.52	
12:36:54.98	+62:16:27.40	−19.15	−1.70	0.29	4.52	
12:37:03.11	+62:15:00.38	−19.64	−1.55	0.25	4.53	
12:36:31.35	+62:10:33.68	−20.19	−2.65	0.29	4.53	
12:37:11.10	+62:15:04.72	−19.90	−2.35	0.25	4.53	
12:37:04.85	+62:15:00.05	−19.55	−2.25	0.26	4.53	
12:36:54.56	+62:14:58.41	−19.64	−2.40	0.26	4.53	
12:37:01.49	+62:17:53.26	−19.93	−2.20	0.26	4.53	
12:36:30.20	+62:11:05.89	−20.05	−1.85	0.24	4.54	
12:36:58.95	+62:12:29.09	−19.59	−2.80	0.27	4.54	
12:37:29.17	+62:19:28.47	−19.86	−1.50	0.31	4.54	
12:36:50.04	+62:07:34.49	−19.58	−1.55	0.39	4.55	
12:36:20.61	+62:15:32.56	−19.45	−2.25	0.26	4.55	
12:36:31.90	+62:12:23.14	−20.15	−2.10	0.25	4.55	
12:36:07.98	+62:11:20.92	−20.24	−2.10	0.25	4.56	
12:36:23.03	+62:15:55.49	−19.64	−1.55	0.26	4.56	
12:36:57.53	+62:16:50.71	−19.41	−1.80	0.26	4.57	
12:36:52.68	+62:11:38.01	−19.53	−1.40	0.26	4.58	
12:37:29.34	+62:18:04.44	−19.70	−2.25	0.31	4.59	
12:36:21.93	+62:15:16.80	−20.81	−1.70	0.25	4.60	
12:37:08.12	+62:14:34.97	−19.68	−2.05	0.27	4.60	
12:36:15.36	+62:15:07.25	−19.90	−1.85	0.25	4.60	
12:36:51.32	+62:14:59.50	−20.34	−2.15	0.25	4.61	

Continued on next page

Table B.4 – continued from previous page

RA	Dec	M_{1500}/AB mag	β	$\delta\beta$	$z_{\rm phot}$	OK low-z?
12:37:39.47	+62:17:35.46	−19.63	−0.95	0.29	4.62	
12:37:05.45	+62:16:10.70	−19.90	−0.65	0.25	4.62	
12:37:57.51	+62:17:18.84	−21.65	−1.85	0.25	4.63	
12:37:40.42	+62:13:16.55	−19.68	−2.40	0.26	4.64	
12:37:23.28	+62:21:10.87	−19.90	−1.00	0.25	4.64	
12:37:54.76	+62:17:18.93	−19.78	−2.05	0.33	4.64	
12:37:26.46	+62:20:17.28	−19.56	−2.15	0.36	4.65	
12:36:35.83	+62:14:28.04	−19.54	−1.85	0.26	4.66	
12:36:15.56	+62:08:38.21	−20.76	−1.60	0.23	4.67	
12:37:27.77	+62:16:13.31	−20.02	−1.55	0.35	4.68	
12:37:02.27	+62:19:14.30	−19.52	−2.10	0.30	4.68	
12:36:18.89	+62:12:24.81	−19.59	−1.80	0.28	4.69	
12:36:49.60	+62:07:57.83	−20.19	−1.25	0.26	4.70	
12:37:19.72	+62:22:23.41	−19.77	−2.10	0.35	4.70	
12:37:37.70	+62:16:05.70	−19.66	−2.05	0.43	4.70	
12:37:29.23	+62:19:28.40	−20.52	−0.60	0.25	4.72	
12:37:44.99	+62:18:20.24	−19.62	−1.25	0.30	4.73	
12:36:54.51	+62:08:24.89	−19.79	−1.95	0.36	4.74	
12:37:09.25	+62:19:02.13	−19.25	−1.50	0.51	4.80	
12:36:57.48	+62:16:50.45	−19.75	−1.85	0.25	4.80	
12:35:50.58	+62:11:39.31	−19.32	−3.45	0.80	4.83	
12:37:29.84	+62:16:33.97	−19.87	−1.80	0.32	4.84	
12:37:20.90	+62:21:38.84	−19.67	−1.85	0.36	4.86	
12:37:40.42	+62:15:35.42	−20.01	−1.50	0.30	4.88	
12:37:20.74	+62:11:18.40	−19.70	−2.10	0.28	4.91	
12:36:24.19	+62:13:12.82	−19.53	−1.80	0.28	4.91	
12:37:14.41	+62:15:18.95	−19.85	−2.35	0.27	4.92	
12:36:26.92	+62:10:06.19	−20.13	−1.60	0.29	4.92	
12:37:09.83	+62:21:11.26	−20.63	−1.40	0.25	4.93	
12:36:18.78	+62:12:00.93	−20.11	−2.10	0.27	4.93	
12:37:26.12	+62:20:11.25	−19.73	−2.75	0.41	4.94	
12:36:39.19	+62:12:32.86	−19.60	−2.45	0.28	4.94	
12:36:26.34	+62:08:55.98	−20.40	−2.10	0.27	4.94	
12:37:31.07	+62:17:24.38	−19.99	−2.05	0.27	4.94	
12:37:52.42	+62:15:50.97	−19.86	−2.85	0.42	4.94	

Continued on next page

Table B.4 – continued from previous page

RA	Dec	M_{1500}/AB mag	β	$\delta\beta$	$z_{\rm phot}$	OK low-z?
12:36:17.15	+62:15:11.78	−19.68	−2.10	0.27	4.95	
12:37:30.71	+62:16:00.12	−19.68	−1.75	0.30	4.95	
12:36:00.04	+62:12:26.09	−20.82	−2.15	0.24	4.96	
12:36:30.70	+62:09:21.43	−19.73	−2.80	0.69	4.96	
12:36:33.70	+62:10:53.73	−20.29	−2.25	0.29	4.99	
12:37:20.05	+62:21:23.82	−20.58	−1.95	0.23	4.99	
12:37:17.85	+62:11:54.08	−19.84	−2.35	0.26	5.01	
12:37:26.88	+62:14:57.10	−19.86	−2.55	0.25	5.01	
12:36:42.61	+62:11:04.40	−19.98	−1.85	0.27	5.03	
12:37:14.44	+62:19:48.91	−20.12	−1.75	0.28	5.03	
12:36:20.14	+62:11:58.50	−20.03	−0.95	0.26	5.03	×
12:36:57.26	+62:11:15.61	−19.63	−1.90	0.29	5.04	
12:37:25.93	+62:20:01.90	−19.98	−2.50	0.36	5.04	
12:36:49.23	+62:15:38.56	−20.98	−2.15	0.24	5.04	
12:36:52.94	+62:15:49.21	−19.25	−2.00	0.33	5.04	
12:36:34.19	+62:17:08.58	−19.83	−2.35	0.25	5.04	
12:36:23.56	+62:15:19.97	−20.40	−1.95	0.25	5.05	
12:36:55.39	+62:15:48.76	−19.55	−2.40	0.30	5.05	
12:36:14.43	+62:13:10.05	−20.15	−2.05	0.24	5.05	
12:36:52.18	+62:16:17.81	−20.02	−1.65	0.26	5.06	
12:36:13.96	+62:12:50.31	−20.20	−2.20	0.25	5.07	
12:36:21.13	+62:16:07.42	−20.37	−1.95	0.25	5.07	
12:37:26.48	+62:20:15.89	−20.35	−1.80	0.25	5.07	
12:37:44.84	+62:18:17.24	−20.42	−1.90	0.25	5.07	
12:37:15.63	+62:16:23.58	−20.62	−2.05	0.25	5.10	
12:36:33.44	+62:06:40.46	−20.21	−1.65	0.29	5.10	
12:36:57.29	+62:12:49.40	−19.80	−2.30	0.30	5.11	
12:37:15.45	+62:14:11.26	−20.54	−1.45	0.25	5.12	
12:38:06.24	+62:17:05.66	−20.08	−2.75	0.35	5.13	
12:36:51.80	+62:11:11.37	−19.89	−1.65	0.26	5.14	
12:36:30.22	+62:13:44.97	−20.30	−1.45	0.24	5.14	
12:37:30.01	+62:17:07.08	−19.75	−1.60	0.34	5.14	
12:36:39.80	+62:09:49.10	−20.47	−1.85	0.25	5.14	
12:37:21.53	+62:18:32.50	−19.88	−1.80	0.35	5.15	
12:36:17.54	+62:10:22.38	−19.98	−1.60	0.30	5.16	

Continued on next page

Table B.4 – continued from previous page

RA	Dec	M_{1500}/AB mag	β	$\delta\beta$	$z_{\rm phot}$	OK low-z?
12:36:47.26	+62:17:04.21	−20.20	−2.10	0.25	5.17	
12:37:12.61	+62:15:04.11	−19.96	−1.55	0.27	5.17	
12:36:28.81	+62:14:19.16	−19.69	−1.80	0.28	5.17	
12:36:45.32	+62:16:11.68	−19.72	−1.90	0.26	5.18	
12:37:17.34	+62:13:25.28	−20.05	−2.10	0.24	5.20	
12:36:07.86	+62:08:38.33	−20.10	−2.55	0.54	5.21	
12:37:40.54	+62:15:34.85	−19.72	−2.40	0.49	5.21	
12:36:42.02	+62:07:30.52	−20.43	−2.55	0.26	5.21	
12:37:44.74	+62:15:54.14	−19.86	−2.20	0.41	5.22	
12:37:06.47	+62:15:22.88	−20.34	−2.25	0.23	5.22	
12:37:14.51	+62:15:32.57	−19.89	−2.35	0.28	5.23	
12:36:51.39	+62:08:56.57	−20.23	−2.15	0.25	5.23	
12:38:05.71	+62:16:43.82	−21.16	−1.75	0.24	5.24	
12:36:09.53	+62:11:15.84	−21.16	−2.05	0.24	5.24	
12:36:19.02	+62:10:58.35	−20.27	−1.95	0.30	5.24	
12:37:12.80	+62:11:31.99	−20.60	−1.55	0.24	5.24	
12:36:11.91	+62:14:38.53	−20.59	−1.65	0.25	5.26	
12:36:13.64	+62:09:58.08	−20.32	−0.85	0.25	5.26	×
12:36:39.72	+62:18:24.76	−20.26	−2.10	0.26	5.26	
12:36:37.52	+62:12:36.04	−19.96	−1.95	0.24	5.26	
12:36:42.17	+62:11:12.08	−20.51	−1.35	0.24	5.26	
12:37:03.94	+62:12:32.99	−20.95	−1.95	0.25	5.27	
12:37:13.38	+62:12:39.22	−21.03	−2.25	0.25	5.27	
12:36:31.69	+62:09:23.83	−19.94	−1.75	0.39	5.27	
12:36:40.78	+62:16:38.28	−20.48	−2.00	0.24	5.29	
12:36:12.16	+62:10:24.88	−20.64	−2.25	0.26	5.29	
12:37:08.47	+62:15:05.08	−19.74	−2.80	0.33	5.31	
12:36:40.20	+62:11:38.41	−20.34	−0.85	0.25	5.31	×
12:36:35.41	+62:06:45.06	−20.09	−2.00	0.35	5.31	
12:36:48.73	+62:12:16.71	−20.89	−0.40	0.24	5.33	×
12:37:08.04	+62:12:10.93	−20.86	−1.45	0.24	5.33	
12:36:34.86	+62:10:03.92	−19.87	−1.65	0.36	5.33	×
12:37:16.87	+62:14:00.32	−20.66	−1.60	0.24	5.33	
12:36:52.34	+62:16:05.11	−20.45	−1.90	0.25	5.33	
12:38:00.78	+62:16:26.00	−21.71	−1.35	0.24	5.33	

Continued on next page

Table B.4 – continued from previous page

RA	Dec	M_{1500}/AB mag	β	$\delta\beta$	$z_{\rm phot}$	OK low-z?
12:36:28.58	+62:14:10.50	−20.46	−2.25	0.27	5.34	
12:37:03.32	+62:13:31.46	−20.65	−2.05	0.25	5.34	
12:36:16.41	+62:10:29.75	−20.47	−0.90	0.25	5.34	
12:35:56.17	+62:11:45.38	−20.27	−0.80	0.25	5.35	×
12:37:11.11	+62:16:38.58	−20.56	−1.70	0.24	5.35	
12:36:59.45	+62:10:01.58	−20.14	−2.05	0.24	5.35	
12:37:24.83	+62:15:02.76	−20.87	−1.40	0.24	5.36	
12:36:13.43	+62:07:47.95	−20.27	−1.90	0.34	5.36	
12:36:56.36	+62:15:26.99	−20.50	−1.65	0.23	5.36	
12:37:45.04	+62:19:05.35	−20.78	−1.35	0.25	5.36	
12:37:02.72	+62:12:28.84	−20.20	−1.65	0.24	5.37	
12:36:26.48	+62:13:31.62	−20.28	−2.10	0.24	5.37	
12:35:52.16	+62:11:20.82	−20.37	−2.40	0.29	5.38	
12:36:24.78	+62:13:10.91	−19.84	−1.90	0.24	5.39	
12:37:26.47	+62:15:27.20	−20.12	−2.60	0.24	5.41	
12:36:16.67	+62:15:33.93	−20.14	−1.85	0.28	5.42	
12:37:22.85	+62:21:43.84	−20.20	−2.75	0.35	5.42	
12:36:54.32	+62:12:42.89	−20.16	−1.40	0.24	5.42	×
12:36:42.47	+62:09:02.62	−20.19	−1.30	0.26	5.44	
12:36:18.19	+62:10:21.88	−21.29	−1.30	0.25	5.44	
12:36:28.07	+62:13:19.49	−19.76	−1.75	0.29	5.44	
12:35:59.01	+62:12:45.28	−20.53	−1.35	0.24	5.45	
12:35:54.26	+62:10:18.81	−20.07	−2.05	0.37	5.45	
12:36:25.57	+62:07:06.54	−20.12	−2.45	0.39	5.45	
12:37:49.79	+62:17:22.43	−20.33	−2.70	0.34	5.45	
12:35:42.64	+62:12:08.68	−21.01	−1.05	0.23	5.47	
12:37:27.51	+62:18:39.09	−20.16	−2.05	0.30	5.47	
12:36:53.10	+62:12:59.52	−19.81	−2.40	0.29	5.47	
12:35:56.64	+62:11:43.22	−19.96	−1.85	0.36	5.47	
12:36:28.71	+62:14:18.70	−20.04	−2.10	0.25	5.48	
12:37:25.20	+62:18:45.39	−20.48	−1.85	0.25	5.48	

Bibliography

Anders P., Fritze-v. Alvensleben U., 2003, A&A, 401, 1063

Arnouts S., Cristiani S., Moscardini L., Matarrese S., Lucchin F., Fontana A., Giallongo E., 1999, MNRAS, 310, 540

Ashby M. L. N. et al., 2013, ApJ, 769, 80

Astropy Collaboration et al., 2013, A&A, 558, A33

Balestra I. et al., 2010, A&A, 512, A12

Bastian N., Covey K. R., Meyer M. R., 2010, ARA&A, 48, 339

Baugh C. M., Lacey C. G., Frenk C. S., Granato G. L., Silva L., Bressan A., Benson A. J., Cole S., 2005, MNRAS, 356, 1191

Becker R. H. et al., 2001, AJ, 122, 2850

Beckwith S. V. W. et al., 2006, AJ, 132, 1729

Bertin E., Arnouts S., 1996, A&AS, 117, 393

Bessell M. S., Castelli F., Plez B., 1998, A&A, 333, 231

Bolton J. S., Becker G. D., Raskutti S., Wyithe J. S. B., Haehnelt M. G., Sargent W. L. W., 2012, MNRAS, 419, 2880

Bouché N. et al., 2010, ApJ, 718, 1001

Bouwens R. J., Illingworth G. D., Blakeslee J. P., Broadhurst T. J., Franx M., 2004, ApJ, 611, L1

Bouwens R. J., Illingworth G. D., Franx M., Ford H., 2007, ApJ, 670, 928

Bouwens R. J., Illingworth G. D., Franx M., Ford H., 2008, ApJ, 686, 230

Bouwens R. J. et al., 2012a, ApJ, 754, 83

Bouwens R. J. et al., 2011, ApJ, 737, 90

Bouwens R. J. et al., 2013, submitted (arXiv: 1306.2950)

Bouwens R. J. et al., 2010, ApJ, 709, L133

Bouwens R. J. et al., 2012b, ApJ, 752, L5

Bouwens R. J. et al., 2010, ApJ, 708, L69

Bowler R. A. A. et al., 2012, MNRAS, 426, 2772

Bowler R. A. A. et al., 2014, MNRAS, 440, 2810

Bradley L. D. et al., 2012, ApJ, 760, 108

Bradley L. D. et al., 2014, ApJ, 792, 76

Brammer G. B., van Dokkum P. G., Coppi P., 2008, ApJ, 686, 1503

Brammer G. B. et al., 2012, ApJS, 200, 13

Brown M. B., Forsythe A. B., 1974, Journal of the American Statistical Association, 69, pp. 364

Bruzual G., Charlot S., 2003, MNRAS, 344, 1000

Bruzual A. G., 1983, ApJ, 273, 105

Bruzual A. G., Charlot S., 1993, ApJ, 405, 538

Bunker A. J. et al., 2010, MNRAS, 409, 855

Calzetti D., Armus L., Bohlin R. C., Kinney A. L., Koornneef J., Storchi-Bergmann T., 2000, ApJ, 533, 682

Calzetti D., Kinney A. L., Storchi-Bergmann T., 1994, ApJ, 429, 582

Castellano M. et al., 2012, A&A, 540, A39

Castellano M. et al., 2014, A&A, 566, A19

Chabrier G., 2003, PASP, 115, 763

Charlot S., Fall S. M., 1993, ApJ, 415, 580

Charlot S., Fall S. M., 2000, ApJ, 539, 718

Cole S., Lacey C. G., Baugh C. M., Frenk C. S., 2000, MNRAS, 319, 168

Conroy C., 2010, MNRAS, 404, 247

Conroy C., 2013, ARA&A, 51, 393

Conroy C., Gunn J. E., White M., 2009, ApJ, 699, 486

Conroy C., van Dokkum P. G., 2012, ApJ, 760, 71

Conroy C., White M., Gunn J. E., 2010, ApJ, 708, 58

Curtis-Lake E. et al., 2013, MNRAS, 429, 302

Curtis-Lake E. et al., 2012, MNRAS, 422, 1425

Dahlen T. et al., 2013, ApJ, 775, 93

Dayal P., Dunlop J. S., Maio U., Ciardi B., 2013, MNRAS, 434, 1486

Dayal P., Ferrara A., 2012, MNRAS, 421, 2568

de Barros S., Schaerer D., Stark D. P., 2014, A&A, 563, A81

Dey A., Spinrad H., Stern D., Graham J. R., Chaffee F. H., 1998, ApJ, 498, L93

Dijkstra M., Wyithe S., Haiman Z., Mesinger A., Pentericci L., 2014, MNRAS, 440, 3309

Dressel L., 2012, Wide Field Camera 3 Instrument Handbook for Cycle 21 v. 5.0

Dunlop J. S., 2013, in Astrophysics and Space Science Library, Vol. 396, Astrophysics and Space Science Library, Wiklind T., Mobasher B., Bromm V., eds., p. 223

Dunlop J. S., McLure R. J., Robertson B. E., Ellis R. S., Stark D. P., Cirasuolo M., de Ravel L., 2012, MNRAS, 420, 901

Dunlop J. S. et al., 2013, MNRAS, 432, 3520

Dutton A. A., van den Bosch F. C., Dekel A., 2010, MNRAS, 405, 1690

Ellis R. S. et al., 2013, ApJ, 763, L7

Erb D. K., Pettini M., Shapley A. E., Steidel C. C., Law D. R., Reddy N. A., 2010, ApJ, 719, 1168

Eyles L. P., Bunker A. J., Ellis R. S., Lacy M., Stanway E. R., Stark D. P., Chiu K., 2007, MNRAS, 374, 910

Eyles L. P., Bunker A. J., Stanway E. R., Lacy M., Ellis R. S., Doherty M., 2005, MNRAS, 364, 443

Fazio G. G. et al., 2004, ApJS, 154, 10

Finkelstein S. L. et al., 2013, Nature, 502, 524

Finkelstein S. L., Papovich C., Giavalisco M., Reddy N. A., Ferguson H. C., Koekemoer A. M., Dickinson M., 2010, ApJ, 719, 1250

Finkelstein S. L. et al., 2012a, ApJ, 758, 93

Finkelstein S. L. et al., 2012b, ApJ, 756, 164

Finkelstein S. L., Rhoads J. E., Malhotra S., Grogin N., Wang J., 2008, ApJ, 678, 655

Finlator K., Davé R., Papovich C., Hernquist L., 2006, ApJ, 639, 672

Finlator K., Oppenheimer B. D., Davé R., 2011, MNRAS, 410, 1703

Fitzpatrick E. L., Massa D., 1986, ApJ, 307, 286

Fixsen D. J., Cheng E. S., Gales J. M., Mather J. C., Shafer R. A., Wright E. L., 1996, ApJ, 473, 576

Fontana A. et al., 2006, A&A, 459, 745

Fruchter A. S., Hook R. N., 2002, PASP, 114, 144

Fruchter, A., Sosey M., 2009, The MultiDrizzle Handbook, version 3.0

Furusawa H. et al., 2008, ApJS, 176, 1

Galametz A. et al., 2013a, ApJS, 206, 10

Galametz A. et al., 2013b, VizieR Online Data Catalog, 220, 60010

Gall C., Hjorth J., Andersen A. C., 2011, A&A Rev., 19, 43

Geach J. E., Smail I., Best P. N., Kurk J., Casali M., Ivison R. J., Coppin K., 2008, MNRAS, 388, 1473

Gehrz R. D., Sramek R. A., Weedman D. W., 1983, ApJ, 267, 551

González V., Bouwens R., Illingworth G., Labbé I., Oesch P., Franx M., Magee D., 2014, ApJ, 781, 34

González V., Labbé I., Bouwens R. J., Illingworth G., Franx M., Kriek M., 2011, ApJ, 735, L34

González V., Labbé I., Bouwens R. J., Illingworth G., Franx M., Kriek M., Brammer G. B., 2010, ApJ, 713, 115

Grogin N. A. et al., 2011, ApJS, 197, 35

Guhathakurta P., Tyson J. A., Majewski S. R., 1990, ApJ, 357, L9

Gunn J. E., Peterson B. A., 1965, ApJ, 142, 1633

Gunn J. E., Stryker L. L., Tinsley B. M., 1981, ApJ, 249, 48

Guo Y. et al., 2013, ApJS, 207, 24

Habets G. M. H. J., Heintze J. R. W., 1981, A&AS, 46, 193

Hayes M., Schaerer D., Östlin G., Mas-Hesse J. M., Atek H., Kunth D., 2011, ApJ, 730, 8

Heger A., Woosley S. E., 2002, ApJ, 567, 532

Hinshaw G. et al., 2013, ApJS, 208, 19

Hopkins A. M., Beacom J. F., 2006, ApJ, 651, 142

Hopkins P. F., Keres D., Onorbe J., Faucher-Giguere C.-A., Quataert E., Murray N., Bullock J. S., 2013, submitted (arXiv: 1311.2073)

Hu E. M., Cowie L. L., McMahon R. G., 1998, ApJ, 502, L99

Hunter J. D., 2007, Computing In Science & Engineering, 9, 90

Ilbert O. et al., 2006, A&A, 457, 841

Illingworth G. D. et al., 2013, ApJS, 209, 6

Jacoby G. H., Hunter D. A., Christian C. A., 1984, ApJS, 56, 257

Jones T. A., Ellis R. S., Schenker M. A., Stark D. P., 2013, ApJ, 779, 52

Kauffmann G. et al., 2003, MNRAS, 341, 33

Kennicutt, Jr. R. C., 1998, ARA&A, 36, 189

Koekemoer A. M. et al., 2013, ApJS, 209, 3

Koekemoer A. M. et al., 2011, ApJS, 197, 36

Koekemoer A. M., Fruchter A. S., Hook R. N., Hack W., 2002, The 2002 HST Calibration Workshop : Hubble after the Installation of the ACS and the NICMOS Cooling System

Kriek M., Conroy C., 2013, ApJ, 775, L16

Kriek M. et al., 2006, ApJ, 649, L71

Kriek M., van Dokkum P. G., Labbé I., Franx M., Illingworth G. D., Marchesini D., Quadri R. F., 2009, ApJ, 700, 221

Kroupa P., 2001, MNRAS, 322, 231

Labbé I. et al., 2007, ApJ, 665, 944

Labbé I. et al., 2013, ApJ, 777, L19

Laidler V. G. et al., 2007, PASP, 119, 1325

Larson R. B., 1998, MNRAS, 301, 569

Larson R. B., 2005, MNRAS, 359, 211

Larson R. B., Tinsley B. M., 1978, ApJ, 219, 46

Lee K.-S. et al., 2012, ApJ, 752, 66

Lehnert M. D. et al., 2010, Nature, 467, 940

Leitherer C., Heckman T. M., 1995, ApJS, 96, 9

Leitherer C. et al., 1999, ApJS, 123, 3

Lilly S. J., Le Fevre O., Hammer F., Crampton D., 1996, ApJ, 460, L1

Longhetti M., Saracco P., 2009, MNRAS, 394, 774

Lorenzoni S., Bunker A. J., Wilkins S. M., Stanway E. R., Jarvis M. J., Caruana J., 2011, MNRAS, 414, 1455

Lowenthal J. D. et al., 1997, ApJ, 481, 673

Madau P., 1995, ApJ, 441, 18

Madau P., Ferguson H. C., Dickinson M. E., Giavalisco M., Steidel C. C., Fruchter A., 1996, MNRAS, 283, 1388

Madau P., Pozzetti L., Dickinson M., 1998, ApJ, 498, 106

Maraston C., 2005, MNRAS, 362, 799

Maraston C., Pforr J., Renzini A., Daddi E., Dickinson M., Cimatti A., Tonini C., 2010, MNRAS, 407, 830

Massarotti M., Iovino A., Buzzoni A., Valls-Gabaud D., 2001, A&A, 380, 425

McCracken H. J. et al., 2012, A&A, 544, A156

McLure R. J., Cirasuolo M., Dunlop J. S., Foucaud S., Almaini O., 2009, MNRAS, 395, 2196

McLure R. J. et al., 2013, MNRAS, 432, 2696

McLure R. J., Dunlop J. S., Cirasuolo M., Koekemoer A. M., Sabbi E., Stark D. P., Targett T. A., Ellis R. S., 2010, MNRAS, 403, 960

McLure R. J. et al., 2011, MNRAS, 418, 2074

Meurer G. R., Heckman T. M., Calzetti D., 1999, ApJ, 521, 64

Mitra S., Ferrara A., Choudhury T. R., 2013, MNRAS, 428, L1

Mobasher B. et al., 2005, ApJ, 635, 832

Noeske K. G. et al., 2007, ApJ, 660, L43

Oesch P. A. et al., 2010a, ApJ, 709, L21

Oesch P. A. et al., 2010b, ApJ, 709, L16

Oke J. B., Gunn J. E., 1983, ApJ, 266, 713

Oliphant T. E., 2007, Computing in Science & Engineering, 9, 10

Olive K. A., Steigman G., Walker T. P., 2000, Phys. Rep., 333, 389

Ono Y. et al., 2013, ApJ, 777, 155

Ota K. et al., 2008, ApJ, 677, 12

Ouchi M. et al., 2008, ApJS, 176, 301

Overzier R. A. et al., 2008, ApJ, 673, 143

Pacifici C., Charlot S., Blaizot J., Brinchmann J., 2012, MNRAS, 421, 2002

Papovich C., Dickinson M., Ferguson H. C., 2001, ApJ, 559, 620

Papovich C. et al., 2004, ApJ, 600, L111

Papovich C., Finkelstein S. L., Ferguson H. C., Lotz J. M., Giavalisco M., 2011, MNRAS, 412, 1123

Partridge R. B., Peebles P. J. E., 1967, ApJ, 147, 868

Pei Y. C., Fall S. M., Bechtold J., 1991, ApJ, 378, 6

Peng C. Y., Ho L. C., Impey C. D., Rix H.-W., 2010, AJ, 139, 2097

Pentericci L. et al., 2011, ApJ, 743, 132

Pentericci L., Grazian A., Fontana A., Castellano M., Giallongo E., Salimbeni S., Santini P., 2009, A&A, 494, 553

Pentericci L., Grazian A., Fontana A., Salimbeni S., Santini P., de Santis C., Gallozzi S., Giallongo E., 2007, A&A, 471, 433

Pérez F., Granger B. E., 2007, Computing In Science & Engineering, 9, 21

Pickles A. J., 1998, PASP, 110, 863

Planck Collaboration et al., 2013, submitted (arXiv: 1303.5076)

Popesso P. et al., 2009, A&A, 494, 443

Postman M. et al., 2012, ApJS, 199, 25

Raiter A., Fosbury R. A. E., Teimoorinia H., 2010, A&A, 510, A109

Reddy N. et al., 2012a, ApJ, 744, 154

Reddy N. A., Erb D. K., Pettini M., Steidel C. C., Shapley A. E., 2010, ApJ, 712, 1070

Reddy N. A., Pettini M., Steidel C. C., Shapley A. E., Erb D. K., Law D. R., 2012b, ApJ, 754, 25

Renzini A., 2009, MNRAS, 398, L58

Robertson B. E., Ellis R. S., Dunlop J. S., McLure R. J., Stark D. P., 2010, Nat, 468, 49

Robertson B. E. et al., 2013, ApJ, 768, 71

Rogers A. B., McLure R. J., Dunlop J. S., 2013, MNRAS, 429, 2456

Rogers A. B. et al., 2014, MNRAS, 440, 3714

Rolfs C. E., Rodney W. S., 1988, Cauldrons in the cosmos: Nuclear astrophysics. University of Chicago Press

Salpeter E. E., 1955, ApJ, 121, 161

Sargent M. T., Béthermin M., Daddi E., Elbaz D., 2012, ApJ, 747, L31

Sargent W. L. W., Young P. J., Boksenberg A., Tytler D., 1980, ApJS, 42, 41

Schaerer D., 2002, A&A, 382, 28

Schaerer D., 2003, A&A, 397, 527

Schaerer D., de Barros S., 2009, A&A, 502, 423

Schawinski K., Thomas D., Sarzi M., Maraston C., Kaviraj S., Joo S.-J., Yi S. K., Silk J., 2007, Monthly Notices of the Royal Astronomical Society, 382, 1415

Schechter P., 1976, ApJ, 203, 297

Schenker M. A. et al., 2013, ApJ, 768, 196

Schenker M. A., Stark D. P., Ellis R. S., Robertson B. E., Dunlop J. S., McLure R. J., Kneib J.-P., Richard J., 2012, ApJ, 744, 179

Schmidt M., 1965, ApJ, 141, 1295

Searle L., Sargent W. L. W., Bagnuolo W. G., 1973, ApJ, 179, 427

Shapley A. E., Steidel C. C., Erb D. K., Reddy N. A., Adelberger K. L., Pettini M., Barmby P., Huang J., 2005, ApJ, 626, 698

Shapley A. E., Steidel C. C., Pettini M., Adelberger K. L., 2003, ApJ, 588, 65

Shu F. H., Adams F. C., Lizano S., 1987, ARA&A, 25, 23

Smit R., Bouwens R. J., Franx M., Illingworth G. D., Labbé I., Oesch P. A., van Dokkum P. G., 2012, ApJ, 756, 14

Smit R. et al., 2014, ApJ, 784, 58

Sobral D., Smail I., Best P. N., Geach J. E., Matsuda Y., Stott J. P., Cirasuolo M., Kurk J., 2013, MNRAS, 428, 1128

Somerville R. S., Gilmore R. C., Primack J. R., Domínguez A., 2012, MNRAS, 423, 1992

Somerville R. S., Hopkins P. F., Cox T. J., Robertson B. E., Hernquist L., 2008, MNRAS, 391, 481

Somerville R. S., Primack J. R., Faber S. M., 2001, MNRAS, 320, 504

Stanway E. R., McMahon R. G., Bunker A. J., 2005, MNRAS, 359, 1184

Stark D. P., Ellis R. S., Bunker A., Bundy K., Targett T., Benson A., Lacy M., 2009, ApJ, 697, 1493

Stark D. P., Ellis R. S., Chiu K., Ouchi M., Bunker A., 2010, MNRAS, 408, 1628

Stark D. P., Ellis R. S., Ouchi M., 2011, ApJ, 728, L2

Stark D. P., Ellis R. S., Richard J., Kneib J.-P., Smith G. P., Santos M. R., 2007, ApJ, 663, 10

Stark D. P., Schenker M. A., Ellis R., Robertson B., McLure R., Dunlop J., 2013, ApJ, 763, 129

Steidel C. C., Adelberger K. L., Giavalisco M., Dickinson M., Pettini M., 1999, ApJ, 519, 1

Steidel C. C., Giavalisco M., Pettini M., Dickinson M., Adelberger K. L., 1996, ApJ, 462, L17

Steidel C. C., Hamilton D., 1992, AJ, 104, 941

Steidel C. C., Hamilton D., 1993, AJ, 105, 2017

Steidel C. C., Pettini M., Hamilton D., 1995, AJ, 110, 2519

Szalay A. S., Connolly A. J., Szokoly G. P., 1999, AJ, 117, 68

Tinsley B. M., 1968, ApJ, 151, 547

Tinsley B. M., 1972, A&A, 20, 383

Tinsley B. M., 1973, ApJ, 186, 35

Tinsley B. M., Gunn J. E., 1976, ApJ, 203, 52

Todini P., Ferrara A., 2001, MNRAS, 325, 726

Tokunaga A. T., Vacca W. D., 2005, PASP, 117, 421

Trenti M. et al., 2011, ApJ, 727, L39

Trenti M. et al., 2012, ApJ, 746, 55

Tumlinson J., 2007, ApJ, 664, L63

Tumlinson J., Venkatesan A., Shull J. M., 2004, ApJ, 612, 602

van Dokkum P. G., 2008, ApJ, 674, 29

van Dokkum P. G., Conroy C., 2010, Nature, 468, 940

van Dokkum P. G., Conroy C., 2011, ApJ, 735, L13

van Dokkum P. G., Conroy C., 2012, ApJ, 760, 70

van Dokkum P. G. et al., 2009, PASP, 121, 2

Vanzella E. et al., 2008, A&A, 478, 83

Vanzella E. et al., 2009, ApJ, 695, 1163

Vanzella E. et al., 2011, ApJ, 730, L35

Verma A., Lehnert M. D., Förster Schreiber N. M., Bremer M. N., Douglas L., 2007, MNRAS, 377, 1024

Wagoner R. V., 1973, ApJ, 179, 343

Weingartner J. C., Draine B. T., 2001, ApJ, 548, 296

Weinmann S. M., Neistein E., Dekel A., 2011, MNRAS, 417, 2737

Whitaker K. E. et al., 2011, ApJ, 735, 86

Wiklind T., Dickinson M., Ferguson H. C., Giavalisco M., Mobasher B., Grogin N. A., Panagia N., 2008, ApJ, 676, 781

Wild V., Charlot S., Brinchmann J., Heckman T., Vince O., Pacifici C., Chevallard J., 2011, MNRAS, 417, 1760

Wilkins S. M., Bunker A., Coulton W., Croft R., Matteo T. D., Khandai N., Feng Y., 2013, MNRAS, 430, 2885

Wilkins S. M., Bunker A. J., Ellis R. S., Stark D., Stanway E. R., Chiu K., Lorenzoni S., Jarvis M. J., 2010, MNRAS, 403, 938

Wilkins S. M., Bunker A. J., Stanway E., Lorenzoni S., Caruana J., 2011, MNRAS, 417, 717

Wilkins S. M., Gonzalez-Perez V., Lacey C. G., Baugh C. M., 2012, MNRAS, 424, 1522

Windhorst R. A. et al., 2011, ApJS, 193, 27

Wuyts S. et al., 2011, ApJ, 738, 106

Yan H., Dickinson M., Giavalisco M., Stern D., Eisenhardt P. R. M., Ferguson H. C., 2006, ApJ, 651, 24

Yan H. et al., 2005, ApJ, 634, 109

Yan H. et al., 2011, ApJ, 728, L22

Zackrisson E., Bergvall N., Leitet E., 2008, ApJ, 676, L9